

Measurement of the Cosmic Ray Proton Spectrum with H.E.S.S. and Characterization of the TARGET ASICs for the CTA

Messung des Energiespektrums
kosmischer Protonen mit H.E.S.S.
und Charakterisierung der TARGET ASICs
für das CTA

Der Naturwissenschaftlichen Fakultät
der Friedrich-Alexander-Universität Erlangen-Nürnberg
zur Erlangung des Doktorgrades Dr. rer. nat.

vorgelegt von
David Jankowsky
aus Neustadt an der Waldnaab

Als Dissertation genehmigt von der Naturwissenschaftlichen Fakultät
der Friedrich-Alexander-Universität Erlangen-Nürnberg

Tag der mündlichen Prüfung:

Vorsitzender des
Promotionsorgans:

Prof. Dr. Georg Kreimer

Abstract

Through the study of cosmic rays, a lot can be learned about mechanisms in particle physics as well as about astronomy. An interesting component of the cosmic rays are protons since they are the most abundant particles. This component was already measured by various experiments but mainly at high altitudes with balloons or even satellites. Because of their small detection area, they suffer from low statistics, especially at high energies. A solution to this problem are ground-based telescope systems due to their large detection area but with the downside of larger systematic errors. In this work, a current-generation imaging atmospheric Cherenkov telescope system, namely H.E.S.S., was used to detect these particles and to reconstruct their energy spectrum. Since protons are usually the most prominent background in gamma-ray analyses, the standard approach of reconstruction had to be adapted. The first step was the verification of the hadronic simulations since they play a crucial role in the analysis and are sensitive to errors. The reconstruction itself is based on the well known Hillas approach but was optimized for the needs of the proton analysis. After various tests that verified the stability of the analysis, real data from the first H.E.S.S. phase with the four small telescopes was analyzed. In the developed approach, it was possible to measure the proton spectrum from around 3 TeV to roughly 100 TeV because of difficulties in the reconstruction at low energies and significant contamination with heavy nuclei at high energies. In contrast to expectations from theory, not a pure power law was observed but rather a broken power law with a change in the spectral index from $\gamma_1 = 2.66$ to $\gamma_2 = 2.93$ at 12.3 TeV. This break was only very recently discovered by other experiments and the results in this work harden the evidence of this break in the proton spectrum. Besides, a second break was already discovered at GeV energies even before. Both discovered breaks in the spectrum challenge the current picture of cosmic ray theories.

Since the current generation of imaging atmospheric Cherenkov telescopes were already built more than 15 years ago, a lot of experience as well as new technologies became available. Therefore, new gamma-ray experiments are getting ready, and one of the most exciting ones is the Cherenkov Telescope Array. This experiment will outperform the current generation in every aspect, but one of the most important parts is the extension of the energy range due to the use of three different, specialized telescope types. The highest energies will be accessible by the so-called SSTs, the small-sized telescopes. In the second part of this work, the front end electronics of these telescopes were tested. The most crucial parts of the electronics are two ASICs, the TARGET C ASIC, which handles the digitization of the measurements and the T5TEA ASIC, which is responsible for the creation of trigger signals. Both ASICs were heavily tested, calibration techniques were developed as well as investigated and the charge resolution was calculated as a final performance parameter. Both ASICs showed a very good behavior, met all requirements and recently, the camera which uses this ASICs, called CHEC, was chosen to be part of the Cherenkov Telescope Array.

Zusammenfassung

Durch Beobachtung und Messung kosmischer Teilchen kann viel über Prozesse der Teilchenphysik und der Astronomie gelernt werden. Die vielleicht interessanteste Komponente sind Protonen, da sie den Großteil aller kosmischer Teilchen ausmachen. Diese Protonen wurden bereits von einigen Experimenten, hauptsächlich Ballon- und Satellitenexperimente, vermessen, jedoch mit dem Nachteil einer relativ kleinen Detektionsfläche, was vor allem bei hohen Energien zu schlechter Statistik führt. Eine Lösung dieses Problems ist das Nutzen von bodengebundenen Experimenten, da diese eine sehr viel größere Detektionsfläche besitzen. Allerdings haben diese Experimente wiederum mit größeren, systematischen Fehlern zu kämpfen. In dieser Arbeit wurden Daten eines aktuellen Cherenkov Teleskopsystems, genannt H.E.S.S., benutzt um diese Protonen zu detektieren und deren Energiespektrum zu rekonstruieren. Im normalen Betrieb solcher Teleskope sind Protonen der größte Untergrund, der nicht für die eigentliche Analyse verwendet wird. Deshalb musste für die Rekonstruktion eben dieser Teilchen das standardmäßige Vorgehen stark angepasst werden. Die ersten Schritte waren Test und Verifikation von den genutzten, hadronischen Simulationen, da diese eine wichtige Rolle bei der Rekonstruktion spielen und relativ fehleranfällig sind. Die eigentliche Analyse nutzt die bekannte Rekonstruktion nach Hillas, welche jedoch für Protonen optimiert wurde. Diese Herangehensweise wurde ausgiebig getestet und da es sich zeigte, dass sie gut und stabil funktioniert, auch auf reale Daten angewandt. Mit dieser Analyse konnte das Energiespektrum der Protonen von ungefähr 3 TeV bis zu 100 TeV vermessen werden. Dabei wurde die untere Grenze des Energiebereichs durch Probleme in der Rekonstruktion vorgegeben und die obere Grenze durch eine beginnende Kontamination der Protonen mit schwereren Kernen. Im Gegensatz zu den theoretischen Erwartungen wurde kein einfaches Potenzgesetz beobachtet, sondern ein gebrochenes, welches seinen spektralen Index von $\gamma_1 = 2.66$ zu $\gamma_2 = 2.93$ bei einer Energie von etwa 12.3 TeV wechselt. Eine solche spektrale Änderung wurde erst vor kurzem von anderen Experimenten beobachtet, weswegen die Ergebnisse dieser Arbeit als weiterer Beweis eben jener Beobachtung dienen können. Da neben dieser Änderung auch bereits weitere im Spektrum beobachtet wurden, müssen die vorhandenen, theoretischen Modelle weiter verfeinert und angepasst werden.

Die aktuelle Generation solcher Cherenkov Teleskope ist bereits seit mehr als 15 Jahren im Einsatz und so konnte in diesem Zeitraum viel Erfahrung gesammelt und neue Technologien entwickelt werden. Deshalb sind bereits einige neue Experimente im Gebiet der Gammastrahlungsastronomie in den Startlöchern und das Cherenkov Telescope Array scheint eines der vielversprechendsten zu sein. Dieses neue Experiment wird die aktuelle Generation in allen Belangen übertreffen, wobei der erweiterte, zugängliche Energiebereich eines der auffälligsten Merkmale ist. Dies ist durch die Nutzung von drei verschiedenen, spezialisierten Teleskoptypen möglich. Die höchsten Energien werden dabei von den sogenannten SSTs vermessen, den kleinsten aber dafür zahlreichsten Teleskopen. In dieser Arbeit wurde deren Auslese- und Triggerelektronik getestet, wobei die wichtigsten Bauteile zwei ASICs sind, der TARGET C ASIC zur Digitalisierung der gemessenen Daten und T5TEA, welcher für die Generierung von Triggersignalen zuständig ist. Beide ASICs wurden ausgiebig getestet, es wurden Techniken zur Kalibration entwickelt und analysiert und am Ende wurde als finaler Parameter die Ladungsauflösung bestimmt. Es zeigte sich, dass beide ASICs eine sehr gute Leistung haben und allen Ansprüchen des Cherenkov Telescope Arrays genügen. Zum zeitlichen Ende der Arbeit wurde außerdem entschieden, dass die Kamera, welche die TARGET ASICs nutzt, für dieses neue Experiment genutzt werden wird.

Contents

I	The Cosmic Ray Proton Spectrum	1
1	An introduction to cosmic rays	3
1.1	The discovery of cosmic rays - a short historical timeline	4
1.2	The cosmic ray spectrum	5
1.3	Acceleration and origin of cosmic rays	13
1.3.1	Acceleration of cosmic rays	13
1.3.2	Supernova remnants as possible CR sources	16
1.3.3	Gamma rays	17
2	The detection of cosmic rays	21
2.1	Particle showers in Earth's atmosphere	22
2.1.1	Extensive air showers	22
2.1.2	Emission of Cherenkov light	25
2.1.3	Detection of Cherenkov light with IACTs	27
2.2	H.E.S.S. - The High Energy Stereoscopic System	29
2.2.1	The telescopes and cameras	29
2.2.2	Raw data calibration	30
2.2.3	Hillas analysis - the standard reconstruction	32
2.3	Simulation of air showers and the detector response	40
3	The analysis of cosmic ray protons	43
3.1	Validation of the Monte Carlo simulations	43
3.1.1	Method and first results	44
3.1.2	Verification of simulation settings and parameters	46
3.1.3	Results and conclusion	55
3.2	Event selection and reconstruction	57
3.2.1	Optimization of the reconstruction	57
3.2.2	Performance of the reconstruction	60
3.3	Background rejection	63
3.3.1	Heavy nuclei	63
3.3.2	Gamma rays and electrons	65
3.4	Run selection and data set	66

4	The reconstruction of the cosmic ray proton spectrum	69
4.1	Spectral analysis	69
4.1.1	Forward folding	73
4.1.2	Flux calculation and model fitting	74
4.1.3	Reconstruction of a MC proton spectrum	75
4.2	The proton energy spectrum with real data	77
4.3	Studies of systematic uncertainties	80
4.3.1	Observational conditions	82
4.3.2	Analysis conditions	83
4.3.3	Interaction models	84
5	Discussion, interpretation and outlook	89
A	Appendix - the cosmic ray proton spectrum	99
A.1	Validation of Monte Carlo simulations	99
A.2	Reconstruction of a MC proton spectrum	103
A.3	Thoughts on the helium contamination	105
A.4	The proton energy spectrum with real data	107
II	Characterization of the Target C and T5TEA ASICs	109
1	The future of VHE gamma-ray astronomy	111
1.1	The current status of gamma-ray astronomy	112
1.2	CTA - The Cherenkov Telescope Array	112
1.2.1	Science and performance goals	113
1.2.2	Two sites and three different telescopes	114
1.3	The highest energies - CHEC and its electronics	117
2	TARGET - front end electronics for the CTA	119
2.1	TARGET C and T5TEA	120
2.1.1	T5TEA	120
2.1.2	TARGET C	122
2.2	TARGET modules	123
3	General performance and calibration of the TARGET ASICs	125
3.1	T5TEA - trigger performance	125
3.1.1	Tuning of T5TEA performance - parameter scans	127
3.1.2	Output signal of T5TEA	130
3.1.3	Crosstalk of the trigger path	131
3.2	TARGET C - digitization	132
3.2.1	Pedestal calibration and baseline noise	132
3.2.2	Signal injection and digitization	134
3.2.3	Time base tuning and sampling frequency	135
3.2.4	Crosstalk of the sampling path	138
3.2.5	DC transfer functions	141
3.2.6	AC transfer functions	142
3.3	TARGET - large scale tests for the camera	150

4	Final electronic performance - the charge resolution	155
4.1	Definition of the charge resolution	155
4.2	The electronic charge resolution of TARGET	156
4.2.1	Charge resolution of different calibrations, channels and modules . . .	161
4.3	The final charge resolution	163
5	Conclusion and outlook	165
B	Appendix - characterization of the TARGET C and T5TEA ASICs	167
B.1	Electronic equipment used for the measurements	167
B.2	T5TEA - configuration values after optimization	168
B.3	Target C Measurements	168
B.3.1	Pedestal Calibration and Baseline Noise	168
B.3.2	AC Transfer Functions	169
B.4	Available and tested modules	172
B.5	Charge resolution	173
B.5.1	Optimization of the summing method	173
B.5.2	Influence of the shaping on the pulse shape	174
B.5.3	Influence of the position in the sampling array on the measured area .	175
	Bibliography	177

Part I

The Cosmic Ray Proton Spectrum

CHAPTER 1

An introduction to cosmic rays

“I SEE THAT IT IS BY NO MEANS USELESS TO TRAVEL, IF A
MAN WANTS TO SEE SOMETHING NEW.”

Jules Verne (1873)



Figure 1.1: Victor Franz Hess, in the center of the basket, directly before the start of one of his balloon flights sometime between the years 1911 and 1912. (Reference: VF Hess Society, Echophysics, Schloss Pöllau/Österreich)

1.1 The discovery of cosmic rays - a short historical timeline

The second half of the 19th century brought many breakthroughs regarding the research of electricity and radiation. There was the discovery of X-rays by Conrad Röntgen in 1895 or the observation of radioactivity by Henri Becquerel in 1896. Later on, Marie Curie detected that this radioactive radiation had the ability to ionize the surrounding air. This ionizing radiation can be measured with the help of so-called electroscopes, which were developed by her husband, Pierre Curie: charged electroscopes discharge again in the vicinity of radioactive sources or even without additional sources because of natural radiation. Besides other investigations regarding the newly found ionizing radiation, Franz Linke, a meteorologist, started to perform balloon flights to measure the ionization of the atmosphere in the years 1902 and 1903. During these flights, Linke already found hints of an increase of ionized particles at higher altitudes, which was not expected at that time. It was thought that all of this ionizing radiation comes from Earth's radioactivity, not from extraterrestrial radiation. However, in the following years, other scientists found similar but also contradicting results. It took almost ten years until another physicist solved the mystery of this ionizing radiation: Victor Franz Hess, at that time a research assistant at the Institute for Radium Research in Vienna. He did more balloon flights, to larger altitudes and with better equipment. In Figure 1.1, he is shown shortly before the start of one of his balloon trips. After the evaluation of his measurements, he obtained the results shown in Figure 1.2 and drew the following conclusion:

“The results of the present observations seem most likely to be explained by the assumption that radiation of very high penetrating power enters from above into our atmosphere, and even in its lowest layers causes part of the ionization observed in closed vessels.” (Hess 1912)

The results were soon confirmed independently by Werner Kolhörster, an assistant at the University of Halle. He also made balloon flights in the following years 1913 / 1914 and reached altitudes of up to 9300 m where he measured an even larger ionization of $80.4 \text{ cm}^{-3}\text{s}$. He came to the same conclusion that this radiation is of cosmic origin. After a research break due to World War I, Robert Millikan “rediscovered” these cosmic rays in the year 1926, but nevertheless, Victor Hess was honored with the Nobel Prize in physics for his discovery in the year 1936.

This discovery of cosmic particles was also a primary driving force for the development of particle physics. Many invented devices were used to measure and analyze the newly found cosmic rays. In the following time until now, particle physicists, who use earthbound particle accelerators, work closely together with astroparticle physicists, who use cosmic accelerators in the whole universe. A lively exchange of knowledge, analyses and techniques helped to push astroparticle physics even further. Other scientific milestones on the way to the current cosmic ray experiments include (Walter 2012):

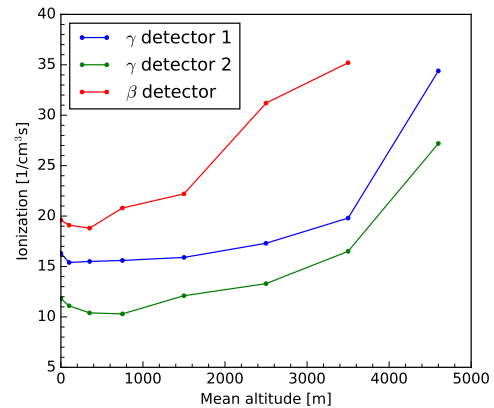


Figure 1.2: Combined results of all seven balloon flights of Victor Hess. (Data taken from Hess (1912))

- the use of the coincidence method with Geiger-Müller counters for the measurement of cosmic rays by W. Bothe and W. Kolhörster in 1928,
- the first air Cherenkov counter, built in 1953 by W. Galbraith and J.V. Jelley out of a rubbish bin and a photomultiplier,
- the launch of the satellites Sputnik 2 and 3 in the years 1957 and 1958, which included cosmic ray counters,
- the development of water Cherenkov detectors by N. Porter in the year 1958,
- the Volcano Ranch extensive air shower experiment, which was operating three years from 1960 to 1963 and measured cosmic rays with energies greater than 10^{20} eV for the first time,
- or the detection of gamma rays from the Crab Nebula with the Whipple telescope in 1989.

All these important experiments and many more led to the current generation of cosmic ray experiments. These include, besides many others, the Imaging Atmospheric Cherenkov Telescopes (IACTs) like H.E.S.S. (Hinton 2004), the neutrino detectors IceCube (Aartsen et al. 2018b) and ANTARES (Ageron et al. 2011), the largest extensive air shower array Pierre Auger Observatory (Pierre Auger Collaboration 2015) or even space born experiments like the gamma-ray satellite Fermi (Atwood et al. 2009) or AMS (Aguilar et al. 2013), which is part of the International Space Station. However, despite that this part of astrophysics exists for more than one hundred years and that many experiments were carried out, some riddles are still unsolved, even the exact origin of the highly energetic particles or their acceleration mechanisms are not fully understood by the scientists.

The goal of the analysis in this thesis is the measurement of the cosmic ray proton spectrum with imaging atmospheric Cherenkov telescopes as an additional access to CR protons at TeV energies. Thus, the following two sections will give a short overview of the cosmic rays itself. In Section 1.2, the cosmic ray energy spectrum measured here at Earth will be discussed, including the spectra of different particles, distinct features in the spectra as well as theoretical models that are able to explain these features. Section 1.3 will focus on the production and acceleration mechanisms of different source types of cosmic rays. Chapter 2 outlines the physics behind the detection of cosmic rays with an IACT, the development of particle showers in the atmosphere, the emission of Cherenkov radiation and their detection with H.E.S.S. as well as the simulation of all corresponding processes. Afterward, Chapter 3 presents the development of a stable analysis chain for the reconstruction of CR protons followed by Chapter 4, which focuses on the reconstruction of the spectrum itself, including tests and verifications on simulations. Chapter 5 completes the work on the proton spectrum with a discussion and an outlook.

1.2 The cosmic ray spectrum

The cosmic ray (CR) spectrum, as it is measured at the Earth, is shown in Figure 1.3 over the full energy range of more than 12 decades. The figure combines the all-particle cosmic ray spectrum with the ones measured for protons, electrons and positrons, neutrinos, gamma

rays and antiprotons. The cosmic rays can be split into primary and secondary cosmic rays regarding their origin. Primary cosmic rays are thought to originate and to be accelerated directly at their sources. This group combines the electrons, protons, helium and all heavier nuclei that were abundantly created in the nucleosynthesis during the big bang and in stars. Secondary cosmic rays are all other particles that are created by the primary cosmic rays during collisions with the nuclei of atoms and molecules of the interstellar medium. This combines the mentioned antiparticles and nuclei with larger abundances as created during nucleosynthesis (e.g lithium, beryllium or boron). Neutrinos and gamma rays are also created during interactions of the primary cosmic rays, however, they usually are not counted as cosmic rays.

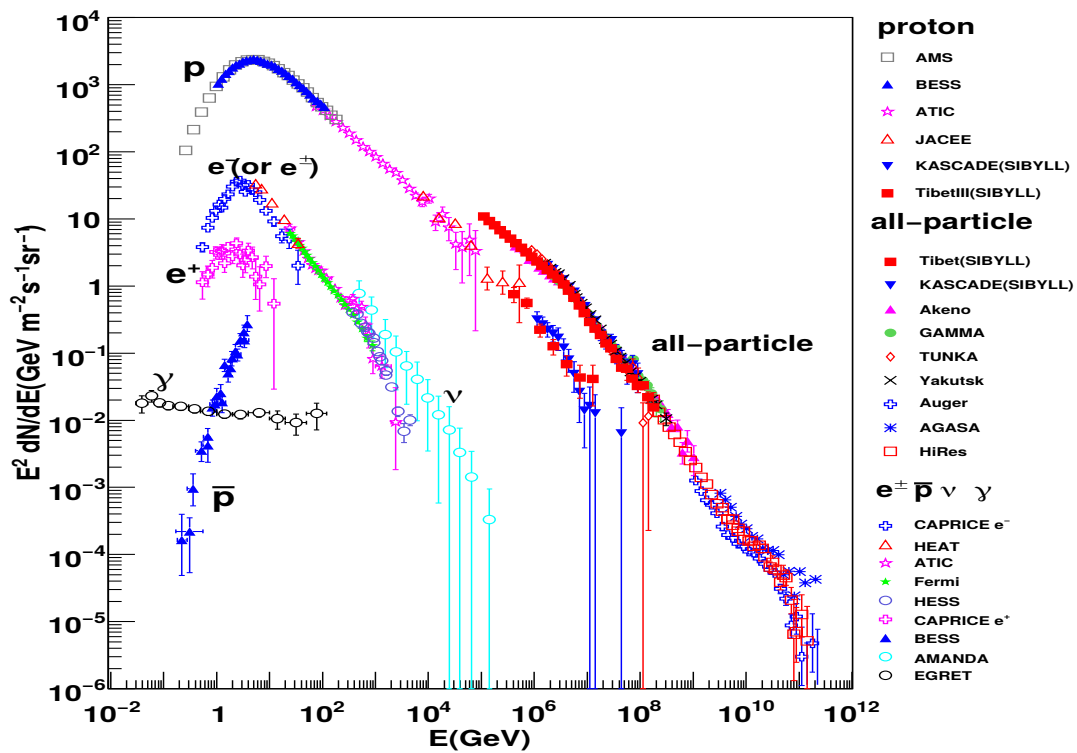


Figure 1.3: The differential cosmic ray spectrum measured with various experiments. In addition to the all-particle spectrum, the spectra of protons, electrons and positrons, neutrinos, diffuse gamma rays and antiprotons are shown. (Hu 2009)

Since the main focus of this work lies on the nucleonic part of the cosmic ray spectrum, the proton and all-particle spectrum will be explained in more detail. The spectra of the electrons and of the antiparticles will be shortly described hereafter. By looking again at Figure 1.3, three main parts can be noticed. Most abundant in the nucleonic CRs are the protons contributing around 87%, followed by helium nuclei with roughly 12% abundance and the small part of remaining particles, only 1%, are heavier nuclei. Figure 1.4 shows the measured spectra of some heavier, primary nuclei up to the element iron.

One distinct feature of all spectra is the decreasing flux towards low energies, e.g. for protons below 1 GeV. This effect is caused by the outflow of particles from our sun, the so-called solar wind. These particles create disturbances in the magnetic fields of the planets that interfere with the propagation of cosmic rays with lower energies. Thus, the cosmic rays do not reach the Earth anymore, leading to the observed cutoff in the spectrum towards low energies. This effect also follows the periodic solar activity and is therefore called solar modulation. Above the cutoff, the all particle cosmic ray spectrum of primary nuclei can be well described by power laws. For the energy range from a few GeV to some 100 TeV, it can be roughly approximated by the following energy-dependent intensity (Tanabashi et al. 2018):

$$I_N(E) \approx 1.8 \times 10^4 (E/1 \text{ GeV})^{-\gamma} \frac{\text{nucleons}}{\text{m}^2 \text{ s sr GeV}}, \quad (1.1)$$

where $\gamma \approx 2.7$ is the differential spectral index and E the energy of the nucleons. The different elements can also be described by power laws, however, they differ in their flux levels and their spectral shapes since they show different slopes or spectral features. Some of these differences and features will be touched in the next paragraphs and some additional references will be given since the effects and their explanations are quite complex.

Many of such observations can be explained by the propagation of cosmic rays that is usually modeled with the diffusion-loss equation (e.g. Longair (2011)):

$$\frac{\partial N_i}{\partial t} = D \nabla^2 N_i + \frac{\partial}{\partial E} (b(E) N_i) + Q_i - \frac{N_i}{\tau_i} + \sum_{j>i} \frac{P_{ji}}{\tau_j} N_j. \quad (1.2)$$

The index i names the particle species and N_i the number density of the corresponding particles. The following terms describe the different mechanisms that influence the particle density. $D \nabla^2 N_i$ is the diffusion term, $\partial/\partial E (b(E) N_i)$ (with $b(E) = -dE/dt$) describes energy losses and gains, Q_i is the rate of injection and the last two terms model spallation. The first spallation term is for the destruction of particle i with a lifetime τ_i , the second one is for the production of particle i by the destruction of particles j with corresponding lifetimes τ_j and the probability P_{ji} to create the particle i from j . A more detailed discussion of the transport equation can also be found in Strong et al. (2007) but a few interesting measurements regarding the cosmic ray spectra at intermediate energies will be explained here.

As was already mentioned, the abundances of different nuclei can be measured. When they are compared to the existing nuclei in the solar system, some of the elements are more abundant in cosmic rays, e.g. the light elements lithium, beryllium and boron, the heavier elements with atomic numbers below iron but above calcium or even some of the ultra heavy nuclei with $Z > 42$. This observation can be explained by spallation effects that appear while the particles propagate through the interstellar medium towards Earth (see e.g. the slab or leaky box models (Strong et al. 2007)). Similar, unexpected abundances can also be observed while studying isotopes. By looking at the isotopes of hydrogen or helium (^1H , ^2H , ^3He and ^4He) in the CR composition, the isotopes ^2H and ^3He are much more common than observed in the solar system or expected from the nucleosynthesis during the Big Bang. They are also created while propagating through the interstellar medium, particularly through the spallation of ^4He and through the process $p + p \rightarrow ^2\text{H} + \pi^+$ (Adriani et al. 2013; Coste et al. 2012). Other interesting isotopes are radioactive ones since their limited lifetime can be used to measure time scales of CR propagation processes ("cosmic clocks"). One of the most known cosmic clocks is the beryllium isotope ^{10}Be with a half-life of 1.5 My, which is

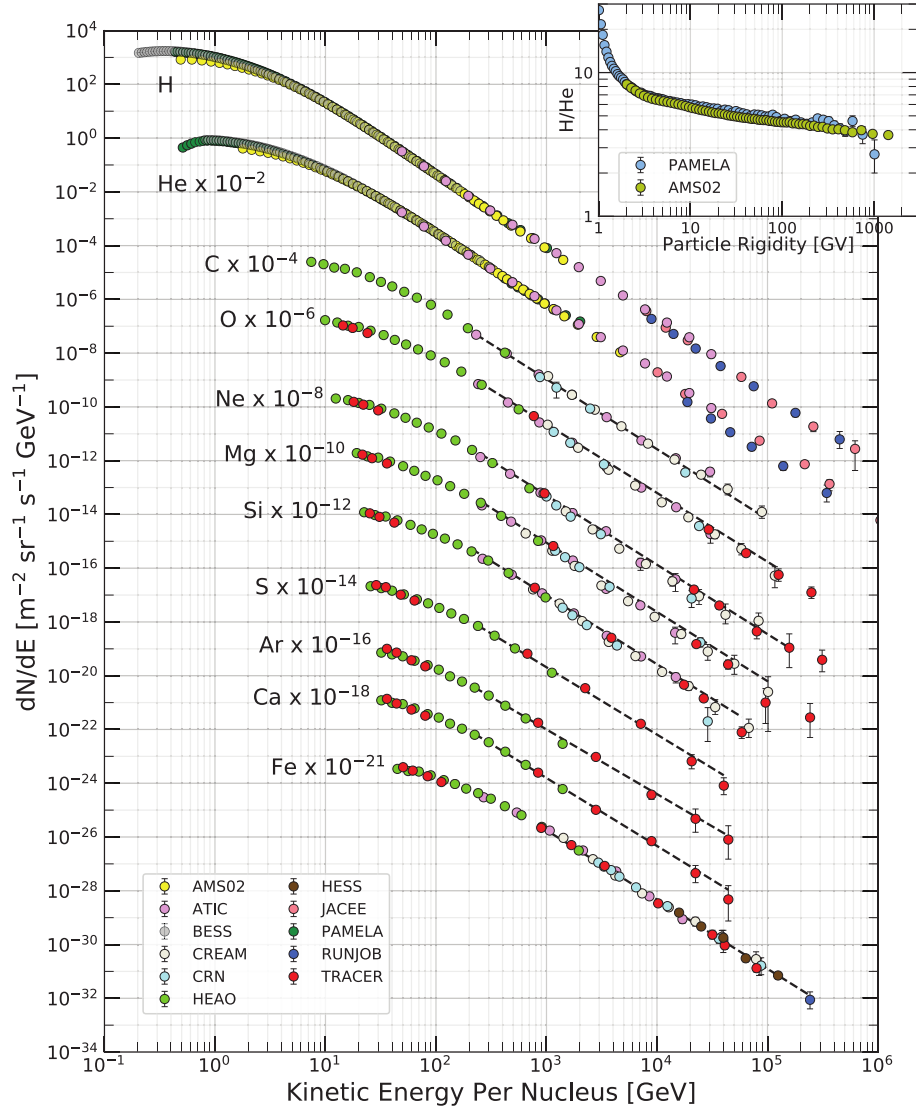


Figure 1.4: The differential spectra of all major components of the cosmic radiation with a primary origin. The smaller figure shows the proton to helium ratio. (Tanabashi et al. 2018)

already mostly decayed after CR propagation, giving a good estimate of the confinement time to be $\tau_{esc} \approx 10^7$ years (Mewaldt et al. 2001). Another important measurement is the ratio of primary and secondary cosmic rays, like boron (secondary) to carbon (primary), which gives further insight into propagation models (Aguilar et al. 2016). It was furthermore found that this ratio depends on the energy that can be explained by energy-dependent escape rates or differences during the acceleration processes.

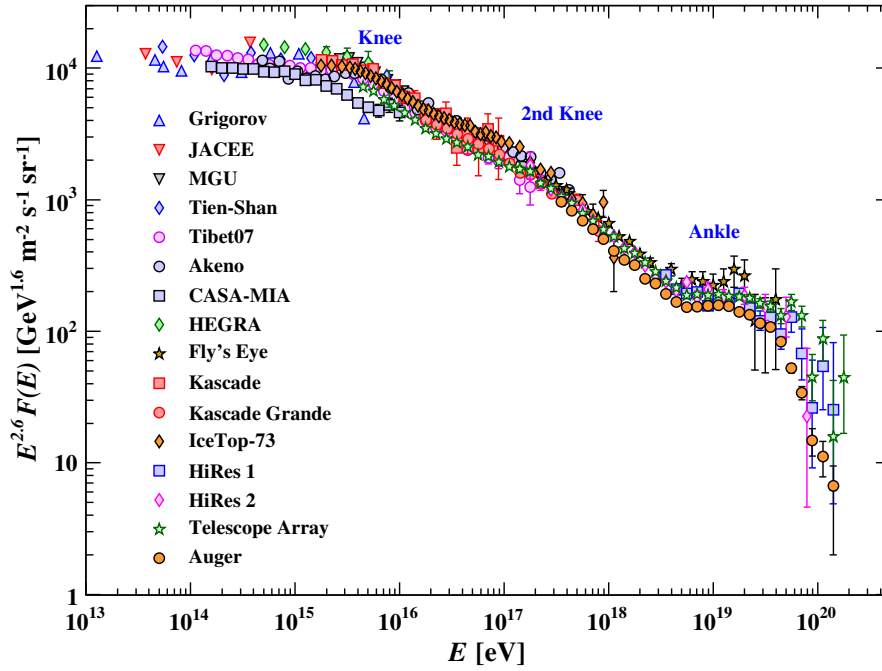


Figure 1.5: The all-particle cosmic ray spectrum for the highest energies ($> 10^{13}$ eV) measured with various experiments. The data is scaled by $E^{2.6}$ to emphasize the spectral breaks. (Tanabashi et al. 2018)

At the highest energies, cosmic rays are measured indirectly by looking at the extensive air showers they create in the Earth's atmosphere (see also later Section 2.1). It is not (easily) possible to measure the charge and thus the type of the incident particle with this kind of experiments, thus only an all-particle spectrum is available at these energies. Figure 1.5 shows the all-particle spectrum for energies above 10^{13} eV up to 10^{20} eV, scaled with $E^{2.6}$. This presentation reveals further spectral breaks in the cosmic ray spectrum.

At around 10^{15} eV, a first steepening of the spectrum is visible, now showing a power law index of $\gamma = 3.1$ instead of $2.5 < \gamma < 2.7$ for the different nuclei at lower energies. This first spectral break is also known as the *knee*, followed by the *second knee* at 8×10^{16} eV, where the spectrum steepens even further. These spectral features are usually connected to a transition from a regime dominated by Galactic cosmic rays to a domination by extragalactic particles. The beginning of this transition can be likely caused by the maximum achievable energy E_{max} of Galactic accelerators so that they simply can not reach the highest energies. The smooth transition might be caused by heavier nuclei since the acceleration mechanisms are dependent on the atomic number Z : $E_{max}(Z) = Z \cdot E_{max}(Z = 1)$ (see Eq. 1.9 in Section 1.3 about the CR acceleration), so the maximum energy of iron would be 26 times larger than that of the

protons, leading to the so-called iron knee (see e.g. Fig. 1.6 where only the iron component extends until the transition regime). Thus, with rising energy, more and more types of nuclei will drop out of the cosmic ray composition. This feature was also confirmed by KASCADE-Grande (Apel et al. 2011). However, a cutoff in the power law spectrum of Galactic particles might leave a gap of missing particles between the knee and the ankle. This would happen if only protons are accelerated in supernova remnants since their highest achievable energy is expected to be below 10^{17} eV (see upcoming Section 1.3.1), at energies just below the second knee. Hence, there might exist more than one cosmic ray population in our Galaxy, differing in source type, acceleration mechanism or composition with heavier nuclei, which extend to higher energies up to the second knee (Gaisser et al. 2013). So, multi-population models are able to explain the extension to energies above the first knee and the creation of a second knee. Furthermore, other effects might play an additional role in the steepening of the spectrum: the diffusion (see Equation 1.2) gets less and less effective with increasing energies and the particles start to escape the Galaxy (Hörandel 2004).

At energies above the knees, at around $10^{18.5}$ eV, the spectrum flattens again, a feature called the *ankle*, which is followed by a cutoff at the highest ever measured energies ($\sim 10^{20}$ eV). This flattening of the spectrum is likely connected to the domination of extragalactic particles. Such a change from Galactic to extragalactic particles can also be visualized by calculating the gyroradius, Equation 1.3, of the cosmic rays, which describes the average movement of charged particles in a magnetic field.

In this equation, $R = p/Ze$ is the rigidity, θ the angle between the moving particle and the surrounding magnetic field and B the strength of this magnetic field. By estimating a magnetic field of $B = 3 \times 10^{-10}$ T, the gyroradius of a proton with an energy of 10^{19} eV becomes ~ 3 kpc that is already larger than the thickness of the Galactic disc. For energies $> 10^{20}$ eV, the particles are basically moving freely since they are not deflected by the magnetic fields. Thus, at these high energies, the Galactic cosmic rays are not confined to the Galaxy anymore and are able to leave the Galaxy. This leads to a decline in Galactic cosmic rays and a dominance of extragalactic ones. The general structure of the ankle and the following cutoff can be explained by different models, namely the ankle model, the dip model or the mixed composition model (Aloisio et al. 2012).

$$r_{gyro} = \frac{R \sin \theta}{Bc} \quad (1.3)$$

The *ankle model* is the most natural one and carries on the thoughts from above that the ankle is also a feature of the transition from Galactic to extragalactic cosmic rays. At the beginning of the ankle, the fluxes of the Galactic and extragalactic particles are thought to be equal. After that, a harder (injection spectrum $\propto E^{-2}$), extragalactic proton component takes over. To model this transition, a second Galactic component (as described above) is needed, consisting of heavy nuclei that can be accelerated to higher energies than protons. The transition from Galactic to extragalactic domination according to the ankle model is shown in Figure 1.6 on the right. The needed maximal energy for the iron component needs to be at a few EeV to sustain the Galactic flux. This is in contradiction with the extensive air shower experiments HiRes and Pierre Auger Observatory (PAO) that show a proton dominance at these energies (see Figure 1.7).

The *dip model* makes the assumption that the cosmic ray spectrum is dominated by extragalactic protons at energies > 1 EeV. This leads to two energy loss effects of the protons, which are also observed: the pair production dip and the GZK cutoff. Both effects appear when the protons have high enough energies to start interacting with the photons of the cosmic microwave background (CMB). The pair production dip is located at the energy range from

1 EeV to 40 EeV and describes the creation of electrons and positrons:

$$p + \gamma_{CMB} \rightarrow p + e^- + e^+ . \quad (1.4)$$

The rapid falling of the cosmic ray flux at 100 EeV is then caused by the GZK cutoff (Greisen, Zatsepin and Kuzmin) where the protons start to generate pions while interacting with the CMB:

$$p + \gamma_{CMB} \rightarrow \pi + X . \quad (1.5)$$

The proton dominance at the highest energy, which is needed for both reactions to happen, is again in contradiction with measurements of the PAO (see Fig. 1.7). This experiment measured a dominance of iron at the energies of the dip and GZK cutoff.

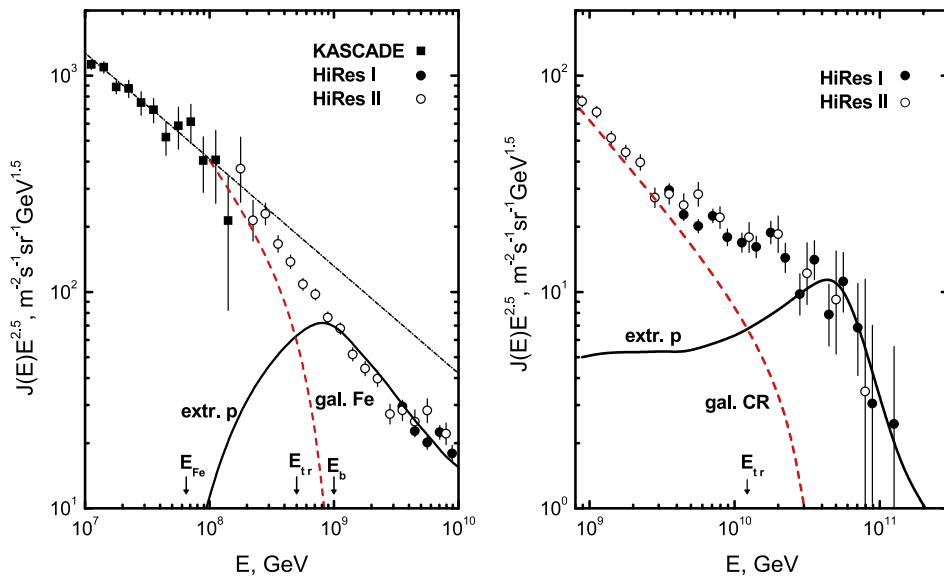


Figure 1.6: Transition from Galactic to extragalactic cosmic rays at the high energy end of the CR spectrum according to the dip model (left) and the ankle model (right). The dashed line is the Galactic component, the solid line the extragalactic component. E_{tr} is the energy where both fluxes become equal, E_{Fe} is the position of the iron knee and E_b is the energy where the transition to extragalactic particles is completed. (Aloisio et al. 2012)

The last model is the *mixed composition* model whose main concept is that the cosmic rays at these high energies are of a mixed composition and not dominated by a single nuclei. Thereby, the extragalactic composition is usually assumed to be very similar to the Galactic one, with protons as their dominating particles. For higher energies (> 10 EeV), the heavy nuclei are more and more destroyed by the photo-disintegration by the extragalactic background light (EBL) photons, leaving the protons as the most abundant species. This also leads to the GZK cutoff in this model.

Isotropy and anisotropy of cosmic rays

The origin of the cosmic ray particles is generally very isotropically distributed since all directional information is lost during the diffusive propagation through the Galactic magnetic

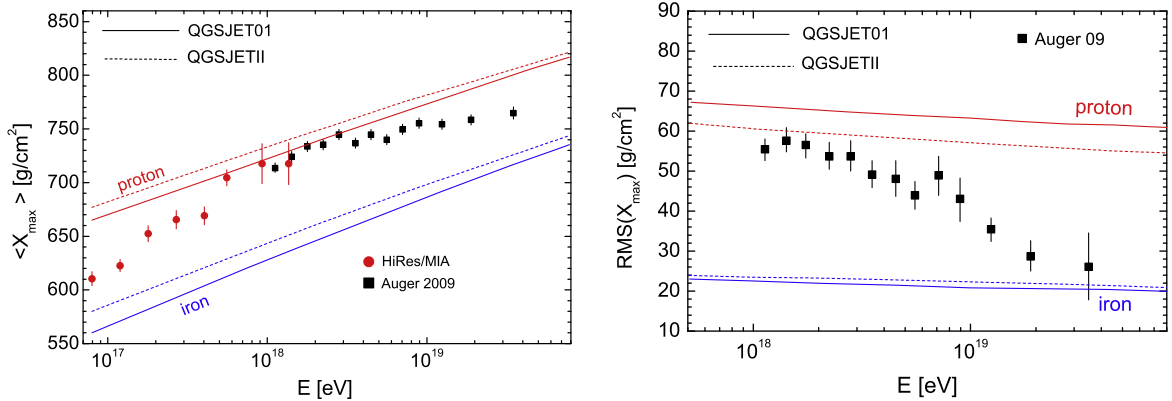


Figure 1.7: Average atmospheric depth of the shower maximum $\langle X_{max} \rangle$ (left) and the width of its distribution (right) as a function of energy. Measurements of the HiRes and Pierre Auger Observatory are shown together with simulations of protons and iron with two different interaction models. (Aloisio et al. 2012)

fields. But as already discussed above (see e.g. Equation 1.3), particles are less affected by the magnetic fields if they have higher energies. Thus, anisotropies due to source distributions or the orientation of the Galactic magnetic fields are expected to be visible at high energies. Such anisotropies were indeed already observed. At a few TeV they were seen, for example, by the IceCube detector (Abbasi et al. 2010), and at the highest energies, above 4 EeV, they were detected by the Pierre Auger Observatory (Aab et al. 2018).

Electrons, antiparticles and gamma rays

Electrons, antiparticles and gamma rays are not of main interest for this proton analysis, but they are nevertheless part of the cosmic ray spectrum and will contribute to the background of the analysis. So, they will be shortly mentioned in the context of cosmic rays.

The electrons in CRs suffer much larger radiative energy losses due to synchrotron radiation because of their small mass compared to nuclei. Therefore, a much steeper spectrum is expected at energies > 5 GeV, above the regime where solar modulation influences the leptonic cosmic rays. For these energies, a spectral index of $\gamma = 3.1$ was found, see Figure 1.8 on the left, which combines electrons and positrons. The IACT H.E.S.S. found a spectral break at 1 TeV where the index steepens further to $\gamma = 4.1$ (Kraus 2018). An excess of electrons at 600 GeV found by ATIC could not be confirmed by other experiments.

Also, a discrimination between particle and antiparticle can be done by some experiments, see Figure 1.8 on the right. Above 10 GeV, an increase of the positron fraction was observed by PAMELA and AMS-02 that is in contradiction with an expected decrease. The spectral shape as well as the rising positron fraction could be explained by a single individual source, propagation effects or dark matter decay/annihilation. Electrons and positrons will be treated as background in this work.

The other antiparticles, which were detected in cosmic rays so far, are the antiprotons. The ratio of antiprotons to protons is around 2×10^{-4} at 10 to 20 GeV and shows a large dependence on the solar cycle. Also, antiprotons are currently thought to be of secondary origin since no hints of sources that accelerate these were found.

Gamma rays are seen as emission from point sources since they are unaffected by magnetic

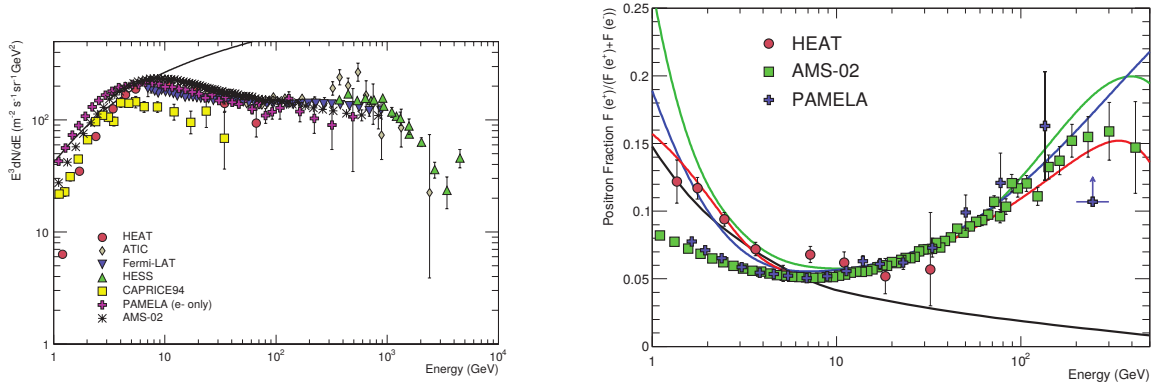


Figure 1.8: Measurements of the leptonic part of the cosmic ray spectrum. The plot on the left shows the combined e^+e^- spectrum multiplied by E^3 . The one on the right shows the fraction of positrons, including different theoretical models; black line: positrons as only secondaries, green: positrons from dark matter decay, blue: excess by propagation, red: positrons by pulsars. (both from Tanabashi et al. (2018))

fields, or as diffuse emission. The observation of point sources gives the opportunity to study possible CR sources directly, like the aforementioned supernova remnants. The diffuse emission is created by multiple effects, so unresolved sources can contribute to it but also gamma rays that are created during interactions of CRs with gas or radiation fields. Since gamma rays behave quite differently than the hadronic and leptonic CRs, they are not counted as primary cosmic rays. But since the used experiment was built for the detection of gamma rays, their creation processes are further explained later on, in Section 1.3.3.

1.3 Acceleration and origin of cosmic rays

The last section gave an overview of experimental results on the cosmic ray spectrum, showed its distinct features and tried to explain them in the context of propagation, interaction and composition of the cosmic particles. Besides, there remains the big question which acceleration mechanisms are able to get the particles to such high energies and at which Galactic or extragalactic sources they can happen. This section will first shed light on the currently most promising acceleration theories and on the most promising source candidates, afterward.

1.3.1 Acceleration of cosmic rays

There are two different types of acceleration mechanisms that are widely discussed (Hillas 1984). The first one is the acceleration of charged particles by extended electric fields, which can be created by fast rotating, highly magnetized objects like pulsars or black holes. Such electric fields are able to accelerate the particles to high energies rapidly. However, these particles also suffer large energy losses due to the high energy densities at the source regions.

The other mechanism is statistical acceleration, where the particles gain energy by various encounters with existing magnetic field irregularities. The theory of a statistical acceleration was firstly proposed by Fermi (1949) and further developed by many other scientists. The first approach by Enrico Fermi assumed that particles are accelerated by interactions with

large magnetic fields (“magnetic mirrors”) in Galactic clouds. The typical energy gain is $\Delta E/E \sim (v/c)^2$, where v is the speed of the randomly moving magnetic mirrors. Because of the squared dependence on the velocity, this mechanism is also called second-order Fermi acceleration. This approach already gives the expected power law behavior in the energy $N(E) \sim E^{-\gamma}$, however, there remain some problems: this mechanism is quite inefficient due to the second-order and the small velocities of the magnetic mirrors and does not result in the observed spectral index directly. Later on, modified versions of the Fermi acceleration mechanism were proposed, where the cosmic rays are stochastically accelerated at strong shock fronts (e.g. Bell (1978) or Blandford & Ostriker (1978)). In this so-called diffusive shock acceleration (DSA), the strong shock moves through a diffuse medium (e.g. the interstellar medium) and highly energetic particles (with speeds close to the speed of light) are present on both sides of this supersonic shock. These particles then scatter on turbulent magnetic fields that are apparent at the shock front. In this case, the energy gain is $\Delta E/E \sim v/c$, thus in first order of v/c leading to a faster energy increase. Because of this dependency, the mechanism is also called first-order Fermi acceleration.

The resulting spectrum and maximum energy according to the DSA can be estimated (following Longair (2011) or Bell (2013)). It is assumed that a particle gains the energy $\Delta E = \beta E$ after crossing the shock front, where β describes the energy gain. So, the energy after n acceleration cycles becomes

$$E_n = E_0 (1 + \beta)^n , \quad (1.6)$$

with E_0 as the initial energy after the particle is injected into the acceleration region. The number of cycles can be calculated to be

$$n = \frac{\ln(E/E_0)}{\ln(1 + \beta)} . \quad (1.7)$$

Furthermore, the probability for the particle to stay in the acceleration region after n cycles is assumed to be $(1 - P_{esc})^n$ with P_{esc} the probability of the particle to leave the region. With these assumptions, the differential spectrum can be already calculated:

$$\frac{dN(> N)}{dE} \propto \frac{1}{P_{esc}} \left(\frac{E}{E_0} \right)^{-\gamma} . \quad (1.8)$$

The spectral index of the deduced power law then depends on the characteristics of the shock front, i.e. its density compression ratio r : $\gamma = (r + 2)/(r - 1)$. For supersonic shocks, the density ratio reads $r = 4$, resulting in a spectral index of $\gamma = 2$. Thus, this acceleration mechanism already results in the desired power law spectrum with an index close to the observed one. It should be noted that this spectral index after acceleration is not the one measured at Earth since it is further softened, by roughly $\Delta\gamma = 0.3$ to 0.5 depending on the theory, during propagation.

Additional to the shape of the cosmic ray spectrum, the maximum achievable energy can be calculated to test if the DSA is able to accelerate particles up to the observed energies. First calculations were done by Lagage & Cesarsky (1983) who came to the result $E_{max} \sim 10^{14}$ eV, a bit too low for the observed energies of Galactic cosmic rays (see the knee feature in the cosmic ray spectrum). However, newer investigations and theories suggest that non-linear amplification of the magnetic field, caused by the cosmic rays, can lead to even higher energies (Schure & Bell 2013). Protons might be accelerated to $E_{max} \sim 10^{17}$ eV and heavy ions even

further, to $E_{max} \sim Z \times 10^{17}$ eV. Thus, acceleration up to the observed energies of Galactic cosmic rays is achievable by the diffusive shock acceleration.

As it was shown, there are mechanisms that can produce cosmic particles up to the observed energies. But the source candidates that can meet the needed conditions still need to be discussed. Galactic and extragalactic sources can be characterized by the Hillas criterion (Hillas 1984): the gyroradius of the accelerated particles can not be larger than the size of the source itself. This means that the particles need to be confined in the source region. This condition is (by using the definition of the gyroradius):

$$E_{max} = ZeBr_{source} \quad \text{with } r_{source} = r_{gyro} . \quad (1.9)$$

The Hillas criterion is illustrated in Figure 1.9. It shows the source size and magnetic field that is needed to accelerate protons to different energies. Additionally, various source types with their distinct properties are included.

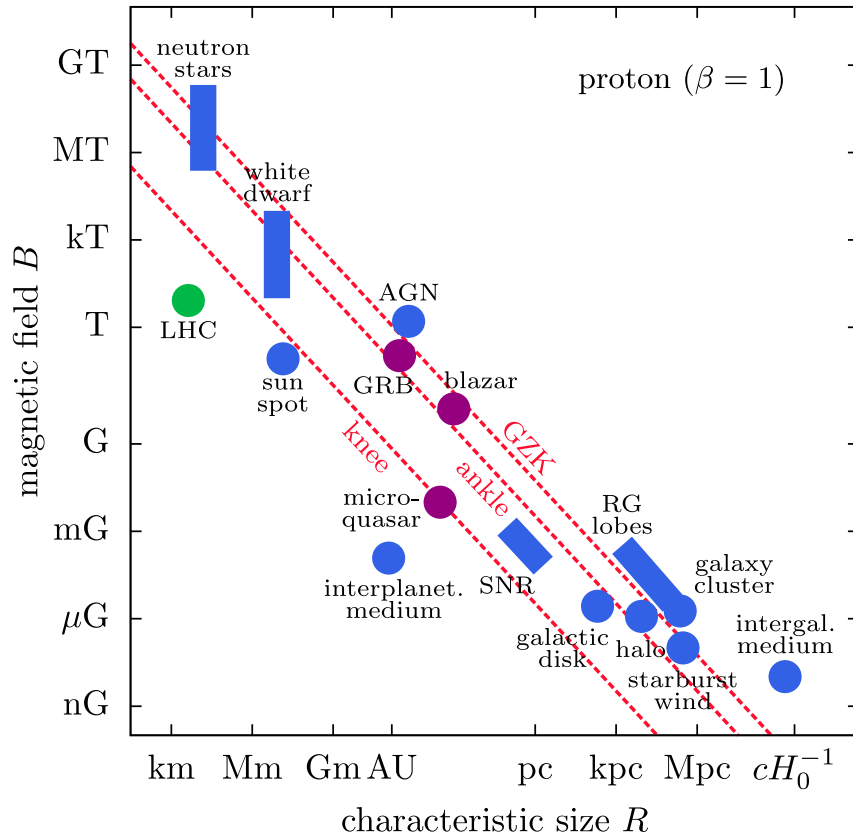


Figure 1.9: The so-called Hillas plot. It shows different source types that are thought to be able to accelerate cosmic rays together with their typical sizes and magnetic fields. These characteristics are connected to the maximum energy that is achievable by the sources (see Equation 1.9). The red lines indicate typical proton energies at different positions in the cosmic ray spectrum, i.e. at the knee, the ankle and the GZK cutoff (see previous discussion). Sources above these lines are able to produce particles with such high energies. (modified, Aartsen et al. (2018a))

It can be seen that there are indeed several source candidates that are able to produce and accelerate cosmic particles up to the highest energies, which are observed today. For energies up to the knee, dominated by Galactic cosmic rays, supernova remnants are the prime candidate for potential cosmic rays inside the Galaxy, which are heavily discussed and investigated. To reach the highest energies, up to the GZK cutoff, the prime candidates are neutron stars (NS) (Fang et al. 2012) or active Galactic nuclei (AGN) (Fang & Murase 2018; IceCube Collaboration and others 2018). Besides, various other possible candidates exist, which might be the sources of cosmic rays.

In the following, only supernova remnants will be discussed in detail since they are likely the origin of most of the proton cosmic rays in the energy range that is of interest for this work.

1.3.2 Supernova remnants as possible CR sources

Supernovae (SN) are transient, astrophysical phenomena that can happen at the end of a star's life. The end of a massive star with multiple solar masses is marked by an energetic explosion, so bright that they can outshine whole galaxies and can be seen by the naked eye. Thus, these phenomena were already observed before any telescopes were invented. After the discovery of cosmic rays, supernovae were suggested as a source of these energetic particles for the first time by Baade & Zwicky (1934). This idea was further followed by Ginzburg & Syrovatsky (1961) and many more scientists until today, where the remnants of supernovae are the prime candidates for Galactic CR sources (see also discussion above). In principle, two requirements need to be fulfilled so that supernova remnants (SNR) could be the possible origin of cosmic rays. SNRs have to produce enough energy to sustain the measured CR energy rate and have to generate the conditions for DSA to create the spectral shape and maximum energy.

By using the measured local energy density of cosmic rays, the needed injection rate of high energy particles into the Galaxy can be estimated (following Longair (2011)):

$$P_{CR} = \frac{\epsilon_{CR} V_{Gal.disc}}{\tau_{esc}} \approx 3 \times 10^{40} \text{ erg/s} , \quad (1.10)$$

where $\epsilon_{CR} \approx 1 \text{ eV/cm}^3$ is the cosmic ray energy density, $V_{Gal.disc} \approx 6 \times 10^{66} \text{ cm}^3$ the volume of the Galactic disc and $\tau_{esc} \approx 10^7$ years the escape time. The average energy output of a supernova explosion is around 10^{51} erg , and they occur roughly every 30 years in our Galaxy. Thus, the energy rate of SNs can be calculated to $P_{SN} \approx 1 \times 10^{42} \text{ erg/s}$. By comparing both numbers, P_{CR} and P_{SN} , it can be concluded that SN can cover the CR energy rate by assuming that only a few percent of the total energy budget is converted to particle acceleration.

Furthermore, the above mentioned conditions for the diffusive shock acceleration need to exist at SNRs, namely shock fronts and strong magnetic field amplifications. The existence of such conditions could be observed with the help of X-ray experiments (Uchiyama et al. 2007). The shock fronts of a SNR, e.g. Cassiopeia A, can be seen in Figure 1.10 on the left. The blue structures show strong, non-thermal X-ray emission, which is created by very energetic electrons. By using such observations, the magnetic fields could also be measured whose strength can be as large as a few mG, which is needed for acceleration up to Galactic CR energies (Vink & Laming 2003; Völk et al. 2005).

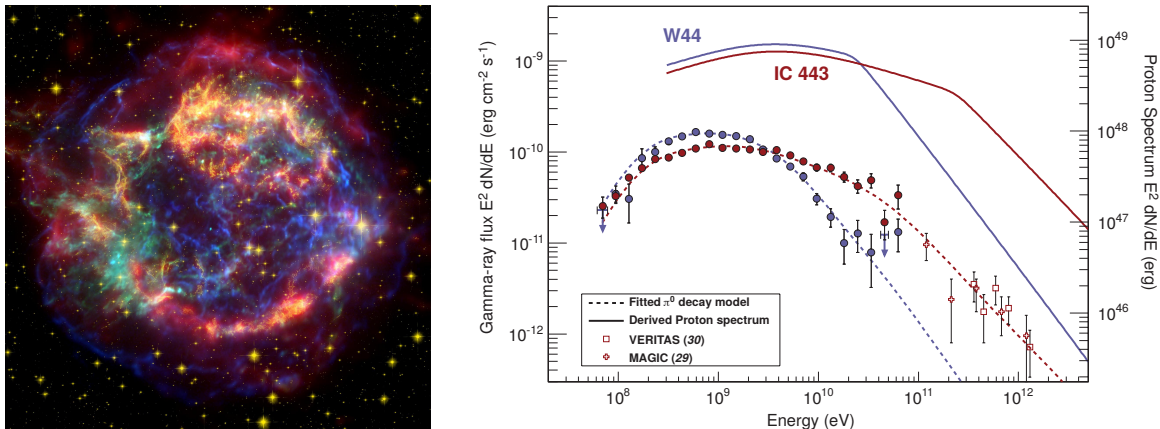


Figure 1.10: Observations of supernova remnants. The image on the left shows Cassiopeia A, a SNR in the Milky Way, in false colors. Red colors show infrared data from the Spitzer Space Telescope, orange are visible data from the Hubble Space Telescope and blue as well as green are X-ray data from the Chandra X-ray Observatory (Image credit: NASA/JPL-Caltech). The plot on the right shows the gamma-ray and proton spectra for two SNRs (W 44 and IC 443). The dotted line is the fit of a π^0 decay model that shows the pion bump. (Ackermann et al. 2013)

Besides the detection of accelerated electrons in SNRs, it was also observed that hadrons are accelerated in these shock fronts. This was achieved by measuring the so-called *pion bump*, a feature in the observed gamma-ray spectra. This pion bump is a characteristic decrease of the gamma-ray flux below 200 MeV, see Fig. 1.10 on the right, which is caused by the decay of neutral pions π^0 , created by hadronic interactions. This feature was already observed for a few supernova remnants, like W44, IC 443 (Ackermann et al. 2013) or W51C (Jogler & Funk 2016).

By looking at the acceleration theory as well as the observations, SNRs are indeed prime candidates for the acceleration of CRs inside our Galaxy. Nevertheless, all these theories are still part of heavy discussions in the scientific community since several problems and uncertainties remain.

1.3.3 Gamma rays

Some of the results shown so far were deduced with gamma-ray experiments, like the H.E.S.S. experiment, whose data will also be used in the analysis of the proton spectrum. But in contrast to primary cosmic rays, gamma rays are not directly created at the source itself. They are secondary particles and are produced through various interactions of the primary cosmic rays. The unique feature that makes gamma rays interesting for CR astrophysics is their missing charge so that they are not influenced by magnetic fields. By detecting them, their place of origin can be determined and the sources, acceleration mechanisms and interactions can be investigated directly.

Gamma rays can be produced by two different primary particle types, leptonic or hadronic ones. In leptonic processes, they are created by accelerated electrons and positrons via mul-

multiple processes: synchrotron radiation, Bremsstrahlung and inverse Compton scattering. In the first two processes, the gamma radiation is created by deflected charged particles. In the case of synchrotron radiation, they are deflected in the presence of cosmic magnetic fields. In the case of Bremsstrahlung, they are accelerated in Coulomb fields of other charged particles, like nuclei in the surrounding medium. Both processes can happen for all charged particles, however, these interactions are much more likely for lightweight charged particles like electrons. In the third process, inverse Compton (IC) scattering, highly energetic electrons can transfer some part of their energy to photons from ambient photon fields (e.g. from the cosmic microwave background or from radiation fields in the interstellar medium).

Accelerated, hadronic cosmic rays, like protons or also heavier nuclei, can produce pions during inelastic interactions with the surrounding interstellar medium:



The pions themselves are unstable and produce further decay products:

$$\pi^\pm \rightarrow \mu^\pm + \nu_\mu , \quad (1.12)$$

$$\pi^0 \rightarrow \gamma + \gamma . \quad (1.13)$$

For gamma-ray astronomy, the decay of the neutral pion into two gamma rays is, of course, the more interesting decay. In the case of pions at rest (or at low energies), their rest mass is split evenly between the two photons $E_\gamma = m_{\pi^0}/2 = 67.5 \text{ MeV}$.

All these leptonic and hadronic processes are shown for a starburst region at a distance of 3.5 Mpc in Figure 1.11. For these models, conditions of typical starburst regions, like M 82 or NGC 253, were assumed. Protons and electrons are continuously injected over a time scale of 2×10^5 years, with an energy input of $3 \times 10^{41} \text{ ergs}^{-1}$ for the protons and a magnitude lower for the electrons. Furthermore, two different assumptions were made for magnetic fields B , radiation energy density U_{rad} and spectral injection index α : a magnetic field of $B = 100 \mu\text{G}$, an energy density of $U_{rad} = 2500 \text{ eVcm}^{-3}$ and a index of $\alpha = 2.0$ (model 1) and $B = 200 \mu\text{G}$, $U_{rad} = 250 \text{ eVcm}^{-3}$ and $\alpha = 2.3$ (model 2), respectively.

Concluding, it can be said that gamma-ray astronomy is a powerful tool for cosmic ray astrophysics and is done by various experiments. The next chapter gives detailed insight into one of these gamma-ray experiments, H.E.S.S., its technical design as well as standard analysis procedures. However, in the case of the later analysis of the proton spectrum, this experiment is not used to detect gamma rays but to detect CR protons, which arrive at the Earth.

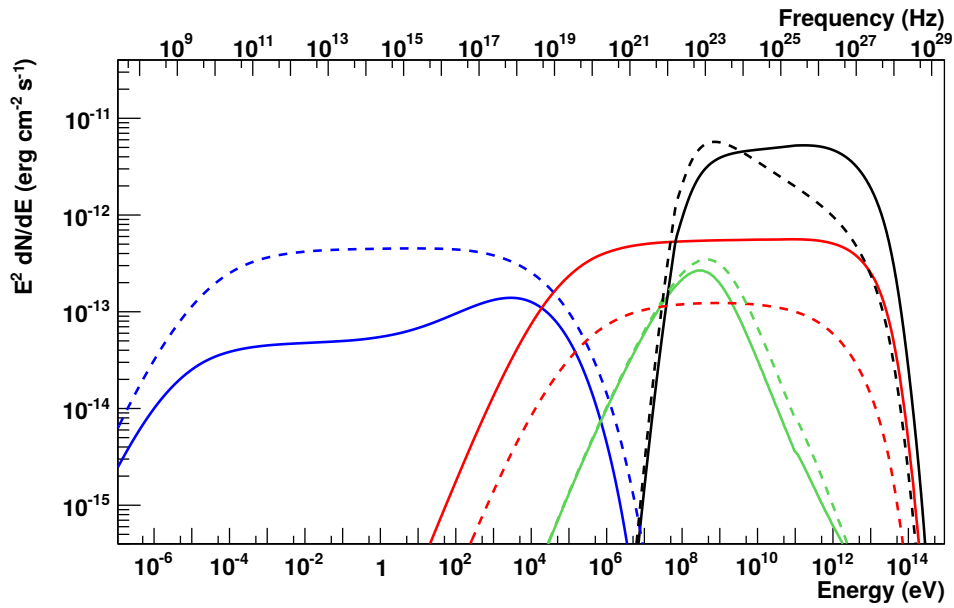


Figure 1.11: Spectral energy distribution models for a starburst region. The different colors depict different gamma-ray creation processes: synchrotron radiation (blue), Bremsstrahlung (green), inverse Compton scatterings (red) and π^0 decay, the “pion bump” (black). The solid (model 1) and dashed lines (model 2) represent two different models with differences in the injected proton spectral index, the surrounding radiation field energy density and the strength of the apparent magnetic fields. (Ohm & Hinton 2011)

The detection of cosmic rays

Since the former chapter focused on the creation and propagation of cosmic rays until they reach Earth, this chapter will explain how these particles, primaries as well as secondaries, can be detected and their information gathered. As was already mentioned in the beginning, many diverse experiments using different techniques emerged over the last decades. The type of experiment changes depending on the particle and energy range to be detected. Compact instruments can be used for low energy particles, cosmic rays as well as gamma rays, giving the opportunity to put them at the top or above the atmosphere. This approach brought, for example, the satellite Fermi (Atwood et al. 2009) in the lower Earth orbit or the AMS module (Aguilar et al. 2013) on the International Space Station (ISS). Another approach, similar to the first experiments by Victor Hess, are balloon-borne experiments where detectors are brought to the top of the atmosphere to measure the cosmic rays: ATIC (Ahn et al. 2006), CREAM (Yoon et al. 2011) or RUNJOB (Derbina et al. 2005). When moving to higher energies, cosmic ray particles become increasingly rare due to the falling power law. This results in less statistics for compact experiments. The solution is to move the experiments to the ground where they can be built larger without getting too expensive. Unfortunately, these experiments can not measure the particles directly anymore since the particles do not penetrate the atmosphere. However, these cosmic rays and gamma rays create particle showers in the atmosphere, which can be detected with various methods and can be used to reconstruct the first incident particle. This approach is used in the Pierre Auger Observatory (Pierre Auger Collaboration 2015), which detects the highest energetic cosmic rays, or in Imaging Atmospheric Cherenkov Telescopes (IACTs). The latter technique is also used in this thesis.

The first detection of a TeV gamma-ray source with an IACT was achieved by the Whipple telescope (Weekes et al. 1989) in 1989. The next system, HEGRA, established the stereoscopic approach with multiple telescopes, thus increasing the sensitivity (HEGRA Collaboration: A. Daum 1997). The pioneering work of these systems led to a new field in astronomy, very high energy (VHE) gamma-ray astrophysics, with currently three large systems in operation, MAGIC (Aleksić et al. 2012), VERITAS (Holder et al. 2008), H.E.S.S. (Hinton 2004) and a few smaller experiments. They detected many new sources that emit gamma rays at TeV energies and contributed a lot to cosmic ray astrophysics. The next milestone in VHE gamma-ray astronomy will be the Cherenkov Telescope Array (CTA) (Acharya et al. 2013), which is currently being developed and built. For a more detailed description of CTA, see the second part of this thesis, Chapter 1.

This chapter focuses on the physics of particle showers and their detection. Section 2.1

explains in detail how cosmic rays create particle showers in the atmosphere and how they can be detected by their emitted Cherenkov light. Section 2.2 outlines the setup, mechanics as well as functionality of H.E.S.S., how the hardware works, how the recorded data is processed and how the standard analysis works. The last section of this chapter, Section 2.3, then illustrates how simulations of cosmic rays and particle showers as well as their detection are carried out since the real reconstruction and analysis heavily depend on these simulations.

2.1 Particle showers in Earth's atmosphere

2.1.1 Extensive air showers

Cosmic rays and gamma rays that hit the atmosphere (from now on called primary particles) are not able to pass it since they interact with the atomic nuclei in the air. In these interactions, further secondary particles are created, which in turn can create even more particles. Thus, a particle shower is initiated. Since the particles are very energetic, they move faster than the local speed of light and emit Cherenkov light, which is measurable by the instruments. The particle showers can be split into two types, depending on the particle which started the shower: electromagnetic or hadronic.

Electromagnetic showers

If the primary particle is an electron, positron or photon, an electromagnetic cascade consisting of such particles is created since they only interact via the electromagnetic force. The mainly occurring processes are Bremsstrahlung and pair production. Bremsstrahlung is created when a charged particle (like an electron or positron in this case) is deflected by another charged particle (for example, atomic nuclei in the atmosphere), thus losing energy that is emitted as photons. Pair production, on the other hand, happens when a photon with enough energy (more than two times the rest mass of an electron) is in the vicinity of another nucleus where it can create an electron-positron pair. Both processes repeat many times which creates the electromagnetic cascade. The number of particles in such a shower rises exponentially until the energy of the particles drops below a certain critical energy (E_c) where ionization becomes the dominating process. At this point, the particle shower stops.

A simple but sufficient model to describe the creation of such particle showers was first created by Bethe and Heitler (Bethe & Heitler 1934) and is shown in Figure 2.1 for a primary photon that creates the electromagnetic cascade. This model takes only Bremsstrahlung and pair production into account, and the radiation length X_0 is assumed to be equal for both processes. For Bremsstrahlung, the radiation is usually equal to the distance were the electron or positron loses $1/e$ of its energy, for pair production, it is equal to the mean free path of a photon. The energy of the incident photon is E_0 that is split evenly between the newly created particles after each step. By using this approach, the distance after which the number of existing particles in the shower is doubled and the energy is split in half is calculated to $d = X_0 \cdot \ln 2$. So, the number of particles N and their energy E after the distance $n \times d$ can be calculated to:

$$N = 2^n \quad \text{and} \quad E = E_0/2^n . \quad (2.1)$$

Also, the position of the shower maximum after n_{max} steps which is reached at the critical

energy E_c and the amount of particles N_{max} at this point can be calculated:

$$N_{max} = E_0/E_c \quad \text{and} \quad n_{max} = \frac{\ln(E_0/E_c)}{\ln 2}. \quad (2.2)$$

One can see that the maximum number of particles in the shower depends linearly on the energy E_0 of the primary particle, the height of the maximum logarithmically. By using $E_c \approx 80 \text{ MeV}$, which is a suitable assumption for the atmosphere, and a primary photon with $E_0 = 1 \text{ TeV}$, one gets a maximum number of particles of around 12×10^3 . The depth of the shower maximum can be calculated to

$$X_{max} = X_0 \cdot \ln\left(\frac{E_0}{E_c}\right) \approx 350 \text{ g/cm}^2, \quad (2.3)$$

where $X_0 \approx 37 \text{ g/cm}^2$ is assumed. By using an average atmospheric density distribution, one can calculate the height of the shower maximum to be around 9 km above sea level, whereas the point of first interaction of the particle shower is at roughly 25 km.

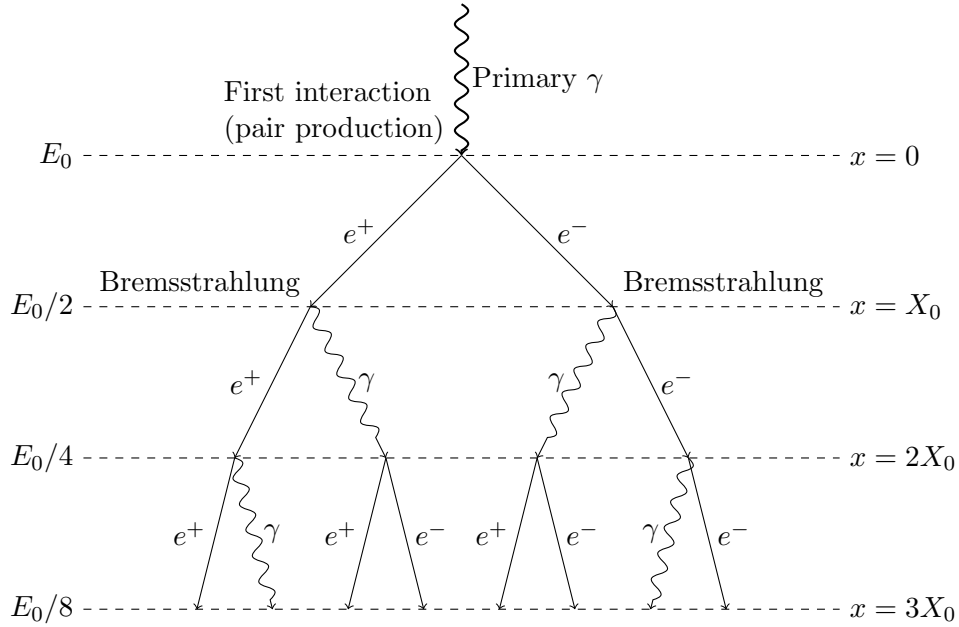


Figure 2.1: Illustration of an electromagnetic particle shower initiated by a gamma ray following the Bethe and Heitler model. The space between the dashed lines corresponds to one radiation length, where also the energy per particle is divided in half.

Hadronic showers

In contrast to electromagnetic showers, hadronic ones are more complex to describe theoretically since also strong and weak interactions occur. So, more different and complex particles can be created. When protons, which are the most common particles among cosmic rays, enter the Earth's atmosphere, they interact with other nuclei in the air (or rather the nucleons inside them). Most secondary particles which are created during these interactions are pions,

π^+ , π^- and π^0 . Also, strange particles, like Kaons, can be created, which are rarer. Furthermore, nucleons can be kicked out of the nucleus, leaving it in an unstable state while being in excited states themselves. These spallation products are able to create further short-lived radioactive isotopes. A schematic view of the processes in a hadronic shower is visualized in Figure 2.2.

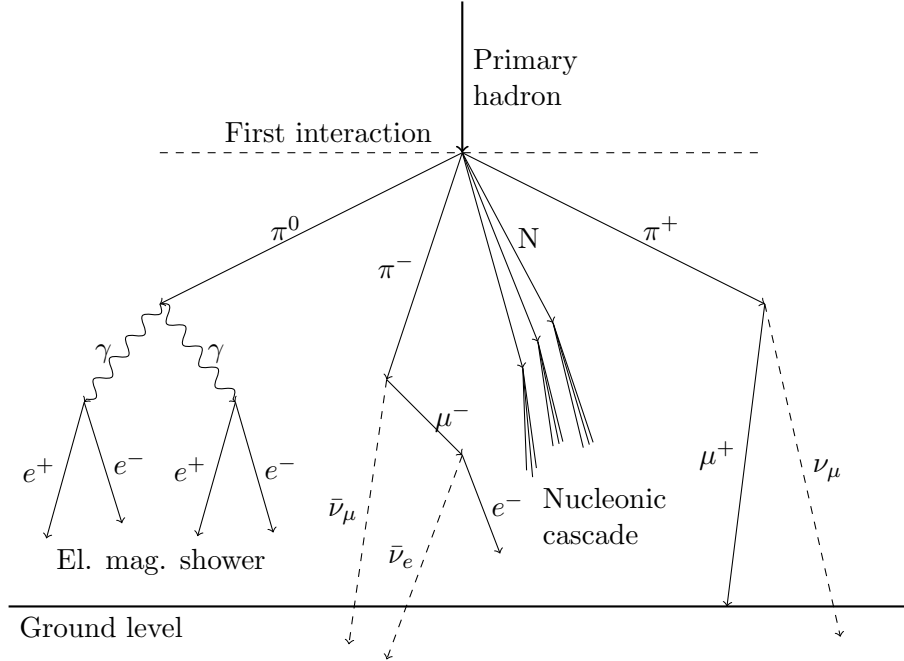


Figure 2.2: Illustration of a hadronic particle shower.

Since the most common secondaries are pions, hadronic showers can be approximated by only looking at these particles. This approach is then quite similar to the approach of Bethe and Heitler for the electromagnetic case and is explained in more detail in the work of Matthews (2005), among others. These highly energetic pions interact with further nuclei in the atmosphere, thus creating more and more pions. This process is called *pionization* and continues until their energy drops below the critical energy where the pions decay rather than creating new particles. The critical energy lies in the range of GeV but is also highly dependent on the energy of the incident proton.

The neutral pions π^0 decay very fast, with a decay time of 8.52×10^{-17} s, into two photons:

$$\pi^0 \rightarrow \gamma + \gamma . \quad (2.4)$$

These photons create electromagnetic subshowers which behave in the same way as it was already outlined for an incident primary photon above. Since the charged pions are unstable, further particles are created via the following decay channels

$$\pi^+ \rightarrow \mu^+ + \nu_\mu \quad \text{and} \quad \pi^- \rightarrow \mu^- + \bar{\nu}_\mu , \quad (2.5)$$

which further decay via

$$\mu^+ \rightarrow e^+ + \nu_e + \bar{\nu}_\mu \quad \text{and} \quad \mu^- \rightarrow e^- + \bar{\nu}_e + \nu_\mu . \quad (2.6)$$

Especially the muon components are important since they do not interact strongly and only lose little energy due to ionization. Thus, muons are able to reach the ground, making them part of the unwanted background in experiments but also giving the opportunity to use them for calibration.

Another essential difference between hadronic and electromagnetic showers is their lateral distribution. Hadronic showers have a more extensive lateral spread and are more irregularly shaped since strong interactions create more lateral momentum as well as more different particles. The different shapes of both shower types can be seen in Figure 2.3 where different air showers were simulated for different incident particles. Also, the interaction length of hadrons, around $\lambda \approx 90 \text{ g/cm}^2$, is larger compared to the radiation length of photons and electrons. Thus, air showers of hadrons have their point of first interaction at lower heights. These differences can be used later on to discriminate the different particles during analysis with IACTs.

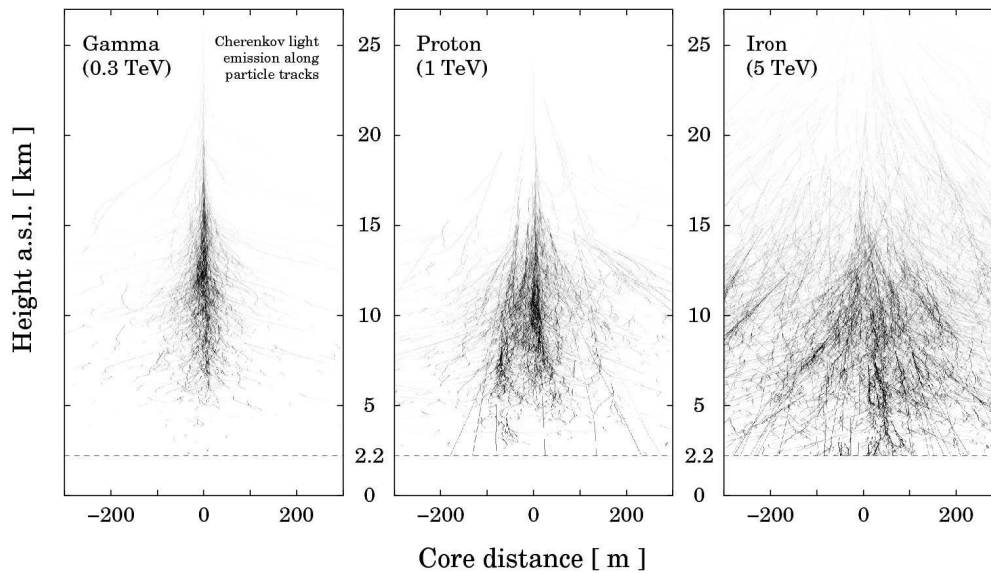


Figure 2.3: Simulated air showers for different incident particles. The image on the left shows an electromagnetic shower caused by a 300 GeV photon. The images in the middle and on the right show hadronic showers caused by a 1 TeV proton and a 5 TeV iron, respectively. (Bernlöhr 2008)

2.1.2 Emission of Cherenkov light

When cosmic rays or gamma rays hit the atmosphere, air showers are created. But particle showers in the range of a few TeV usually do not reach the ground where IACTs are positioned so they cannot be detected directly. However, they can be detected indirectly by measuring the Cherenkov light emitted by these particles. This effect was first detected experimentally by Pavel Alekseyevich Cherenkov (Cherenkov 1934) in the year 1934. Later on, in the year 1958, he even received the Nobel prize for his detection.

The blueish Cherenkov emission is created when charged particles move faster than the local speed of light of the surrounding medium. When such a charged particle moves through a medium, the atoms around it are polarized and emit radiation. Usually, this radiation

interferes destructively but if the charged particle moves faster than the local speed of light, they interfere constructively. This results in the Cherenkov emission, which can be detected. Since the speed of light in a medium c_n can be calculated by taking into account the refractive index n of the medium, the condition for the emission of Cherenkov light can be calculated to

$$c_n = c/n \Rightarrow v \geq c/n . \quad (2.7)$$

The refraction index for air is $n = 1.000273$ (at 20°C and 1 atm), so the needed velocity for Cherenkov emission is $v = c_n = 299710637\text{ m/s}$. This means that an electron needs a kinetic energy of more than 21.4 MeV. The angle Θ_C under which the Cherenkov light is emitted can be calculated according to Figure 2.4:

$$\Theta_C = \arccos\left(\frac{1}{n\beta}\right) , \quad (2.8)$$

with $\beta = v/c$. For an electron with a few GeV this angle can be calculated to 1.4° at sea level with the same assumptions as above. Since the emission angle depends on the refraction index, which depends on the density of the atmosphere, the value of the angle increases while the particles travel through the atmosphere. This is also shown in Figure 2.4. Through the superposition of the Cherenkov light and the changing emission angle, a so-called Cherenkov cone is created that illuminates a circular area on the ground with a diameter of roughly 250 m. Such circular shapes on the ground only appear for electromagnetic cascades. Because of the irregular shape of hadronic air showers with their sub showers, also the illuminated area on the ground is more irregular.

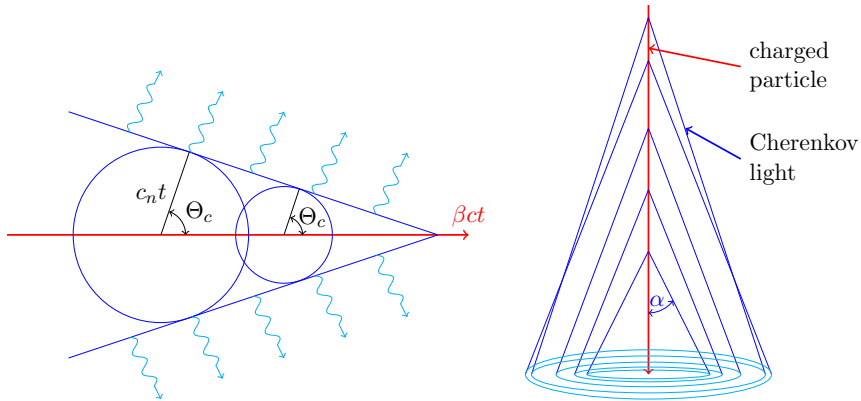


Figure 2.4: Illustration of the Cherenkov effect. The image on the left shows how a single charged particle forms an optical shock front and emits the Cherenkov radiation. The image on the right illustrates how the Cherenkov cone on the ground is formed by the variation of the Cherenkov angle. Additionally, the Cherenkov light of many particles is superimposed, forming a filled circle on the ground.

Also, the intensity of the emitted Cherenkov light can be calculated. A detailed theory of Cherenkov emission was developed by Ilya Frank and Igor Tamm (Frank & Tamm 1937) who were honored with the Nobel prize together with Pavel Cherenkov. The emitted energy

per unit length and wavelength can be calculated with the Frank-Tamm-formula:

$$\frac{d^2 N}{dx d\lambda} = \frac{2\pi\alpha Z^2}{\lambda^2} \left(1 - \frac{1}{\beta^2 n^2(\lambda)} \right). \quad (2.9)$$

Here, α represents the fine structure constant, Z the charge of the particle that creates the emission and λ the wavelength of the emitted radiation. Since the emitted intensity is indirectly proportional to the squared wavelength, more Cherenkov photons are emitted at lower wavelengths (i.e. at UV wavelengths). But Earth's atmosphere tends to absorb photons with low wavelengths below the optical range, moving the maximum intensity to wavelengths of $\lambda \approx 330$ nm. So, the color of Cherenkov radiation is usually referred to be blueish. Nevertheless, the Cherenkov emission can not be seen by the human eye, since all the emitted photons arrive on the ground within a few nanoseconds.

2.1.3 Detection of Cherenkov light with IACTs

The physics of air showers and Cherenkov light already explains how Imaging Atmospheric Cherenkov Telescopes (IACTs) work: they use the Earth's atmosphere as a detector material and use the faint and short Cherenkov flashes to detect the created particle shower and to reconstruct the primary particle which hit the atmosphere. The general principle of how these telescopes work is illustrated in Figure 2.5 below.

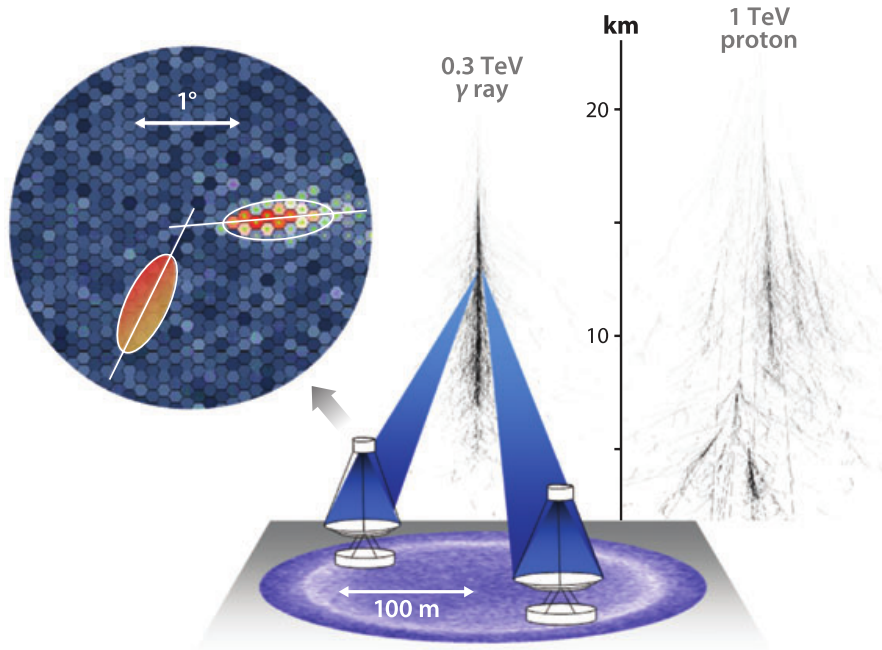


Figure 2.5: Illustration of the detection principle of cosmic rays or gamma rays with Imaging Air Cherenkov Telescopes. Visualized are the air showers which emit Cherenkov light and create an illuminated area on the ground. If telescopes are inside the illuminated area, the light is reflected by their mirrors to the camera. A simulated camera image of a gamma ray is shown on the upper left. (Hinton & Hofmann 2009)

Because of the vast extension of the Cherenkov light pool on the ground, the effective area where telescopes can detect a shower is rather large, especially compared to satellite experiments. The telescopes collect the Cherenkov light with the help of large mirrored areas that focus it onto the camera. The camera itself captures the Cherenkov light with fast working photon detectors. The images recorded by the cameras follow the shape of the particle shower, thus, images of air showers initiated by gamma rays have an elliptical shape. The optical path of Cherenkov photons of an air shower into the camera is shown in Figure 2.6. The large Cherenkov light pool on the ground gives the opportunity to use multiple telescopes to observe the same shower. This allows the usage of coincidence triggers, which reduces the background of night sky light and of muons from the irregular hadronic showers since they are usually only seen within one telescope. Therefore, the energy threshold is reduced but also the reconstruction is improved due to the observation of the particle showers from different angles, resulting in more available information usable for the reconstruction.

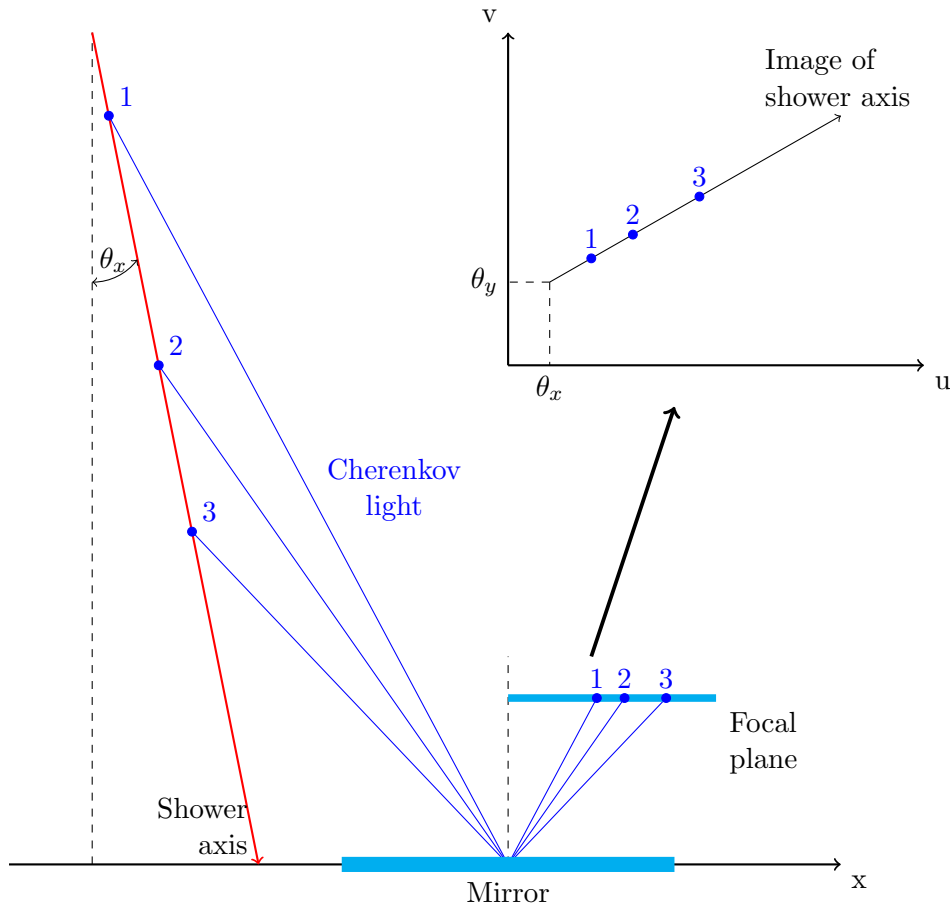


Figure 2.6: A schematic illustration of the optical path of Cherenkov photons. The light from the shower is reflected by the mirror surface onto the focal plane of the camera. The upper right coordinate system shows the focal plane of the camera.

2.2 H.E.S.S. - The High Energy Stereoscopic System

The High Energy Stereoscopic System, or in short H.E.S.S., is an array of imaging atmospheric Cherenkov telescopes to detect gamma rays in the energy range from a few tens of GeV to a few tens of TeV. The system is named after Victor Hess, who discovered cosmic rays roughly 100 years ago (see Section 1.1). The telescope array is located in Namibia, near the Gamsberg mountain in the Khomas Highlands at an altitude of 1800 m. This area was chosen because of the good weather conditions and the perfect optical quality. H.E.S.S. started officially in the summer of 2002 and a year later, in December of 2003, all four telescopes of phase I were in operation (Aharonian et al. 2006). The second phase started roughly ten years later, in July of 2012, where a fifth larger telescope began its operation (H.E.S.S. Collaboration et al. 2018b). The four first and smaller telescopes are arranged in a square with 120 m side length, the fifth telescope is placed in its center. In 2016 the cameras of the small telescopes were replaced with newly developed cameras that use state of the art hardware and concepts already intended for the next generation IACT array, the Cherenkov Telescope Array (H.E.S.S. Consortium 2019). A picture of the array with all five telescopes is shown in Figure 2.7.

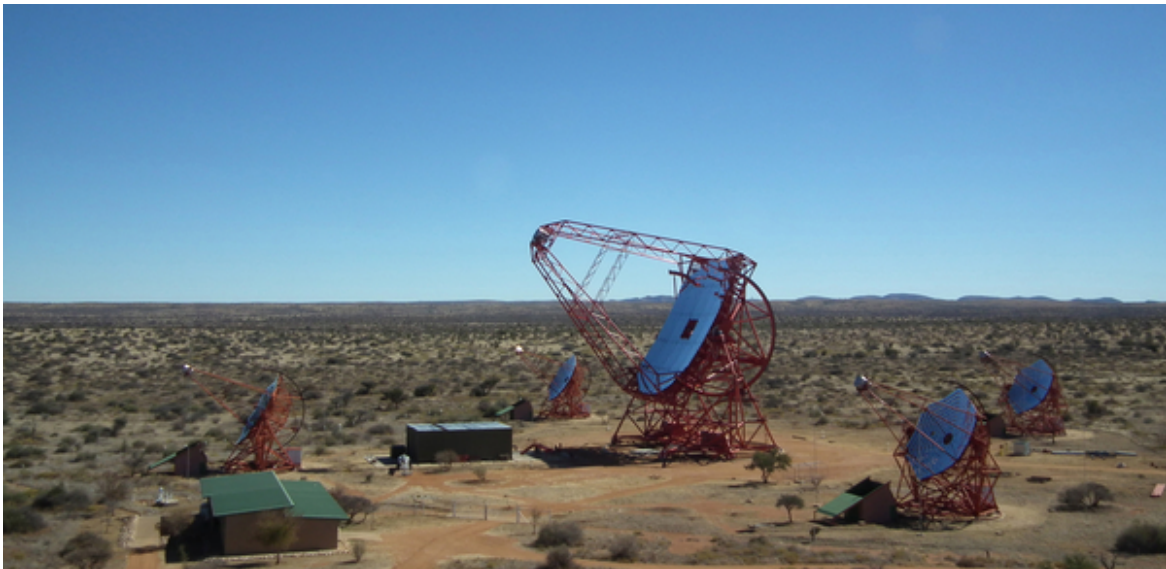


Figure 2.7: The H.E.S.S. telescope array in Namibia. Shown are the four small telescopes, CT1 to CT4, and also the newer, large telescope, CT5, which was inaugurated in the year 2012. (Reference: H.E.S.S. Collaboration)

In the following, the telescopes, cameras, their calibration as well as the standard analysis are described in detail. However, the focus will be on the four small telescopes of phase I since only data from this time is used in the proton analysis. Also, aspects that will only play a minor role in the proton spectrum analysis are left out. For further information, literature references will be given.

2.2.1 The telescopes and cameras

The four small telescopes are constructed out of steel and use an altitude-azimuth mounting. The drive system is able to move the telescope with a speed of $100^\circ/\text{min}$ and achieves a

pointing accuracy of a few arc-seconds. Additionally, the pointing is monitored by an extra CCD camera. The mirror dish is not made of one piece but consists of 382 round segments with 60 cm diameter, which results in a total mirror area of 108 m^2 . The mirror segments are arranged according to the Davis-Cotton-design, and their orientation can be adjusted individually. A more detailed description of the structure and mirrors can be found in Bernlöhner et al. (2003) and Cornils et al. (2003).

The cameras of the small telescopes consist of 960 pixels. The pixels are photomultiplier tubes (PMTs) with attached Winston cones, which help to collect the light and reflect it onto the PMTs. Each PMT has a field of view (FoV) of 0.16° , which results in a total field of view of 5° for the whole camera. Each pixel consists of three channels, a trigger channel and two data acquisition channels. For the data channels, there is a high gain channel (HG) and a low gain channel (LG). The HG channel is used for small signals, measuring up to 200 photoelectrons. The LG channel, on the other hand, is used for larger signals, spanning a total range of around 15 to 1600 photoelectrons. The signals in the PMTs caused by the fast Cherenkov flashes are recorded with a sampling speed of 1 GHz with Analogue Ring Samplers (ARS) and are stored in a 128 ns long memory. To reduce electronic noise, these readout electronics are located directly behind the PMTs. If a trigger signal is received, data taking stops, and the recorded waveform is readout. This is done by integrating the waveform in an interval of 16 ns. The cameras are described in more detail in Punch et al. (2001), the trigger system of the telescopes and the whole array in Funk (2005). As already mentioned, the cameras of the small telescopes were upgraded in 2016. But since no data of the new cameras are used in this thesis, they are not further explained here. An overview of all improvements of the upgraded cameras can be found in Giavitto et al. (2015). An image of the cameras, old and new, as well as the mirror surface, can be seen in Figure 2.8.



Figure 2.8: Images of the H.E.S.S. I cameras, including a part of the mirror surface. The image on the left already shows one of the new, upgraded cameras, the one on the right is an old camera. (Reference: H.E.S.S. Collaboration)

2.2.2 Raw data calibration

For a proper reconstruction of all shower properties, the raw data of the camera can not be used directly but rather a good calibration is needed to get the exact number of photoelectrons

(p.e.) per pixel. This section shortly describes the different calibration steps to outline all parts that play a particular role in the later reconstruction of the proton spectrum. The full description of the calibration can be found in Aharonian et al. (2004).

The aim of the calibration is to convert the measured ADC counts (measured value from the used analog to digital converter) to corrected photoelectrons. This is done for both channels, HG and LG, in the following manner:

$$\begin{aligned} A^{HG} &= \frac{ADC^{HG} - P^{HG}}{\gamma^{ADC}} \times FF \quad \text{and} \\ A^{LG} &= \frac{ADC^{LG} - P^{LG}}{\gamma^{ADC}} \times (HG/LG) \times FF . \end{aligned} \quad (2.10)$$

The different parts of formulas are:

- The pedestal P , i.e. the position of the baseline.
- The gain of the high gain channel γ^{ADC} .
- The ratio of the gain of both channels HG/LG , transferring the gain of the HG channel to the LG channel.
- The flat field coefficient FF , which corrects for all further differences between individual pixels that are not considered through the other parts.

The pedestal value P describes the measured ADC value per channel when no Cherenkov signal is present in the pixel. There are two different ways on how the pedestal is measured. One is the dark pedestal, which is measured with a closed camera lid so that no further signal is present. This measures the electronic baseline whose width is only influenced by electronic noise. Furthermore, the pedestal is also measured during observations for pixels without a Cherenkov signal. In this case, photons from the night sky, e.g. from stars, are included, which influences the baseline and its width. By looking at the pedestal values during observation, pixels with a large night sky background level can be excluded from the analysis since they affect it negatively.

The gain factor γ^{ADC} is responsible for the conversion from measured ADC counts to photoelectrons and takes the gain itself, the amplification of the channels and the integration window into account. Typical values for the gain are around 1.22 mV/count. It is measured by dedicated single-photon runs where all pixels are illuminated by LED flashers with an average illumination of a single photoelectron. The ratio HG/LG is determined by using the overlapping linear range of both channels.

The flat field coefficient FF corrects further differences between single pixels and is not connected to the already described calibration chain. These differences are mainly caused by differing optical efficiencies of the used Winston cones and by the collection efficiencies of the PMTs. This coefficient is again determined through dedicated flat field runs where the camera is uniformly illuminated by LEDs but this time with higher illumination levels compared to the single photoelectrons from the gain calibration mentioned before.

Another essential step during calibration is the timing of the readout window, which is not mentioned in Equation 2.10 above. The position of the readout window needs to be placed so that the signal from the Cherenkov flash lies in the middle of the window, i.e. the measured charge is maximal. This position is described by the N_D value, which is the time difference

from trigger signal to the integration window. Thus, the 16 ns window is integrated starting from the sample $(128 - N_D)$. This value is adjusted regularly in sampling runs where the ADC value of each cell of the memory is read out so that the full waveform can be digitized.

Also tracked is the number of broken pixels meaning pixels that are not usable for the analysis, including pixels

- with a too large NSB level,
- with missing calibration coefficients,
- with problems in the ARS during digitization,
- with problems with the high voltage supplies of the PMTs,
- and with too many or too little signals.

These pixels are flagged as broken and are not used in any analysis.

2.2.3 Hillas analysis - the standard reconstruction

After the full calibration, the reconstruction of the primary particle can be done. The standard way to do a reconstruction with IACTs is with the so-called Hillas parametrization (Hillas 1985), which is used to describe the image in a simple way. These parameters can be used to fully reconstruct the geometry of the shower, its energy and even to do a separation between signal particles and background particles. This standard approach will also be used for the reconstruction of the proton spectrum but optimized for these particles. Thus, the following paragraphs will describe the standard Hillas approach as used for gamma rays. Chapter 3 will describe the adapted Hillas approach, optimized for protons. This standard approach is also explained in detail in Aharonian et al. (2006), which will give an extensive explanation of all steps for gamma-ray analysis.

Image cleaning

After the application of the full calibration, the next step is the cleaning of the image. This is done to exclude all pixels without a shower signal and to keep only pixels that will be used for the analysis. Therefore, a short algorithm is applied to remove all background pixels: pixels with either a signal larger than 10 p.e. and a direct neighbor with more than 5 p.e. or the other way around, a pixel with a signal larger than 5 p.e. and a direct neighbor with more than 10 p.e. are kept. This so-called 5–10 cleaning is the standard in most of the H.E.S.S. analyses, but also other combinations are possible.

Parametrization

With the Hillas approach, the shower images are approximated with an elliptical shape, and its properties are used for further reconstruction. This can be done since cleaned gamma-ray images already show such a shape. The most important parameters, which are determined for this kind of analysis, are shown in Figure 2.9. The parameters with a short description are:

- The image amplitude (also called size) is the number of measured photoelectrons of the shower image after cleaning.

- The length and width are the two major axes of the elliptical shape of the measured air shower. They are used for the geometrical reconstruction and particle separation. Higher moments of the pixel distribution, skewness and kurtosis, are not shown in the image.
- The local distance is the distance from the center of the camera to the center of gravity of the shower image. This parameter can be used to reject events that lie too far outside of the camera and might be cropped.
- The angle ϕ is the orientation of the shower image in the camera plane.

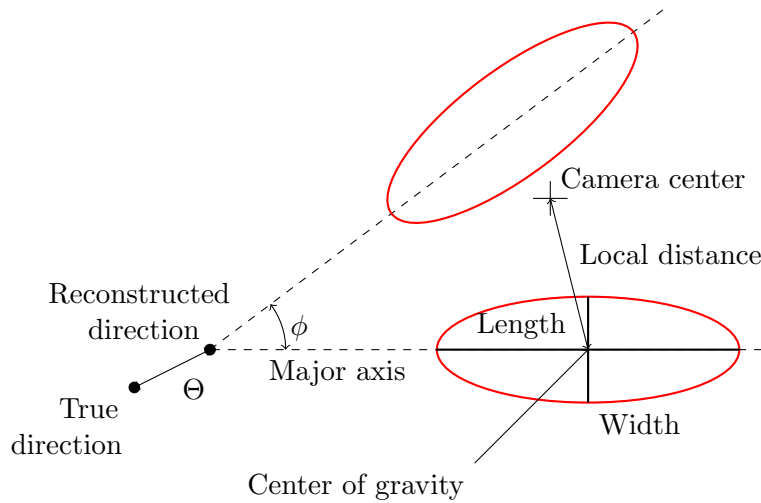


Figure 2.9: Definition of the Hillas parametrization where the shower image is approximated by an elliptical shape. Two camera images are indicated by the red ellipses.

Stereo geometrical reconstruction

For the reconstruction of the shower geometry, i.e. its direction and impact point on the ground, the availability of multiple telescopes and their angle-preserving imaging is utilized. The principle of the reconstruction is shown in Figure 2.10. The images of all participating telescopes with data are combined in one common coordinate system, either the camera system or the ground system. The two-dimensional camera system has its origin in the focal plane of the cameras and is used to describe the image of the camera. The ground system is fixed at the center of the telescope array, and its abscissa is oriented towards the north. Since the image in the camera represents the shower, the major axis represents the propagation direction of the particle shower on which also its origin lies. Thus, if the major axes of all telescopes are intersected, the intersection point gives the direction if done in the cameras system, or the impact point on the ground if done in the ground system.

When more telescopes are used for the reconstruction, it can be further improved by applying a weighting on the individual telescopes to prefer bright and clear images. This will be especially needed for the proton reconstruction since their images are not as sharp as the

ones from gamma rays. Different image properties can be used for the weighting, see, for example, Hofmann et al. (1999). In this case, for the weighting are used:

- The sine of the angle between the two major axes of the shower image to prefer large angles (e.g. 90°) where the geometry reconstruction works best.
- The image amplitude since brighter images are clearer and the major axes can be identified more easily.
- The ratios of width over length because it gives a measure of the distance of the shower so that telescopes which are close to the shower are preferred. Also crucial for the proton reconstruction is that such showers have a more elliptical shape that is better reconstructable.

By adding these weights, the geometry reconstruction works well enough for proton air showers as will be seen later on.

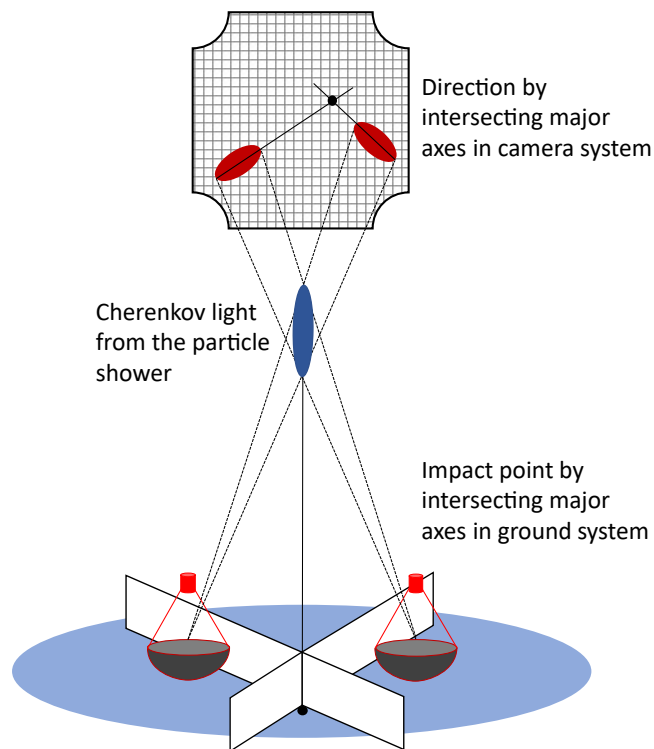


Figure 2.10: Illustration of the stereoscopic geometrical reconstruction. By using the stereoscopic view of the shower, the major axes of the images can be intersected, resulting in its direction (upper part) or the impact point (lower part).

Energy reconstruction

As the next step, the energy of the primary particle is determined by using the intensity of the shower image and the reconstructed impact position on the ground. This information is enough to get the energy of the incident particle. Simulations are done to create so-called

energy lookup tables. They store the energy of the simulated, primary particle as a function of its intensity (image amplitude) and impact distance to the telescope. An example of an energy lookup for primary gamma rays is shown in Figure 2.11. These are created for each telescope and also for various pointing directions of the telescopes since they have influence on the shower shape and development. The parameters that are varied to get the energy lookups are the zenith angle, the azimuth angle, the offset between pointing and shower direction as well as the optical efficiency. This is done in discrete steps in a way that the whole possible parameter space is covered while not consuming too much computing time to do the needed simulations. To match the configuration of the real observations best, the energy is interpolated between the available parameter combinations. Besides the already simulated optical efficiency of the whole system for specific points in time, the energy is further corrected to match the current efficiency at the time of data taking. This efficiency is measured with muon events, which will be explained next. The energy is determined for each single telescope that took part in the event reconstruction. Afterward, the average energy is calculated by weighing each telescope by its error of the energy reconstruction, also deduced with the simulations.

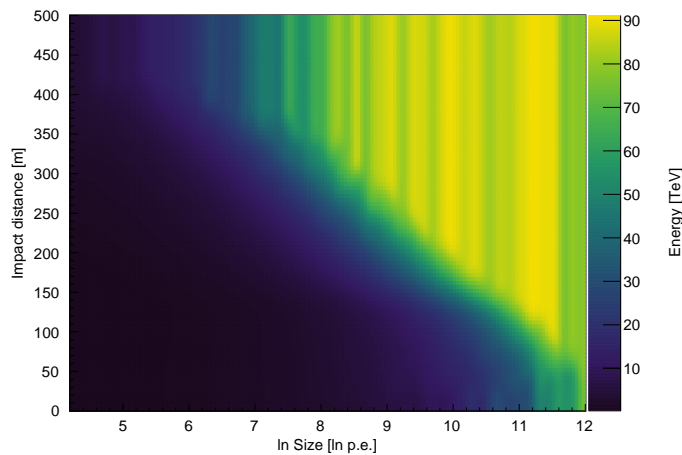


Figure 2.11: A smoothed and extrapolated energy lookup for primary gamma rays.

Optical efficiency

In addition, the optical efficiency of the whole telescope needs to be monitored since it has a significant influence on the number of measured photoelectrons in each pixel. This, of course, has an impact on the reconstruction, especially of the energy of the primary particles. On the one side, most of the effects of the optical efficiency are taken care of by the simulations, which are used for the reconstruction. The general efficiency of the mirrors and the PMTs, mirror free spaces between the tiles or shadows cast by the structure are already simulated. Also, the simulations are repeated every few years or after severe changes to account for the degradation effects of the mirrors and PMTs. Thus, the simulations are split into so-called muon phases that resemble the best simulated efficiency for a given time. The interesting muon phases for this work are called phase 1 (1.0/1.0/0.93/1.0), 1b (0.7/0.7/0.7/0.7) and 1c (0.6/0.54/0.6/0.6) with the additional downscaling of the optical efficiency for each telescope given in parentheses.

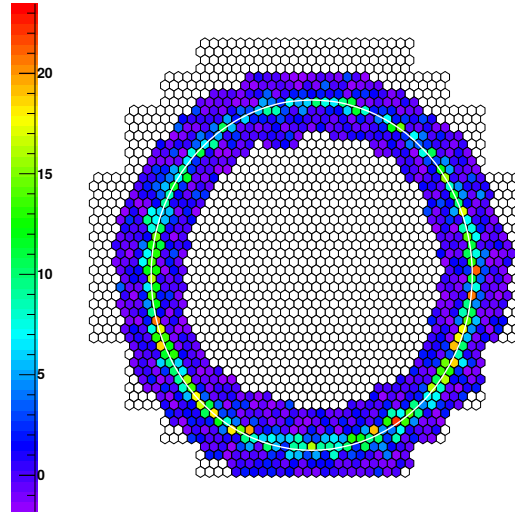


Figure 2.12: A measured muon event in the camera of the large telescope CT5. The color resembles the charge per pixel in photoelectrons after calibration. (Mitchell et al. 2015)

However, the efficiency changes gradually from phase to phase. This also needs to be considered to get the right number of photoelectrons in the end. Therefore, muon events, which are created in hadronic air showers, are used for further correction. Compared to other particles, muons lose almost no energy while traveling through the atmosphere and are able to reach the telescope directly where their direct Cherenkov light can be measured. If the muons arrive parallel to the optical axis of the telescopes, the resulting image has a ring-like shape. An example of a muon event is shown in Figure 2.12. By simply measuring the geometry of these images, the total emitted light, which would be expected at a camera with 100% efficiency, can be calculated analytically. This expected light intensity can be compared to the measured one to determine the optical correction factors. With the help of these, differences between the simulated efficiency and the current efficiency can be corrected. The algorithms which are used to do these calculations are outlined in detail in Bolz (2004) or Mitchell et al. (2015). The measured optical efficiencies for different periods are shown later in Section 3.1 (Fig. 3.7), where the effects of the optical efficiency on the data and the simulations are investigated.

For the correction, the measured efficiency is compared to the one which was used in the simulations, and a correction factor is calculated. This factor can be applied to the image amplitude or directly to the reconstructed energy, which is usually done.

Gamma – hadron separation and selection cuts

During the standard gamma-ray analysis, the hadronic background needs to be suppressed since it is much more abundant than gamma rays from a typical source. Therefore, the so-called *mean scaled width method* is used. The basic idea behind this approach is to use the differences between the images of gamma rays and hadronic particles (see Fig. 2.13). Due to the strong interactions of the hadronic particles, these air showers show a more extensive lateral spread as well as more sub showers, which make the resulting images in the camera broader and more irregular.

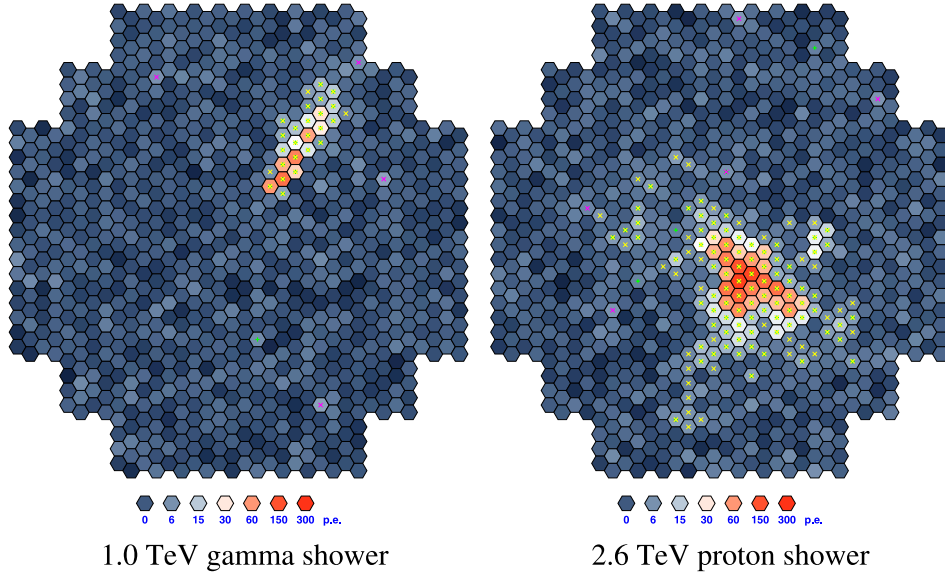


Figure 2.13: Simulations of a gamma-ray shower and a proton shower. The differences in the camera images between an electromagnetic and a hadronic air shower are clearly visible. (Völk & Bernlöhr 2009)

To decide if a measured image looks like the one from a gamma ray, the Hillas width and length are compared to simulated gamma rays. Therefore, lookup tables are created in a similar way as it is done for the energy reconstruction. This time, they are filled with the typical length and width of a gamma-ray shower as a function of its image amplitude and distance. The measured values are then compared with the expected values from the simulations. The reduced scaled width of a single shower image, RSW_i , is defined as follows:

$$RSW_i = \frac{W_i - \langle W_i \rangle}{\sigma_i}, \quad (2.11)$$

where W_i is the measured width of an individual telescopes and σ_i is the spread of the mean simulated width $\langle W_i \rangle$. The results of each telescope with data are then combined to the mean scaled width, $MSCW$:

$$MSCW = \frac{\sum_i \omega_i \cdot RSW_i}{\sum_i \omega_i} \quad \text{with} \quad \omega_i = \frac{\langle W_i \rangle^2}{\sigma_i^2}. \quad (2.12)$$

The calculation for the mean scaled length is done in the same way. By using a cut on the mean scaled length and especially the width, already a good gamma – hadron separation can be achieved. For bright sources like the Crab Nebula, the signal to noise ratio can be brought to the order of 1 by just using these cuts. However, this also shows the need for further background estimation methods to eliminate the remaining background events in the signal (see next section).

Typical cuts for gamma-ray analysis with the standard Hillas approach are shown in Table 2.1. The cuts are applied to different Hillas parameters:

- The cuts on the image amplitude and the local distance are usually used combined with

the term preselection since they are used to select bright and not truncated events that are well reconstructable.

- The cuts on the MSCW and MSCL cuts are used to reduce background events and to select only gamma like events. These cuts are called postselection cuts.
- Θ^2 is the squared angle between the true source direction and the reconstructed event direction. This cut ensures that only events from the source itself pass the cuts.

These cuts were optimized for detection significance so that a possible gamma-ray source is detected in the shortest time possible. The standard cuts are intended for sources with a flux of 10% of the Crab nebula. The hard cuts are for weak sources (1% Crab) with a hard spectrum, the loose cuts for bright sources (100% Crab) with a soft spectrum. The extended cuts are usually used for extended sources since the Θ^2 cut is loosened so that all events from an extended source pass the cuts.

Configuration	Image amplitude	Local distance	MSCW	MSCL	Max. Θ^2
	[p.e.]	[m]			[degrees ²]
	Preselection		Postselection		
Standard	80	0.525	[-2.0:0.9]	[-2.0:2.0]	0.0125
Hard	200	0.525	[-2.0:0.7]	[-2.0:2.0]	0.01
Loose	40	0.525	[-2.0:1.2]	[-2.0:2.0]	0.04
Extended	80	0.525	[-2.0:0.9]	[-2.0:2.0]	0.16

Table 2.1: Selection cuts for gamma-ray analysis with the standard Hillas approach. (Aharonian et al. 2006)

However, these cuts need to be changed to ensure a proper reconstruction of protons which behave differently than gamma rays. The optimization of the reconstruction and event selection for the proton spectrum will be discussed in detail in Chapter 3.

Background rejection

As was already stated, there is still the need for an additional background estimation after the application of the aforementioned cuts. This is usually done by using off regions in the FoV of the gamma-ray source where no signal is expected. The signal region, also called on region, is defined by the expected position of the source and the region around it defined by Θ (see above). The expected excess of gamma-ray events from the source can be calculated by

$$N_{\text{excess}} = N_{\text{on}} - \alpha N_{\text{off}} . \quad (2.13)$$

Here, N_{on} are the measured counts from the source region, N_{off} the number of counts from the off region and α is a normalization factor which accounts for differences between the on and off region. This normalization factor is affected by the area of the used regions, the observation position, the energy, the exposure time or the camera acceptance. Thus, α heavily depends on the used method to estimate the background events. The currently used methods are called:

- Ring background
- Reflected-region background

- Template background
- Field of view background
- On/Off background

The first two are the ones mostly used and will be explained in the following. A detailed description of all methods is given in Berge et al. (2007). Both methods are visualized in Figure 2.14, the ring background on the left, the reflected-region on the right. Data for both methods are usually taken in the wobble observation mode. In this mode, the telescopes are pointed beside the gamma-ray source (typically with an offset of 0.5°) to keep the source as well as the background region in the same field of view. This reduces systematic effects since source and background are measured at the same time and acceptance gradients in the FoV are reduced.

For the ring background method, a ring is defined around the expected source position and used for the background estimation. The size of the ring and thus the normalization factor α is given by the solid angles of on and off region and is usually set so be $\alpha = \Omega_{\text{on}}/\Omega_{\text{off}} = 1/7$. Furthermore, this method needs an acceptance correction since the ring has different offsets to the observation position.

For the reflected-region background, multiple off regions are defined around the observation position in a way that they have the same offset as the source region and also the same size and shape. By choosing the regions like that, no further correction of the acceptance is needed. In the ring around the pointing position, as many regions as possible are placed while keeping some distance to the gamma-ray source to avoid contamination with signal events. The normalization factor can be calculated to $\alpha = 1/n_{\text{off}}$ with the number of off regions n_{off} .

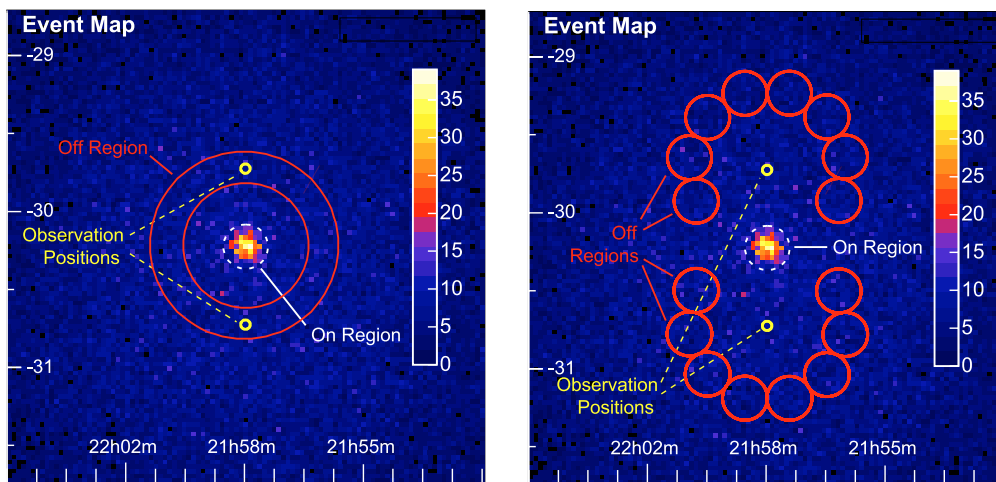


Figure 2.14: Visualization of the ring (left) and reflected-region (right) background methods. The count map shows events from the source PKS 2155-304 after 5 h of observation with H.E.S.S. taken in wobble mode. (Berge et al. 2007)

These methods can be applied to point sources as well as to extended sources. However, for the analysis of isotropic events, like cosmic ray protons, these methods can not be used anymore since no off regions can be defined. Therefore, other approaches need to be used to get rid of the background contamination in this case. The used approach for the proton analysis is explained later, in the chapter about the proton analysis, Section 3.3.

2.3 Simulation of air showers and the detector response

It was already mentioned that the most crucial parts of the reconstruction of IACT data depend on simulations, meaning that the final results can only be as good and trustworthy as the simulations are understood. Also, part of the later investigation was the verification and optimization of the proton simulations. Therefore, the two software packages which were used for the simulations are described in the following.

Air shower simulation with Corsika

For the simulation of extensive air showers, the software package CORSIKA (Cosmic Ray Simulation for KASCADE) (Heck et al. 1998) was used. It was originally developed for the KASCADE experiment (Apel et al. 2010) but is now widely used in cosmic ray experiments and especially also for IACTs. Corsika is updated regularly, so different versions are available that also have an impact on the shower simulations itself. In this work, version 74100 is used, but other versions were also tested.

The simulations can be controlled via many different input parameters. The type of the primary particle can be chosen out of 50 elementary particles and nuclei up to atomic masses of $A = 56$. Its origin in the sky can be modeled as point-like or as diffuse emission, and also its energy can be set while energies of more than 1 EeV are possible. Also, the location of the experiment can be modeled in detail by setting, for example, the height above sea level, Earth's magnetic field or atmospheric conditions. The atmosphere is built with its main components, 78.1% of N_2 , 21.0% of O_2 and 0.9% of Ar , and its density fluctuations are modeled with five layers.

Interactions of particles while moving through the atmosphere, the first interaction of the primary as well as further interactions of all secondary particles, are determined by the mean free path of the individual particles. The different interactions which may happen depend on the particle type, especially if it is of hadronic or electromagnetic origin (see also the theory of extensive air showers in Section 2.1). For electromagnetic showers and sub showers, the EGS4 (Electron Gamma Shower system version 4) software package is used. The package simulates all important interactions of electromagnetic showers like pair production and Bremsstrahlung but also annihilations, Bhabha scattering, Moeller scattering, Compton scattering or photoelectric reactions. Also, further modifications are included to model the behavior of muons or photonuclear interactions.

As the physics of hadronic air showers is more complicated than the one of electromagnetic showers, also their simulation is more complex. Especially, it is tough to correctly model the interactions at the high energies in forward direction of the particles which are present in the extensive air showers since no experimental data exists. Therefore, data from particle accelerators needs to be extrapolated to such energies, which, of course, gives rise to some uncertainties. For the simulations, there exist various models that also depend on the energy of the particle. The transition energy from low energy to high energy regime is at 80 GeV. The model which is used for the low energy regime is called UrQMD (Bass et al. 1998; Bleicher et al. 1999). But more important than the low energy models are the high energy models since the focus of the proton spectrum lies on energies above a few TeV. For the higher energies, there are more models available, but mainly three of them were used for further investigations: EPOS LHC (Pierog & Werner 2009; Werner et al. 2006), SIBYLL 2.1 (Ahn et al. 2009; Engel 1999; Fletcher et al. 1994) and QGSJET II-04 (Ostapchenko 2011, 2014). But there are also

other models implemented in the Corsika software package: For the low energies there are two other models available, called Gheisha (Fesefeldt 1985) and Fluka (Fasso' et al. 2003), for the high energies three, called VENUS (Werner 1993), DPMJET (Ranft 1999a,b) and NEXUS (Drescher et al. 2001). Furthermore, different versions of these interaction models are available. In the later Section 3.1.2, which compares the different models, mainly image parameters are investigated, but the main differences of the models are already caused in the physical processes during the air shower simulation (see e.g. Parsons et al. (2011)). Some differences from model to model are the energy fraction of electromagnetic and hadronic sub showers, the number of different particles (e.g. muon or pion fractions) or the longitudinal and lateral distributions of the shower itself. Figure 2.15 shows, for example, differences in the emission of Cherenkov photons between different models. This is, of course, also observable in the simulated images. Thus, the used models already have a significant impact on the analysis itself which relies on these simulations.

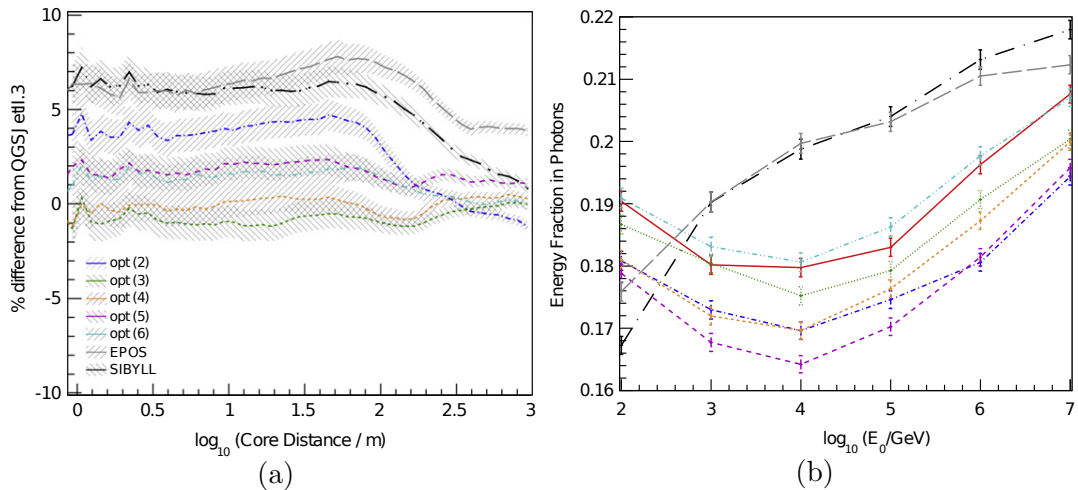


Figure 2.15: Differences in the emission of Cherenkov photons between different interaction models. The used models are the QGSJET-II model, also with differently set options (opt (2) to opt (6), for a detailed description, see Parsons et al. (2011)), the EPOS model and SIBYLL. The plots show the Cherenkov photon density compared to the interaction model QGSJET-II (a) and the energy fraction transferred to photons in hadronic showers (b). (Parsons et al. 2011)

Besides all these interactions, also the decay of unstable particles is included. In this case, the interaction length and decay length are calculated and the shorter one determines if the particle interacts or decays. Additionally, the energy loss of charged particles due to ionization processes, multiple scatterings (modeled with Molière's theory) and deflections on Earth's magnetic field are included. For the simulation of IACTs, the emission of Cherenkov light is especially important since this is the component of the extensive air shower that is measured with the telescopes. The code which simulates the emission of Cherenkov photons was originally written by the HEGRA collaboration but is now also included in the Corsika software package. The emission of Cherenkov light is modeled after the physics, which was already explained in Section 2.1.2 before. The refractive index of the atmosphere is determined by the density of the atmosphere, and the waveband of the simulated Cherenkov photons can be set during configuration. The photons are not treated individually, but they are grouped

into bunches of specified size to reduce the needed computation costs. For each bunch, its propagation to the telescope is calculated individually. These Cherenkov photon bunches are also the information that is used as input for the detector response simulation, which is described in the following.

Detector response simulation with `sim_telarray`

The next part is the simulation of the detector response, whose output is structured like the raw data from the H.E.S.S. experiment itself. The goal of this simulation step is to model the used hardware as precisely as possible to not introduce further biases and differences after the shower simulations. Therefore, most simulation parameters are determined by doing measurements of the real hardware and the environmental conditions at the site of the experiment. The used software is called `sim_telarray` (Berndlöhr 2001, 2008) and was also developed for the HEGRA telescope system but is now widely used in the H.E.S.S. community and was also adopted for simulations for the next generation IACT experiment CTA. Compared to the simulation of the particle showers, the simulation of the detector response is less costly in computing time. Thus, it is common practice to use a simulated air shower multiple times by shifting its impact point on the ground, resulting in different images of the particle shower in the telescopes. As input for the simulation, the Cherenkov photon bunches of the Corsika simulation can be directly used to reduce the needed storage space of the data.

The simulation combines all steps of the detector response in full detail. It includes everything from ray tracing of the photons, to the measurement with PMTs and its digitization:

- The optical system which takes into account the optical path of the photons, the reflection on the mirrors (including, for example, their reflectivity, shape or alignment), shadowing due to the telescope structure, the angular acceptance of the pixels (caused by the Winston cones) and atmospheric transmission.
- The photon detection efficiency which combines all of the above-mentioned effects as well as the quantum efficiency of the used PMTs.
- The night sky background which is usually modeled at a rate of 100 MHz but is also settable on the pixel level. Additionally, the afterpulsing of such night sky photons is included in the simulation.
- The electronics which combines the simulation of trigger signals and digitization in full detail down to considering the switching of discriminators and comparators. This full electronics simulation is done in a time window that is set to contain the complete time evolution of the Cherenkov signal in the camera. The trigger is simulated on the level of pixels to form a telescope trigger, which is then combined to the system trigger that initiates the data readout. The digitization is simulated for two channels, low gain as well as high gain, and can be done in sum mode (like for standard H.E.S.S. data taking) or sample mode where the full waveform is stored. For the simulation of the signal, which is then digitized, the single photoelectron response of the PMTs is used and transit times are included.

When the full simulation is finished, the data can be analyzed in the same way as real data from the H.E.S.S. experiment. Since the simulations have this critical role in the analysis of the proton spectrum, they are analyzed and optimized in Section 3.1 later on.

The analysis of cosmic ray protons

H.E.S.S., or IACTs in general, are built and designed for the detection and reconstruction of gamma rays of Galactic or extragalactic origin. However, for the reconstruction of the cosmic ray proton spectrum, it will be used to reconstruct the particles that are usually treated as background and are rejected. For a good reconstruction of these diffuse protons, the standard detection and reconstruction approach, which was outlined in the chapter before, needs to be adapted and optimized. The following sections focus on the different steps of the reconstruction of the CR proton spectrum with the H.E.S.S. experiment.

As Monte Carlo (MC) simulations are the most crucial part of the analysis and reconstruction with an IACT, the used simulation configuration is optimized and validated with respect to the used real data in Section 3.1. These simulations are used later on to optimize the standard Hillas approach for CR protons. This process along with the final expected performance of the reconstruction are shown in Section 3.2. To deal with the background, the common background rejection techniques are not applicable anymore since no background regions can be defined due to the diffuse origin of the protons. The existing background for the proton analysis and its rejection is explained in Section 3.3. After the steps of the proton reconstruction, the selection of the final real data set is presented in Section 3.4.

3.1 Validation of the Monte Carlo simulations

After data tacking, the calibration and the geometric reconstruction of the shower, all further steps in the reconstruction are based on simulations (at least to some extent). Furthermore, all tests and optimizations of the proton analysis chain are carried out with the help of MC simulations. So, the first step before even starting with the reconstruction of CR protons is the validation of the simulations, including the particle showers and especially the telescope response. This is needed since the simulation and detection of protons is not as widely tested as the simulations of gamma rays. The general approach of the validation is to compare the distributions of the image parameters (after cleaning) of simulated showers with real measured showers. This approach was chosen because the Hillas reconstruction uses the image parameters as a starting point without already using simulations in the reconstruction process. So, only image or geometrically reconstructed parameters are used. This approach is explained next. Found discrepancies between simulated and real data, as well as the steps to fix them, are presented afterward.

3.1.1 Method and first results

For a reasonable comparison of simulated CR data with real CR data, both used data sets need to be as equal as possible so that no additional discrepancies are introduced. The selection and preparation process before the direct comparison of both data sets follows.

Adjustments for both data sets

Since the analysis uses the Hillas approach, the first steps are the same for both data sets. Calibration, image cleaning, Hillas parametrization as well as geometry reconstruction are done in the same way. Afterward, cuts are applied to assure that only well-reconstructed events remain in the data set. The cuts are chosen to be harder than the standard Hillas cuts (see Table 2.1) but are not yet optimized for the reconstruction (see Section 3.2):

- A multiplicity of 4 to use only events seen by all four telescopes,
- image amplitudes of > 500 p.e. to select only bright images,
- a local distance of < 0.525 m to exclude truncated images,
- and no postselection cuts since they already use simulations.

Further adjustments to match both data sets are done individually and are outlined in the following.

Simulated data

The simulated data set needs to be as equal as possible compared to the real data set while keeping the computing costs low. Since not a full, isotropic simulation of all existing CR particles over the whole energy range can be done, only a suitable and representative part is computed. The used configuration of the simulations is as follows:

- As a framework, Corsika 74100 with the interaction models UrQMD 1.3cr and QGSJET II-04 together with sim_telarray was used.
- Several particle types were simulated to model the real CR spectrum: protons (p), helium (He), carbon (C), silicon (Si) and iron (Fe). These types were chosen since they are the most abundant ones of all cosmic ray particles. The way to combine these particles is described below.
- An energy range from 200 GeV to 100 TeV with a power law index of $\gamma = 1.5$ was simulated. Later on, the energy range was extended up to 1 PeV since, of course, events with energies larger than 100 TeV are expected and were tried to reconstruct.
- The emission of the particles was chosen to be diffuse within a cone of 2.2° radius from a direction with 20° zenith and 180° azimuth (i.e. facing south). The view cone was chosen to be smaller than the experiments FoV to save computing time but the real data set is adjusted to that.

The spectral index of the simulations was chosen to be $\gamma = 1.5$ to increase the abundance of high energy events and to save computing time during the simulation. The drawback of this

approach is that the simulated spectra do not match the real cosmic ray spectra anymore, which are at roughly $\gamma = 2.7$. Since the image parameters and their distributions highly depend on the energy of the events, the differing spectral index needs to be corrected, which is done by re-weighting the individual events according to their true energy:

$$w = \left(\frac{E_{\text{true}}}{0.1 \text{ TeV}} \right)^{\gamma_{\text{sim}} - \gamma_{\text{real}}}, \quad (3.1)$$

where γ^{real} is the powerlaw index of the real CR spectrum as determined by Hörandel (2003) and $\gamma_{\text{sim}} = 1.5$ is the simulated index. The factor 0.1 TeV ensures that the weight is always smaller than one. After this correction, the spectral behavior of MC and real data matches again.

Not only the spectral indices of the simulations need to match the real ones but also the flux, i.e. the amount of used particles within the simulated data set. Therefore, the results of Hörandel (2003) are used again. Although these measurements are already quite old, newer results are still similar. So, for the first investigations, the values of the spectral index and of the flux levels are used from this publication.

For the calculation of the amount of each individual, used particle, the real spectral shapes along with trigger and cut efficiencies are taken into account. The fraction of a single particle compared to the whole data set is then calculated as follows:

$$\text{frac}_i = \frac{\int \epsilon_i(E) \Phi_i E^{-\gamma_i} dE}{\sum_i (\int \epsilon_i(E) \Phi_i E^{-\gamma_i} dE)} \quad \text{with } i \in \{p, He, C, Si, Fe\}, \quad (3.2)$$

Particle	Fraction
Proton	0.709
Helium	0.157
Carbon	0.025
Silicon	0.083
Iron	0.026

Table 3.1: Used particle fractions for simulated data.

where Φ_i is the flux normalization, γ_i the index according to Hörandel (2003) and ϵ_i the energy-dependent trigger and cut efficiency given by the simulated telescope array. The resulting fractions are listed in Table 3.1, the total number of all particles is chosen to match the number of particles in the real data set.

Real data

The other way around, there are a few restrictions needed for the real data set, mainly because of the simulations which were only done for certain configurations. Thus, the following cuts are applied to the real data:

- Only zenith angles from 15° to 25° and azimuth angles from 175° to 185° are used to match the simulated pointing directions,
- only offset angles, meaning the angle between telescope pointing and shower direction, of $< 2.2^\circ$ are allowed to match the simulated diffuse emission
- and only data from the time period between 26. of May 2004 to 3. of July 2007 (muon phase 1b) is used since it matches the simulated optical efficiencies.
- Any gamma-ray sources in the data set are excluded to get rid of contamination with gamma rays.

Besides, no further restrictions were applied to the real data set.

Comparison of simulated and real data

After the preparation of both data sets, distributions of the Hillas image parameters and geometrically reconstructed shower parameters can be compared. The distributions of the Hillas length and width are shown in Figure 3.1, the distributions of the Hillas kurtosis, Hillas skewness, local distance and shower offset are shown in the appendix, Figure A.1. Additionally, the Hillas length distribution for different distances of the shower impact point to the array center (Fig. A.2) and the number of used pixels within the cleaned images (Fig. A.3) are shown in the appendix.

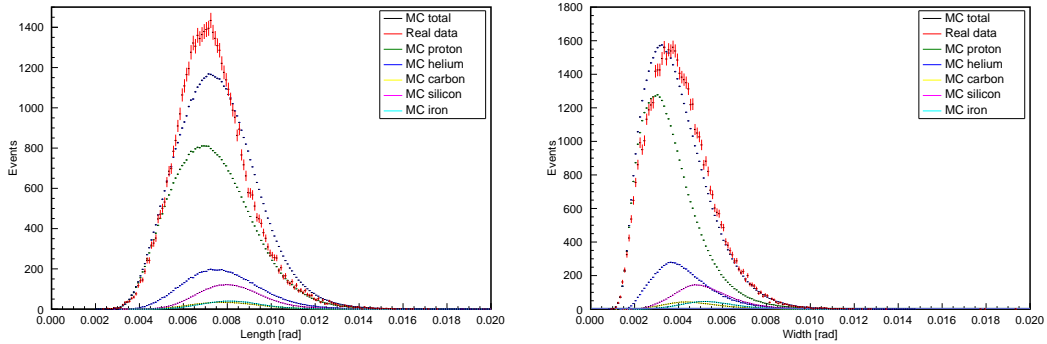


Figure 3.1: Comparison of the most differing image parameter distributions, the Hillas length on the left and the Hillas width on the right, between simulations and real data. The red color represents real data, the black color all simulated particles and the other colors the different simulated particle types.

By comparing the different distributions of simulated and real data, one can already see that they do not agree ideally. Especially, the width and length of the Hillas ellipse disagree significantly. Simulated showers appear longer (around 3%, see length) but narrower (also around 3%, see width) in the camera. Furthermore, the general shapes of the distributions are different, especially the real length distribution is more narrow than the simulated one. Besides, the higher moments of the shower images, skewness and kurtosis, look more similar. The local distance and the offset are in good agreement. By looking at the Hillas length distribution for different distances, Figure A.2, one can see that the discrepancies grow larger for larger distances. The differences of the images can also be seen in the number of used pixels in the cleaned images, Figure A.3: simulated images contain more pixels. This can, at least partly, be explained by the longer images of the simulated showers, which results in a higher pixel number. These findings already imply that the simulations do not perfectly resemble the real data.

3.1.2 Verification of simulation settings and parameters

Contrary to the expectation, simulations with the standard configuration usually used for the old H.E.S.S. I phase with only four small telescopes do not perfectly match the measured real data. Since it is not clear a priori, where these discrepancies come from, various tests were carried out to find a solution to these problems. Thereby, the focus of the investigations lies on the distribution of the image parameters and the simulation configurations. However, it was not possible to check and tune all configuration parameters due to time restrictions.

Furthermore, most of them should also match the real settings quite well since such adaptations were already carried out at the beginning of the H.E.S.S. experiment. Thus, only configuration parameters that are thought to have an impact on the observed image parameters are investigated. In the following, some of the more interesting investigations which led to solving these problems are presented and explained.

Interaction models

It was already mentioned in Section 2.3 that different interaction models influence the development of hadronic showers in the atmosphere. Differences in the shower development can also be seen in the image parameters. The parameter distributions of all tested interaction models and Corsika versions are compared to the currently most commonly used model in H.E.S.S., QGS II-04, in this case, used with Corsika 74100. This is done to see if the differences from model to model are large enough to cause the found discrepancies. These results are shown in Figure 3.2.

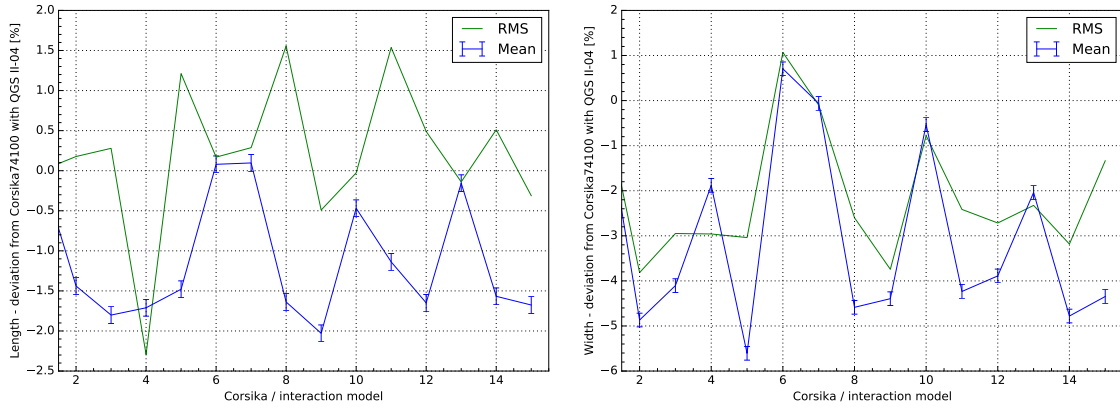


Figure 3.2: Deviations of the Hillas length and width distributions of different interaction models and Corsika versions from QGS II-04 with Corsika 74100. Shown are the mean together with the error on the mean and the RMS of the distributions. The corresponding models and versions to the numbers on the abscissa are shown in Table 3.2.

Number	Version	Model	Number	Version	Model
1	74100	QGS II-04	9	75700	EPOS LHC
2	74100	Sibyll 2.1	10	76400	QGS II-04
3	74100	EPOS LHC	11	76400	Sibyll 2.3c
4	74100	QGC 01c	12	76400	EPOS LHC
5	74100	DPMJET 2.55	13	6990	QGS II-03
6	74100	VENUS 4.12	14	6990	Sibyll - 2.1
7	75700	QGSII-04	15	6990	EPOS 1.99
8	75700	Sibyll 2.3			

Table 3.2: The tested interaction models and Corsika versions that were investigated in Figure 3.2.

By looking at the deviations from model to model, one can see that they deviate only in the range of a few percent. The mean of the Hillas length has deviations not larger than 2% and cannot fully explain the observed differences. Also, the differences of the RMS from model to model are not significant enough to explain the broader distribution of the simulated data. The mean of the Hillas width shows somewhat larger differences from model to model, which might be part of the reason of the observed differences. This is expected since differences in the interaction cross sections are more linked to the lateral particle distributions in the particle showers that cause differences in the measured Hillas width. A direct comparison of the different interaction models with real data also confirmed that the observed differences are not (entirely) caused by the interaction models since no model showed a perfect agreement with real data. The remaining differences of the length were always larger than 1.5% and of the width of more than 4%. Even though the interaction models do not seem to cause the large observed discrepancies completely, they are investigated further later on when the simulations are thoroughly verified for the spectrum since they still have an impact on the final proton spectrum (see Section 4.3.3).

Raw parameters and calibration

After the investigations of the shower simulations with Corsika, the simulated telescope response with `sim_telarray` needs to be analyzed. First, simulated raw images are compared to the real, measured ones to check for inconsistencies during the calibration. The investigated parameters were already explained in Section 2.2.2 when the calibration chain of the H.E.S.S. experiment was outlined. However, the different steps during calibration are modeled slightly differently in simulations. So, only the pixel intensity after calibration is directly comparable. Of particular importance is the case of saturation since saturated PMTs are hard to model. For validation of the saturation regime, which will be necessary for high energy events, the intensity values of the brightest pixel in the shower images are investigated. The results for the low gain channel (LG), used for bright and energetic events, of real measurements is shown in Figure 3.3, the results for simulated measurements in Figure 3.4. For completeness, all important calibration parameters in the simulations, from raw ADC values to photoelectrons, are shown in the appendix, Figure A.4.

By comparing the maximum intensities of real data with simulated data computed with the standard configuration (Fig. 3.4, plot on the left), one can see that the general shape of the distribution is similar. However, the saturation regime is different: in MC simulations, the saturation starts at higher photoelectron values, at ~ 4200 p.e. instead of ~ 2800 p.e., and the saturation regime is more narrow. The different starting points of saturation are caused by differently set linear ranges of the ADCs. By adjusting the pedestal value in the configurations of the simulation to the ones used in the real experiment, the linear ranges also align. This adaption results in the intensity distribution in Figure 3.4 on the right where the start of the saturation now matches with real data. The broader saturation regime and slightly later saturation in real data is caused by various effects in the real PMTs, which cause the individual PMTs to behave differently. All these different effects cannot be modeled in simulations, meaning that there will be discrepancies at high saturation.

The best way to circumvent systematic differences is to avoid high saturation levels entirely. To see if such a high saturation is reached during the analysis, one can check how many of the PMTs are saturated at which proton energies. Figure 3.5 shows the number of saturated PMTs in an image as a function of the measured size and the impact distance of

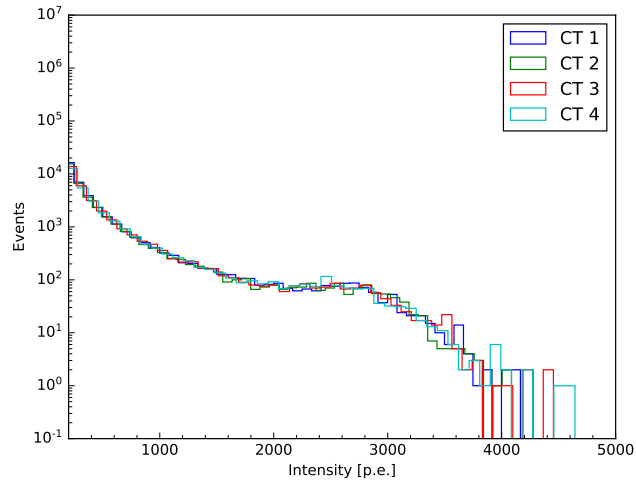


Figure 3.3: Pixel intensity after calibration of the brightest pixel for the low gain channel of real data.

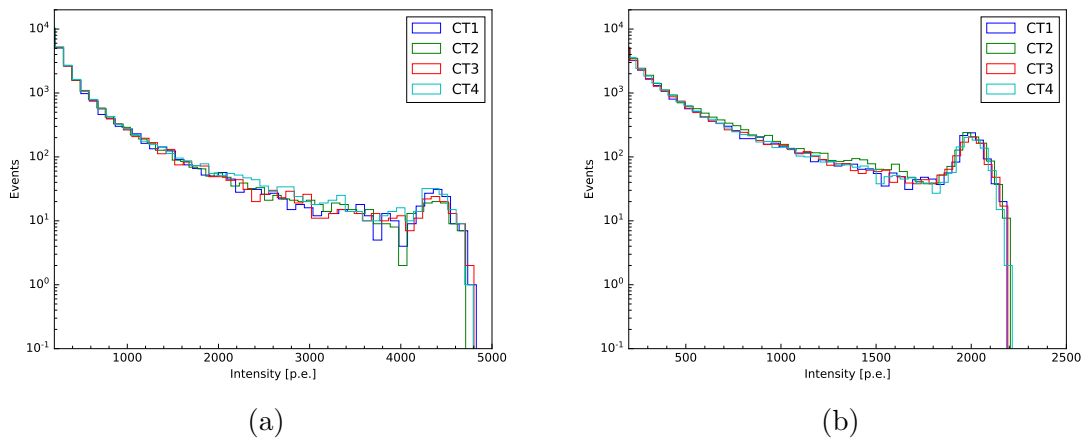


Figure 3.4: Pixel intensity after calibration of the brightest pixel for the low gain channel of simulated data. Shown are the intensities with standard configuration (a) and with adjusted configuration (b).

the shower. Thereby, saturation is defined as individual PMTs with an intensity above 2000 photoelectrons. Since this plot is structured like an energy lookup, every point in it can be transferred to a corresponding energy. A maximum of 5% of saturated PMTs in an image are allowed since it showed that above that value, the reconstructed energy deviates to more than 5% from the true energy. With this limit, image amplitudes of up to 300k p.e. are still usable without introducing a too large bias during the reconstruction. This size value would be equivalent to energies of roughly 1 PeV, but as will be seen later, the available energy range of the proton spectrum will be much smaller, meaning that saturation effects can be neglected in the analysis.

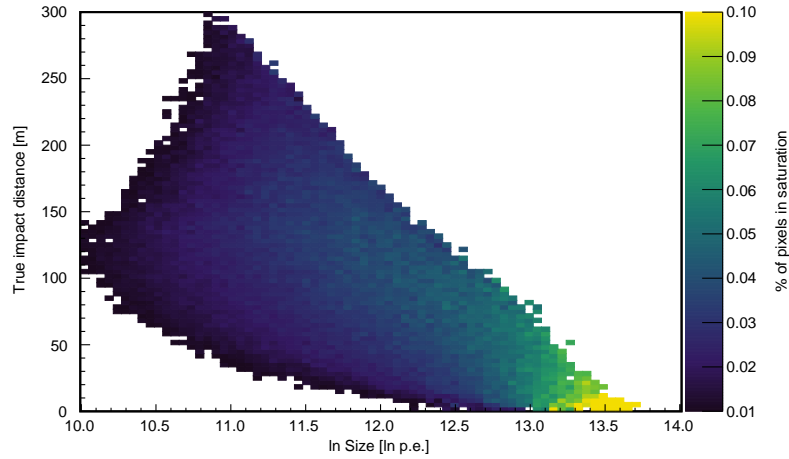


Figure 3.5: Percentage of saturated pixels (>2000 p.e.) in the cleaned image.

Pedestal width and night sky background

Also connected to the last investigations of the raw parameters is the width of the pedestal. With a closed camera lid and thus no extra light in the PMTs, the pedestal line is quite narrow since it is only affected by electronic noise. During observations with an open lid, photons from the night sky can fall onto the PMTs. Such photons within the readout window can broaden the pedestal width (see e.g. Aharonian et al. (2004)). Thus, the variation of the pedestal gets larger with higher night sky background (NSB) rates. A broader baseline can also influence the image parameters because more pixels might survive the image cleaning. Since the NSB is usually simulated at a fixed value, it might cause discrepancies if the real NSB rate deviates too much from the simulated one. Therefore, simulations with different NSB rates were carried out, and the corresponding pedestal width is determined and compared to the measurements of a few real observation runs. The pedestal width as a function of the NSB rate is shown in Figure 3.6 on the left.

The results are shown for one of the used optical efficiency phases where an NSB rate of 70 MHz (after an applied reduction of the optical efficiency due to aging effects) is used in the simulation, marked by the black star. The green data points are from real observation runs with low, medium and high NSB rates, whereby most of the used runs have rates in the medium range. This means that the simulated NSB rates are in rough agreement with most of the observation runs. Additionally, the variations of the Hillas parameters due to occurring

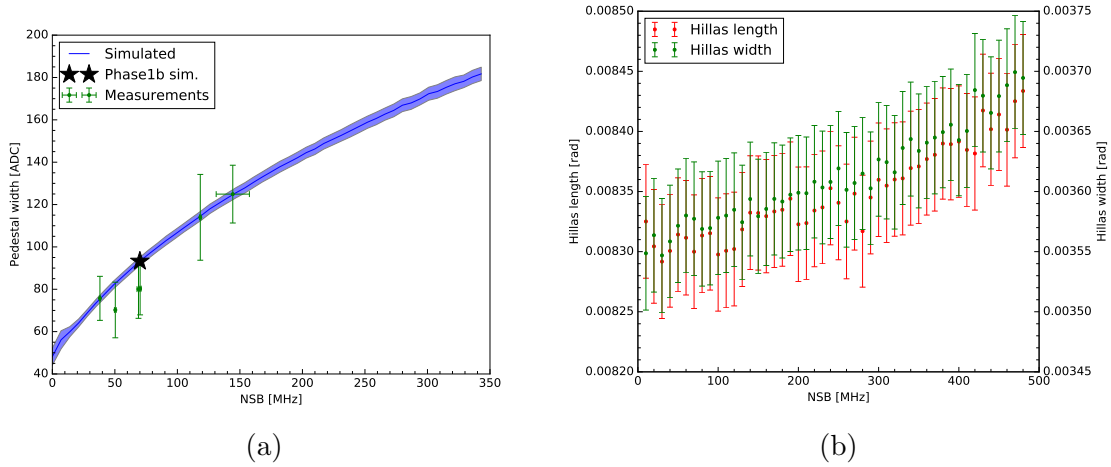


Figure 3.6: Measured pedestal widths for different night sky background levels (a). The blue curve was determined with simulations with different NSB levels, the black star is the resulting NSB level for simulations of muon phase 1b. The green data points are real measurements for data that was taken in the same muon phase. The NSB levels of all real data that will be used for the proton analysis lies between both outer points, thus between roughly 50 MHz and 150 MHz. The plot on the right (b) shows the influence of the NSB on the Hillas width and length.

NSB rate changes are rather small, see Figure 3.6 on the right, only around one percent, and thus not the origin of the large observed differences.

Further adjustments would also not be reasonable since the current value already resembles the pedestal width quite well. However, there are efforts to use runwise simulations that are tailored to each individual run (Holler et al. 2017), but this would not be feasible for such an extensive data set, which will be used for the proton spectrum.

Optical efficiency

Already mentioned was the optical efficiency of the telescope system that describes how many of the emitted Cherenkov photons are lost due to optical inefficiencies (e.g. from mirrors or shadowing). Similar to the pedestal width, the optical efficiency is also simulated but deviations from the real optical efficiency might explain differences in the shower images. Therefore, the simulated optical efficiency is compared to measured ones. As was already explained in Section 2.2.3, the optical efficiency is determined with images of muon events. Such events were simulated, and the optical efficiency was determined for both used optical phases. These results are compared with the optical efficiency of each observation run. Simulated, as well as measured efficiencies, are shown in Figure 3.7.

It can be seen that the optical efficiencies which are used in the simulations match the mean of the observed optical efficiency quite well. Nevertheless, from the beginning to the end of the phases, the deviations can be significant but the influence on the Hillas parameters is again quite small: if realistic changes on the optical efficiency are assumed, like from 0.09 to 0.07 (from the beginning to the end of phase 1b), the Hillas length varies less than 1.5% and the Hillas width less than 3%. So, the changes in the length are too small to explain the

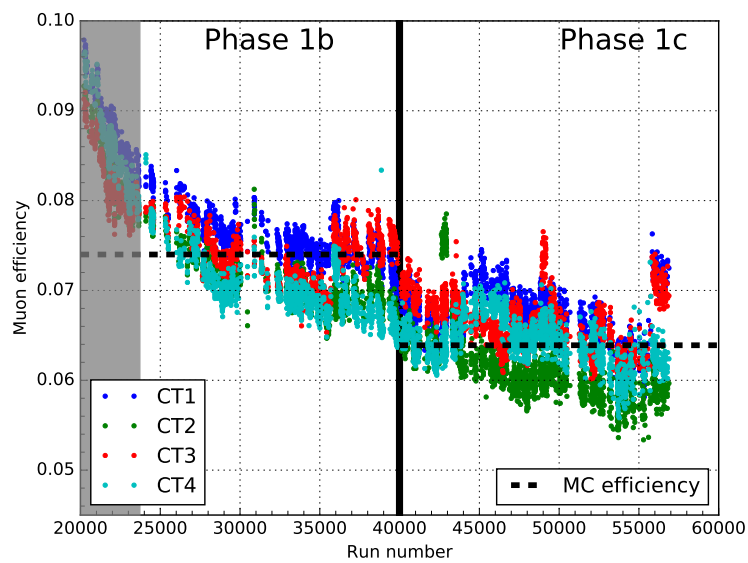


Figure 3.7: Comparison of the simulated optical efficiency with the measured efficiency. Data from both muon phases which will be part of the final proton spectrum was used (phase 1b, from 26. May 2004 to 3. July 2007, and 1c, from .3 July 2007 to 27. April 2010). The colored dots represent the runwise measured efficiencies for all four telescopes, the dotted, black lines give the efficiency which was used in the simulations. The shaded region marks runs with a larger deviation from the simulated efficiency that will not be used in the final data set.

observed discrepancies. Since such large differences in the optical efficiency only occur for a few runs, the effect of the muon phase on the Hillas width distribution is not as large as shown here, so it is only partly responsible for the observed discrepancies and the dominant effect is still the choice of the interaction model. Additionally, further corrections of the optical efficiencies are carried out during the energy reconstruction, see Section 2.2.3 so that the effects should be even smaller at the end. Nevertheless, the runs at the beginning of phase 1b are not used in the final data set since they show a large deviation from the simulated optical efficiency.

As was already mentioned, runwise simulations might help to model the optical efficiency even further. But for the analysis of the proton spectrum, optical efficiencies will be used as shown here.

Broken pixels

Another important factor that might influence the measured shower images is the number of broken pixels in a run (see Section 2.2.2). As for the NSB or the optical efficiency, it is not feasible to simulate the exact broken pixels for each individual run so that usually no broken pixels are simulated at all. If only a small number of pixels is broken, this should be a sufficient assumption. As will be explained later on, runs with a too high number of broken pixels are excluded anyway. To ensure that the number of allowed broken pixels does not influence the measured image parameters, a few simulations are carried out with included broken pixels. Therefore, a typical broken pixel pattern from an observation run was chosen at random and the broken pixels were simulated. In the simulations, the intensities of broken pixels are set to zero so that they do not count for the Hillas analysis but are still part of the trigger. This is also the way how most of the broken pixels usually influence real observations. The broken pixels of the camera, which was used to investigate the influence of broken pixels on the Hillas distributions, are shown in Figure 3.8. For this camera, a total of 50 pixels were set to broken, compared to a mean of 52 broken pixels in all runs used for the proton analysis (see Fig. A.5 in the appendix for an overview of the broken pixels of all runs used for the proton analysis). Afterward, the Hillas parameter distributions of simulations with broken pixels are compared to ones without broken pixels, shown in Figure 3.9. Some expected changes in the distributions are visible. The number of pixels in a cleaned image goes down and with that, the length and the width. But only the observed shift in the number of pixels is able to explain the discrepancies of the used pixels between simulated and real data. The variation of the mean of the Hillas parameter distributions is below 1% and thus not able to account for the observations. Therefore, the usual way of not including broken pixels in the simulations is kept since it greatly reduces the complexity and amount of needed simulations.

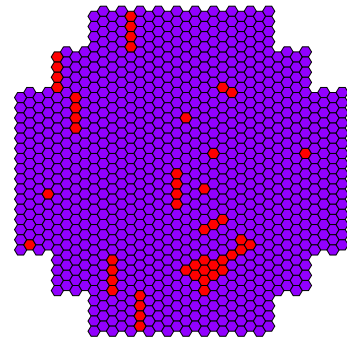


Figure 3.8: Broken pixels of CT1 for a typical run.

Peak time of the pulses in the readout window

As was also mentioned in the calibration chapter before, the timing of the readout window has to be set in the right way so that the Cherenkov pulses are located in the digitized sample.

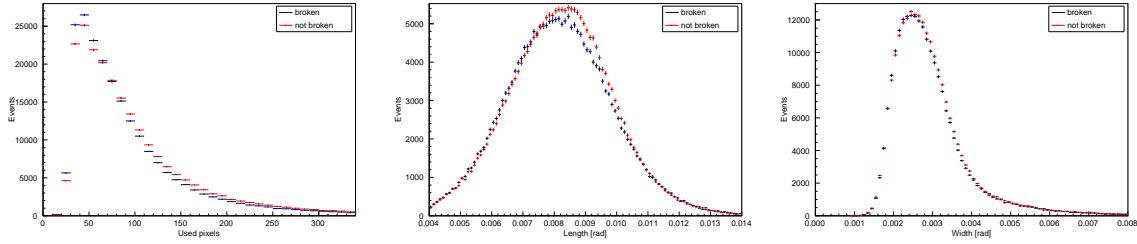


Figure 3.9: Impact of broken pixels on the image parameter distributions. Shown are the distributions of the used pixels (left), the Hillas length (middle) and the Hillas width (right).

The position of the readout window has to be at the same place in simulations and real data. If this is not the case, it might happen that pulses are cropped at the end or the beginning of the window, either for simulations or real measurements. Differences in the position of the window would, therefore, cause discrepancies in the number of registered photoelectrons and, of course, also in the Hillas parameter distributions.

During normal operations, the signal in the readout window is integrated and only the full charge is stored on disk so that there is no possibility to retrieve the position of the signal. But there is the possibility to operate the cameras in the so-called sample mode where the full waveform is recorded and stored. For the upcoming investigations, sample mode data from observation runs and flat field runs are used. To get the peak position from the uncalibrated observation data, events with a signal have to be separated from events without signal so that the position of the peak is not biased by electronic noise. Therefore, the position of the baseline was determined by fitting expected distributions to all pixels without a Cherenkov signal. For the determination of the pulse position, only events with signals larger than ten times the pedestal width are used.

For the simulations, there exists the possibility to simulate and store the full waveform, making it comparable to real data. This time, the spectral index was simulated to be 2.7, adapting it to the expected spectrum in real data. This needs to be done since the peak positions of Cherenkov light from particle showers depends on the energy: high energy events trigger the telescope system also from a large distance where the shower images show a larger extension and take a longer time to evolve in the camera. For cosmic ray simulations, events without signal are again excluded. This is not necessary for simulations of flat field events since there every pixel shows a signal.

The mean pulse positions of sample mode observation runs of all four telescopes from the period, which will be used later for the proton spectrum, are shown in Figure 3.10. In the same figure, simulated events with different pulse positions are shown. Since the pulse amplitude was not further investigated, the amplitudes of all peaks was arbitrarily chosen.

The best agreement between the pulse position of sample observation runs and simulations can be achieved by setting the simulation configuration to an offset of 3 or 4. This offset value corresponds to the N_D value of real data, mentioned earlier during the explanation of the calibration procedures of H.E.S.S. data, Section 2.2.2. By also taking into account the sample flat field runs (see appendix Figure A.6), the best pulse offset is found to be at a value of 4. For the real sample flat field runs, CT4 had to be excluded since no reliable data was available for the needed time period. In the standard configuration for the simulations, this

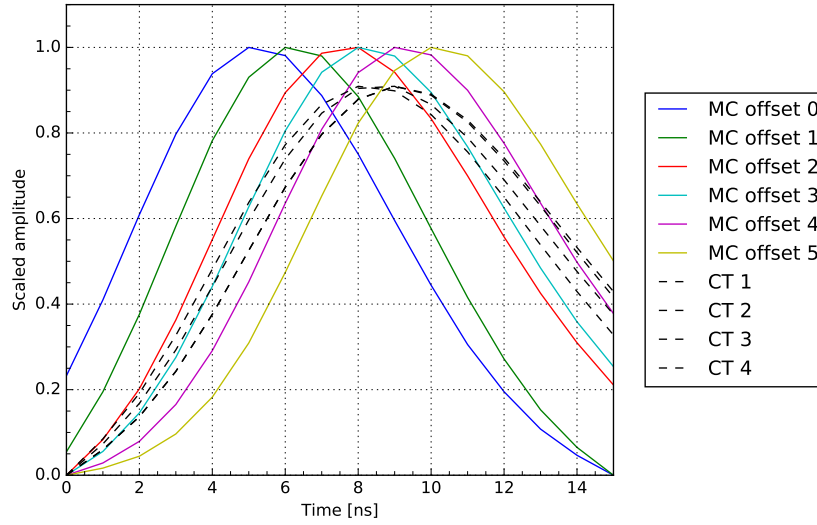


Figure 3.10: Comparison of the mean pulse position of simulated observation runs with real observation runs taken in sample mode. The colored signals are from simulations with different pulse offsets, the black, dashed curves are from real observation runs.

value was set to 3 together with a smaller simulation window of only 30 ns for trigger and 25 ns for digitization. For all upcoming simulations, the simulation interval was increased to 60 ns and the peak offset was set to be 4.

3.1.3 Results and conclusion

Besides the outlined investigations from above, several other things were studied: influences of the atmospheric density and transmissivity, the used fluxes and spectral indices from other experiments, selection effects of the data sets and the contamination of gamma-ray showers. However, they all showed only small or no impact on the observed discrepancies. All found inconsistencies in the simulations were changed and adjusted, as mentioned above. Furthermore, the simulated energy range was extended up to 1 PeV and some additional analysis cuts were applied, which will be used for the final analysis (see next Section 3.2). These cuts also include the cuts on the parameters MSCW and MSCL, which are usually used for particle separation. In this case, they improve the reconstruction of the protons and remove all particles which are heavier than helium (see also next section). Although the calculation of both parameters is already based on simulations, only simulated gamma rays are needed whose simulations are less complex and more tested, meaning that they will only have a negligible influence on the Hillas distributions of proton simulations that showed discrepancies when compared to real data. After all these adjustments and the application of additional cuts, the final distributions of the Hillas parameters are calculated again, which is shown in Figure 3.11 and Figure 3.12.

As can be seen, all distributions of the Hillas parameters are now in good agreement with the observed real data. Also, the effect of the distance of the shower impact point on the

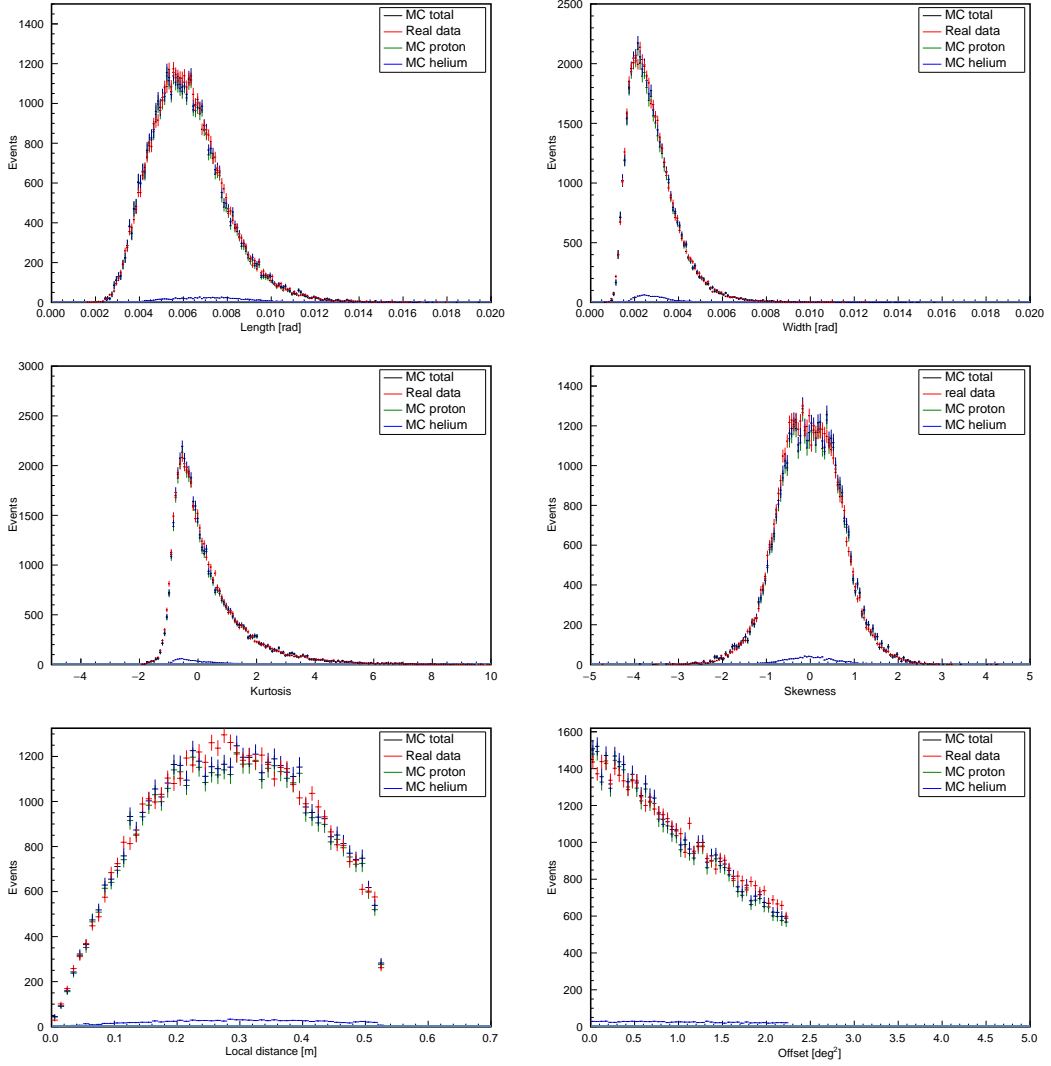


Figure 3.11: Comparison of image parameter distributions between simulations and real data after all mentioned adjustments of the simulation configuration were carried out. The red color represents the real data, the black color simulations and the other colors, green and blue, the different particle types that were combined for the black curve. In this case, only protons and helium are included since all heavier nuclei are excluded by the introduced cuts. Shown are the Hillas length, the Hillas width, the Hillas skewness, the shower offset the local distance and the Hillas kurtosis (clockwise, starting from the upper left).

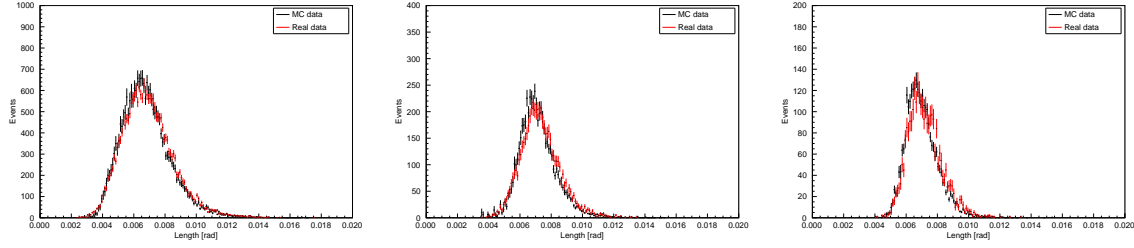


Figure 3.12: Comparison of the Hillas length distribution of simulations and real data for different bands of distances between shower impact point and array center after all mentioned adjustments of the simulation configuration were carried out. The distances are 80-150 m (left), 150-200 m (middle) and > 200 m (right).

observed Hillas length vanished, giving well matching distributions. This means that the deficiencies in the simulations could be eliminated by adjusting some configurations to match the real experiment in a better way. For all upcoming tests and investigations, including the reconstruction of the proton spectrum, simulations with the mentioned adjustments are used.

3.2 Event selection and reconstruction

After the investigations and improvements of the simulations above, they are in good agreement with real observations. Therefore, they can now be used to develop and test the reconstruction and analysis chain for the CR proton spectrum. First, a good reconstruction of the protons needs to be assured. Since the standard Hillas analysis is optimized for the reconstruction of gamma rays, some adjustments to the general approach are needed.

3.2.1 Optimization of the reconstruction

The most important parameter during the reconstruction of the proton spectrum is the energy of the primary proton, which initiates the observed particle shower. As was shown before (Fig. 2.11), the energy is reconstructed using lookup tables where the energy is stored as a function of the measured image amplitude and impact point. Therefore, the following optimizations are carried out by improving the accuracy of the reconstructed impact point. The general approach for the optimization is to use only bright particle showers that are fully contained in the camera and have an elliptical shape. Such a shape helps during the reconstruction of the direction and impact points since the major axes of the different camera images, which are intersected for the reconstruction, can be better determined. The cuts, which are investigated, are:

- A higher **multiplicity**, i.e. the number of used telescopes during the reconstruction of an event, improves the reconstruction since more information of the shower is available.
- A larger **image amplitude** means brighter images in the camera for which the Hillas parametrization is more efficient.
- A cut on the maximum **local distance** ensures that shower images are fully contained in the camera and no helpful information for the reconstruction is lost.

- Cuts on the parameters **MSCW** and **MSCL** result in proton events that look like gamma-ray events, thus having a more elliptical shape, which results in a better reconstruction.

Since the final data set for the reconstruction of the proton spectrum will have large statistics, the cut on the multiplicity is set to four. So, only events that were seen by all four telescopes will be used in the analysis. The other cuts will be chosen to ensure a reasonable reconstruction of the impact point but without excluding too many events, thus causing low statistics. The measure to determine the accuracy of the reconstruction of the impact point are the bias and the resolution of the reconstructed values. The bias is defined as

$$\text{bias} = \frac{d_{\text{reco}} - d_{\text{true}}}{d_{\text{true}}} \quad (3.3)$$

with the reconstructed distance from the shower impact point to the position of the individual telescopes d_{reco} and the true distance d_{true} from the MC simulations. The resolution is then defined to be the spread of the bias. The fraction of remaining events after the cut is also calculated to verify that not too many events are excluded from the analysis.

The first two parameters which are optimized are the image amplitude and the local distance, analyzed together in a 2d grid scan. The results of these investigations are shown in Figure 3.13, the remaining events on the left, the resolution of the reconstructed impact point on the right. The bias of the impact point is not presented since it already showed a mean value centered at around zero. One can see that the local distance does not show a considerable influence if set to be < 0.6 m. The cut on the size has a more significant impact on the resolution of the impact point since a better reconstruction is possible with higher size values. By choosing a high size cut of up to 1000 p.e., one would not lose many events but the lowest detectable energy will be higher, which is also not desired. Thus, the cuts on both parameters are chosen to be: size > 300 p.e., which is larger than the standard Hillas cut, and local distance < 0.525 m, equal to the standard cut. These cuts already result in a resolution of the reconstructed impact point of all events of smaller than 25%.

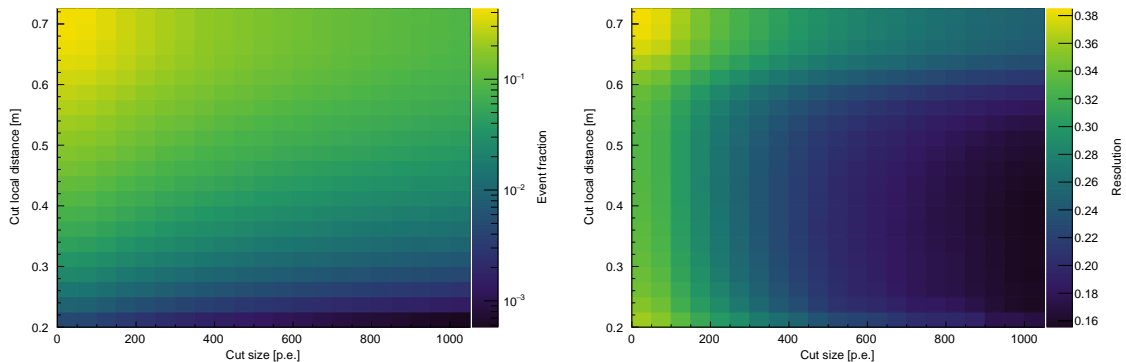


Figure 3.13: Cut optimization of the image amplitude and the local distance. Shown are the fraction of remaining events after cuts on the image amplitude and the local distance on the left and the resulting resolution of the reconstructed impact point on the right.

The next parameters to be optimized are the **MSCW** and **MSCL**. Therefore, the cuts found above are already applied, and the accuracy of the reconstructed impacted point is

again investigated for different sets of cuts. The results of this investigation are shown in Figure 3.14, where only the upper cut on the parameters is shown. The lower cut is not shown since it does not influence the accuracy of the reconstruction because it would only exclude gamma like events which are already well reconstructable. The plots show that the MSCL parameter, connected to the Hillas length, has basically no influence on the reconstruction in contrast to the MSCW, connected to the Hillas width. Good cut values for the MSCW lie in the range of 3 to 8, but by looking ahead to the determination of the background, the cut is chosen to be 6 since this will exclude most of the expected background of heavy nuclei. Since the MSCL parameter does not have a big impact on the analysis, it is chosen to be the same. Thus, the resulting cuts are: MSCL in the interval $[-6;6]$ and MSCW in the interval $[0;6]$ by already taking into account the results from the background determination. The application of all so far mentioned cuts results in a resolution of the reconstructed impact points of $< 15\%$, already a good enough performance that will result in a proper energy reconstruction.

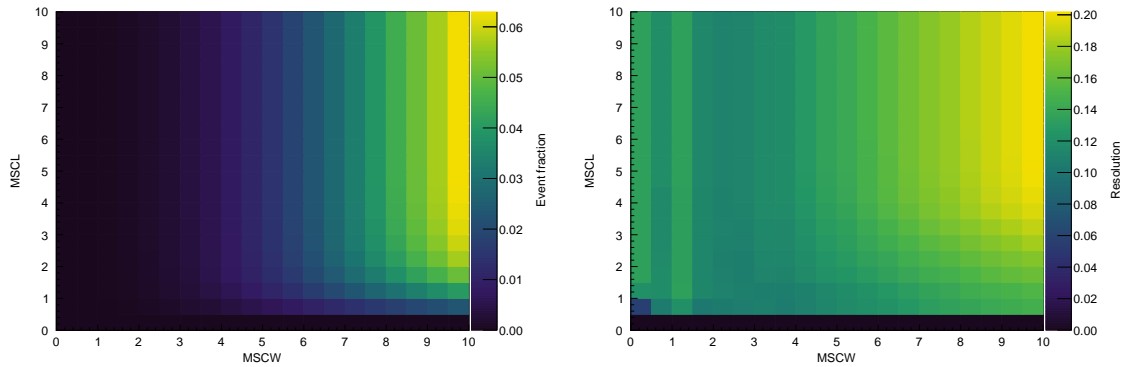


Figure 3.14: Cut optimization of the separation parameters MSCW and MSCL. Shown are the fraction of remaining events after cuts on the scaled parameters MSCW and MSCL on the left and the resulting resolution of the reconstructed impact point on the right.

In addition to the above-mentioned cuts, further analysis cuts were added since they proved to enhance the reconstruction of protons. These cuts, with a short description of how they improve the analysis, are:

- A cut on the distance from the shower impact point to the array center, called **core distance**, of < 200 m is used to exclude distant showers that suffer a worse reconstruction. The inferior reconstruction is caused by the geometric approach of intersecting the major axes of the Hillas ellipse. For remote showers, the major axes become more and more parallel, making the exact determination of the intersection point more difficult and more sensitive to errors. These reconstructed distances tend to be smaller than the actual value, which results in too low estimated energies.
- A cut on the goodness of the reconstructed shower impact point is introduced. The **core goodness** is represented by two parameters, the mean deviation of each intersection point of two telescopes from the final reconstructed core and their spread. Both values are set to be < 30 m, which excludes showers with an unreliable reconstructed impact point.

- A cut on the angle between telescope pointing direction and direction of the particle shower, called **offset**, of $< 1.5^\circ$ is used to exclude showers from the outer edges of the FoV. The reasoning is the same as for the core distance.

All the mentioned cuts before are summarized in Table 3.3. These cuts were found to assure a good reconstruction performance, see the next section, while maintaining a low background of other particles, see Section 3.3.

Selection cut	Allowed values	
Multiplicity	4	Pre-selection
Image amplitude	> 300 p.e.	
Local distance	< 0.525 m	
MSCW	[0.0:0.6]	Post-selection
MSCL	[-6.0:6.0]	
Core distance	< 200 m	
Core goodness	< 30 m	
Offset	$< 1.5^\circ$	

Table 3.3: Final analysis and selection cuts for the CR proton spectrum. Results of the background investigations are already included (see Section 3.3).

Creation of the lookup tables for the reconstruction

As was already outlined in Section 2.2.3, the next step in the analysis chain after the geometry reconstruction is the energy reconstruction. But before the performance of the energy reconstruction can be determined, proton energy lookup tables have to be created. Additionally, new gamma-ray lookup tables are needed for the determination of the MSCW and MSCL parameters since the configurations of the simulation were changed. Such new gamma-ray lookup tables were already used for the MSCW and MSCL cut optimization outlined in the section before. The parameter combinations for which the proton and gamma-ray simulations were carried out are listed in Table 3.4. For the creation of the gamma-ray lookup tables, the standard Hillas preselection cuts (see Table 2.1) were used without further adjustments. In contrary, for the proton energy lookup tables, the postselection cuts from above were used. Because of these harder cuts, more simulations are needed to get enough statistics. Lookup tables for the effective area and energy migration were also produced in that way but will be explained in more detail in Section 4.1.2, which deals with the reconstruction of the proton spectrum.

3.2.2 Performance of the reconstruction

After developing a robust set of cuts and creating the lookup tables, the reconstruction performance of the proton analysis chain can be tested. Therefore, diffuse proton simulations of optical phase 1b with a zenith angle of 20° and an azimuth angle of 180° were created. In the same manner as shown in Equation 3.3, the bias and resolution can be determined both for the impact point and for the energy reconstruction. The results are shown in Figure 3.15 below.

Configuration values	protons & gamma rays
Spectral index	$\gamma = 1.5$
Zenith angle	$0^\circ, 10^\circ, 20^\circ, 30^\circ$
Azimuth angle	0° (north), 180° (south)
Optical phase	1, 1b, 1c
Emission type	point source
Offset angles	$0.0^\circ, 0.5^\circ, 1.0^\circ, 1.5^\circ, 2.0^\circ$

Table 3.4: Parameter combinations for which the simulations of the gamma-ray and proton lookup tables were produced.

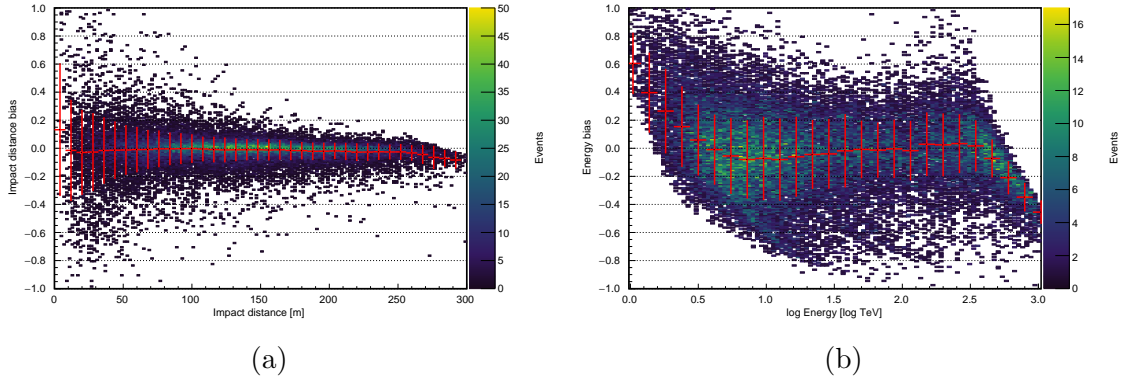


Figure 3.15: Bias and resolution of the impact distance (a) for one telescope as well as for the energy reconstruction (b). The colored entries represent individual events, the red data points the mean and resolution of the reconstructed values for given energies.

A good reconstruction performance is characterized by a bias close to zero and a small resolution, meaning that a reconstructed parameter is always close to the true one from the simulations. Since the set of cuts was optimized with respect to the impact distance, the bias and resolution of the reconstructed impact point are already quite small. Close to the telescope, the resolution worsens, and far away from it, the bias becomes negative. The latter effect is caused by the cut on the array impact distance, meaning that only events with a too small reconstructed distance survive the cut leading to a negative bias.

However, the more crucial part is the reconstructed energy. Of course, the final energy bias is not as good as for the reconstruction of gamma rays. Nevertheless, the bias is below 5% over a broad range of energies, from roughly 3 TeV to 500 TeV, with a resolution of 30% and less. The steep increase of the energy bias towards both ends of the simulated energy spectrum is again caused by selection effects. Because of the upper end of the simulated energies used for the creation of the energy lookups, only fluctuations towards lower energies compared to the true energy are possible, leading to the negative bias. At the low energy end, the contrary happens, which leads to a positive energy bias. There, another effect is superimposed: low energy events are usually not as well reconstructed, tending to larger impact distances compared to the true one, which leads additionally to a positive bias. The rise of the energy bias at both ends of the energy range will also be later used to determine the energy range usable for the reconstruction of the spectrum.

Another important test for the performance is the angular resolution. Similar to above, it is defined as the 68% containment radius of the bias. The energy-dependent angular resolution is shown in Figure 3.16. For high energies, a good resolution of roughly 0.1° can be achieved with a worsening towards lower energies. For the analysis of gamma rays, the angular resolution is still better since it is below 0.1° . But for the reconstruction of a proton energy spectrum, a very good angular resolution is not mandatory since diffuse emission is analyzed and not the exact position of a point source determined.

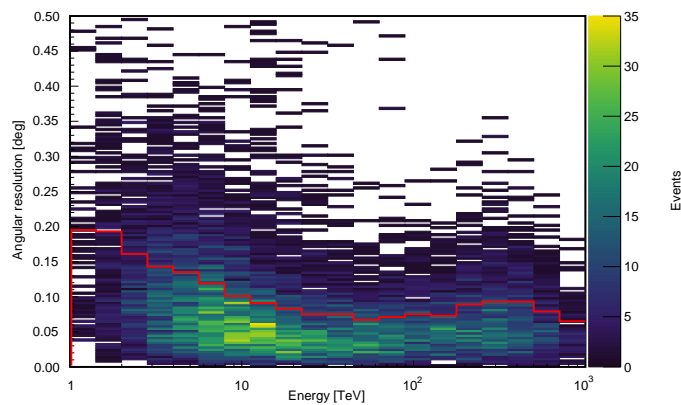


Figure 3.16: The angular resolution which describes the accuracy of the directional reconstruction. The colored entries represent individual events, the red line the mean angular resolution for a given energy.

3.3 Background rejection

The next point of the proton analysis, which needs to be treated differently compared to the standard analysis of gamma-ray point sources, is the rejection of the occurring background. Due to the diffuse nature of CRs, they are seen as signals from the whole field of view, making it impossible to define regions for the determination of the background signal (as it is done for gamma rays from point sources, see Section 2.2.3). The expected background can be split into two categories with respect to their origin:

- Hadronic particle showers, initiated by all other CRs heavier than the protons;
- Electromagnetic particle showers, initiated by gamma rays or electrons.

The general approach to get rid of this background in the context of the proton spectrum is to use the parameters from the adapted Hillas analysis outlined above to reduce the background to levels where it can be neglected. In the following, the actions carried out to reduce the expected background contamination are explained for both categories.

3.3.1 Heavy nuclei

By looking back to Figures 1.3 and 1.4 in the introduction, one can see that the cosmic rays consist of various particles. Among these nuclei, protons are the most abundant nuclei, while all heavier nuclei are less abundant. Besides the varying flux from particle to particle, also their spectral indices vary from the before stated value of $\gamma \approx 2.7$. In general, one can expect that the contamination of heavier nuclei becomes less and less critical with a rising atomic number because of the lower fluxes.

For the examination of the background from these heavy particles, one can have a more detailed look at the MSCW and MSCL parameters. Until now, they were used to select protons with an elliptical shape since they result in a better reconstruction. However, these parameters were originally developed for the separation of gamma rays from protons and other heavy nuclei (see Section 2.2.3). The plot on the left in Figure 3.17 shows the distribution of the MSCW parameters for electromagnetic and hadronic showers after slightly harder cuts on the size and the local distance, as mentioned before, i.e. > 500 p.e. and < 0.525 m. Since this plot intends to show the differing MSCW distributions from particle to particle, the number of used events does not follow the real, expected spectra as measured by other experiments. As can be seen, the distributions for more massive particles are centered at higher MSCW values. This is observed since the particle showers of heavy nuclei carry more lateral momentum, which results in a broader and thus less elliptical image in the camera. The distributions for gamma rays and electrons are centered at zero, which comes with the construction of the method itself: the MSCW parameter represents the deviation of the measured width of a particle shower from the mean expected width of a gamma-ray shower. Since particle showers initiated by electrons are of the electromagnetic type, they closely resemble gamma-ray showers. Thus, their distributions look very similar. This means that by using cuts on the MSCW parameter, the heavy nuclei can be already mostly excluded with only helium left as a possible contamination. By also using a cut on the lower end of the MSCW distribution, like $[0.0 : 6.0]$, some part of the electron and gamma-ray contamination can be excluded (see also next section).

Since helium is the heavy nuclei closest to protons in the MSCW distribution, the expected contamination of helium in the data set is calculated. Therefore, more recent measurements

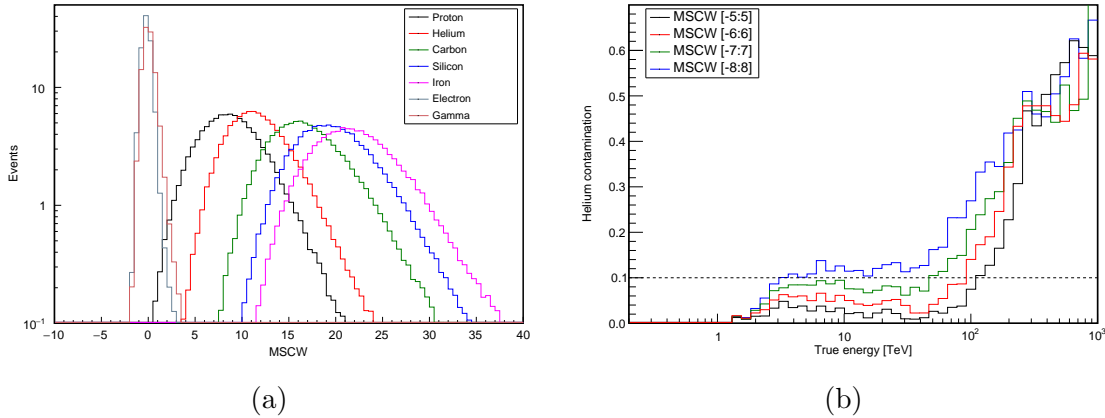


Figure 3.17: Behavior of the diffuse background for the proton spectrum (gamma rays, electrons and positrons as well as heavy nuclei) with respect to the width parameter. The distributions of the MSCW parameter, which is mainly used for particle discrimination, is shown (a) where the electromagnetic particles, gamma rays and electrons, are centered at zero and the protons and heavy nuclei to the right with heavier ones at larger values. Hard cuts on the size and local distance can already sort out many of the background particles. The main background of the heavy nuclei is helium, whose energy-dependent contamination after postselection cuts with varying cuts on the MSCW parameter is also shown (b). For all hadronic interactions shown here, the QGS II-04 interaction model was used.

of the proton and helium spectra from the CREAM experiment were used (Yoon et al. 2011). The data set was prepared in the same way as was explained before in Equation 3.2 in the section about the MC validation. This time, all cuts (preselection and postselection) are included, and the cut on the MSCW parameter is varied to get its influence on the helium contamination. The energy-dependent contamination is then defined to be

$$\text{Contamination}(E) = \frac{N_{He}(E)}{N_{He}(E) + N_p(E)} = \frac{\epsilon_{He}(E)\Phi_{He}E^{-\gamma_{He}}}{\epsilon_{He}(E)\Phi_{He}E^{-\gamma_{He}} + \epsilon_p(E)\Phi_pE^{-\gamma_p}}, \quad (3.4)$$

with the same definitions as before: Φ is the flux normalization, γ the spectral index (according to Yoon et al. (2011)) and ϵ the energy-dependent trigger and cut efficiency. The resulting, expected contamination for the QGS II-04 interaction model is shown on the right plot in Figure 3.17. Investigations with other interaction models, given in the appendix (Fig. A.13), showed that for Sibyll 2.1 and EPOS LHC, the rise of the contamination with helium starts at slightly lower energies. For small energies < 100 TeV, the helium contamination is at a bearable level of below 10% for MSCW cuts of 7 or below. For high energies, the helium contamination starts to rise to a contamination of around 50%. This steep rise has mainly two reasons: on the one hand, the CR helium spectrum is harder compared to the CR proton spectrum, which leads to a higher helium fraction at higher energies. On the other hand, the used separation technique becomes less effective at high energies. High energetic and nearby showers result in very extensive images in the camera and can also fill it completely. For such large images, a discrimination based on the width of the images is simply not possible anymore since the shower images look more and more the same. This effect is shown in the appendix, Figure A.11, on the left. Further thoughts on the helium contamination can be

found later on in Section 4.2 where a possible extension of the spectrum to higher energies is discussed. A detailed look at the MSCL parameters, which resembles the gamma-likeness of the measured Hillas length, is skipped since it has, compared to the MSCW parameters, basically no discrimination power for the heavy nuclei.

To further reduce the helium contamination, other parameters were also investigated on their separation power. One of the more promising parameters is the height of the shower maximum, usually called Hmax, which is connected to the type of nucleus. Unfortunately, the reconstruction of this parameter fails at high energies and gives deviating values, visible in the appendix, Figure A.11 on the right. There, Hmax becomes very similar between protons and helium for higher energies. Figure A.12 in the appendix shows the expected helium contamination as a function of cuts on the height of the shower maximum. Especially for energies above 100 TeV, no further reduction of the helium contamination was observed by using the reconstructed Hmax parameter.

Taking all these findings into account, the final cuts on the separation parameters are $MSCW \in [0.0 : 6.0]$ and $MSCL \in [-6.0 : 6.0]$. Unfortunately, the helium contamination restricts the high energies to be below 100 TeV even if the energy reconstruction would work up to ~ 500 TeV.

3.3.2 Gamma rays and electrons

Another part of the background are particle showers that are initiated by electromagnetic particles, namely gamma rays and electrons. The background caused by gamma rays can be split again into two types, gamma rays from point sources and diffuse gamma rays. A special region in the sky is the Galactic plane, which contains many densely packed point sources as well as diffuse emissions. The H.E.S.S. Galactic plane survey of very high-energy gamma rays, HGPS (H.E.S.S. Collaboration et al. 2018a), revealed 78 VHE sources and diffuse emission above 1 TeV for galactic latitudes of $|b| < 2^\circ$ (Abramowski et al. 2014). This diffuse gamma-ray emission from the Galactic plane was also observed by the satellite experiment Fermi (Ackermann et al. 2012). Because of the complexity of the Galactic plane region, it is excluded from the analysis of the cosmic ray proton spectrum with a generous cut of $|b| < 7^\circ$. Besides the already excluded sources in the Galactic plane, all known extragalactic sources are excluded as well to avoid contamination by gamma rays. Therefore, all events which come from within 0.4° around a source are not used in the analysis.

Another contributing factor to the background is the extragalactic, isotropic and diffuse emission, which was observed for gamma rays and electrons. Since this emission is isotropic, no background regions can be defined. The isotropic electron spectrum at TeV energies was measured by Fermi (Abdollahi et al. 2017) and H.E.S.S. (Kraus 2018). The isotropic gamma-ray emission was measured up to 100 GeV by EGRET (Strong et al. (2004), not shown in the figure) and Fermi (Abdo et al. 2010) but was later extended up to 820 GeV by Fermi (Ackermann et al. 2015). Since this diffuse emission can not easily be rejected, its expected flux is compared to the expected proton flux. For the proton spectrum, results of various balloon experiments are used (Ahn et al. 2006; Asakimori et al. 1998; Derbina et al. 2005; Green 2016; Yoon et al. 2011). The comparison of the proton spectrum with the diffuse gamma-ray and electron emission is shown in Figure 3.18 on the left. It is already recognizable that the isotropic background emission is magnitudes below the expected proton flux. However, the reconstruction technique eliminates not all particles in the same way. Therefore, the trigger and cut efficiencies are determined and included in the investigations.

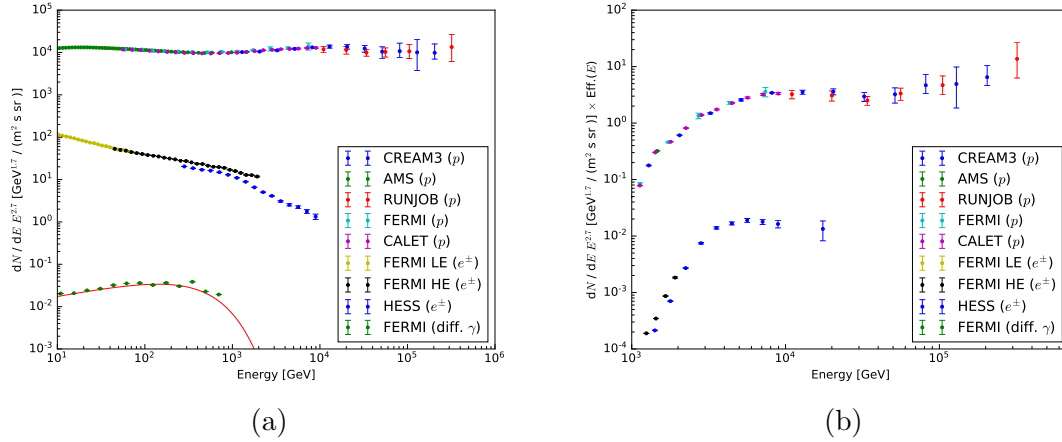


Figure 3.18: Expected diffuse background for the proton spectrum of gamma rays and electrons. Shown are the measured spectra of protons, electrons (+ positrons) and diffuse gamma rays (shown with a fitted broken power law) (a). Since the efficiency of the experiment (trigger and cuts, see Table 3.3) modifies the expected number of particles in the used data set, they are also included (b). The data points of the diffuse gamma rays are below the shown flux range and thus not visible in the plot.

The results are shown in the same figure on the right. After including the efficiencies, the expected contamination of electrons is more than two magnitudes below the expected number of protons at the lowest reconstructable energies and at the main energies even further below. The expected gamma-ray contamination is more than five magnitudes below the expected number of protons. Therefore, diffuse gamma rays and electrons are neglected in the analysis of the proton spectrum.

3.4 Run selection and data set

Different steps are carried out to find a suitable data set for the analysis of the CR proton spectrum. In the H.E.S.S. data quality selection, various parameters to estimate the quality of the observations are used (Hahn et al. 2013). They are continuously monitored, and the quality is estimated for every individual run. The parameters and the used cuts on them are listed in Table 3.5 and can be split into two groups, cuts related to the hardware and cuts related to the atmospheric conditions.

The hardware cuts verify the integrity of the array and the telescopes. The run duration is checked since short run times (< 10 min) usually imply terminations due to technical problems. The other cuts are related to single telescopes. If one telescope fails a criterion, it is excluded but the run can still be used. The participation fraction of the telescopes on the observed events is controlled since too low values hint at hardware problems with this telescope. As was already discussed before, broken pixels can have a significant influence on the reconstructed energy because of the missing photoelectrons. Therefore, the maximum number of broken pixels is restricted. The broken pixels are also split into two types, ones with hardware problems (“hardware flag”) and ones that were switched off (“HV-off flag”).

Criterion	Cut range [units]
Hardware cuts	
Run duration	600:7200 [sec]
Participation fraction	0.4:1.0 [rel. fraction]
Pixels with hardware flag	0:120 [number]
Pixels with HV-off flag	0:50 [number]
RMS of Az dev. distr.	0:10 [arcsec]
RMS of Alt dev. distr.	0:10 [arcsec]
Mean deviation in RA	0:1 [arcmin]
Mean deviation in Dec	0:1 [arcmin]
Atmosphere cuts	
Transparency coefficient	0.8:1.2 [arb. units]
Trigger rate fluctuation	0:10 [% of mean value]
Trigger rate slope	-30:30 [% of mean value]

Table 3.5: Quality selection criteria for H.E.S.S. (Hahn et al. 2013).

The last cut focuses on the tracking of the telescopes. Only telescopes are allowed that point at the nominal position with less than 1 arcmin mean deviation and without spread around this position of more than 10 arcsec.

The other criteria focus on the atmospheric conditions during data taking. Good atmospheric conditions are essential for the energy reconstruction and the determination of an energy spectrum since all simulations for the creation of the lookups are done under the assumption of a clear atmosphere. Adverse atmospheric conditions, caused by clouds, haze or dust, absorb Cherenkov light before it hits the cameras. This leads to an underestimation of the energy and raises the energy threshold. For that reason, runs with bad conditions are excluded from the analysis. To detect short scale changes of atmospheric conditions, the trigger rates of the system are tracked. A decline (“trigger rate slope”) or multiple fluctuations (“Trigger rate fluctuation”) in the trigger rate indicate that clouds or haze are moving through the field of view, which interferes with the transmission of Cherenkov light. Large scale changes on the order of weeks, e.g. caused by agricultural fires, are tracked by the transparency coefficient (Hahn et al. 2014). This coefficient can be calculated by the telescope trigger rates if accounted for other effects that have an impact on the rate (e.g. the optical efficiency or electronic amplifications).

Besides the quality criteria that are commonly used during the analysis of H.E.S.S. data, further cuts are introduced, which meet special requirements of the cosmic ray proton analysis:

- All four telescopes, CT1 to CT4, have to be part of the run,
- the mean zenith angle of a run has to be below 28 degrees since the reconstruction tends to be worse at high zenith angles,
- the pointing of the telescope system needs to have a sufficient distance to the Galactic plane ($|b| > 7^\circ$) to exclude gamma-ray background,
- the runs have to come from the period between 01. January 2005 and 27. April 2010 (optical phases 1b and 1c) since simulations for the reconstruction were only carried out for these times.

If all of these cuts are applied to the H.E.S.S. data, 2456 runs with total livetime of 1039 h are available for the reconstruction of the proton spectrum. For an overview of all runs, the pointing positions of the telescopes on the sky are shown in Figure 3.19. The excluded Galactic plane is also marked.

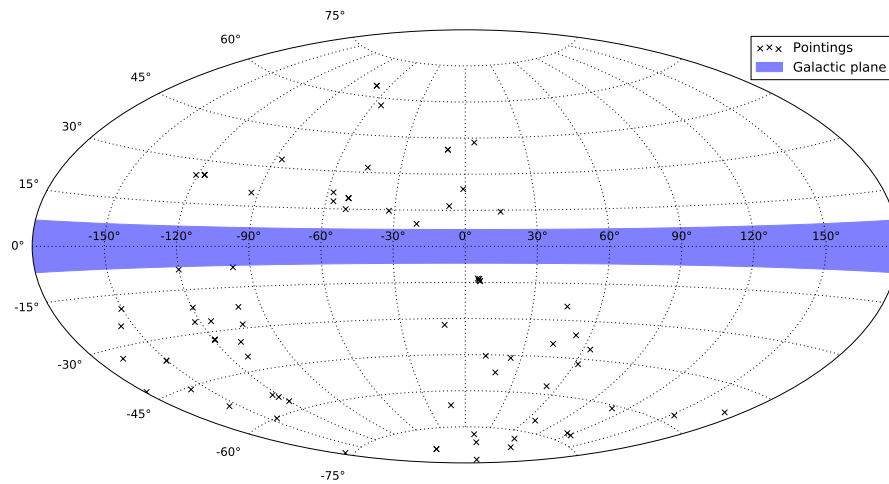


Figure 3.19: Telescope pointings of all runs that are used for the proton spectrum. The blue shaded region is the galactic plane, which is excluded in the analysis.

The reconstruction of the cosmic ray proton spectrum

The last chapter presented in detail how the reconstruction of individual proton events is done, especially compared to the standard reconstruction of gamma rays. Furthermore, the remaining background after the application of different separation cuts was investigated, and the data set of real observations that will be used for the reconstruction of the spectrum was presented. With the help of this analysis, the number of measured particles per energy interval can be determined. Next, the differential spectrum of the CR protons can be calculated.

At first, the general steps towards the spectrum are outlined in detail in Section 4.1, which is closed with tests of the spectrum reconstruction of MC data in Section 4.1.3. Following this, the reconstructed cosmic ray proton spectrum is presented in Section 4.2 and the determination of the systematic uncertainties in Section 4.3. Interpretation, discussion and a short outlook follow afterward in Chapter 5.

4.1 Spectral analysis

The differential spectrum is defined as the number of incident particles $N_p(E)$ per energy interval ΔE , livetime $T(E)$, solid angle Ω and effective detection area A_{eff} :

$$F(E) = \frac{N_p(E)}{\Delta E \cdot T(E) \cdot \Omega \cdot A_{eff}(E)} . \quad (4.1)$$

The differential spectrum is assumed to follow a specific model distribution, which is determined by the physics of particle acceleration and propagation. A simple assumption for a model is a pure power law that only consists of a flux normalization Φ at a specified reference energy E_0 and a spectral index γ . However, it showed that the real proton spectrum is more complex and shows spectral features like changes of the spectral index (see also the introduction to cosmic rays in Chapter 1). The spectrum is given with the true energy of the individual events, a quantity that is not directly accessible with the H.E.S.S. experiment. The quantity which is measured is the number of detected particles as a function of the reconstructed energy $N_p(E_r)$ in the energy interval $\Delta E = E_2 - E_1$. This can be determined from the differential flux from above by folding it with the energy migration matrix $P(E, E_r)$,

which describes the connection between measured and actual energy (see Fig. 4.2):

$$N_p(E_r) = \int_{E_1}^{E_2} \int_0^\infty P(E, E_r, \theta, \phi, \psi) \cdot F(E) \cdot A_{eff}(E, \theta, \phi, \psi) \cdot T(E) \cdot \Omega \, dE dE_r . \quad (4.2)$$

For this formula, further parameters were introduced, the zenith angle θ , the azimuth angle ϕ and the offset angle ψ since the energy migration matrices P as well as the effective areas A_{eff} heavily depend on the observational conditions. The livetime $T(E)$ is the deadtime corrected observation time of all used runs for the analysis. Its energy dependence comes from the runwise determined energy threshold, which will be explained in detail later on. The solid angle Ω is determined by the field of view from which particle showers are accepted. In this analysis, a cut on the offset angle of 1.5° was introduced, which also determines the solid angle.

For the reconstruction of the underlying spectrum $F(E)$, this equation needs to be inverted. Unfortunately, this can not be done analytically, so other approaches are needed to determine the spectrum. One approach is to absorb the energy bias and resolution into the effective collection area by calculating it as a function of the reconstructed energy. With this approach, the spectrum can be calculated directly with Equation 4.1 by changing the effective area to $A_{eff}(E_r)$. The other possibility is the more advanced technique of forward folding, which takes the energy migration into full account. There, the expected energy distribution, calculated from an assumed source spectrum, is compared to the measured energy distribution. By using a fit routine, the normalization Φ and spectral index γ can be determined. This forward folding approach will be explained later on in more detail.

In the following, the different parts of the flux determination will be shown in detail, followed by the fitting of a flux model and final tests on MC data.

Effective collection areas

One important part of the calculation of the spectrum is the effective collection area A_{eff} , which resembles the detection efficiency of the full telescope array. It is determined with the help of MC simulations:

$$A_{eff} = \frac{N_{sel}(E)}{N_{sim}(E)} \times A_{sim} . \quad (4.3)$$

$N_{sim}(E)$ is the number of all simulated events, $N_{sel}(E)$ the remaining number of events after the trigger and selection cuts. The total area for which simulations were carried out is A_{sim} . Usually, the effective area is given as a function of true energy. For the reconstruction of a spectrum, it can also be determined as a function of the reconstructed energy E_r so that energy bias and resolution are included in the effective collection area. When the effective area is determined with the reconstructed energy, it is affected by the spectral index of the simulations. Since the simulations were done with an index of $\gamma = 1.5$ but an index of $\gamma \approx 2.7$ is expected for the CR proton spectrum, the effective area needs to be re-weighted.

Similar to the creation of the energy lookup tables, the determined effective areas are also stored in similar lookup tables and are created for different observational conditions. They are again produced for different zenith angles, azimuth angles, offset angles and optical efficiencies and are interpolated between these available parameter combinations to get the result best matching with the real observational conditions. Since the effective areas are

calculated in bins of energy, they are further processed and smoothed. Therefore, the data points are fitted by high order polynomials to get a smooth transition from energy bin to energy bin. Some example effective areas from the created lookups for different observation conditions are shown in Figure 4.1.

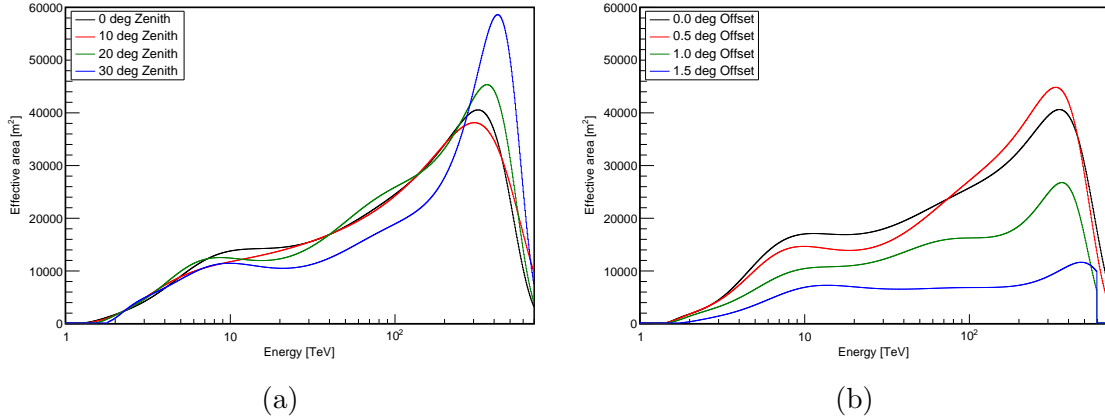


Figure 4.1: Smoothed effective collection areas as a function of the reconstructed energy for different observation positions. Both plots show the effective areas for 180° azimuth and for optical phase 1b while the zenith angle at 0.5° offset (a) or the offset angle at 20° zenith (b) is varied. The offset represents the angular distance between pointing and event direction.

The general shape of the effective areas for the proton analysis can not be directly compared to ones used for gamma-ray analysis since the cuts and the trigger efficiencies are different. The low energy regime is mostly affected by the cut on the image amplitude, which throws away less bright and thus less energetic showers. Therefore, the detection efficiency starts to rise only above 1 TeV, a much higher value than for gamma-ray analyses. Above this threshold, the collection area stays roughly constant up to 100 TeV. Because of the cut on the impact distance, a drop in the effective area for higher energies would be expected since far away showers, which are usually more energetic, are not allowed in the reconstruction. However, an increase in effective area is seen. This is caused by the applied cut on the separation parameters MSCW and MSCL. For very energetic and very bright showers, the whole camera is filled with the shower image so that hadronic and electromagnetic showers look very similar. Therefore, most of the protons are kept in the data sample, and the effective area increases.

In the two plots in Figure 4.1, also some dependencies on the observation conditions are visible. The plot on the left shows the influence of the zenith angle on the effective area. A rise in the energy threshold at low energies for higher zenith angles can be observed. This is caused by the thicker atmosphere at larger zenith angles that leads to more absorbed Cherenkov photons. Thus, low energy showers with a small number of emitted photons are not seen anymore. At large energies, a rise in the effective area is expected since the Cherenkov cone on the ground widens due to projection effects. This is only visible at very high energies since this effect is superimposed by the MSCW cut for the intermediate energies. The plot on the right shows the influence of the offset angle on the effective area. The observed drop in the effective area for larger offset angles ($> 1^\circ$) is expected since it is mainly caused by the cut on the local distance, which rejects exactly such showers.

Probability density functions and the energy migration matrix

The probability density function (PDF) resembles the probability that an event with true energy E is reconstructed with energy E_r . Therefore, the resulting energy migration matrix is directly related to the energy bias and resolution, which were already introduced before in the chapter about the energy reconstruction. The PDF is determined in the same manner as the effective area before. Simulations for various observation conditions are done, and lookup tables are created for each parameter combination. The lookup tables are filled as 2D histograms with the true energy on the abscissa and the corresponding reconstructed energy on the ordinate. Afterward, the PDF is normalized in each column ($E = \text{const.}$) so that

$$\sum_{i=0, E=\text{const.}}^N E_{i,\text{reco}} dE_{i,\text{reco}} = 1 . \quad (4.4)$$

An energy migration matrix for a specific observation condition is shown in Figure 4.2. For the final observation, the PDFs are again interpolated to match the present conditions best. Additionally, the PDF is combined with the corresponding effective area $A_{eff}(E)$ and the livetime $T(E)$.

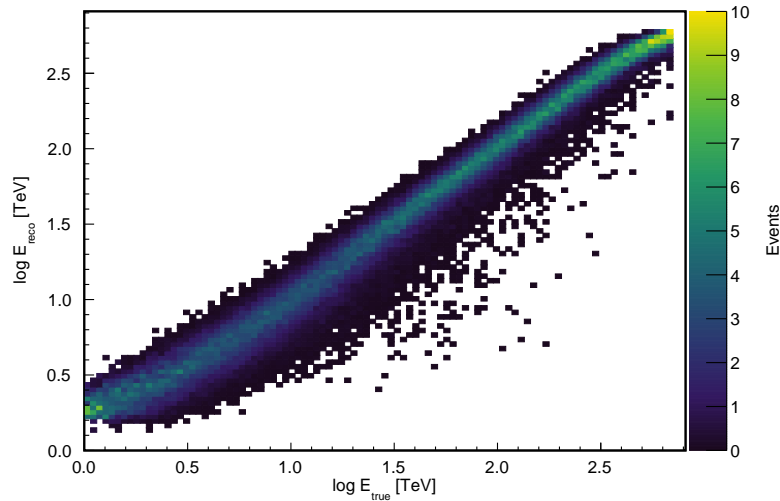


Figure 4.2: Energy migration matrix for 20° zenith, 180° azimuth, 0.5° offset and optical phase 1b.

Energy thresholds

For the reconstruction of the energy spectrum, a safe energy range needs to be determined to ensure that only events with a well reconstructed energy are used. The safe energy range is determined for each run separately since it depends heavily on the observational conditions. One way to determine the spectral range is with the help of the energy bias (see Fig. 3.15). The safe range is then defined as the range where the energy bias is below 10% for low energies as well as for high energies. The second method uses the effective area (see Fig. 4.1). There, the minimum and maximum energies are defined by the points where the effective area drops

below 10% of its maximum value. However, in the analysis of MC protons, it showed that the energy bias is the main factor which determines the safe energy range. For the analysis of gamma-ray data, also the expected maximum gamma-ray rate for an assumed spectrum is used for the low energy threshold. But this method is omitted in the analysis of the proton spectrum.

Additionally, the maximum energy is influenced by the expected helium contamination (see Fig. 3.17). Usually, a contamination of below 10% is assumed to be bearable, but it showed that with the current approach, the contamination rises above 10% for energies above 100 TeV. Therefore, for the analysis of a pure proton spectrum, the upper safe energy threshold needs to be set to this value to exclude a too high helium contamination.

4.1.1 Forward folding

The forward folding approach for the determination of the spectrum is not as simple as the calculation following Equation 4.1. The general idea is to calculate the number of expected events while taking into account the full energy migration matrix and an assumed underlying spectral model. The calculated number of expected counts is then compared with the number of measured events. By varying the spectral model, the most likely spectrum can be determined.

The expected number of events is calculated in a similar manner as was already presented in Equation 4.2, which shows the real observed number of events of the H.E.S.S. experiment. The difference to the formula above comes from the splitting of the observations into runs. For the number of total expected events, the individual results with different observational conditions are summed. A spectral model $F_{fit}(E)$ has to be assumed, which will be used for the fit to the real measurement. The model needs to be chosen so that it matches the real observations best. For the cosmic ray proton spectrum, a simple power law or a broken power law with a change in the spectral index are thought to be most suitable. The final equation then reads as:

$$n_p \Big|_{E_r,i}^{E_r,i+1} = \sum_{\text{Runs}, \theta, \phi, \psi} \int_{E_r,i}^{E_r,i+1} \int_0^{\infty} P(E, E_r, \theta, \phi, \psi) \cdot F_{fit}(E) \cdot A_{eff}(E, \theta, \phi, \psi) \cdot T(E) \cdot \Omega \, dE dE_r . \quad (4.5)$$

The variables and parameters are the same as introduced above. Since no substantial background is expected in the proton analysis and a definition of a background region is not possible, a sole consideration of the proton events and a neglect of all background events is sufficient. By using Poisson statistics and the calculated number of expected events, the probability of measuring N_p events is

$$P(N_p | n_p) = \frac{n_p^{N_p}}{N_p!} \exp(-n_p) . \quad (4.6)$$

To get the most likely underlying spectrum, the parameters of the spectral model $F_{fit}(E)$ are varied so that the following negative log-likelihood function $-\ln L$ is minimized:

$$\begin{aligned} -\ln L &= -\ln P(N_p | n_p) = N_p \ln(n_p) - n_p - \ln(N_p!) \\ &= N_p \ln(n_p) - n_p . \end{aligned} \quad (4.7)$$

The term $-\ln(N_p!)$ can be omitted in the minimization process since it is independent of the assumed spectral model. With a successful minimization, one gets the parameters of the spectral model that describes the most likely spectral shape of the underlying cosmic ray proton spectrum.

4.1.2 Flux calculation and model fitting

Next, the application to data and the calculation of the flux graph along with the fitting of a spectral model needs to be described. As was already mentioned above, the different calculation steps are carried out in bins of the reconstructed energy. Usually, the total energy range is split into fine bins with 24 bins per decade. The number of measured proton events is then filled into these bins while considering the runwise determined energy threshold (Section 4.1). The same is done for the other energy-dependent parameters, the effective area and the livetime. The solid angle does not depend on energy and is constant over the whole energy range. Because of the fine binning, there is the possibility of bins with a very small or vanishing number of events. Therefore, a rebinning procedure is carried out before moving on: starting at the largest energies, where the least events are expected due to the falling power law distribution, every bin with less than five events is grouped with the bin next to it. This ensures that enough events per bin are available for the forthcoming analysis.

The next step is the calculation of the flux of the measured protons to which the source model is fitted. For the determination without using the forward folding method, Equation 4.1 can be used directly. Therefore, the measured binwise proton counts are divided by the bin width ΔE and the flux is calculated with the corresponding total livetime of all runs with applied energy threshold $T(E)$, the solid angle Ω and the average effective area of all used runs as a function of the reconstructed energy, $A_{eff}(E_r)$. The calculation with the forward folding technique uses the fitted spectral model F_{Fit} and determines the flux point as the ratio of measured proton events with the number of expected proton events:

$$F(E) = \frac{N_p}{n_p} \times F_{Fit}(E) . \quad (4.8)$$

The corresponding error on the calculated flux points is the statistical error on the number of measured counts which follows a Poisson distribution:

$$\Delta F(E) = \sqrt{\left(\frac{\partial F(E)}{\partial N_p} \Delta N_p(E)\right)^2} = F(E) \times \frac{\sqrt{N_p(E)}}{N_p(E)} . \quad (4.9)$$

The placement of the flux points along the energy axis is determined by the binning if no rebinning was carried out. Then, the flux points are placed at the bin center on the logarithmic axis. If a rebinning was carried out for bins with insufficient events, the mean energy of the grouped bins is calculated by taking into account the number of expected events due to the fitted spectral model. For the energy, the error bars in the flux graphs resemble the width of the energy bins.

The spectral model, which describes the underlying cosmic ray proton spectrum, is determined by fitting the assumed function to the flux points. For the method without the use of the energy migration matrix, the model is fitted onto the determined flux points by using a minimum χ^2 method. For the forward folding with the use of the energy migration matrix, the fitted spectral model comes directly by the routine itself (see Section 4.1.1).

4.1.3 Reconstruction of a MC proton spectrum

Before moving to the reconstruction of the real CR proton spectrum, the developed approaches are tested on MC data to verify the technique. Therefore, two different MC data sets were simulated and used to test the full analysis chains. For both data sets, the QGS II-04 interaction model was used for the creation of the different lookup tables as well as for the diffuse data for which the spectral shape is reconstructed. For the optical efficiencies, the values of muon phase 1b were chosen. All other important configuration parameters of both data sets are listed in Table 4.1. Livetimes of the simulated observations were not taken into account since these tests focus on the reconstruction of the pure spectral shapes. Data set 1 has a configuration that matches the simulations of the lookup creation so that they can be used directly. Set 2 has a more realistic configuration which does not directly resemble the lookup tables so that the direct observational conditions need to be determined by interpolation.

	Data set 1	Data set 2
Energy range	200 GeV - 1000 TeV	200 GeV - 1000 TeV
Flux at 1 TeV	$5.92 \times 10^{-2} \text{ TeV}^{-1} \text{ cm}^{-2} \text{ sr}^{-1}$	$3.19 \times 10^{-1} \text{ TeV}^{-1} \text{ cm}^{-2} \text{ sr}^{-1}$
Spectral model	power law, $\gamma = 1.5$	power law, $\gamma = 2.7$
Zenith	fixed, 20°	fixed, 23°
Azimuth	fixed, 180°	fixed, 320°
Viewcone	diffuse, 2.2°	diffuse, 2.5°

Table 4.1: Simulation configurations for the diffuse data sets used for the tests of the spectral reconstruction.

On both data sets, the reconstruction techniques explained in Chapter 3 are applied, and both spectral analysis methods explained before are tested. For the safe energy range, the limits are determined as explained in Section 4.1. So, no upper limit at 100 TeV is introduced, which will be necessary for the real data due to the high helium contamination. Since the energy distribution of the simulated events was chosen to follow a power law, also such a simple power law without any breaks was used as the fitted spectral model:

$$F_{fit}(E) = \Phi \times \left(\frac{E}{E_0} \right)^{-\gamma}. \quad (4.10)$$

The flux normalization, as well as the spectral indices, are reconstructed and compared with the simulated spectra. The results of both data sets and reconstruction techniques are shown in Figure 4.3 and Table 4.2 (as well as individually in Appendix A.2). It should be remarked that the simulated flux normalization is not comparable to the expected real CR proton flux.

By comparing the fit results with the input to the simulations, one can see that the forward folding technique with energy migration gives very good results that are in agreement with the injected parameters. Both fit parameters, flux normalization and spectral index, agree with the simulations within one sigma. The results for the χ^2 fitting method are not in such a good agreement with the simulations since the discrepancy is larger than one sigma. Especially the reconstructed spectral index of data set 1 is off significantly, leading to a greater difference in the flux normalization. The results for data set 2 are in better agreement.

For all calculations regarding the real proton spectrum in the upcoming section, only the forward folding method with energy migration is used since there the energy bias and resolution are taken into account, which proved to lead to better results.

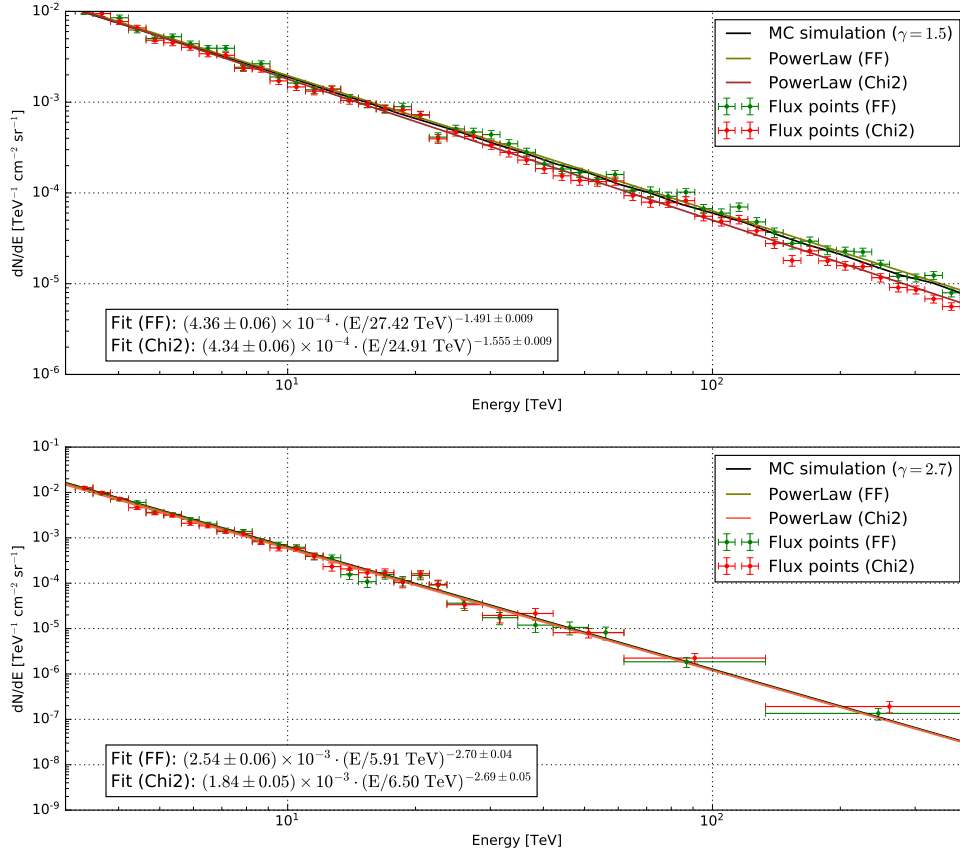


Figure 4.3: Test of the developed routines to determine the proton spectrum on MC data. Two different sets of diffuse proton simulations are tested, one with a spectral index of $\gamma = 1.5$ and pointing corresponding to the available lookup tables (upper panel), and one with a realistic spectral index of $\gamma = 2.7$ and pointing without corresponding lookup tables so that interpolations are needed (lower panel). The solid black line represents the simulated spectrum, the different colors resemble the calculated flux points and the fitted power laws of both methods described before (χ^2 fit without energy migration and forward folded with energy migration). The numbers in the box in the lower left corner are the results of the individual fits.

	Data set 1	Data set 2
Forward folded		
Flux at 1 TeV	$(6.1 \pm 0.3) \times 10^{-2} \text{ TeV}^{-1} \text{ cm}^{-2} \text{ sr}^{-1}$	$(3.1 \pm 0.3) \times 10^{-1} \text{ TeV}^{-1} \text{ cm}^{-2} \text{ sr}^{-1}$
Power law index	-1.491 ± 0.009	-2.70 ± 0.04
χ^2		
Flux at 1 TeV	$(6.4 \pm 0.3) \times 10^{-2} \text{ TeV}^{-1} \text{ cm}^{-2} \text{ sr}^{-1}$	$(2.8 \pm 0.3) \times 10^{-1} \text{ TeV}^{-1} \text{ cm}^{-2} \text{ sr}^{-1}$
Power law index	-1.555 ± 0.009	-2.69 ± 0.05

Table 4.2: Fit results for both data sets and both presented methods, forward folded with energy migration and a χ^2 fit. The errors shown are only statistical errors.

4.2 The proton energy spectrum with real data

Since the analysis chain and the spectral reconstruction proved to work fine, the real cosmic ray proton spectrum can be finally determined. For the used forward folding technique, a flux model needs to be assumed. Before, during the explanation of the method and the tests with MC data, a simple power law was used. In contrast, the real proton spectrum needs a more complex model since other experiments and also the data of the H.E.S.S. experiment saw hints (Atkin et al. 2018; Yoon et al. 2017) or even proof (An et al. 2019) for a spectral break around 10 TeV (see also the discussion of the results in Chapter 5). Therefore, a broken power law as shown in Equation 4.11 is used.

$$F(E) = \begin{cases} \Phi_0 \cdot \left(\frac{E}{E_b}\right)^{-\gamma_1}, & \text{for } E < E_b \\ \Phi_0 \cdot \left(\frac{E}{E_b}\right)^{-\gamma_2}, & \text{for } E \geq E_b \end{cases}, \quad (4.11)$$

with the normalization Φ_0 and the break energy E_b where the transition of the spectral index from γ_1 to γ_2 appears.

For the fit of the broken power law to the determined flux points, the forward folding approach with energy migration is used. The energy range for the determination of the flux points needs to be adjusted in contrast to the reconstruction of the MC data set due to the expected helium contamination. The lower threshold will be determined with the energy bias, and the upper threshold is set to around 100 TeV to minimize the helium contamination. Different sources of systematic errors, e.g. changes in the observational conditions or the analysis pipeline, will be discussed in Section 4.3.1 and 4.3.2, respectively. It was already mentioned in Section 3.1 that an influence of the used interaction models on the reconstruction is expected. Therefore, lookup tables for three different models were created: QGS II-04, Sibyll 2.1 and EPOS LHC. Since it is not clear which interaction model represents the reality best, all three will be used to calculate the proton spectrum. Also, it was discovered that the starting point of the helium contamination depends on the different interaction models. Therefore, the upper energy threshold for the fit of the broken power law is lowered further to 70 TeV to ensure that the helium contamination in the results is as low as possible. The spectral points are kept in the full range up to 100 TeV.

The resulting flux points for the EPOS LHC interaction model are listed in Table A.1 in the appendix, Figure 4.4 shows the fitted broken power law and their residuals. The model EPOS LHC was chosen as the reference spectrum since its flux level lies in the middle of

all three investigated models, as can be seen in Figure 4.5. This influence of the interaction model on the resulted spectrum is further discussed in Section 4.3.3 about the systematic error from the choice of a model.

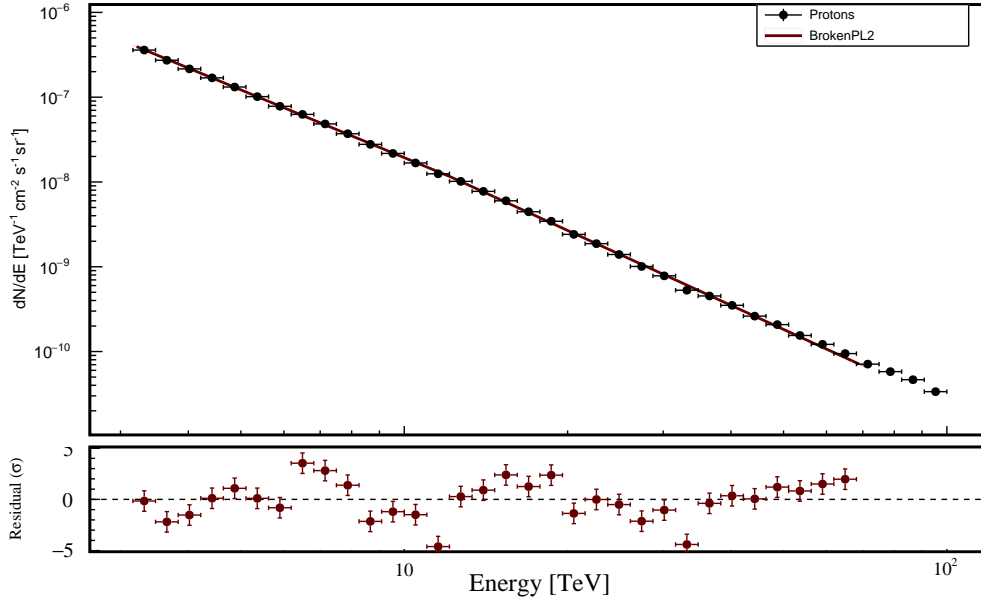


Figure 4.4: Cosmic ray proton spectrum of the real data sample with a fitted broken power law determined with the EPOS LHC interaction model. The lower plot shows the residuals of the flux points from the fit. The shown errors are of statistical origin.

This comparison of the three interaction models with statistical as well as systematic error from observation and analysis is shown in Figure 4.5. The flux was additionally scaled with the factor $E^{2.7}$ to emphasize the spectral break at around 10 TeV. The results of the fit with EPOS LHC, shown with statistical and all systematic errors, are given in Table 4.3. The procedure to determine the errors on the fit results is explained at the end of Section 4.3 that deals with systematic uncertainties. Also visible in the plot with the energy scaled flux is a rise at the high energy end of the energy range, which is likely caused by helium. This is discussed in more detail in the following.

Parameter	Fit result $\pm \sigma_{stat} \pm \sigma_{ana} \pm \sigma_{had}$
Norm	$(1.13 \pm 0.21 \pm 0.06 \pm 0.38) \times 10^{-8} \text{ TeV}^{-1} \text{ cm}^{-2} \text{ sr}^{-1} \text{ s}^{-1}$
γ_1	$2.6563 \pm 0.0009 \pm 0.1173 \pm 0.0976$
γ_2	$2.933 \pm 0.020 \pm 0.072 \pm 0.066$
E_{break}	$(12.3 \pm 0.69 \pm 6.1 \pm 2.8) \text{ TeV}$

Table 4.3: Resulting fit parameters of the broken power law deduced with the EPOS LHC interaction model, shown together with statistical errors σ_{stat} , systematic errors σ_{ana} from observation and analysis and the error from the different interaction models, σ_{had} .

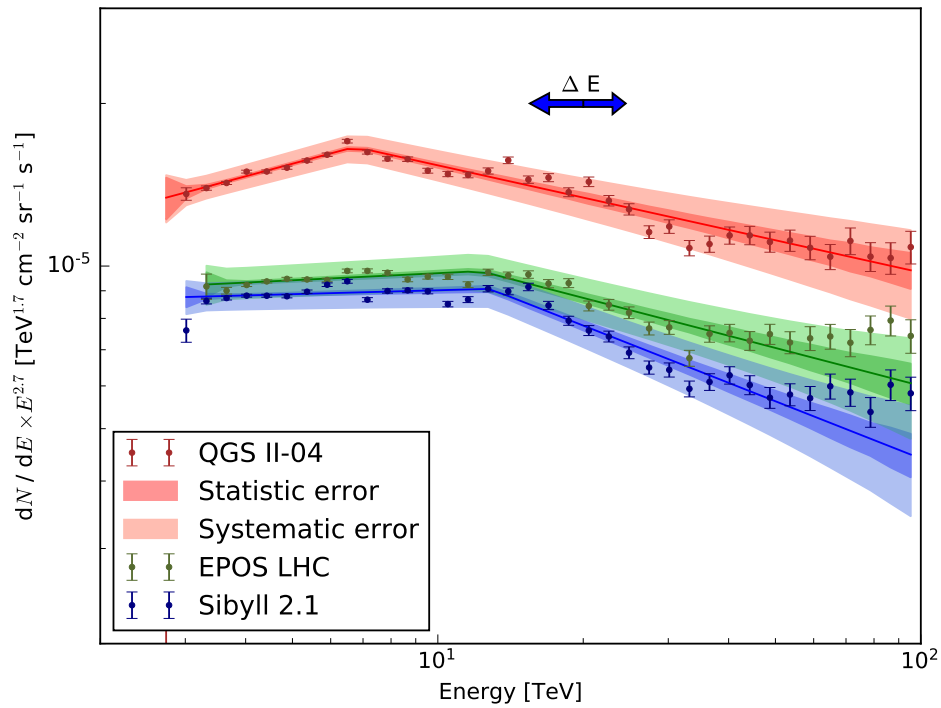


Figure 4.5: Proton spectra with fitted power laws for all three interaction models, QGS II-04, Sibyll 2.1 and EPOS LHC. The flux is scaled with $E^{2.7}$ to emphasize the observed steepening of the spectrum. The error bars on the flux points are only statistical, the different error bands represent the statistical and systematic error. The systematic error contains contributions from changes of the observational and analysis conditions. The blue arrow resembles the error on the energy scale of 15%.

Extension to higher energies

In Section 3.3, the handling of the hadronic background was investigated, which showed an excess of helium events for energies above 100 TeV. But the upper energy threshold determined by the energy bias would lie around 500 TeV, which would allow determining the CR proton spectrum up to these energies. However, the significant helium contamination of about 50% limits the available energy range. Further cuts on various parameters were tested to see if they can be used to reduce the helium contamination. Since no reliable parameter was found (see also Section A.3 in the appendix), no further reduction of the contamination was achievable. To verify the findings from the background studies, a simulated data set containing protons and helium, which follows the particle numbers (flux) and spectral indices of real observational measurements, was created and analyzed. The simulations for the protons were done with a spectral index of $\gamma = 2.7$, for helium with an index of $\gamma = 2.6$ and the flux normalization was chosen to match the results of other experiments (Yoon et al. 2017). The number of observed proton and helium events is shown in Figure 4.6 on the left. It is visible that the number of detected protons and helium nuclei becomes very similar for energies above 100 TeV even with small statistics.

Furthermore, the real data sample was investigated by extending the energy range from 100 TeV to roughly 500 TeV, the threshold which is determined from the energy bias. In this case, the QGS II-04 interaction model had to be used since it is the only one where simulations up to such high energies were processed. In Figure 4.6 on the right, the deduced flux points over the large energy range are shown together with the fit for the small range, also including statistical and systematic errors. For energies above 100 TeV, a steep rise in the flux is observed. No such substantial change in the spectral shape of the proton spectrum was observed with other experiments or is expected due to theoretical calculations. Therefore, it is concluded that this change is connected to the rise of the helium contamination and probably of other heavy nuclei as well. This justifies that the upper energy limit is set below 100 TeV.

Since only single parameters were studied for the particle separation, it can not be excluded that further improvements in the available energy range are possible. A promising tool to improve the separation power is the use of so-called Boosted Decision Trees (BDTs), which combines various parameters into a final decision on the type of the particle. It was already proven with H.E.S.S. data that this technique works to distinguish gamma rays from the hadronic background (Ohm et al. 2009). In newer developments, Convolutional Neural Networks (CNNs) are used for the particle separation, which already showed further improvements when compared to BDTs even if the usage of CNNs within VHE gamma-ray astronomy is very new (Shilon et al. 2019). Also, the first steps into the direction of separating heavy nuclei from each other and to reconstruct properties of these particles with the help of CNNs were undertaken (Hillig 2019). These developments hint at possibilities for further improvements in the reconstruction of the CR proton spectrum but were not investigated in the range of this work.

4.3 Studies of systematic uncertainties

Due to the large available data set and high abundance of protons in the cosmic ray spectrum, only low statistical errors are expected and observed, even after the hard cuts that are used to improve the reconstruction of the protons. The more significant source of errors are

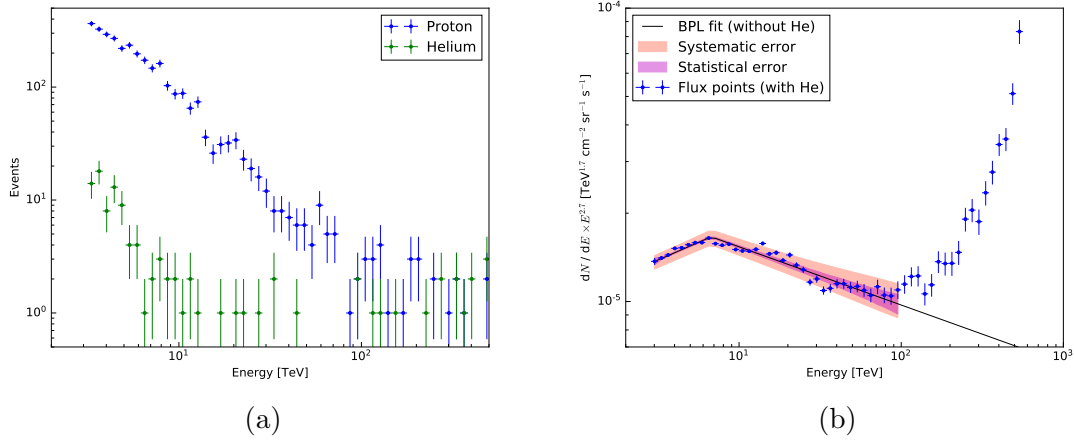


Figure 4.6: Helium contamination as expected from background studies. Simulated proton (with $\gamma = 2.7$) and helium (with $\gamma = 2.6$) samples with expected fluxes are shown in (a) where an equal amount of both nuclei can be seen for energies > 100 TeV. A real measurement of the spectrum with an extension up to ~ 500 TeV is also shown (b). There, the upper energy threshold was determined with the energy bias as it is done for the low energies. The fit of a broken power law was determined for energies below 100 TeV. Clearly, an excess of events can be seen for energies above 100 TeV.

systematic effects caused by changing observation conditions (see Section 4.3.1), the more challenging analysis of protons (see Section 4.3.2) and the underlying interaction models of the hadronic showers in the simulations (see Section 4.3.3, which explains the influence of the interaction models in greater detail since they affect the results most). The systematic error from the observational conditions and the analysis are combined at the end to the systematic error of the analysis, σ_{ana} . The systematic error of the interaction models, σ_{had} , is treated independently.

The general approach which is used for the determination of the systematic error is to vary the conditions of the observation, the analysis or the interaction model and to compare the resulting spectrum with changed conditions to the spectrum created with the full data set, the optimized cuts as specified before and the best matching interaction model.

The error band on the reconstructed flux is calculated by comparing the flux points determined with changed conditions with regard to the reference flux. For every set with changed conditions, the percental deviation is calculated and summed in quadrature to get the total error. Thereby, the direction of the deviations is considered so that the error band becomes asymmetric. The sum of all errors is smoothed by fitting a second-order polynomial to the data points of the deviation.

The error on the fit parameters of the broken power law is calculated in a similar manner: the fitting process is carried out for all data sets with varied conditions, and the fit parameters are determined. The full approach for the fit parameter error is explained at the end of this section.

By adding all the errors in quadrature, one assumes that all errors which are determined by changing observation and analysis conditions are independent. However, this is not the case since they will likely depend on each other. Additionally, the changing event numbers

per data set, influenced by the changing conditions, also cause the statistical error to vary so that statistical changes are also included to some extent in the systematic error. This effect is neglected since the systematic effects clearly dominate the statistical effects. Therefore, the shown errors are presumably an overestimation compared to the actual systematic one. Since it is not clear if all systematic errors are taken into account, the overestimated error is kept nevertheless.

A last source of errors is the absolute scale of the energy, which is assumed to be 15% and shown as a blue arrow in some of the plots. This value was adapted from the analysis of the electron spectrum, which is comparable to the proton analysis (see e.g. Aharonian et al. (2008)). This effect should also be kept in mind for the flux of the energy scaled plots since it would further affect it besides the already shown statistical and systematic errors.

The results and implications of the different sources of systematic errors are explained in the following sections.

4.3.1 Observational conditions

It was already mentioned several times throughout this thesis that the observational conditions influence the shower development and its imaging. To consider such variations, which certainly happened in the large, used data set, the full set is split into different ones with different observational conditions. The parameters used are

- the zenith angle, where the data set is split into runs with a mean zenith angle $< 16.5^\circ$ and $\geq 16.5^\circ$,
- the azimuth angle, where the data set is split into runs which are facing south (angles $> 125^\circ$ and $< 235^\circ$) and facing north (angles $< 125^\circ$ and $> 235^\circ$),
- and the optical phase, 1b and 1c, resembling the changing optical efficiency of the telescope system.

The zenith angle is changed since it has a direct influence on the shower development and the energy threshold. A larger zenith angle leads to a thicker atmosphere the particles and the Cherenkov light need to travel through. The azimuth angle is changed because it influences the magnetic field the charged particles of the showers experience. However, only a small impact is expected from this. The two optical phases are used since the optical efficiency changed by a larger factor between them due to aging effects. By considering both phases independently for the systematic error, the applied efficiency correction by using dedicated lookups and muon events is tested and included in the error. Short time scale changes, as caused by clouds or haze, are not taken into account since not enough data would be available. But by using only runs with good atmospheric conditions, no significant impact is expected.

The error is then calculated as described above. The deviations from the reference model, as well as the total error, are shown in Figure 4.7 on the left. The individual flux points of the changed data sets in the same figure on the right, in combination with the reference flux points and the fitted broken power law. The resulting error band due to systematics from the observational conditions is already included. The errors from the observational conditions are found to be symmetric since both, positive and negative deviations, show a similar behavior. The error is the lowest at small energies, starting at roughly 3%, and tends to be larger at the highest energies, up to 8% at 100 TeV.

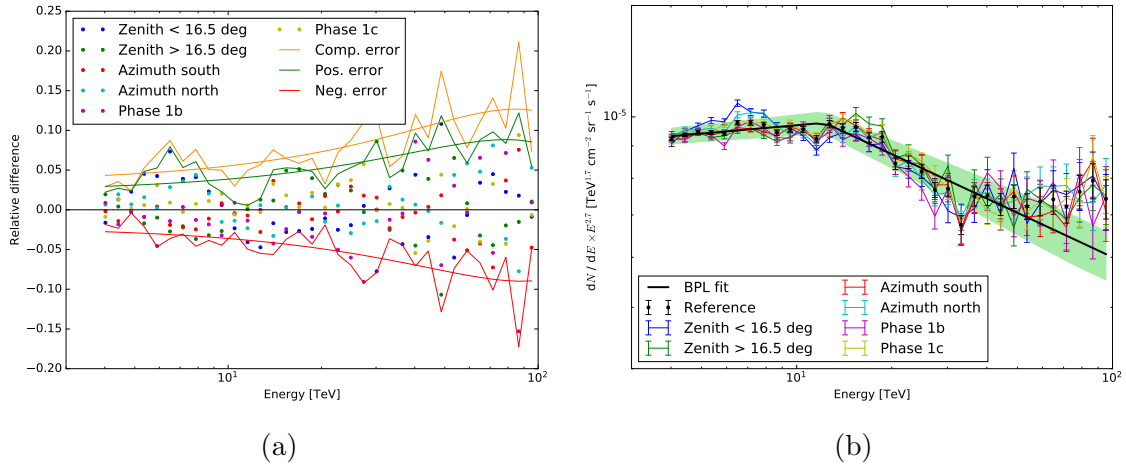


Figure 4.7: Deviations from the full data sample after changing observational conditions (zenith angle, azimuth angle and optical phase) (a). The errors were summed quadratically to get the total error as well as positive and negative errors. To smooth the behavior of the error, second-order polynomials were fitted. The resulting, asymmetric error band, as well as the individual flux points together with the reference of the full data set, are also shown (b).

4.3.2 Analysis conditions

In addition, systematic errors arising from the analysis are expected. To take them into account, certain applied cuts are varied that are thought to have a larger impact on the results. They are

- the mean scaled width (MSCW) which is changed to [0.0:5.0] and [0.0:7.0] (compared to the standard cut [0.0:6.0]),
- the core impact distance to the array center which is changed to < 150 m and < 250 m (compared to < 200 m),
- and the offset angle, which is changed to < 1.25° and < 1.75° (compared to < 1.5°).

The cut on the MSCW has a large influence on the expected background level of heavy nuclei and also on the goodness of the core (and thus the energy) reconstruction. By varying this cut, uncertainties regarding these two crucial points are considered. The cuts on the impact distance and the offset angle were introduced to improve the energy resolution since the reconstruction of the impact points becomes worse for remote or off-axis showers. So, these cut variations take into account problems in the reconstructed energy. Variations of other cuts were neglected since they showed only smaller influences on the results.

The final error from the analysis cuts is shown in Figure 4.8. The deviations from the reference model on the left, the individual flux points of the different data sets on the right. The resulting error from the changing analysis conditions is larger compared to the error from the observational conditions. The error trend starts again symmetrical at roughly 5% at a few TeV but tends to a larger positive error at the highest energies, around 17%, while the negative error stays more or less equal at 5% like in the beginning. This change to larger

fluxes at the highest energies is likely connected to the rising helium contamination due to the loosened MSCW cut (see green data points in the left plot of Figure 4.8).

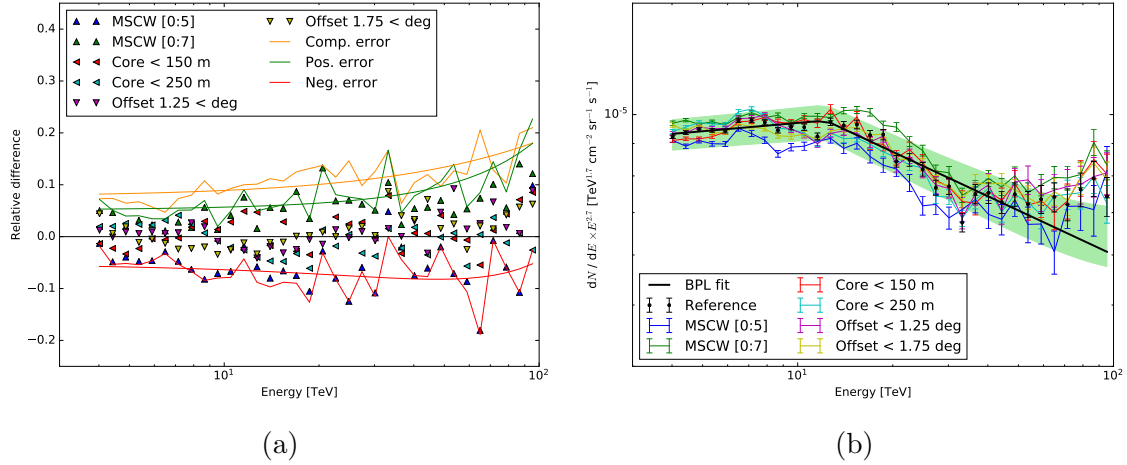


Figure 4.8: Deviations from the full data sample after changing the used set of cuts (MSCW, core and offset) (a). The errors were summed quadratically to get the total error as well as positive and negative errors. To smooth the behavior of the error, second-order polynomials were fitted. The resulting, asymmetric error band as well as the individual flux points together with the reference of the full data set are also shown (b).

4.3.3 Interaction models

During the investigation and verification of the MC simulations, it was already discovered that the used interaction model has a noteworthy influence on the shower development and the imaging. Even if the observed differences from interaction model to interaction model were too small to explain the detected discrepancies in the shapes of the imaged showers between real data and simulations before (see Section 3.1), it became clear later on that the impact on the final reconstructed proton spectrum is significant. Therefore, three different interaction models were used to calculate the spectrum: QGS II-04 (Ostapchenko 2011), Sibyll 2.1 (Engel 1999) and EPOS LHC (Pierog & Werner 2009; Werner et al. 2006). First, similar investigations as in Section 3.1.2 are repeated to find the interaction model that agrees most with real data. This time, all cuts which are used for the spectrum determination are included. Then, following different parameters, which depend mostly on the chosen interaction model, are investigated:

- MSCW and MSCL; they were chosen since they are strongly influenced by the interaction model and have a large impact on the cut efficiency (especially MSCW) and are therefore dominating the shape of the effective area.
- Hillas width and length; they are also influenced by the interaction model and are used to calculate the scaled parameters from the first point.
- Hmax, the height of the shower maximum, determined by the interaction probability of the incident particles. This parameter is calculated geometrically and might suffer larger errors for high energetic events where the reconstruction becomes more difficult.

The relative deviation of the chosen parameters from the real data set, $(p_{MC} - p_{real})/p_{real}$, is shown in Figure 4.9 for low and high (reconstructed) energies, and the error bars are calculated from the error of the mean value. For this figure, also Sibyll 2.3c (Ahn et al. 2009; Riehn & et al. 2017) was included to check for differences from the older version Sibyll 2.1. However, no lookups were created for this model out of time constraints.

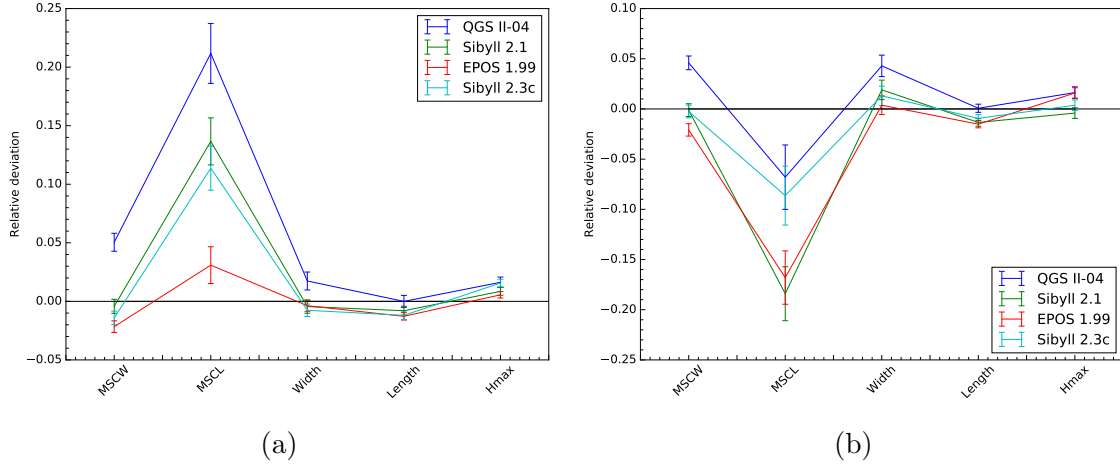


Figure 4.9: Comparison of various parameters between different interaction models and real data for low energies, $E_{reco} < 10$ TeV (a), and high energies, $E_{reco} > 10$ TeV (b). The parameters were chosen since they are strongly influenced by the choice of the interaction model. The shown error bars are calculated from the error on the mean of the different parameter distributions.

For low energies, the comparison suggests that EPOS LHC is the model which agrees best with real data while QGS II-04, the one which was mainly used so far, agrees worst. The Sibyll models are in the middle and both seem very similar, meaning that the changes from the old to the new version do not have a large impact on the reconstruction at low energies. The most considerable differences are found for the scaled parameters MSCW and MSCL, which also explains the significant differences for the different spectra since they strongly influence the effective areas. The Hillas width and length are in better agreement because they were already used before for the comparison between simulations and real data. For the shower height, all models are a bit too large compared to the real data. For high energies, the behavior changes a bit. The best agreeing model is now QGS II-04 (if one leaves out Sibyll 2.3c for which no lookups are available), while Sibyll 2.1 and EPOS LHC show worse agreements. This hints at different properties at different energies between the tested interaction models, and especially the newer Sibyll version seems to have improved for the high energies. These observations also suggest that one model might fit the real proton spectrum (as measured by other, dedicated experiments) better at low energies while another one does at high energies. This is indeed observed when the H.E.S.S. results are compared to other experiments in the next chapter. But for now, the EPOS LHC model will be chosen as a reference spectrum, and the other models will be used to estimate the systematic error which is introduced by the hadronic simulations.

In Figure 4.5, the resulting spectrum with all three interaction models was shown as it is not entirely clear which one resembles the reality. But since it was found that the EPOS LHC model seems to fit the reality best, the other two used models, QGS II-04 and Sibyll

2.1, are used to calculate the systematic error from hadronic interactions. Therefore, the same approach is used as before, the deviations to the reference model (EPOS LHC) are calculated and asymmetrically taken into account. The resulting error from this is presented in Figure 4.10. When compared to the two other investigated error sources, observation and analysis, it becomes clear that the largest source of error are the hadronic interaction models since the error can be as large as 60% (deviation of the QGS II-04 model at the lowest energies). As was already discussed before, the deviation from the interaction model is also energy-dependent: at lower energies, the results of Sibyll 2.1 are very similar to the results of EPOS LHC while QGS II-04 shows the largest deviation. For higher energies, the observed trend is turning since the error from QGS II-04 starts to approach the EPOS LHC results while Sibyll 2.1 begins to deviate. This means that the implemented interactions work differently at different energies, which is also expected; one interaction model might be closer to the real interaction at a given energy and another model at another energy.

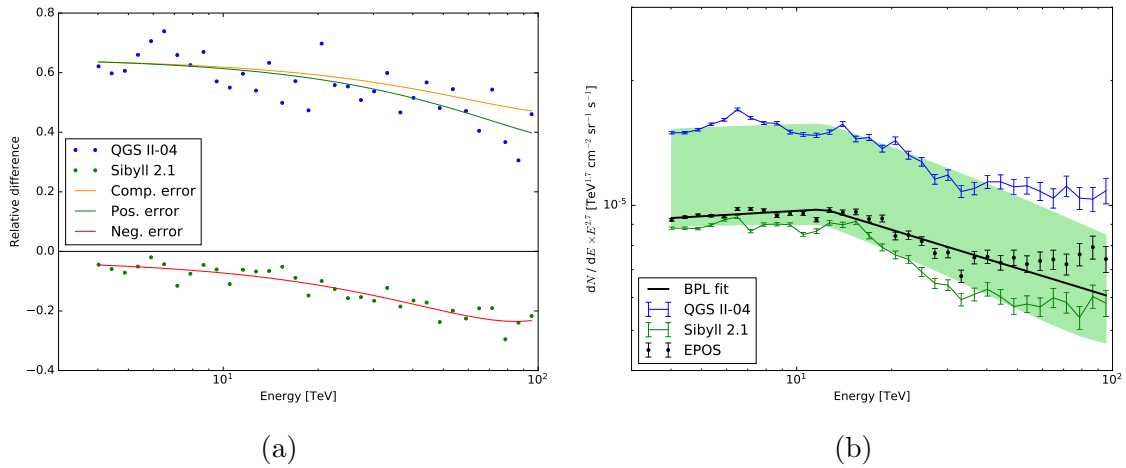


Figure 4.10: Deviations from the reference spectrum with the EPOS LHC interaction model after using other interaction models (QGSJet II-04 and Sibyll 2.1) (a). The direction of the error is taken into account, and an asymmetric error band is deduced, meaning that both other models determine the error band. The resulting error band, as well as the individual flux points together with the reference spectrum, is also shown (b).

Error on the fit parameters

As the last point, the error on the resulting fit parameters of the broken power law function is calculated. Therefore, the broken power law is fitted to the same changed data sets as used before and the resulting fit parameters, the norm Φ_0 , the indices γ_1 and γ_2 and the energy of the spectral break E_{break} , are compared to the results of the reference spectrum, in the current case the one with EPOS LHC and the full data set. To get the systematic error, the standard deviation of the reference value and the results from the changed data sets are calculated. This is done for every changed condition individually. Afterward, the different contributions are again summed in quadrature but this time symmetrically. The influence of the observational conditions and the analysis cuts are combined as σ_{ana} , the error from the interaction models separately as σ_{had} . For the calculation of the error of the normalization

Φ_0 , the break energy E_{break} is fixed at the determined break energy of the reference spectrum since the normalization is given at this point. A visualization of the different fit results can be found in Figure 4.11, the final error on the fit parameters was already shown before in Table 4.3.

The figures below confirm the findings from the error discussions before. The largest deviations are again caused by the chosen interaction models. Especially, the error on the normalization due to observational and analysis conditions is almost negligible if compared to the hadronic interaction models; the large deviation to a higher flux is caused by the QGS II-04 model while Sibyll 2.1 only shows a slightly lower flux, compared to the reference model EPOS LHC. The influence on both indices and the break energy is not fully dominated by the interaction models since other error sources show similar levels of systematic error. Here, the systematic error on both indices is smaller, deviations $< 10\%$, than the error on the break energy, deviations $< 50\%$. The influence of the observational conditions is mainly dominated by the zenith angle while the influence of the azimuth angle is lower and the deviations of the optical phase even agree with the reference spectrum within statistical errors. This shows again that the correction of the optical efficiency with muon events works quite well while the consideration of changing zenith and azimuth angles within the simulations still could be improved (e.g. with runwise simulations as mentioned in Section 3.1). The analysis cuts show slightly less deviations when compared to the reference spectrum, the lowest influence on the fit parameters seems to come from the MSCW cut while the influence from the shower core distance and the offset cut is larger.

It can be concluded that the systematic errors clearly dominate over the statistical ones, which are low because of the large used data set. The large systematic errors are caused by the challenging analysis of protons with an IACT that is primarily built for the analysis of gamma rays and the rejection of protons. However, the largest impact on the spectral results comes from the used hadronic interaction models within the simulations since no direct experimental data at these high energies in forward direction is available to feed the simulations. Therefore, the proton analysis could be further improved by more detailed studies regarding the error sources or the simulation of hadronic interactions. However, such comprehensive studies were not possible within this work due to time constraints.

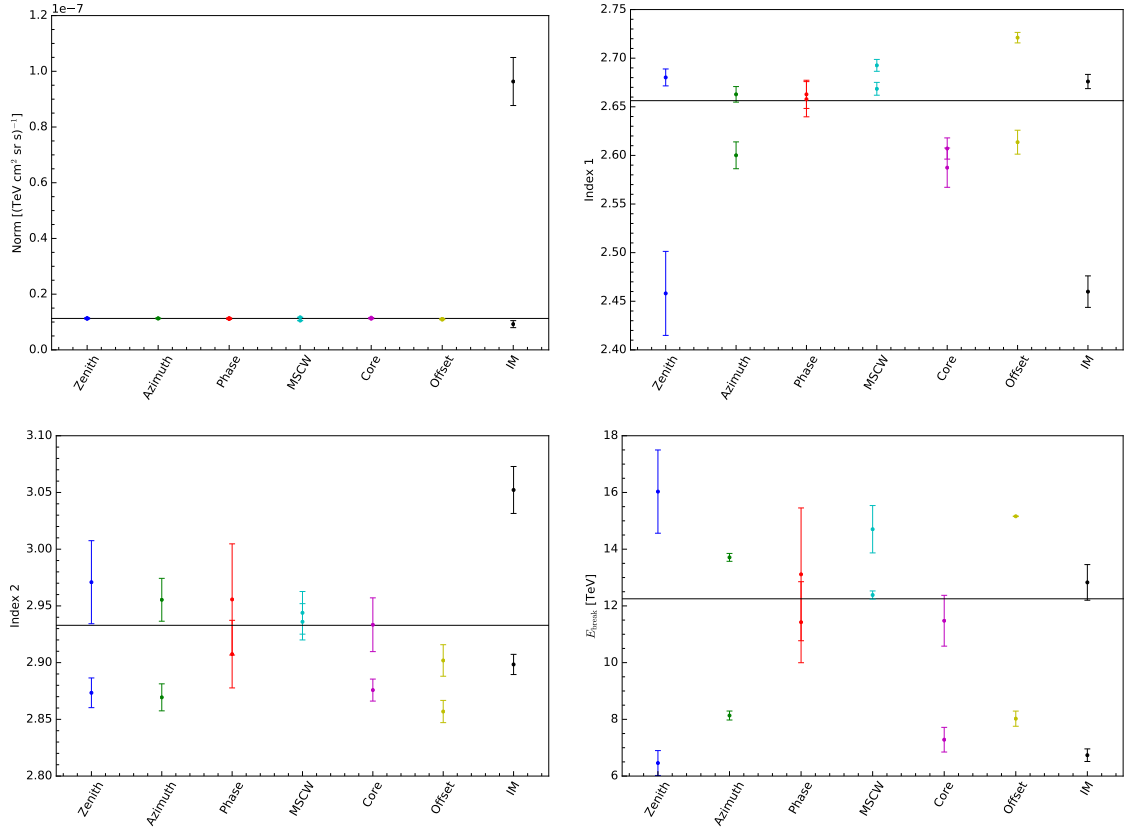


Figure 4.11: Determination of the systematic errors on the fit parameters of the broken power law (normalization Φ_0 , index γ_1 , break energy E_{break} and index γ_2 , in clockwise ordering). The black line represents the results of the reference model (calculated with EPOS LHC, the full data set and the optimized cuts), and the data points are the fit results of the altered data sets with respect to the parameters shown on the abscissa. The error bars are the statistical errors determined through the fitting process.

Discussion, interpretation and outlook

The last chapter gave the results on the CR proton spectrum determined with the IACT H.E.S.S. and presented the different sources of errors, statistics and systematics from the analysis and the used interaction models. This chapter will now compare the results with other experiments that measured the proton as well as the all particle spectrum, put the findings into the context of established and new theoretical work and give a short outlook on possible improvements of the proton spectrum with H.E.S.S. along with future scientific missions.

Discussion and a comparison with other experiments

The most exciting result of the spectral reconstruction is the change in the spectral index from $\gamma_1 = 2.66$ to $\gamma_2 = 2.93$ ($\Delta\gamma \approx 0.27$) at an energy of 12.3 TeV which is not expected in theoretical work. If all errors, statistic and systematic, of both spectral indices are taken into account, the change $\Delta\gamma$ is still larger than the error, making it very unlikely that the spectral break is caused artificially by statistical fluctuations or systematic effects. Also, a likelihood-ratio hypothesis test was carried out with a power law as the null hypothesis and the broken power law as the alternative hypothesis. This test also gave the result that the broken power law describes the measurements significantly better. But only statistical errors were included in this test, which made the resulting significance very likely to be overestimated. Therefore, the exact number is not given here. This already hints at the general problems of the proton spectrum with reconstructed H.E.S.S. that were also discussed in the last chapter: the large amount of available data gives very small statistical errors, but since the telescope system was not specifically built to measure particle showers from protons, one has to deal with significant systematic effects.

In the energy range, which is analyzable by H.E.S.S., from roughly 5 TeV to 100 TeV, several other experiments measured the cosmic ray proton spectrum. Depending on the type of experiment, the sources of their errors are different, but usually, they have to deal with worse statistics while having smaller systematic problems compared to the IACT analysis. The results of H.E.S.S. and various other experiments are shown in Figure 5.1, which shows the proton spectrum over a broad energy range along with the all particle CR spectrum, and in Figure 5.2, which shows the proton spectrum restricted to the available H.E.S.S. energy range.

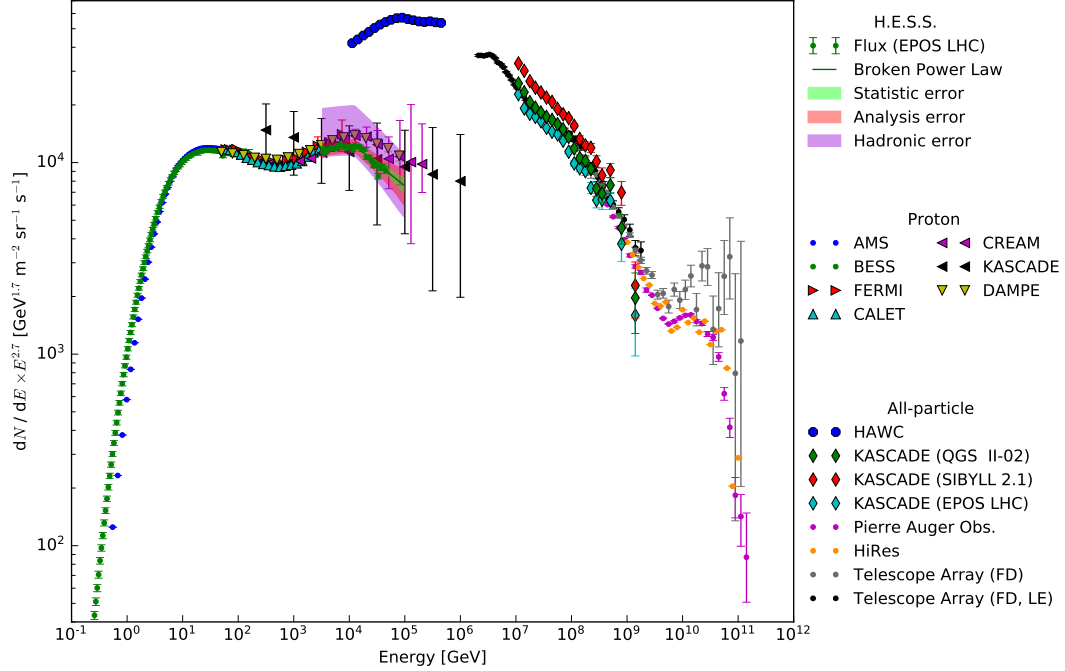


Figure 5.1: The final results of the cosmic ray proton spectrum deduced with data from H.E.S.S., shown as the green flux points with statistical error bars. Also included are the fitted broken power law (dark green) and the different error bands of a statistic (green), analysis (observation conditions and analysis cuts, red) and hadronic (purple) origin. The results on the proton spectrum of other experiments are also shown to compare them with the results of this work. Included are AMS (Aguilar et al. 2015), BESS (Abe et al. 2016), Fermi (Green 2016), CALET (Adriani et al. 2019), CREAM (Yoon et al. 2017), KASCADE (Antoni et al. 2004) and DAMPE (An et al. 2019). To put the proton spectrum into context with the all particle spectrum, further experiments are included: HAWC (Alfaro et al. 2017), KASCADE with three different hadronic interaction models (Apel et al. 2012, 2014), Pierre Auger Observatory (Collaboration et al. 2018), HiRes (Hanlon 2008) and Telescope Array (Abbasi et al. 2016, 2018). The shown errorbars of the other experiments are only of statistical origin except for the proton results of KASCADE, where only the full systematic error was available.

First, one can compare the proton spectrum measured with H.E.S.S. and other experiments with the all particle spectrum. Since the general shape of the CR spectrum at the highest energies was already explained in detail in the introduction, Section 1, it will not be fully repeated here. One finding of the all particle spectrum is that the knee is located at around 10^{15} eV, the lower end of the Telescope Array data (Abbasi et al. 2018), at energies way larger than the observed proton break. This observation suggests that the observed spectral break of the protons is not yet connected to the knee of the all particle spectrum since theoretical models would then result in a knee at lower energies than observed (Guo & Yuan 2018). Furthermore, there are all particle results, determined with different interaction models, of KASCADE available ((Apel et al. 2012, 2014): the green, red and cyan diamonds in Fig. 5.1) which show comparable differences as the different results of the IACT analysis with three interaction models. This also confirms the large influence of the used interaction model on the spectral result, which was also discovered in the H.E.S.S. analysis. But most interesting for the proton spectrum are probably the results of HAWC for the all particle spectrum (Alfaro et al. 2017) since the energy range overlaps with H.E.S.S. and other experiments. The HAWC measurement shows a spectral break at 45.7 TeV where the power law index changes from $\gamma_1 = 2.49$ to $\gamma_2 = 2.71$. Even if the break in the all particle spectrum appears at slightly higher energies than observed in the proton spectrum by DAMPE (An et al. 2019), CREAM III (Yoon et al. 2017) or H.E.S.S., they are very likely connected since protons are the most abundant particles in the full cosmic ray spectrum.

Next, the cosmic ray proton spectrum itself should be investigated in more detail. At the low energy end of the spectrum, at a few GeV, AMS (Aguilar et al. 2015) and BESS (Abe et al. 2016) show a rapid drop in the observed proton flux. As was already discussed in the introduction to this work, the cause of this drop is widely known and created by the solar wind and magnetic fields in the solar system, which interfere with the CR particle propagation. At higher energies, established theories (see also the introduction, Section 1) predict a pure power law spectrum without further features. However, two further features appeared in the spectrum by several experiments: a hardening at GeV energies followed by a softening at TeV energies. The first change in the spectral shape is already more established since it was observed by several experiments, while the second change was only observed very recently and is not seen by all experiments which have access to this energy range.

The first break was, among others, observed by AMS (Aguilar et al. 2015), but their measurement suffered from low statistics at the break energy. Better measurements of the break are available from Fermi (Green 2016), CALET (Adriani et al. 2019) or DAMPE (An et al. 2019). They give a break energy at around 480 TeV and a change of the spectral index from roughly $\gamma_0 = 2.8$ to $\gamma_1 = 2.6$ ($\Delta\gamma = 0.2$). This feature is not detectable by the H.E.S.S. proton analysis since its energy is too low, however, the second spectral break was observed. A more detailed view of the second spectral break measured with H.E.S.S. and other experiments is shown in Figure 5.2.

As was already stated before and can be seen in this figure, other experiments were also able to see a softening in the spectral shape at TeV energies. Very recently, DAMPE (An et al. 2019) published their results on both spectral features but before, there were already hints of this spectral break observed by CREAM (Yoon et al. 2017) or NUCLEON (Atkin et al. 2018). However, some experiments did not observe such features, like KASCADE (Antoni et al. 2004), which suffered large systematic uncertainties, or ARGO-YBJ (Bartoli et al. 2015), which measured the proton plus helium spectrum and observed a flat spectrum. The results of the shown experiments are also listed in Table 5.1 for a better comparability.

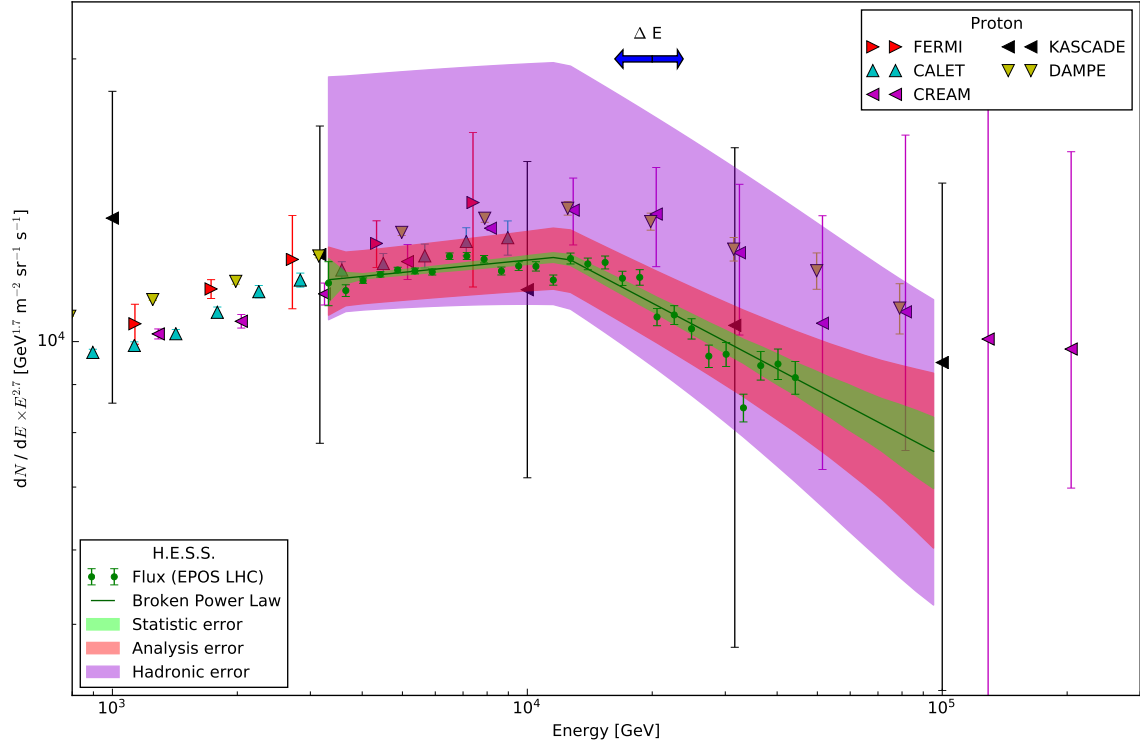


Figure 5.2: The final results of the cosmic ray proton spectrum deduced with data from H.E.S.S. but restricted to the energy range that is also available to this IACT. The H.E.S.S. flux points are shown with statistical error (green) together with the fitted broken power law (dark green) and the different error bands from statistical (green), analysis (observation conditions and analysis cuts, red) and hadronic (purple) origin. The blue arrow resembles the energy scale uncertainty of the H.E.S.S. experiment. Further experiments that measured the proton flux are included: Fermi (Green 2016), CALET (Adriani et al. 2019), CREAM (Yoon et al. 2017), KASCADE (Antoni et al. 2004) and DAMPE (An et al. 2019). The shown errorbars of the other experiments are only of statistical origin except KASCADE, where only the full systematic error was available.

The deduced flux normalization of the H.E.S.S. experiment with the EPOS LHC model lies a bit lower than DAMPE or CREAM. At the low energy regime below the spectral break, H.E.S.S. agrees more with the other experiments, while the difference becomes larger above the break. This effect might be caused by the used interaction model since Figure 4.9 from the last chapter suggested that EPOS LHC matches better with real data at lower energies than at high energies. Following this argument, the low energy results of EPOS LHC should be closer to the real CR proton spectrum than the high energies. Furthermore, this figure showed that QGS II-04 has the best agreement with real parameters at high energies. This is also observed in the measurement of the proton spectrum since this interaction model had a better agreement with the other experiments at high energies than at low energies.

	H.E.S.S.	DAMPE	CALET	Fermi	CREAM	KASCADE
Index γ_1	2.65 ± 0.16	2.60	2.57	2.60	2.61	2.78
Index γ_2	2.93 ± 0.10	2.85	-	-	2.61	2.78
E_{break} [TeV]	12 ± 7	13.6	-	-	-	-

Table 5.1: Parameter of fitted (broken) power laws of several experiments. Besides the H.E.S.S. results also DAMPE (An et al. 2019) observed the break. CALET (Adriani et al. 2019) and Fermi (Green 2016) did not measure up to these energies but can contribute γ_1 . CREAM (Yoon et al. 2017) saw hints of a break but fitted a normal power law and KASCADE (Antoni et al. 2004) was not able to see a break because of large uncertainties, so both experiments contribute one index over the full energy range. Errors are only shown for the H.E.S.S. experiment, as a combination of statistical and systematic errors, since not all experiments listed both errors, which makes them not directly comparable.

The spectral indices, γ_1 and γ_2 , and the break energy, E_{break} , of H.E.S.S. can only be compared with DAMPE since it is currently the only experiment that published results of this spectral change. If one takes into account the errors from H.E.S.S., statistical and systematic errors, the results of both agree with each other. The results of CALET and Fermi for γ_1 are also comparable with the H.E.S.S. results within the calculated errors. The results of CREAM and KASCADE can not directly be compared to the results of this work since they are calculated for the whole energy range covering both sides of the spectral break. But nevertheless, they are located at similar values, CREAM closer to the spectral shape below the break while KASCADE recovered an average value of both indices, below and above the spectral break.

As conclusion, one can say that the reconstruction of the CR proton spectrum with H.E.S.S. suffers significant systematic uncertainties caused by the analysis itself and the used interaction models but was nevertheless able to reconstruct the spectral break which was also seen by other experiments. The deduced parameters of a fitted broken power law are within the calculated errors and thus comparable with other measurements. These results support the statement that the CR proton spectrum does not follow a pure power law spectrum but has a rather complex shape with distinct features.

Interpretation of the results

The results of recent measurements of the cosmic ray proton spectrum are in tension with the established astrophysical theories, which were shortly outlined in the introduction. Following these theories, one would expect a single index power law without any spectral features and an index of roughly $\gamma \approx 2.0 + 0.5$, generated by first-order Fermi acceleration and diffusive propagation. But both features were not observed; there were multiple breaks in the spectrum detected, and the index tends to be larger than the one expected by theories. These results are similar to the detected spectral features of the highest energetic CRs, like the knees or the ankle. There, already different theories, like presented in the introduction, are established that are able to model the features. For the behavior of the proton spectrum, similar or even completely different theories exist that might explain the observed features. A short overview of the different existing ideas will be given in the following with the corresponding references to further literature.

One point where the theories can be changed and extended lies in the acceleration mechanisms of the particles itself. If further features are added to the established diffusive shock acceleration models, the resulting observed proton spectrum is changing. Non-linear effects, like magnetic field amplification by the accelerated particles or the acceleration by reverse shocks, can be included in the models. In the work of Ptuskin et al. (2010, 2013), such modifications were included in their calculations together with the different existing types of supernovae, called type I and II, which consist of further sub-types. Their results are shown in Figure 5.3 on the left, together with measurements of various experiments. It can be seen that the modified theory already results in some spectral features like the ones which were observed by the experiments. Especially the spectral change at GeV energies is quite prominent but also the softening at TeV energies is visible. Unfortunately, no good resolved data was available at these energies at the time of the publication. The work of Caprioli (2012) also includes different phases in the development of SNRs, where especially the ejecta-dominated phase and the adiabatic phase (called Sedov–Taylor phase) play an important role and cause differences in the resulting spectra. The time evolution affects the spectral index and the maximum achievable energy: old supernovae show a softer spectrum and a lower, maximum energy. Another effect that might occur is the re-acceleration of cosmic rays while they are traveling through the Galaxy (Thoudam & Hörandel 2013, 2014). During the propagation, they might encounter the shock fronts of other SNRs where they get additional momentum. It is generally thought that it is more likely that they are affected by older SNR since they are already more expanded and span a larger volume. As already stated, the created spectra of old SNRs are softer, meaning that the particles show a steeper spectrum after their re-acceleration. If such effects are included, the re-accelerated particles dominate at low energies creating a softer spectrum, and the particles which were accelerated by strong shocks dominate at high energies, which creates a harder spectrum. The results of this theory are shown in Figure 5.3 on the right where the spectral break at GeV energies is modeled very well.

Another possible origin of the observed spectral features lies in the propagation of the particles after they were accelerated. One propagation effect which influences the spectral shape of the particles is the self-generation of magnetic turbulences of the particles while they are traveling through the interstellar medium (Aloisio et al. 2015; Blasi et al. 2012). The diffusion through these self-generated turbulences dominates at lower energies, below a few 100 GeV, where it causes a steeper spectrum. At higher energies, pre-existing turbulences in the ISM

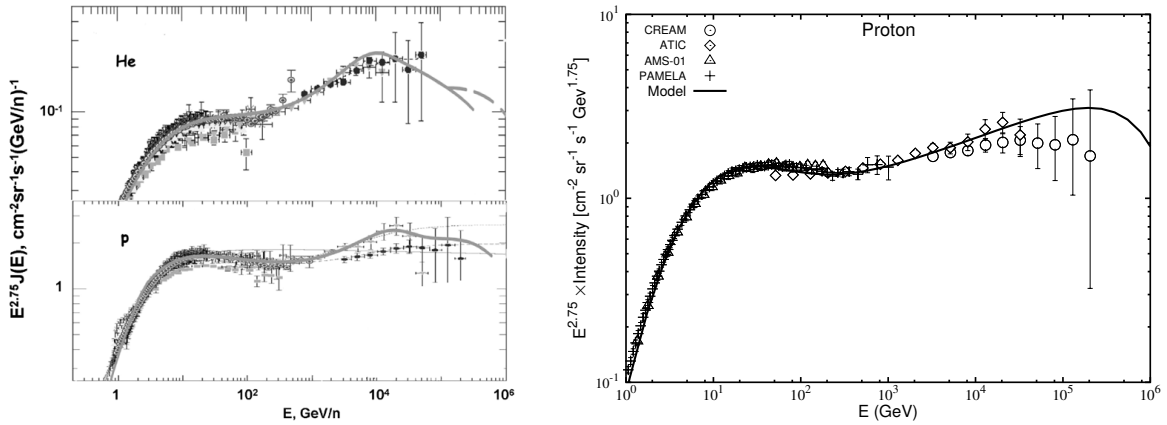


Figure 5.3: Results of different, advanced acceleration theories on the expected proton spectrum. The left plot shows the results after the inclusion of non-linear effects in the calculations. The shown data points are from the experiments BESS, CAPRICE, AMS-01, ATIC-2, CREAM and PAMELA (Ptuskin et al. 2013). The right plot shows the expected proton spectrum after re-acceleration of the particles at older SNRs is included. The shown data points are from CREAM, ATIC, AMS and PAMELA (Thoudam & Hörandel 2014).

start to dominate over the self-generated ones, which leads to a harder spectrum again. This effect can be responsible for the break in the proton spectrum at lower energies. The exact influence of the self-generated turbulences on the proton spectrum is shown in Figure 5.4, where the model is combined with data from Voyager, PAMELA, AMS-02 and CREAM. It can be seen that the transition from self-generated turbulences to pre-existing ones can model the spectral break at a few 100 GeV quite nicely. Another possible explanation of the observed spectral features, which comes from a similar origin as the explanation above, is the “two-halo model” of diffusion (Tomassetti 2012, 2015a). The main idea of this theoretical approach is that there are two zones of diffusion within the galaxy that differ in their energy dependence of the diffusion coefficient. This theory proposes two halos of diffusion, one close to the galactic disk where the diffusion is dominated by turbulences created by SNRs and one halo that contains the other part of the galaxy where CR driven turbulences dominate due to the lack of SNRs. With this model, high energy cosmic rays are dominated by the inner halo which then causes the kink in the proton spectrum at a few 100 GeV. The resulting proton spectrum calculated with this model is shown in Figure 5.4 on the right. Besides the good explanation of the low energy break in the proton spectrum, the model is also able to correctly model the spectra of heavier nuclei, the proton to antiproton ratio or observed anisotropies.

The last topic which should be touched as a possible explanation of the observations concerns the distribution of sources and their different types. As was already shortly mentioned in the introduction to this part, there might be different populations of cosmic rays which can create distinct features in the CR spectra. In the beginning, they were mentioned to be a possible cause of the high energy features like the knee. But different CR components might also be able to cause the features in the proton spectrum (Zatsepin & Sokolskaya 2006). The general idea of this theory is that there are different types of sources that differ in the

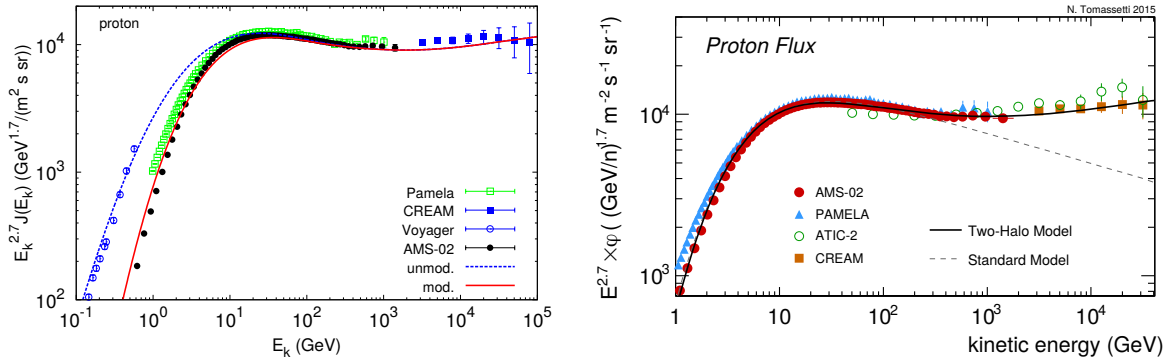


Figure 5.4: Results of different, advanced propagation theories on the expected proton spectrum. The plot on the left shows how the transition from self-generated turbulences to pre-existing turbulences during the diffusion of the CR particles can create a break at a few 100 GeV. The data shown is from Voyager, PAMELA, AMS-02 and CREAM (Aloisio et al. 2015). The right plot compares the expected proton spectrum of a standard diffusion model with the two-halo diffusion model where the latter one is able to describe the observation better. The shown data points are from AMS-02, PAMELA, ATIC-2 and CREAM (Tomassetti 2015a).

spectral indices and maximum energy of the injected particles. These different source types create different components that add up to the complete spectrum. The resulting proton and helium spectra of two and three-component populations are shown in Figure 5.5 on the left. Especially the three-component model is able to explain the different spectral breaks in the observations. Besides these features, such theories are also able to explain other observations like the discovered behavior of the proton to helium ratio (Tomassetti 2015b). In contrast to these various types of sources with distinct properties, a nearby source might be able to explain the found features. In the work of Liu et al. (2017), a close, at 100 pc distance, and young, roughly 10^5 y old, SNR is assumed that accelerates the particles, protons as well as heavier nuclei and leptons. The plot on the right in Figure 5.5 shows the proton spectrum with such a local source and compares it with some measurements. It becomes clear that a nearby source is also able to produce both observed spectral breaks in the proton spectrum and also to model other observed spectra quite well. Additionally, such a nearby source is able to explain observations in the CR anisotropy. However, some discrepancies remain in this regard.

It can be concluded that there are, in fact, a lot of different theories that are able to explain the observed breaks in the cosmic ray proton spectrum. But as was already hinted at, there are also a lot of other interesting features in the measurements of heavier nuclei, anisotropies, anti-particles or leptons, which also need to be explained by the different theories which is not achievable this easily. The next section will take a short look into the future to further possible measurements with H.E.S.S. and also upcoming experiments, which will give even better results on the CR spectra than the current generation of experiments. With the help of these new results, it will be possible to improve or exclude some theories, contributing further to the understanding of the still unsolved mysteries of cosmic rays.

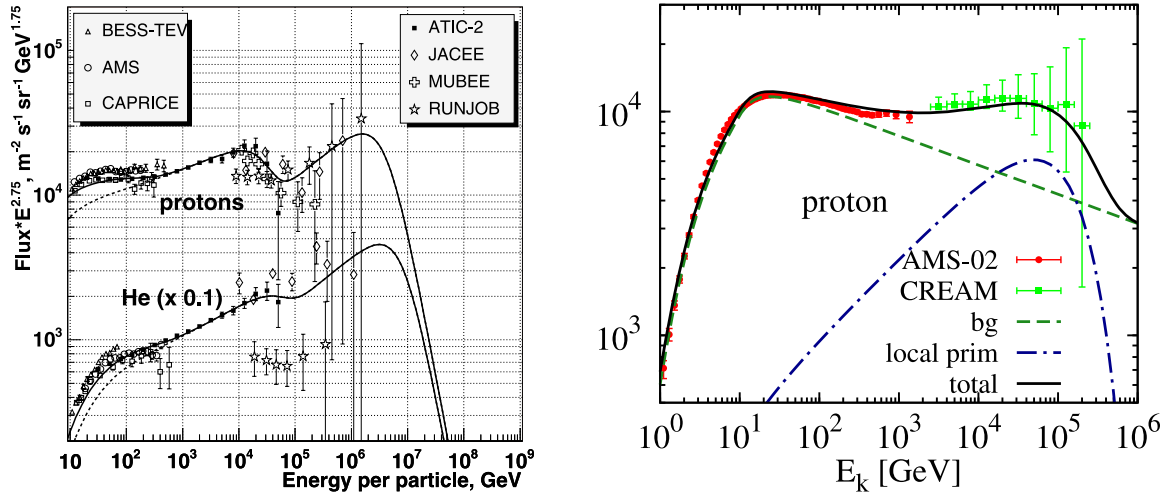


Figure 5.5: Results of different theories regarding the distribution of possible CR sources on the expected proton spectrum. The plot on the left shows the results of two-component (dashed line) and three-component (solid line) CR populations, which are able to explain the observed features in the CR proton and helium spectra (Zatsepin & Sokolskaya 2006). The plot on the right shows the expected proton spectrum when a nearby SNR is added to the standard background CRs. This additional source is able to create a bump in the spectrum that would explain the observed hardening and softening in the spectrum (Liu et al. 2017).

Outlook

The experimental discovery of additional breaks in the proton spectrum created the opportunity to further finetune the theories on cosmic ray acceleration and propagation. But there exist still plenty of opportunities for the experimentalists to improve the measurements or to get new results. The last paragraphs will give a few thoughts on the possibilities of H.E.S.S. to improve the reconstruction of cosmic rays and also on further planned CR missions and experiments.

There are several points in the CR proton analysis with H.E.S.S. that could be further improved:

- It became clear that the hadronic interaction models play a crucial role in the reconstruction of the proton spectrum since they profoundly influence the flux normalization and also the shape of the spectrum. More precise data from earthbound accelerators, like the LHC at CERN, might help to tune the interaction models to agree even more with the particle processes in the atmosphere.
- Further improvements are likely possible in the reconstruction of the proton events itself. The main drawback of the proton analysis with an IACT is that the instrumentation, as well as the analysis pipeline, are specifically developed for the reconstruction of gamma rays. This was overcome by only selecting protons with a more than usual elliptic shape. The choice of certain events and the rejection of more unregular events might also influence the reconstructed spectrum. A dedicated analysis that takes into

account all or most of the proton events could improve the results. But also the usage of more advanced gamma-ray analysis techniques for the proton analysis, like Modell++ (De Naurois & Rolland 2009) and ImPACT (Parsons & Hinton 2014) within H.E.S.S. or CNNs (Shilon et al. 2019), could lead to improvements.

- It was also found that the systematic error is still larger than statistic effects even if the error from the choice of the interaction model is excluded. Dedicated studies to understand these large systematics and to get rid of them would further improve on the resulting proton spectrum. This is also connected to the last point since improvements in the analysis would already lower the systematic errors.
- As was already discussed in detail in Section 4.2 in the last chapter, the contamination with helium and heavier nuclei is still a problem, especially at high energies. The usage of more advanced particle separation techniques might improve the final spectrum and also extend the available energy range for the reconstruction.

Besides these improvements of the analysis itself, there are also further scientific topics regarding cosmic rays that could be investigated with this developed proton analysis. As explained in the introduction to cosmic rays (Chapter 1), there were already anisotropies in the arrival direction of the particles discovered by several experiments. Similar studies could be done with the H.E.S.S. experiments due to the long exposure and, therefore, good statistics, especially if the analysis can be further improved. Similar studies were already carried out by Kraus (2018) for electrons and could be applied for CR protons. If the separation of particles could be improved more, it might even be possible to distinguish the different heavy nuclei to get also spectra of these particles. There, already first efforts were undertaken to use CNNs to get the CR iron spectrum (Hillig 2019), which might also be extendable to other particles. Both topics, the anisotropy as well as the composition of cosmic rays, can give large input to the development and improvement of astrophysical theories.

The next step beyond current experiments that gave the CR proton spectrum presented in this chapter are new experiments that are dedicated to the measurement of cosmic rays, protons, electrons or heavier nuclei. One promising experiment is ISS-CREAM (Seo et al. 2014), the successor experiment of the CREAM balloon flights. The detector was launched in August 2017 to the International Space Station (ISS), was successfully installed on the 22nd of August 2017 and started data taking. It was designed to extend the energy range of direct cosmic ray measurements to $10^{12} - 10^{15}$ eV and to distinguish different nuclei with atomic numbers up to $Z = 26$. Another upcoming experiment is the High Energy cosmic-Radiation Detection facility (Zhang et al. 2017), abbreviated as HERD, which is planned to start its ten-year operation in 2025 on the Chinese Space Station. This experiment is dedicated to the search of dark matter, the measurement of the electron (and positron) spectra and their anisotropy, the exact measurement of CR spectra and their composition as well as the monitoring of the gamma-ray sky.

Appendix - the cosmic ray proton spectrum

A.1 Validation of Monte Carlo simulations

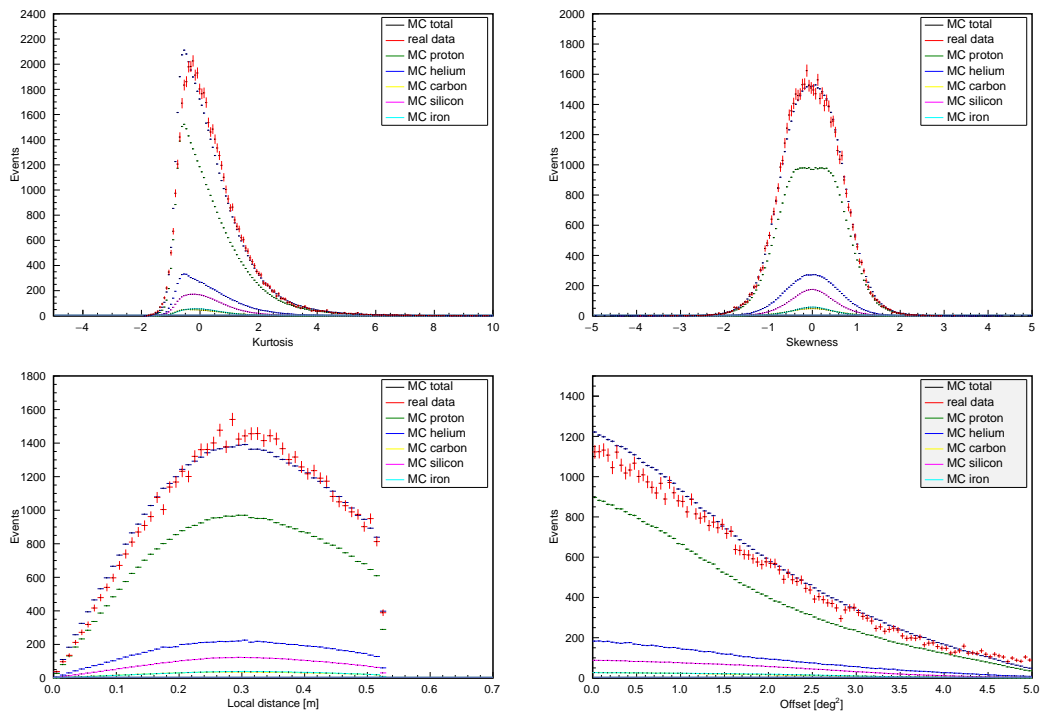


Figure A.1: Comparison of image parameter distributions between simulations and real data. The red color represents the real data, the black color simulations and the other colors the different particle types that were combined for the black curve. Shown are the Hillas kurtosis, the Hillas skewness, the shower offset and the local distance (clockwise, starting from the upper left).

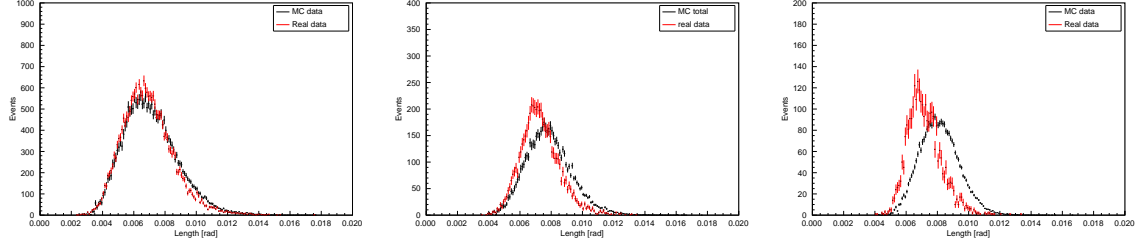


Figure A.2: Comparison of the Hillas length distribution of simulations and real data for different bands of distances between shower impact point and array center. The distances are 80-150 m (left), 150-200 m (middle) and > 200 m. Clearly visible is the larger discrepancy of the Hillas width with rising distances.

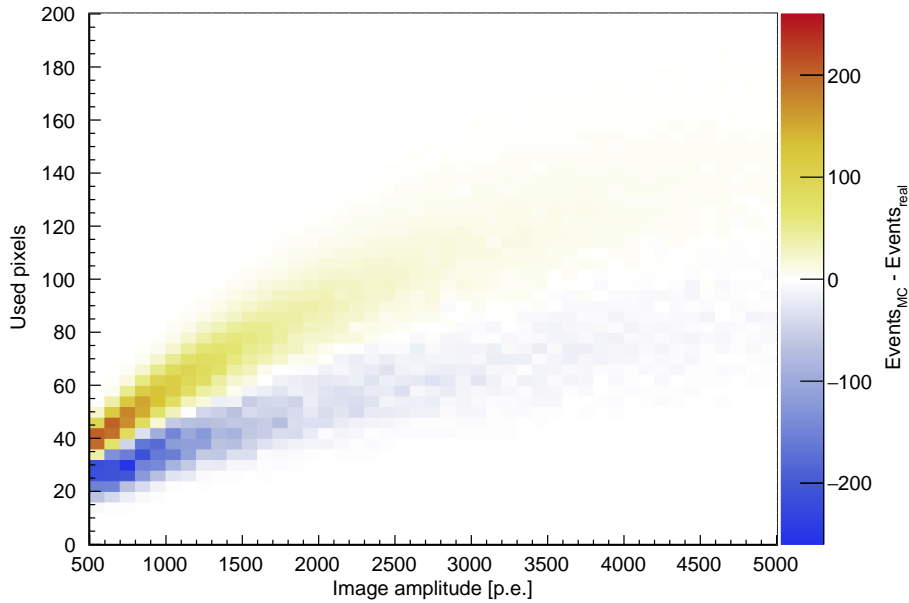


Figure A.3: Comparison of the used pixels in a camera image after cleaning between simulated and real data. Shown is the subtracted distribution (MC - real) of the used pixels as a function of the image amplitude. Red spots imply more simulated events, blue spots more real events, meaning that simulated images after cleaning consist of more pixels than real images.

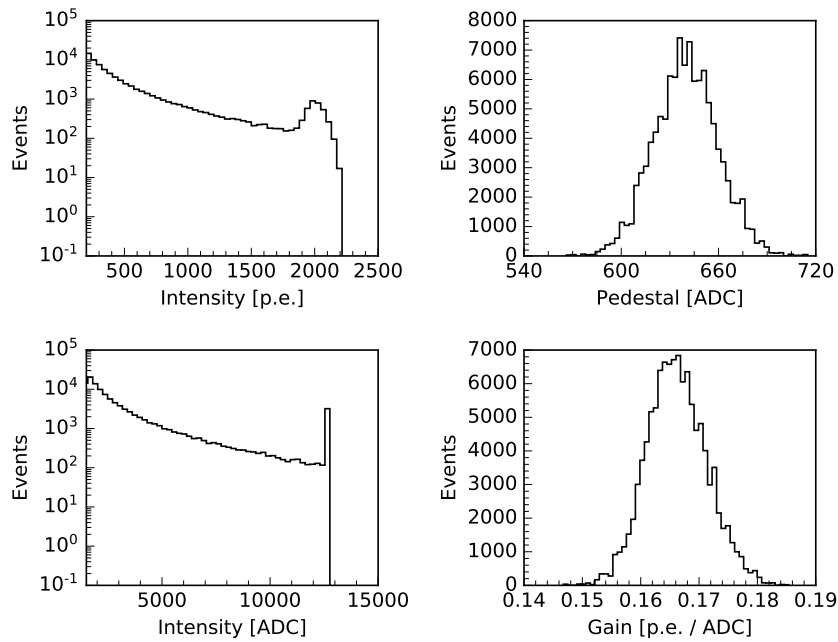


Figure A.4: Distributions of some raw and calibration parameters for the low gain channel of the brightest pixel in an image. The images were created with an adapted simulation configuration.

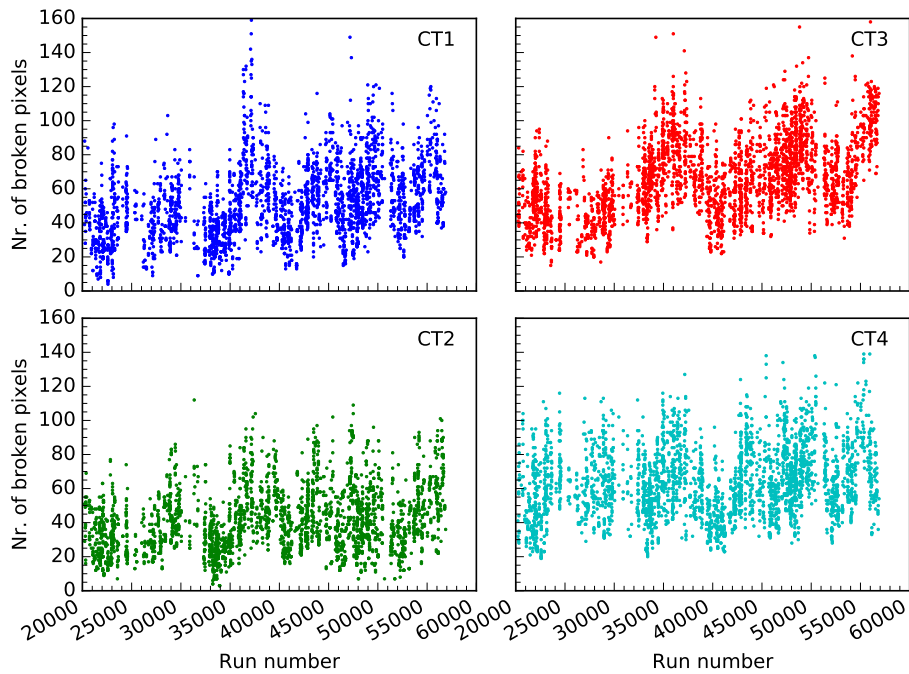


Figure A.5: Number of broken pixels of all four telescopes for the runs which are used for the proton analysis.

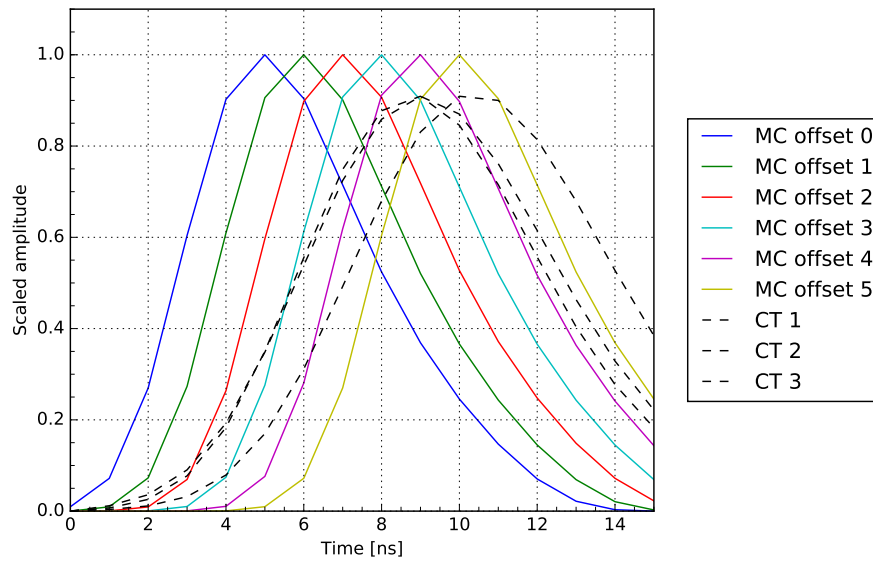


Figure A.6: Comparison of the mean pulse position of simulated flat fielding runs with real flat field runs taken in sample mode. The colored signals are from simulations with different pulse offsets, the black, dotted curves are from real flat field runs. The telescope CT4 is missing since it had no data in the available sample flat field runs.

A.2 Reconstruction of a MC proton spectrum

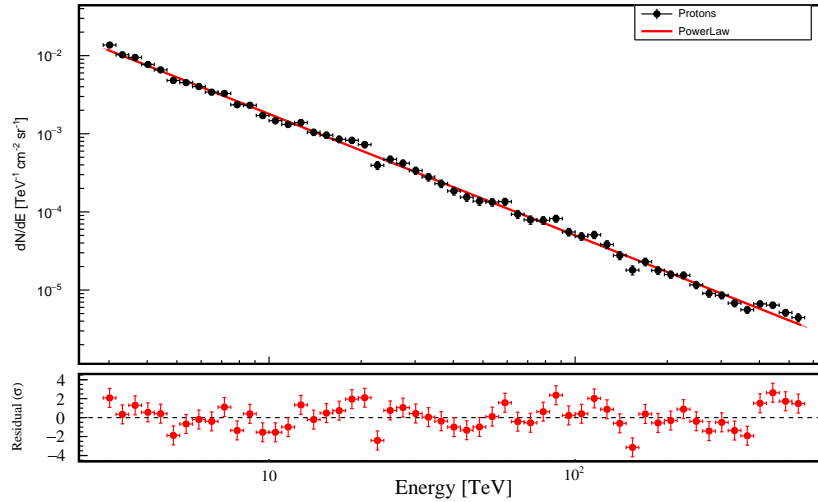


Figure A.7: Reconstruction of the flux and a χ^2 fit of a power law to simulated protons with an index of $\gamma = 1.5$.

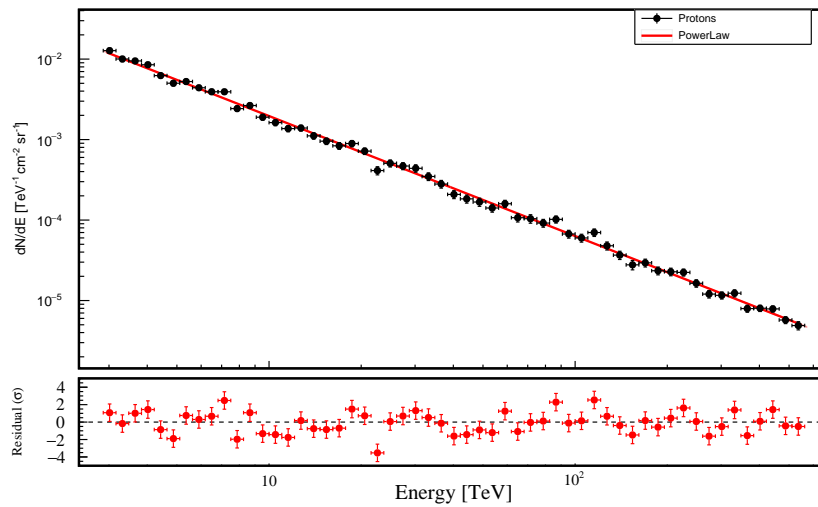


Figure A.8: Reconstruction of the flux and a forward folded fit of a power law to simulated protons with an index of $\gamma = 1.5$.

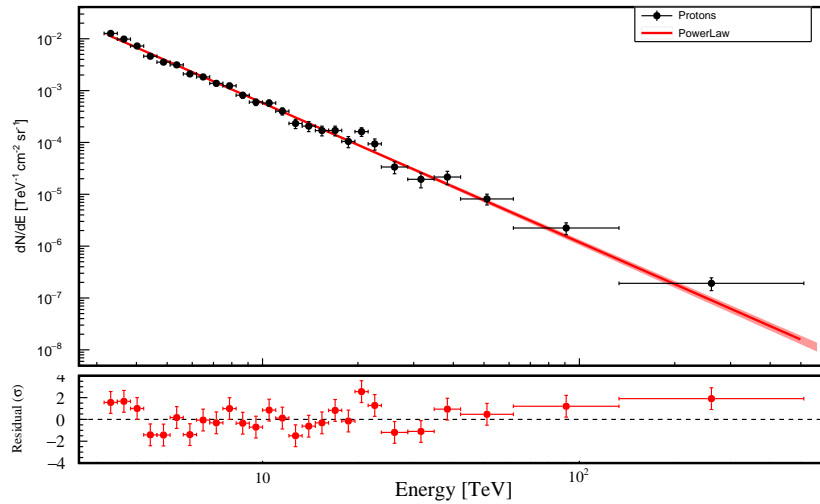


Figure A.9: Reconstruction of the flux and a χ^2 fit of a power law to simulated protons with an index of $\gamma = 2.7$.

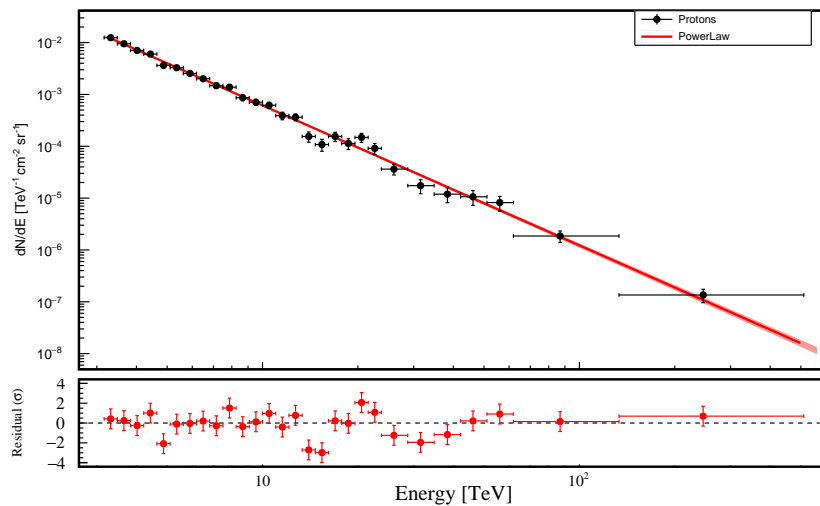


Figure A.10: Reconstruction of the flux and a forward folded fit of a power law to simulated protons with an index of $\gamma = 2.7$.

A.3 Thoughts on the helium contamination

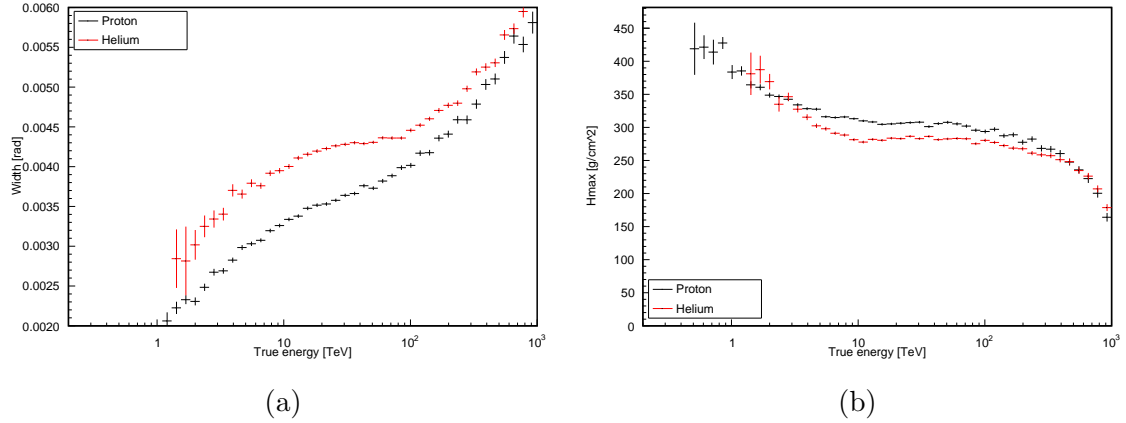


Figure A.11: Comparison of the Hillas width (a) and the shower maximum, H_{\max} (b), between protons and helium without cuts on the shape parameters MSCW and MSCL. The alignment of the Hillas width for energies above 100 TeV, which leads to the failing of the separation with the MSCW parameter, is clearly visible. On the other hand, the reconstruction of the shower maximum for large energies starts to fail so that the reconstructed values for helium and protons align again.

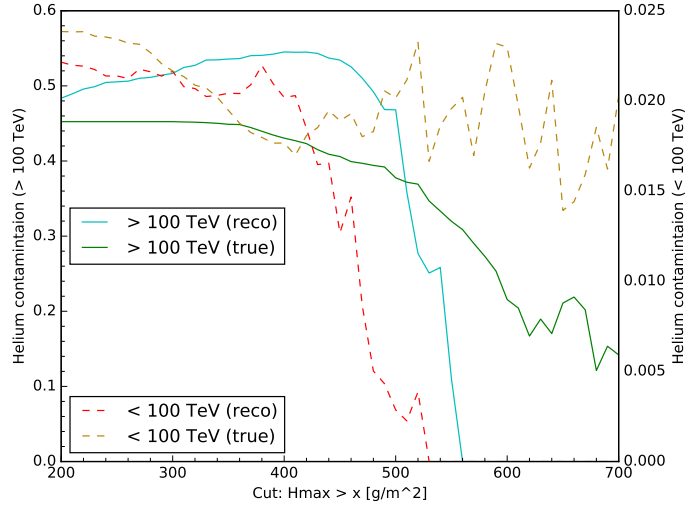


Figure A.12: Tests of different cuts on the shower maximum to further reduce the helium contamination in the data sample. The dashed lines show the contamination for energies below 100 TeV for the true and the reconstructed shower maximum where no further improvements are possible. The sharp drop of the contamination for the reconstructed shower maximum comes from the failing reconstruction. For energies greater 100 TeV, some reduction of the contamination is visible for the true maximum but not for the reconstructed one.

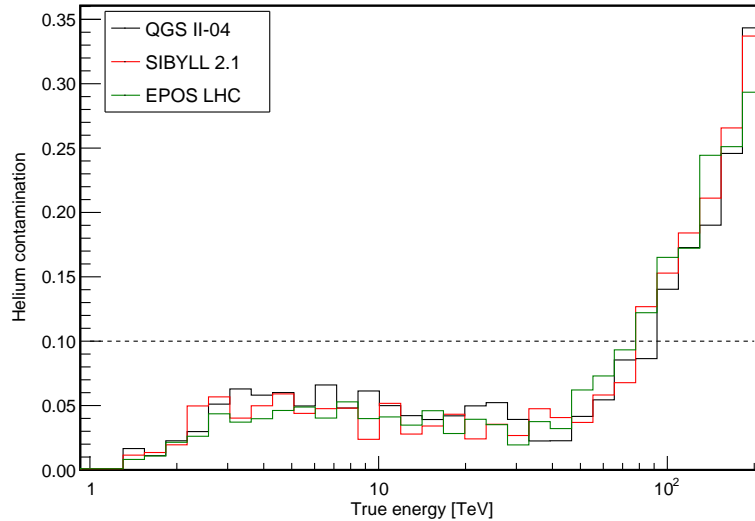


Figure A.13: Helium contamination as a function of the true energy for different, hadronic interaction models, QGS II-04, Sibyll 2.1 and EPOS LHC.

A.4 The proton energy spectrum with real data

\bar{E} [TeV]	E_{min} [TeV]	E_{max} [TeV]	$F \pm \sigma_{stat} + \sigma_{ana} - \sigma_{ana} + \sigma_{had} - \sigma_{had}$ [(TeV cm ² s sr) ⁻¹]
3.32	3.16	3.47	$(3.60 \pm 0.19 + 0.23 - 0.22 + 2.30 - 0.15) \times 10^{-07}$
3.65	3.47	3.82	$(2.73 \pm 0.04 + 0.18 - 0.17 + 1.74 - 0.12) \times 10^{-07}$
4.02	3.82	4.21	$(2.16 \pm 0.01 + 0.14 - 0.14 + 1.37 - 0.10) \times 10^{-07}$
4.42	4.21	4.63	$(1.69 \pm 0.01 + 0.11 - 0.11 + 1.07 - 0.08) \times 10^{-07}$
4.87	4.63	5.10	$(1.32 \pm 0.01 + 0.09 - 0.09 + 0.83 - 0.07) \times 10^{-07}$
5.36	5.10	5.61	$(1.02 \pm 0.01 + 0.07 - 0.07 + 0.64 - 0.05) \times 10^{-07}$
5.90	5.61	6.18	$(7.81 \pm 0.06 + 0.52 - 0.52 + 4.91 - 0.42) \times 10^{-08}$
6.49	6.17	6.80	$(6.27 \pm 0.05 + 0.42 - 0.42 + 3.93 - 0.36) \times 10^{-08}$
7.15	6.80	7.48	$(4.84 \pm 0.04 + 0.33 - 0.33 + 3.02 - 0.29) \times 10^{-08}$
7.87	7.48	8.24	$(3.71 \pm 0.03 + 0.26 - 0.26 + 2.30 - 0.23) \times 10^{-08}$
8.66	8.23	9.07	$(2.78 \pm 0.03 + 0.20 - 0.20 + 1.72 - 0.19) \times 10^{-08}$
9.53	9.06	9.98	$(2.17 \pm 0.02 + 0.15 - 0.16 + 1.34 - 0.15) \times 10^{-08}$
10.49	9.97	10.98	$(1.68 \pm 0.02 + 0.12 - 0.13 + 1.02 - 0.13) \times 10^{-08}$
11.55	10.98	12.09	$(1.25 \pm 0.02 + 0.09 - 0.10 + 0.76 - 0.10) \times 10^{-08}$
12.71	12.09	13.31	$(1.02 \pm 0.01 + 0.08 - 0.08 + 0.61 - 0.09) \times 10^{-08}$
13.99	13.30	14.65	$(7.75 \pm 0.11 + 0.60 - 0.63 + 4.64 - 0.69) \times 10^{-09}$
15.40	14.64	16.12	$(6.00 \pm 0.09 + 0.47 - 0.50 + 3.56 - 0.57) \times 10^{-09}$
16.95	16.12	17.74	$(4.45 \pm 0.08 + 0.36 - 0.39 + 2.62 - 0.45) \times 10^{-09}$
18.66	17.74	19.53	$(3.44 \pm 0.07 + 0.28 - 0.31 + 2.01 - 0.37) \times 10^{-09}$
20.54	19.53	21.50	$(2.41 \pm 0.05 + 0.21 - 0.22 + 1.39 - 0.28) \times 10^{-09}$
22.60	21.49	23.66	$(1.87 \pm 0.04 + 0.16 - 0.18 + 1.07 - 0.23) \times 10^{-09}$
24.88	23.66	26.04	$(1.40 \pm 0.03 + 0.13 - 0.14 + 0.78 - 0.18) \times 10^{-09}$
27.38	26.03	28.66	$(1.01 \pm 0.03 + 0.09 - 0.10 + 0.56 - 0.14) \times 10^{-09}$
30.14	28.66	31.55	$(7.81 \pm 0.23 + 0.76 - 0.82 + 4.26 - 1.16) \times 10^{-10}$
33.18	31.55	34.73	$(5.29 \pm 0.18 + 0.54 - 0.57 + 2.83 - 0.83) \times 10^{-10}$
36.52	34.73	38.23	$(4.52 \pm 0.16 + 0.48 - 0.50 + 2.38 - 0.76) \times 10^{-10}$
40.19	38.21	42.07	$(3.51 \pm 0.13 + 0.39 - 0.40 + 1.80 - 0.62) \times 10^{-10}$
44.24	42.07	46.31	$(2.62 \pm 0.10 + 0.31 - 0.31 + 1.32 - 0.49) \times 10^{-10}$
48.70	46.31	50.98	$(2.08 \pm 0.09 + 0.25 - 0.25 + 1.02 - 0.41) \times 10^{-10}$
53.60	50.97	56.11	$(1.55 \pm 0.07 + 0.20 - 0.19 + 0.74 - 0.32) \times 10^{-10}$
59.00	56.10	61.76	$(1.22 \pm 0.06 + 0.17 - 0.15 + 0.57 - 0.26) \times 10^{-10}$
64.94	61.75	67.98	$(9.46 \pm 0.50 + 1.38 - 1.17 + 4.27 - 2.12) \times 10^{-11}$
71.48	67.97	74.83	$(7.11 \pm 0.41 + 1.11 - 0.87 + 3.11 - 1.64) \times 10^{-11}$
78.67	74.80	82.36	$(5.80 \pm 0.36 + 0.96 - 0.70 + 2.46 - 1.36) \times 10^{-11}$
86.60	82.34	90.66	$(4.65 \pm 0.30 + 0.83 - 0.53 + 1.91 - 1.10) \times 10^{-11}$
95.32	90.64	99.78	$(3.36 \pm 0.24 + 0.65 - 0.36 + 1.34 - 0.78) \times 10^{-11}$

Table A.1: Flux points deduced with the EPOS LHC interaction model and shown with statistical as well as systematic errors.

Part II

Characterization of the Target C and T5TEA ASICs

CHAPTER 1

The future of VHE gamma-ray astronomy

“ANY SUFFICIENTLY ADVANCED TECHNOLOGY IS
INDISTINGUISHABLE FROM MAGIC.”

Arthur C. Clarke (1962)

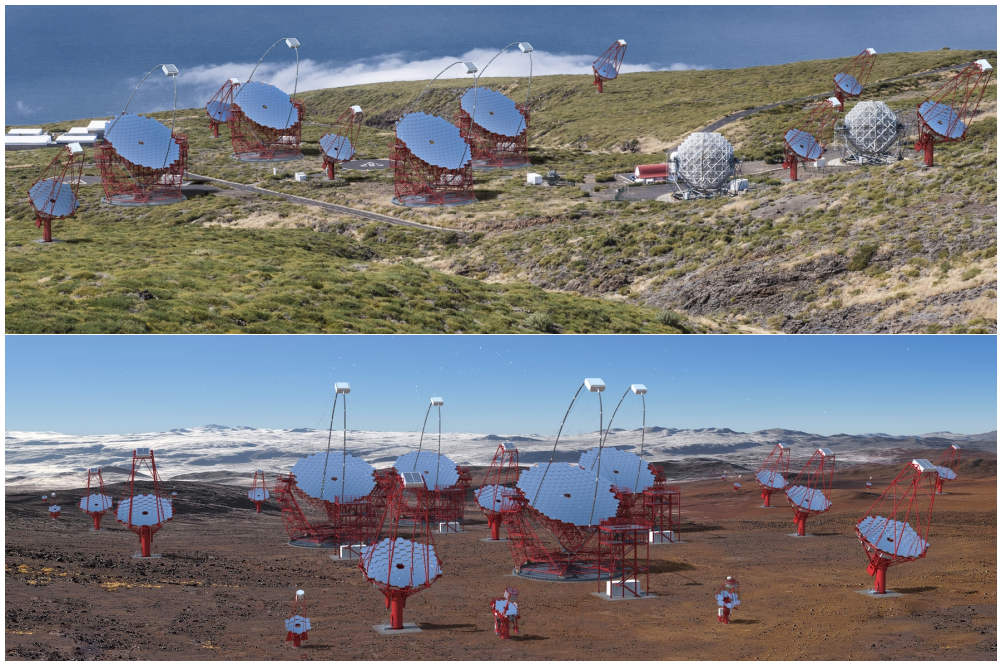


Figure 1.1: Renderings of the two CTA sites; at the top, La Palma, Spain, and at the bottom, Paranal, Chile. (Image credit: Gabriel Pérez Diaz)

1.1 The current status of gamma-ray astronomy

In one of the oldest sciences, astronomy, the investigation of gamma rays at the highest energies in the electromagnetic spectrum is rather new and produced many astonishing publications and advanced technologies in the past decades. The current generation of instruments in gamma-ray astronomy is using basically three different techniques.

Energies up to a few 100 GeV, the so-called high-energy regime, are usually covered by space-based satellites like Fermi (Atwood et al. 2009), Integral (Winkler et al. 2011) or AGILE (Tavani et al. 2009). These satellites can detect the gamma rays directly since they are outside of the impenetrable atmosphere of planet Earth. However, by going to higher energies, the flux of the gamma rays decreases, which makes satellites more and more impractical because of their rather small detection area.

To detect these high energies from a few 10 GeV to roughly 100 TeV, the very-high-energy (VHE) domain, one can use Imaging Atmospheric Cherenkov Telescopes (IACTs). In the first part of this work, one current IACT was described in great detail: H.E.S.S. (Hinton 2004). Other state-of-the-art experiments are MAGIC (Aleksić et al. 2012), situated at the Roque de los Muchachos Observatory on La Palma, and VERITAS (Holder et al. 2008), at Mount Hopkins in southern Arizona. The general idea of this kind of telescopes is to use the atmosphere as a detector and detect the gamma rays indirectly by the emitted Cherenkov light of the induced particle showers (see also Section 2.1 in Part I).

HAWC (Pretz 2015), built on the flank of the Sierra Negra volcano in Mexico, is an air shower detector that uses water tanks to detect the Cherenkov light of the shower particles. It covers roughly the same energy range as IACTs but with better capabilities at higher energies. Advantages are large duty cycles since they can also observe during daytime and full sky coverage. However, this comes with a lower sensitivity.

Since many of the aforementioned experiments are already quite old and are moving to the end of their lifecycles, one has to look into the future and develop new and more advanced experiments. One of these future gamma-ray experiments is the Cherenkov Telescope Array, a successor to the very efficient, current IACT generation.

The following sections focus on the Cherenkov Telescope Array, its science and performance goals (section 1.2.1) as well as its different telescopes (section 1.2.2). Chapter 2 presents in detail the front end electronics (FEEs) of one of the small-sized telescopes, and Chapter 3 will investigate its performance and show calibration techniques. Chapter 4 presents the final electronic performance by the calculation of the charge resolution. This part is finished in Chapter 5 with a conclusion.

1.2 CTA - The Cherenkov Telescope Array

The Cherenkov Telescope Array, short CTA, will be the next big milestone in ground-based gamma-ray astronomy based on the knowledge of the current IACT generation. As of today, the CTA Consortium consists of more than 1400 scientists and engineers from about 200 institutes in 31 countries. Currently, their main efforts go into developing the technologies which will be used and into defining the scientific goals of the experiment.

The array will be built on two sites on both hemispheres and will consist of more than 100 telescopes, thus giving full sky coverage. The array on the northern hemisphere will be at the Roque de los Muchachos Observatory on La Palma, Spain, the one on the southern

hemisphere near the Paranal Observatory in Chile. Renderings of the two sites can be seen in Fig. 1.1. New technologies as well as the large number of telescopes, coming in three different sizes, will improve the energy coverage as well as the sensitivity compared to the current IACT generation. To increase the quality and quantity of the scientific output, the CTA will be operated as an open observatory, in contrast to current gamma-ray telescopes. The science goals of the observations will be driven by proposals, and the final observations will be selected by a peer-review process done by a group of international experts, as it is also the case for any other major observatory. Furthermore, it is planned to make all data public at some certain point. To ensure a smooth operation of the CTA and to keep every process in order, observations, administration, maintenance and upgrades as well as decisions on proposals and management of the data-flow will be conducted by a team of active operators and not by the scientists itself.

1.2.1 Science and performance goals

As it was already outlined before, CTA will be the next big advancement in gamma-ray astronomy. But what exactly are the scientific goals (Cherenkov Telescope Array Consortium et al. 2017)? What is the performance and what are the new technologies that are needed to achieve them? At first, the main goal is, of course, to detect many gamma-ray sources, new ones as well as already known ones but also completely new source classes. To achieve this as good as possible, basically three observation strategies are planned:

- Detailed surveys of the Galactic Plane (Fig. 1.2), the Large Magellanic Cloud, or the extragalactic sky.
- Deep observations of certain sky regions, e.g the Galactic Center or other already known or newly discovered sources.
- Short timescale phenomena, like gamma-ray bursts, flares, or follow up observations after alerts in other wavebands (radio, optical, x-ray, neutrinos, or gravitational waves).

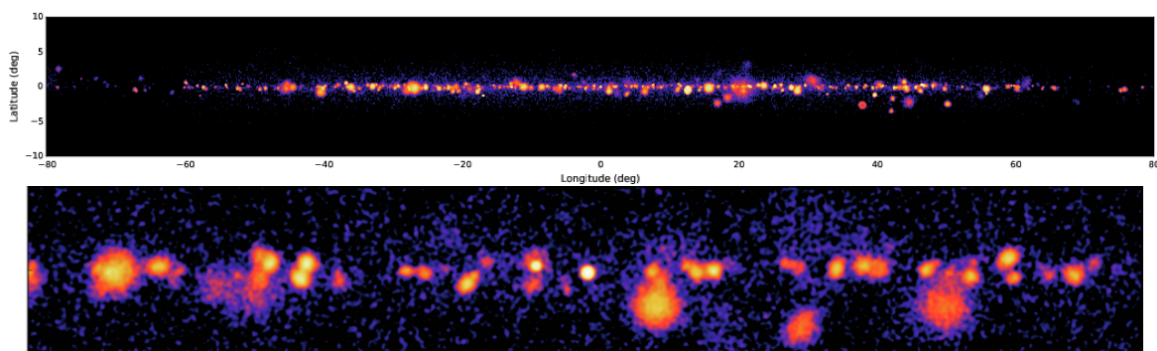


Figure 1.2: Expected view on the inner Galactic Plane by CTA, created through simulations. Bottom: zoom of inner 20° region. (Cherenkov Telescope Array Consortium et al. 2017)

With that much data acquired, one could tackle many different questions of astronomy and particle physics. The main drivers of gamma-ray astronomy are cosmic rays (CRs), their origin

and acceleration, how they propagate through the galaxies and universe or how the highest energies can be created in so-called PeVatrons. One could gather a lot of new knowledge about the different sources of CRs, like supernova remnants (SNRs) or pulsar wind nebulae (PWNe), black holes (BHs), their jets and relativistic outflows, star formation processes or transients like gamma-ray bursts (GRBs) or flares. But also more general questions of physics can be investigated: what is dark matter (DM), do axions exist? Is Lorentz invariance violated or what are the implications of quantum gravity?

To achieve all of these ambitious goals, the CTA has to meet specific key performances. The accessible energy range will be extended by a factor of ten compared to current experiments so that it will range from a few 10 GeVs to several 100 TeVs. Additionally, the energy resolution will be significantly improved, giving the possibility to distinguish between different CR emission models or perform DM line searches. Also, it is planned to push the sensitivity further down by a factor of ten (see Fig. 1.3), giving the opportunity to do deep observations or fast surveys. Moreover, the angular resolution (better than 2 arc minutes for energies above 1 TeV), as well as the temporal resolution (sub-minute time scales), will be significantly improved, allowing to investigate fine structures of sources or detecting short timescale flares.

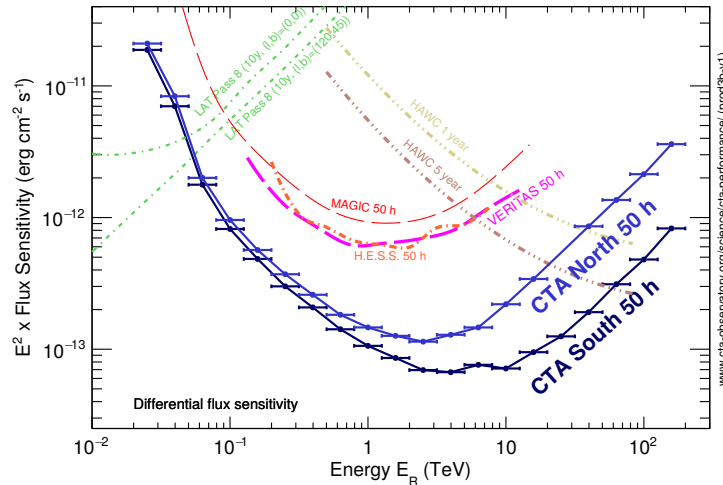


Figure 1.3: Differential sensitivity of CTA North and CTA South, compared to other gamma-ray experiments. The sensitivity is defined as the needed minimum flux to detect a point source within 50 h. (www.cta-observatory.org)

1.2.2 Two sites and three different telescopes

As it was already mentioned before, the unique characteristics of the CTA are that it will be built on two sites and will consist of three different telescope types. The proposed layout of the two arrays, the northern and the southern one, is shown in Figure 1.4. The southern array will be the larger one, combining all three different telescope types: the large-sized telescopes (LSTs), the medium-sized telescopes (MSTs) and the small-sized telescopes (SSTs), covering an area of roughly 4 km². This is necessary since the observable sky of this array is focused on our own Galaxy with its center and extragalactic sources. So, it is desired to cover a

broad energy range, from the lower energies where most of the sources are visible but also up to the highest energies (PeVatrons!), which are only observable in our direct, cosmic neighborhood. The northern array instead will be smaller and only combine LSTs and MSTs. This is sufficient for this array since it looks away from the Galactic Center and focuses on extragalactic sources, which are usually only visible at lower energies because of energy losses.

In the following, the three different telescope types, as shown in Figure 1.5, their characteristics and technologies, are explained in more detail.

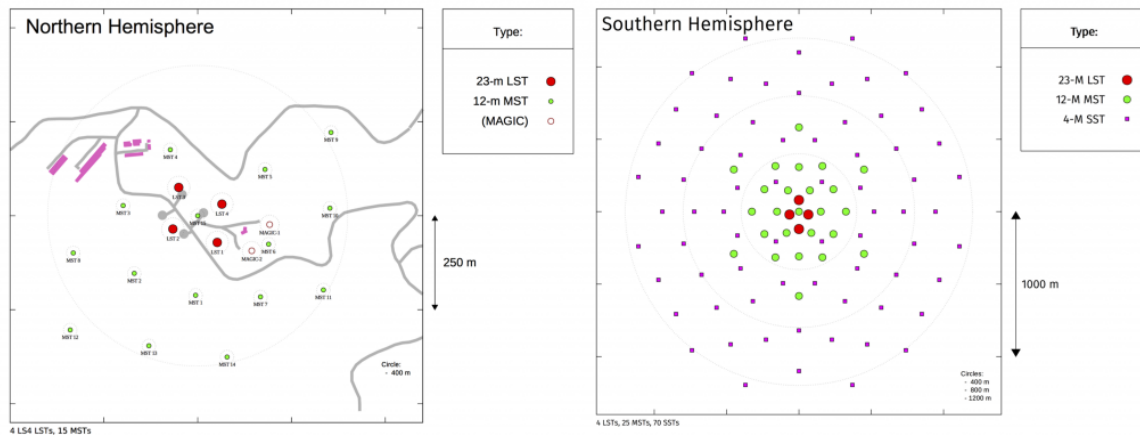


Figure 1.4: Proposed layouts of the CTA on the northern and the southern hemisphere. Note the larger size of the southern array and the SSTs, which are needed to cover the Galactic Center as well as Plane and to detect the expected PeVatrons. (www.cta-observatory.org)

LSTs - The large-sized telescopes

The large-sized telescopes (Cortina & Teshima 2015) are designed for the lowest energies with their highest sensitivity ranging from 20 GeV to 150 GeV but with a total working range up to several TeV. Since particles at such energies are quite common but do not produce much Cherenkov light, large mirror dishes are needed but a small number of telescopes is already sufficient. Furthermore, the LSTs are the most crucial telescope class to observe transients because most of such phenomena happen at lower energies where also absorption due to extragalactic background light (EBL) is less dominant. To meet these requirements, a large but also lightweight and movable telescope is needed. Therefore, the mirror dish will have a diameter of 23 m with a total area of 370 m^2 (including shadowing) and a parabolic optical design. The supporting structure of the camera and mirrors will be made of carbon fiber reinforced polymers and aluminum. This results in a total weight of around 100 t and possible repositioning times below 20 s to any point in the sky. It is planned to place 4 LSTs on each array site. The camera itself will share many elements with the NectarCam from the MSTs (see next subsection), will consist of 1855 pixels with photomultiplier tubes (PMTs) and a field of view (FoV) of 4.3° .

MSTs - The medium-sized telescopes

The medium-sized telescopes (Pühlhofer 2017) will cover the main energy range of CTA with the highest sensitivity from 150 GeV to 5 TeV but total accessible energies from 80 GeV to 50 TeV. Thus, a decent number of such telescopes will be built on both sites, 25 on the southern hemisphere and 15 on the northern. The mirror dish will have a diameter of 12 m following a modified Davies-Cotton (DC) design (Lewis 1990), and the total weight of the telescope will be at roughly 80 t. For the camera, two different concepts are in development and being tested: FlashCam (Puehlhofer et al. 2015) and NectarCam (Glicenstein et al. 2015). Both cameras will have around 1800 pixels with PMTs and a FoV of roughly 8° . The main differences are the used electronics for digitization and trigger: NectarCam is built around the Nectar analog pipeline readout chip, which is already successfully used in the updated cameras of the small telescopes of H.E.S.S. or the MAGIC-II telescopes. Instead, FlashCam uses a fully digital readout and trigger system based on commercial FPGAs and FADCs and became, only very recently, the successor camera for CT5 within the H.E.S.S. experiment.

Additionally, there is another newer concept for the MSTs that follows the Schwarzschild-Couder (SC) design (Schwarzschild 1905; Vassiliev et al. 2007) with two separate mirror dishes which allows finer pixelated cameras resulting in higher optical resolutions and better reconstruction. The telescope itself is called SCT, Schwarzschild-Couder Telescope, (Byrum et al. 2015; Otte et al. 2015). The primary mirror will have a diameter of 9.7 m and the secondary mirror of 5.4 m. The main difference to the other MSTs is the camera, which will consist of 11328 pixels with SiPMs and a FoV of also 8° but with better angular resolution. However, the downside of this concept is that it was never used before so that there is a lack of knowledge and experience compared to the standard MST design. But, as will be seen in the next chapter, the SC design is also used for the SSTs.

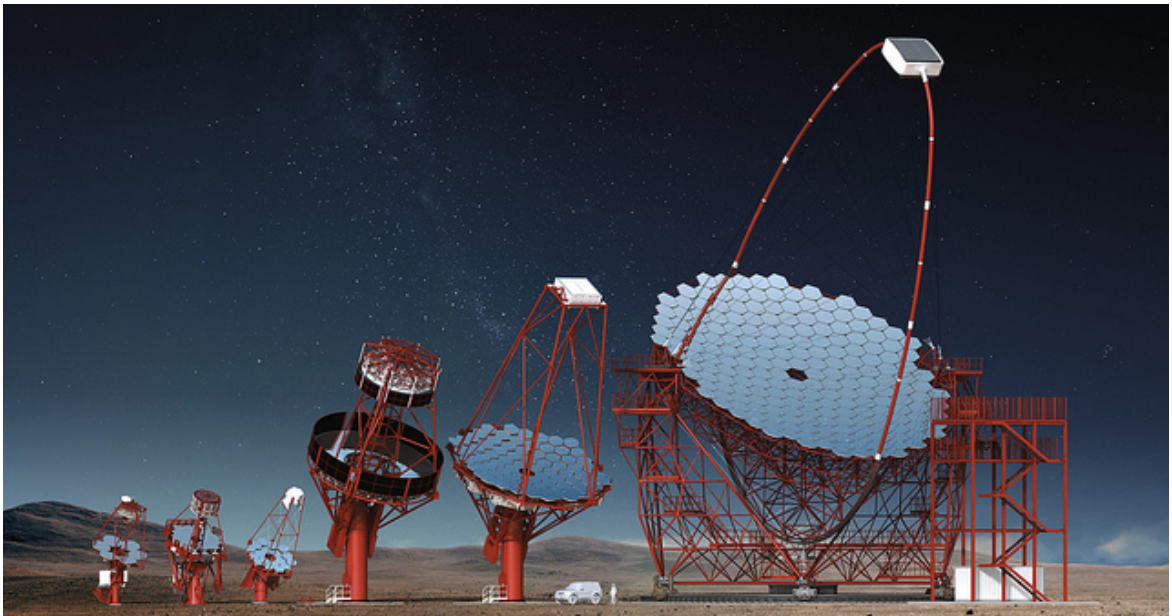


Figure 1.5: Renderings of all planned telescope types for the CTA. From right to left: LST, the two MSTs (with SCT on the left) and the three SSTs (1M, ASTRI and GCT). (www.cta-observatory.org)

SSTs - The small-sized telescopes

The small-sized telescopes (Montaruli et al. 2015) are determined to cover the highest energies with full sensitivity from 5 TeV to 300 TeV. Since the emission of most gamma-ray sources follows steeply falling spectra, very high energy events are very rare and very bright since they emit a lot of Cherenkov light. Thus, only small telescopes are needed to gather enough light for a detection, but they need to cover a large area to see enough events. To achieve this, 70 SSTs will be built on the southern site spreading over a few square kilometers with about 250 m spacing in between the telescopes and with mirror dish diameters of roughly 4 m. Another unique characteristic of these telescopes is the use of silicon photomultipliers (SiPMs). They do not suffer damage at high illumination levels, giving the possibility to observe for longer periods (e.g. with partial moonlight), which further increases the sensitivity. It was already successfully shown with FACT, the First G-APD Cherenkov Telescope (Biland 2011), that even observations during the full moon are possible.

For the final SST design, there are three different implementations available and investigated. The **SST-1M** (Schioppa et al. 2015) follows MST concepts and uses the Davies-Cotton design with one 4 m mirror dish, giving a compact and lightweight structure that is easy to construct, install and maintain. Its camera consists out of 1296 pixels and uses DigiCam as a full digitizing readout system, which is based on FlashCam. **ASTRI** (Maccarone 2017) is a Schwarzschild-Couder telescope with two mirrors, a 4.3 m primary and a 1.8 m monolithic secondary mirror dish. Its camera consists of 2368 SiPM pixels and uses the CITIROC ASIC for digitization. **GCT** (Sol et al. 2017), also a Schwarzschild Couder telescope, features a low mass design and uses two mirrors (with 4.0 m and 2.0 m diameter dishes) with six petal-shaped elements each. The camera, called CHEC, consists of 2048 pixel and makes use of the TARGET ASICs. All of the telescope's cameras have a FoV of larger than 8° giving the opportunity to do extensive surveys or observations of extended sources.

However, to keep costs and effort of infrastructure and operation low, not all three implementations will be used but rather a single design combining different aspects. At this point, the choice fell on a combination of the ASTRI telescope structure with CHEC as its camera.

Since testing and characterization of the Front End Electronics (FEE) of GCT is content of the following chapters, its camera, CHEC, is described in more detail in the next section.

1.3 The highest energies - CHEC and its electronics

The Compact High Energy Camera (White et al. 2017), or simply CHEC, is a promising camera design for the SSTs, developed in collaboration with the GCT structure (Le Blanc et al. 2017). The main concept of CHEC is to get a low cost and compact camera but also with high reliability and high data quality for dual mirror telescopes. It has to record short Cherenkov flashes, typically only lasting a few nanoseconds with an extension of about $0.2^\circ \times 1.0^\circ$. The small focal length of around 2 m allows the usage of 6 mm pixels resulting in an angular size of 0.2° thus matching the expected dimensions of Cherenkov images. The dual mirror design guarantees in addition point spread functions (PSF) below the pixel size of 6 mm and a FoV of more than 8° . The camera itself has a diameter of 0.4 m and consists of 2048 pixels. There are two prototype cameras available and were already heavily tested: CHEC-M with multi-anode photomultipliers (MAPMs) (Zorn et al. 2018) and the newer version CHEC-S with SiPMs (Watson & Zorn 2019) whose FEE are topic of this work. An exploded-view CAD image is shown in Figure 1.6.

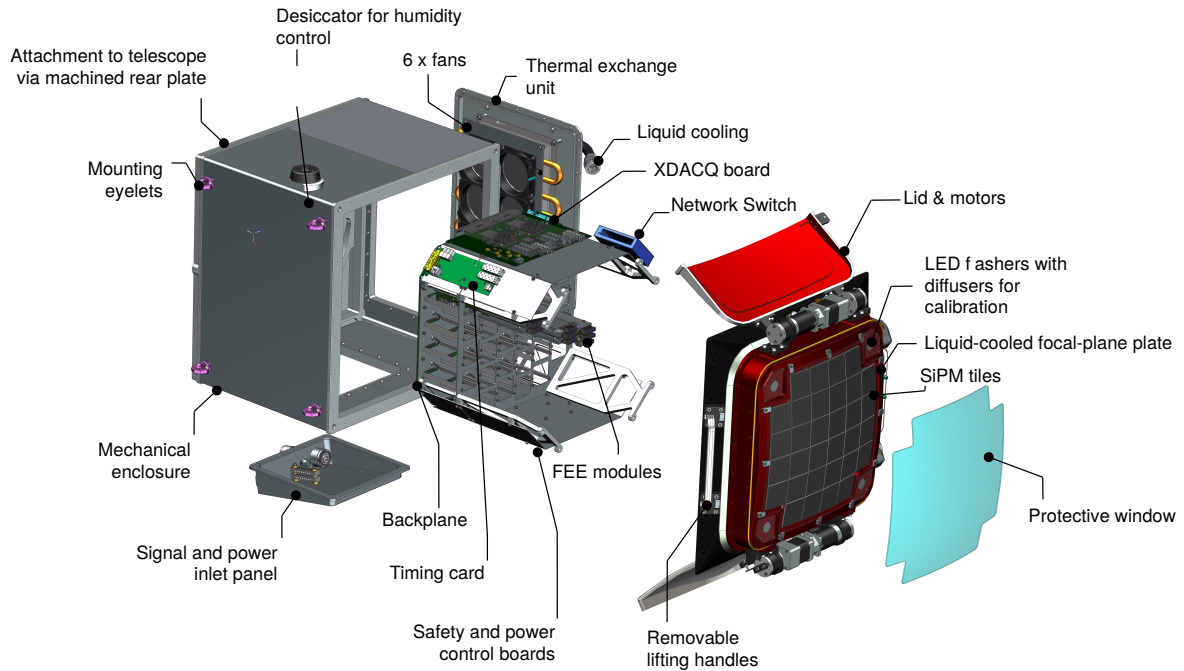


Figure 1.6: Exploded-view schematics of the CHEC-S camera with its key elements (White et al. 2017).

The front end electronics modules are based on the custom-built TARGET ASIC. They combine full-waveform sampling and first-level trigger decisions with preamplifiers and an FPGA for configuration and readout. These modules will be described in full detail in the next Chapter 2.

The FEE modules are managed by the backplane that supplies readout trigger, data interface, clock and power. After getting the first-level trigger signals from the modules, a trigger algorithm is applied, yielding nanosecond accurate trigger decisions. If a full camera trigger signal is received, the data acquired by the FEE is read out, processed by a data acquisition board (DACQ) and routed out via optical fibers. Clock signals are created by White Rabbit boards, which ensure array wide timing. Monitoring, as well as power supply, are managed by a safety board.

Further important parts of CHEC are LED flashers for calibration, a lid to protect the camera if no observations are carried out and a cooling system consisting of fans and chilled liquid to stabilize the electronics and the SiPM temperatures.

TARGET - front end electronics for the CTA

TARGET, TeV Array Readout Electronics with GSa/s sampling and Event Trigger, is an Application-Specific Integrated Circuit (ASIC) and was designed explicitly as a digitization and trigger solution for the cameras of IACTs, especially the Cherenkov Telescope Array. The first ASIC prototype, simply called TARGET 1 (Bechtol et al. 2012), evolved out of former, highly-integrated ASICs which were developed for very precise radio neutrino detection (Varner et al. 2008, 2007a,b). Of course, TARGET itself was developed with the needs of IACTs in mind and is highly specialized for this purpose. Some unique characteristics which are needed and also met by the TARGET ASICs are:

- low costs as well as high reliability since many small-sized telescopes need to be equipped with them. Therefore, several functionalities are combined in a compact design with only a few different parts: sampling and digitization is combined with the creation of trigger signals (internal and external) for 16 parallel input channels
- a several μs deep sample buffer with the possibility to store full waveforms;
- a sampling frequency of 1 GSa/s which is perfectly suited to record Cherenkov flashes with a duration of a few nanoseconds;
- a large dynamic range of more than 10 bit;
- a low power consumption.

The first generation of TARGET was then further improved and enhanced, which resulted in TARGET 5 (Albert et al. 2017), the first ASIC of this kind that was used in a Cherenkov telescope within the CHEC-M camera. But unfortunately, the performance was not as good as desired, especially a high trigger threshold and noise related to the sampling made problems. Therefore, a new generation was developed to overcome these problems: TARGET 7 (Tibaldo et al. 2015), which is also used in the prototype camera for the Schwarzschild-Couder MST. However, the changes (additional insulation and amplification) did not help to solve those problems but rather made them even worse. Thus, further improvements have been implemented in the next TARGET generation, TARGET C and T5TEA (Funk et al. 2017), which will be described in more detail in the next Section 2.1.

2.1 TARGET C and T5TEA

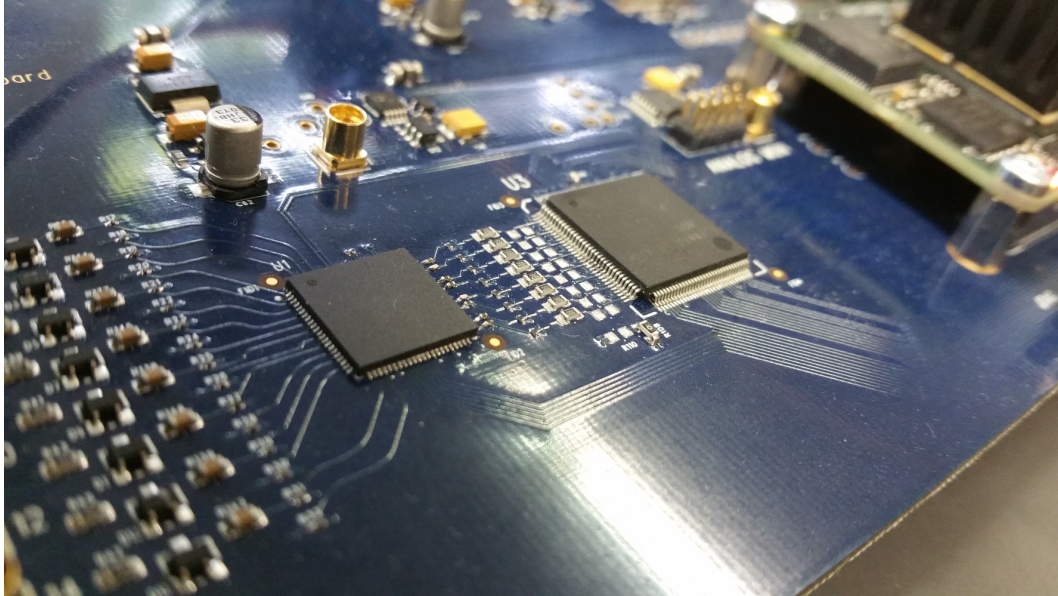


Figure 2.1: TARGET C (ASIC on the right) and T5TEA (ASIC on the left), mounted on a specialized evaluation board. (Funk et al. 2017)

Since previous versions of TARGET showed problems mainly connected to crosstalk between the trigger and sampling path, both paths were divided into two ASICs, TARGET C for sampling and T5TEA, the TARGET 5 trigger extension ASIC, for triggering. Both ASICs are shown in Figure 2.1, where they are mounted on a specialized evaluation board that was designed for testing, characterizing and improving the ASICs before they are used on the final modules. Signals arriving at the two ASICs are split into two signals and routed to both ASICs. TARGET C and T5TEA are usually controlled via a Field Programmable Gate Array (FPGA) whose control parameters are individually adjustable and their configuration values stored in 12 bit registers. These settings are either 12 bit digital-to-analog converters (DACs), e.g. the controlling of the supply voltages, or simple settings, e.g. the controlling of the time base. The general structure of the ASICs can be seen in Figure 2.2. The exact functionality of T5TEA and TC are described in the following.

2.1.1 T5TEA

The amplified signal is sent to T5TEA where four channels are combined to so-called trigger groups via an analog sum. This results in four trigger groups in total for one ASIC since it features 16 channels. The summed signal is then compared to a set threshold via a comparator. If the threshold is crossed, a trigger signal is sent out and further processed, e.g. from an FPGA. A visualization of this process is shown in Figure 2.3.

The exact behavior of the trigger ASIC can be controlled via many different parameters set with an FPGA in 12 bit registers. Thus, the parameter values can be set from 0 ADC to 4095 ADC with an operating voltage range of 0 V to 2.5 V. The three most important ones control the baseline as well as the trigger threshold:

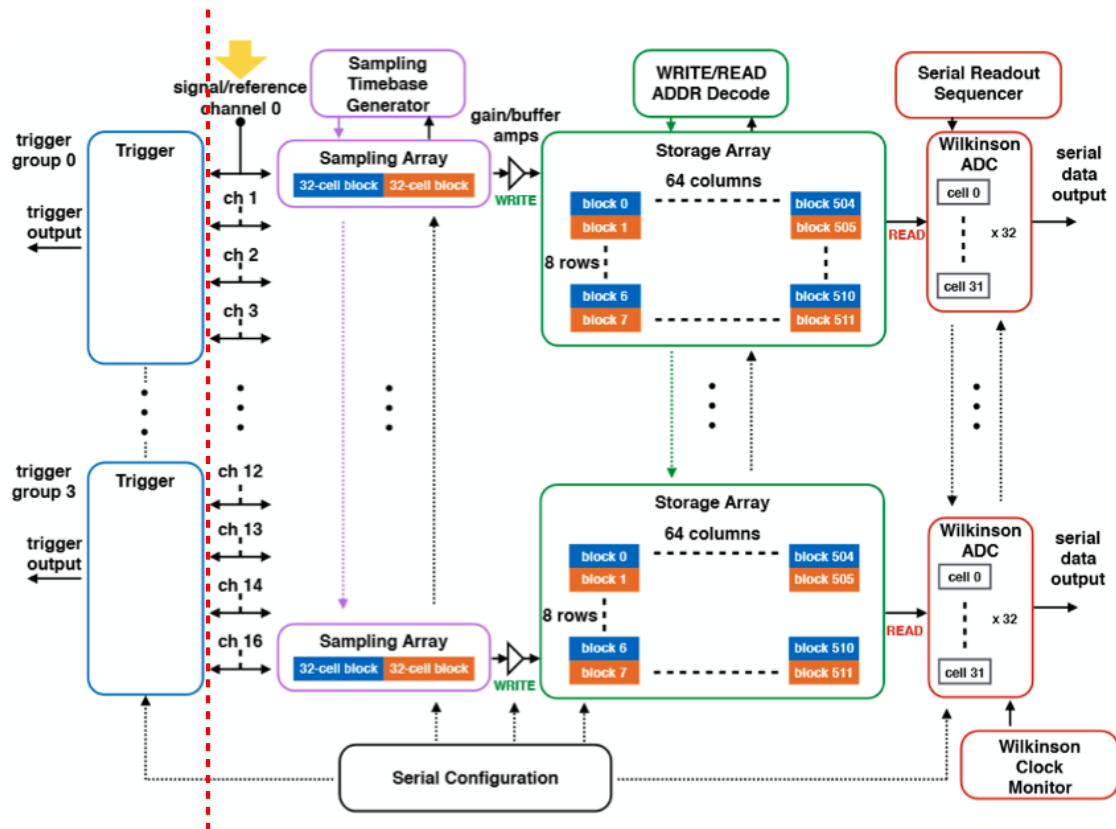


Figure 2.2: Functional block diagram of TARGET 7. This ASIC has the same properties as TARGET C with T5TEA, except that sampling and trigger paths are split. The part left of the dashed red line resembles the trigger ASIC T5TEA and the part right of it the sampling ASIC TC. (modified, Tibaldo et al. (2015))

- V_{ped} , an offset for each channel which is added to the signal before it is inverted by the T5TEA. Thus, larger values shift the baseline closer to the trigger (the negative direction in Fig. 2.3).
- PM_{Tref4} , an additional offset for each trigger group, which is added to the signal after its inversion. So, larger values move the baseline away from the threshold (the positive direction in Fig. 2.3).
- **Thresh** sets the trigger threshold for each trigger group. Larger values put the threshold closer to the baseline and signal (the positive direction in Fig. 2.3).

Besides these parameters, many more are available to set and tune the trigger ASIC T5TEA. They are described more in the upcoming Chapter 3, Section 3.1.1, where the performance and tuning of these parameters is explained and done.

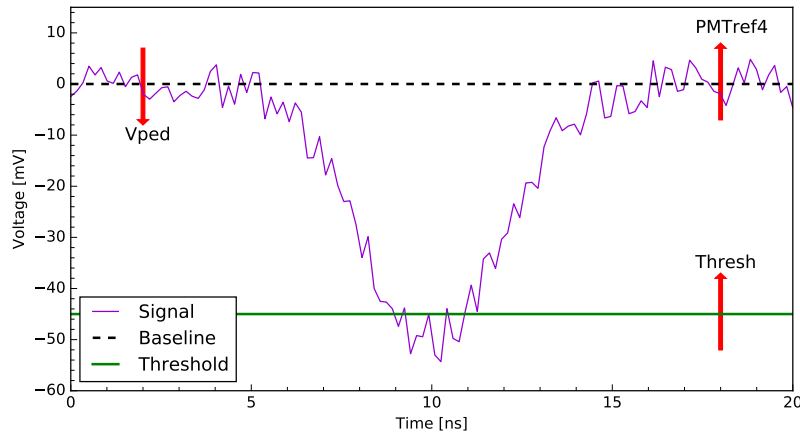


Figure 2.3: Illustration of the trigger behavior. A signal (shaped and inverted) with electronic noise is routed into the T5TEA and added to the baseline. In this case, the applied trigger threshold is crossed and a trigger signal would be sent out.

2.1.2 TARGET C

TARGET C digitizes the applied signals on demand (i.e. if a T5TEA or an external trigger is issued) is received. For the sampling, switched capacitor arrays (SCAs) are used. Firstly, the signal is connected to the so-called sampling array via analog switches. This array consists of two blocks with 32 capacitors each (hereafter also called cells). They are operated in ping pong fashion where one block is sampling the signal while the other one transfers the stored voltages to the next SCA, the storage array. This mode of operation allows basically dead time free measurements with continuous sampling. The storage array is built very similarly to the sampling array but consists of 16348 cells allowing long signal storage, which is needed for triggering and readout between distant telescopes. Usually, the timebase generator, which controls the timing of the samples, is set to hold voltages corresponding to an interval of 1 ns. Together with the desired sampling rate of 1 GSa/s this results in a buffer depth of around 16 μ s. An important characteristic of these SCAs is that each cell has an individual

behavior that needs to be calibrated at the end. Thus, in order to minimize calibration data and effort, the storage array is cut short to 4096 cells, which is still enough storage for SSTs within CTA since they will be used as standalone telescopes. The readout of stored signals is initiated by the FPGA (after a successful trigger) and can be done in blocks of 32 cells. For the digitization of the stored voltages, Wilkinson analog-to-digital converters (ADCs) working at 500 MHz are used. They provide a ramp with adjustable slope and duration and a 12 bit counter. If the voltage ramp crosses the stored sample voltage for one cell, the counter stops, and its current count, the elapsed time, represents the digitized sampling value. Each readout signal starts the parallel digitization of all 16 channels.

2.2 TARGET modules

During regular operation in a Cherenkov camera, not the before mentioned evaluation boards are used but rather complex modules that provide a lot of additional features. A picture of such a TARGET module can be seen in Figure 2.4.

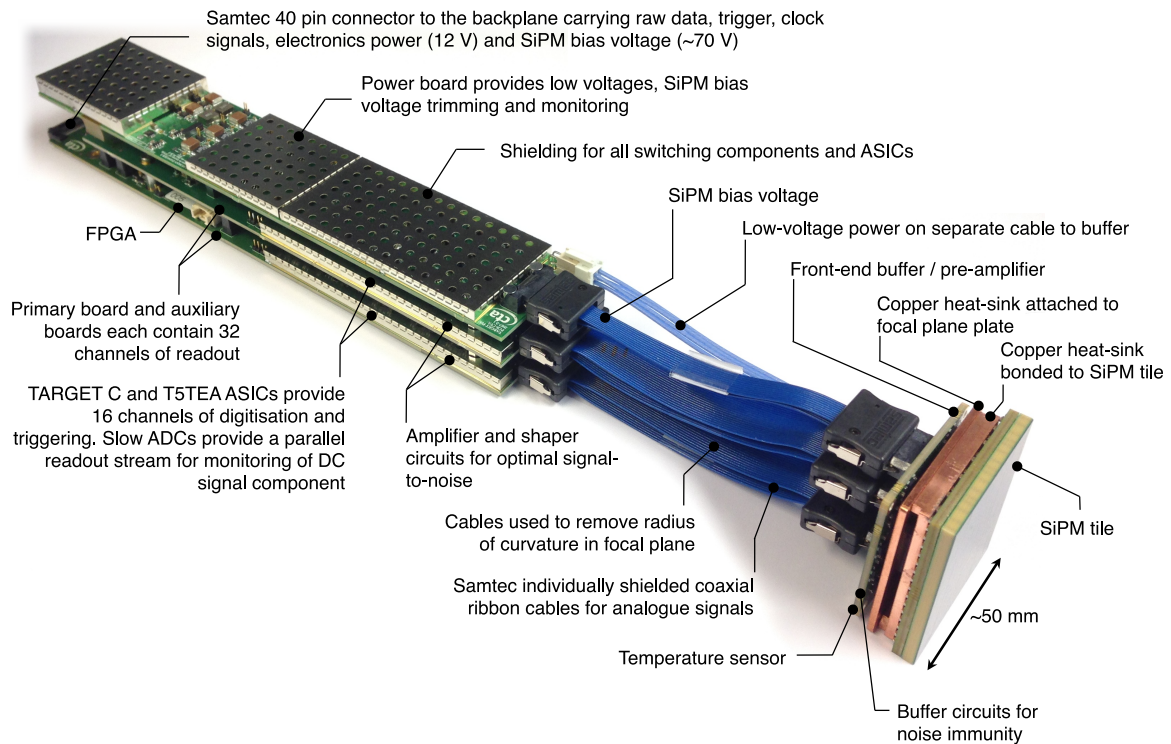


Figure 2.4: A TARGET module with an SiPM tile for CHEC-S. (White et al. 2017)

One module consists of three different boards: the power board which provides low voltages, bias voltage for the SiPM, voltage trimming and monitoring; the primary board with the FPGA and two TC as well as two T5TEA ASICs and the auxiliary board which hosts another two TC and two T5TEA ASICs. Furthermore, slow ADCs, amplifiers and shapers are added. The SiPM tiles, responsible for the detection of the photons, are connected to the boards via shielded, coaxial ribbon cables. Shapers and amplifiers are needed to adjust the

signal from the SiPM, usually featuring a fast-rising edge and a long tail of up to 100 ns, to a shape that is well measurable by both ASICs without pileup of signals. The resulting width after shaping of the input pulse is roughly 10 ns full width at half maximum (FWHM), which is then routed to T5TEA and TC. These ASICs were already described in detail before. The FPGA controls everything on the module: it configures the ASICs, initiates the readout of raw data and handles the packaging and buffering of the data for the output. The slow digitization chain captures the constant DC light level for every pixel, which can be used later on to measure light from stars and track the pointing position of the telescope. The controlling of the module, as well as the data output, is done via UDP, user datagram protocol, and 1 Gbps Ethernet links.

For the upcoming, detailed performance tests, the evaluation board, as well as whole modules, were used since different tests were needed for both of them. It is stated which one of both was used for the individual tests.

CHAPTER 3

General performance and calibration of the TARGET ASICs

The previous chapters focused on the scientific background of the CTA and the electronic parts of one small-sized telescope, especially the front end electronics. This one will now move to the detailed characterization and performance of the FEEs, the TARGET ASICs. The chapter will be split into three parts, the first focusing on the trigger ASIC T5TEA (Section 3.1), the second on the digitization ASIC TARGET C (Section 3.2), and the third one on the large scale testing of multiple TARGET modules (Section 3.3).

Section 3.1.1 shows how certain trigger thresholds can be set by changing configuration parameters and how T5TEA can be tuned to its best performance. The following Sections 3.1.2 and 3.1.3 characterize the crosstalk between the trigger groups and the shape of the trigger output signal.

Section 3.2.1 and 3.2.2 will present how the digitization works with and without signals, as well as the first calibration steps (the pedestal subtraction). Afterward, Section 3.2.3 describes the timebase calibration and the resulting sampling frequency. Section 3.2.4 tests the crosstalk behavior of TARGET C as it was also investigated for T5TEA. Sections 3.2.5 and 3.2.6 go into full detail of the digitization and outline the second step of the low-level calibration, the creation of transfer functions.

In the final section of this chapter, Section 3.3, most of the investigations are repeated with various TARGET modules to characterize the general behavior of the modules and to find the ones with the best performance to use in the prototype camera CHEC-S.

3.1 T5TEA - trigger performance

The technical details and general functionalities of the trigger ASIC T5TEA were explained in the chapter before; this section now focuses on measurements with and tuning of the ASIC (see also Funk et al. (2017)). Two basic measurements that can be done to visualize how the trigger is working are to alter the amplitude of the input pulse or the threshold of the trigger, respectively. Both measurements shown here were done with an evaluation board.

The first one produces a so-called efficiency curve, which visualizes how many signals are detected at which input amplitude. The efficiency ϵ is simply defined as the number of detected signals divided by the number of injected ones:

$$\epsilon = \frac{\text{Nr. of triggered signals}}{\text{Nr. of injected signals}} \quad (3.1)$$

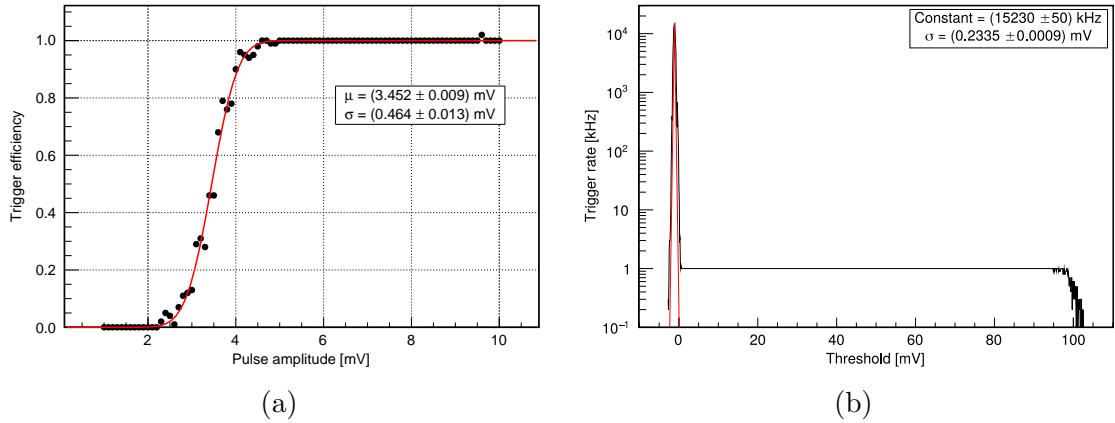


Figure 3.1: Two typical trigger measurements to visualize its behavior: (a) An efficiency curve where the amplitude of the injected signal pulse is increased for a given threshold until every signal results in a trigger. The red curve is a fitted Gaussian error function. (b) A threshold scan where a signal with 100 mV at a frequency of 1 kHz is applied to T5TEA and its set threshold value is reduced (coming from the positive x-direction). In order to characterize the baseline noise, a Gaussian function was fitted to the peak. (see also Funk et al. (2017))

The plot in Figure 3.1 on the left shows such a measurement. The pulses from a function generator (see Appendix B.1 for the exact model) were injected with pulse amplitudes ranging from $A = 1.0$ mV to 10 mV in steps of 0.1 mV at a frequency of 1 kHz. The number of measured trigger signals can be counted with the FPGA. To further describe the trigger behavior, a Gaussian error function (Eq. 3.2) was fitted to the data points.

$$f(A; \mu, \sigma) = \frac{1}{2} \left(1 + \operatorname{erf} \left(\frac{A - \mu}{\sqrt{2}\sigma} \right) \right) \quad (3.2)$$

The value of μ gives the amplitude where an efficiency of 50% is reached, hereafter called threshold, and σ is the width of the rising edge, called trigger noise. Thus, by looking at Figure 3.1 again, one can see the expected behavior that with rising amplitudes T5TEA starts to trigger at some of the injected pulses. This is caused by the noise superimposed to the signal, which sometimes leads to a trigger if it randomly crosses the threshold. Later on, if the amplitudes are clearly larger than the threshold, every single pulse is detected.

For this measurement, the configuration values of T5TEA were already tuned to give a low trigger threshold. The fit of a Gaussian error function then results in a threshold of < 4.0 mV (1 p.e.) with a noise of < 1.0 mV (1/4 p.e.) with an assumed gain of 4 mV/p.e. This meets the needed trigger performance of the camera and shows that the trigger problems of TARGET 5 and TARGET 7 (see Fig. 3.2) could be solved by splitting the trigger and sampling paths.

The other measurement, Figure 3.1 on the right, does it the other way around: a fixed signal (100 mV amplitude at 1 kHz frequency) is injected but the threshold of T5TEA, set by the `Thresh` parameter, is changed and the resulting trigger rate is investigated. Here, the `Thresh` parameter was set to a value corresponding to 100 mV, which was calibrated beforehand. In the plot, three different domains become visible: on the right at 100 mV the trigger rate starts to rise to 1 kHz meaning that afterward all injected pulses cause a trigger signal (since the pulses are injected with this frequency). The trigger rate then stays constant

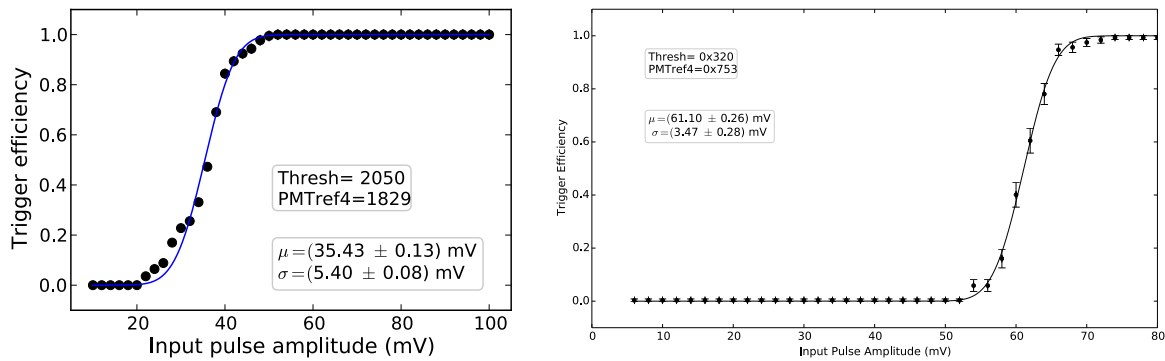


Figure 3.2: Trigger efficiency curves for TARGET 5 (on the left) and Target 7 (on the right). A Gaussian error function was fitted to the data points, and the resulting threshold and noise for the given settings are shown. With analog sampling enabled, the best achievable trigger performance for T5 is a threshold of 20 mV and a noise of 5 mV (Albert et al. 2017), for T7 40 mV and 15 mV, respectively (Stahl 2014). Both shown plots do not resemble the best measurements stated before.

until around 0 mV, where the trigger rate becomes very high, the peak on the left, because the threshold is moved into the baseline causing random triggers (baseline noise).

3.1.1 Tuning of T5TEA performance - parameter scans

Thresh and PMTref4

The trigger threshold and performance can be controlled by mainly two parameters, **Thresh** and **PMTref4**, as it was already described in Section 2.1.1. Thus, a 2D scan of both parameters can be carried out to find the best performance and the general behavior. For this, the two parameters are varied in a certain range, and for every combination, an efficiency curve is taken to determine threshold and noise. The results of such a scan are shown in Figure 3.3 and were gathered with an evaluation board and an ASIC configuration that was adopted from TARGET 5 and 7 (see Appendix B.2 for exact register values, left side of the table).

The smallest achievable threshold with this configuration and an evaluation board is around 3 mV with a corresponding noise of 0.5 mV. This also confirms that the example efficiency curve from Figure 3.1 is already well-tuned. Furthermore, the plot illustrates that the trigger threshold can be set very accurately, even above 100 mV, while retaining noise below 1 mV. Since this was only done in a restricted parameter range (especially in **PMTref4**), a more extensive scan, covering a larger parameter space but restricted to the lowest possible amplitudes, was carried out to test the trigger performance for more parameter combination and to determine the best range to work in. The results of this extensive scan are shown in Figure 3.4. These measurements confirm the results from before, and that the chosen parameter range gives already the best results in lowest achievable threshold and noise. At the outer edges of both parameter ranges, the noise, as well as threshold, start to rise, resulting in worse performance.

All previous measurements were carried out with an evaluation board, but it also needs to be checked if these results can be transferred to the TARGET modules or if the additional

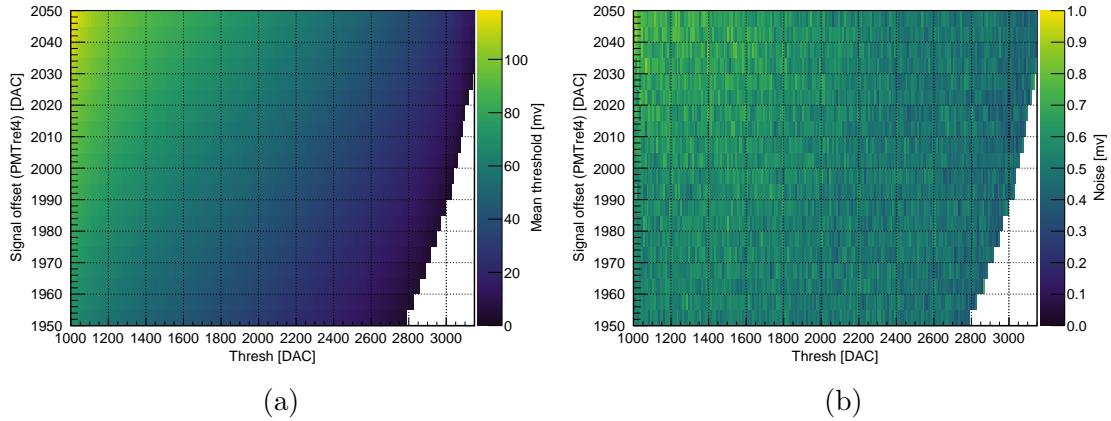


Figure 3.3: Threshold (a) and noise (b) of the T5TEA ASIC as a function of **Thresh** and **PMTref4**. White regions resemble parameter combinations where the trigger does not work, e.g. since it is triggering on the baseline. This scan was carried out with an evaluation board.

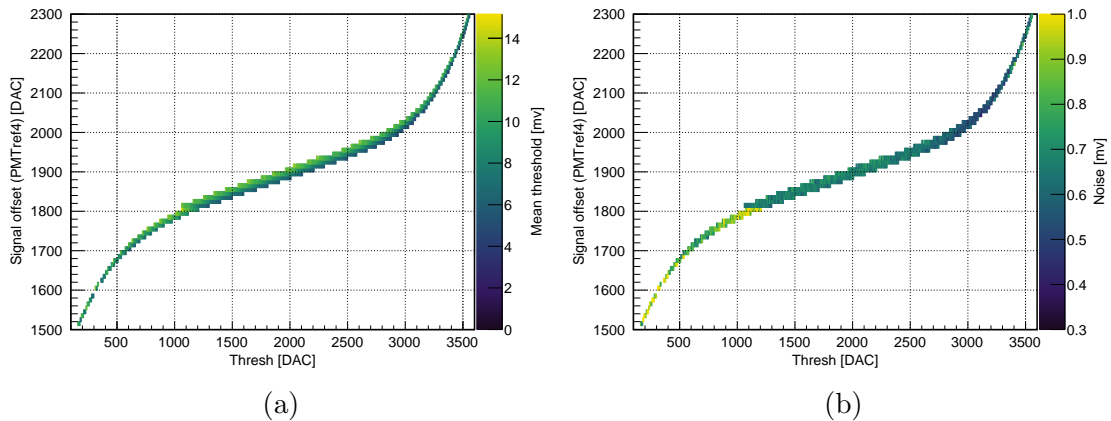


Figure 3.4: Threshold (a) and noise (b) of the T5TEA ASIC as a function of **Thresh** and **PMTref4** over the whole available parameter space. White regions below the results resemble parameter combinations where the trigger does not work, regions above were not measured (and therefore left blank) since only the lowest threshold was of interest in this measurement. This scan was also carried out with an evaluation board. (Data taken from Catalano (2016))

components and modifications change the results. To do this, similar `Thresh - PMTref4` scans were carried out for each of the 64 channels of the module and analyzed if they show the expected behavior. Figure 3.5 presents the minimal achievable trigger threshold with the corresponding noise of one module.

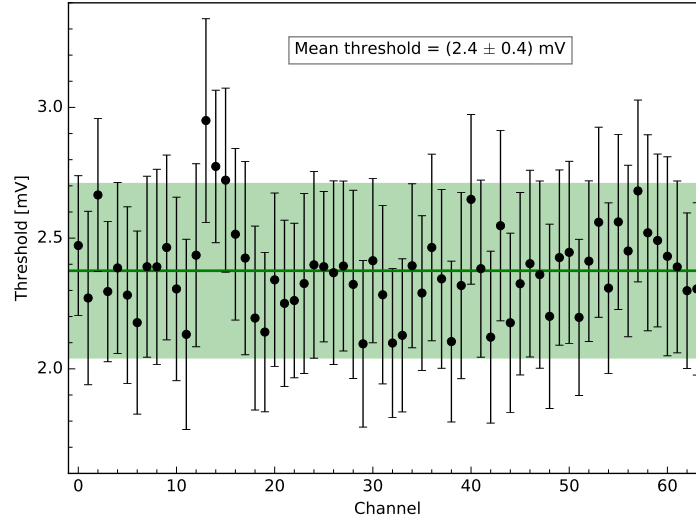


Figure 3.5: Lowest threshold (black dots) and corresponding noise (error bars) for all 64 channels of a TARGET module. The mean minimal threshold and noise are also shown and visualized with the green line (threshold) along with its error band (noise). (Data taken from Reif (2017))

The results clearly show that the trigger behavior of T5TEA on a TARGET module did not change but rather improved with respect to the evaluation board since the minimal mean threshold of the whole module is at 2.4 mV with noise of 0.4 mV. The improvements are likely caused by the parameter tuning (see next Section 3.1.1), whose results were not used in the plots created with the evaluation board. Also, changes in the board design reduced the noise, further reducing trigger threshold and electronic noise.

Further parameters

The configuration of T5TEA for the previous measurements was adopted from experience gained with TARGET 5 and 7 or gathered by trial and error. To get the best possible performance of this trigger ASIC, all configuration parameters should be optimized with regard to efficiency, low power consumption and camera compatibility. There are many different parameters to control T5TEA in every detail, but the remaining most important ones, besides the already mentioned `Vped`, `PMTref4` and `Thresh`, are the following:

- `TTbias` regulates the supply bias of the voltages `Thresh` and `PMTref4` and is settable for each group.
- `TTbias_C` controls the supply bias for `VpedBias`, `TRGBias`, `TRGSumBias` and `TRGGBias`.
- `VpedBias` regulates the supply bias for the internal `Vped` (Offset) generation.

- TRGsumbias controls the supply bias for the trigger summing amplifiers.
- TRGGbias regulates the supply bias for the first preamplifier of the trigger input.
- TRGbias controls the supply bias for the trigger comparators.

The parameters are varied consecutively, each time changing the value in a reasonable range and then performing `Thresh - PMTref4` - scans to get an overview of the minimal achievable threshold and the corresponding trigger noise. A reasonable parameter range denotes values that ensure a smooth operation with all components. Additionally, smaller values for all bias parameters are favored since the overall power consumption rises with higher supply voltages. A very detailed analysis of all configuration parameters can be found in the work of Schaefer (2016). An example result of one optimization process can be seen in Figure 3.6.

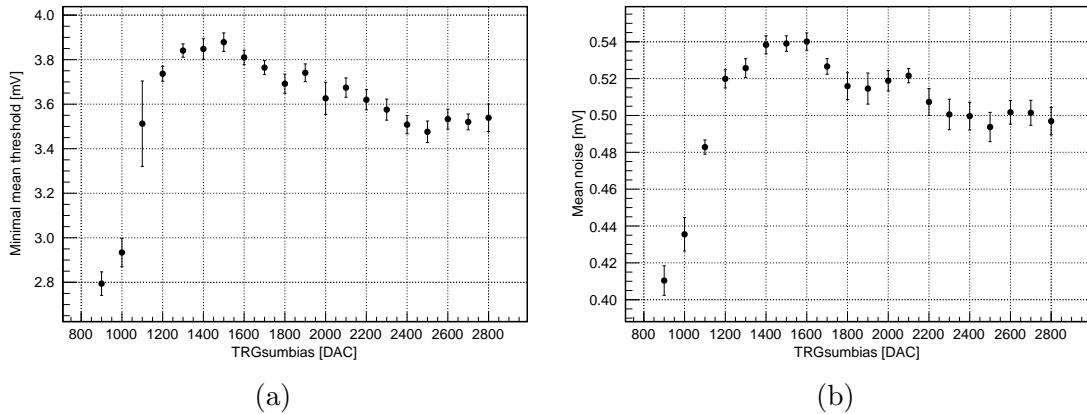


Figure 3.6: Example of a parameter optimization of T5TEA. TRGsumbias was varied from 900 to 2700 DAC, and each time a `Thresh-PMTref4`-scan was carried out to get the minimal mean threshold (a) and mean noise (b) for each TRGsumbias value. (Data taken from Schaefer (2016))

This example shows that the trigger behavior depends to some extent on the TRGsumbias parameter. The best value, also considering a low power consumption and smooth operation, is at 900 DAC counts. By looking at other parameters, such a dependence is not as clear. If this is the case, parameters are kept at the old, default values or changed to reduce the power consumption. The final parameters are listed in Appendix B.2 in the right column of Table B.2.

3.1.2 Output signal of T5TEA

Another trigger group wise configuration parameter is `Wbias`, which has a deviating task compared to the other six configuration parameters since it does not control the trigger itself but its output signal, which is processed by the FPGA. Therefore, it is investigated how this parameter regulates the width of the output signal, in which range it is settable and if the processing with the FPGA affects the signal width. The influence of this parameter is shown in Figure 3.7. There, the width of the signal was measured with an oscilloscope at two different points on the evaluation board: behind the FPGA with a connector (single-ended

output, signal further processed by the FPGA) and in front of the FPGA with a probe (LVDS signal).

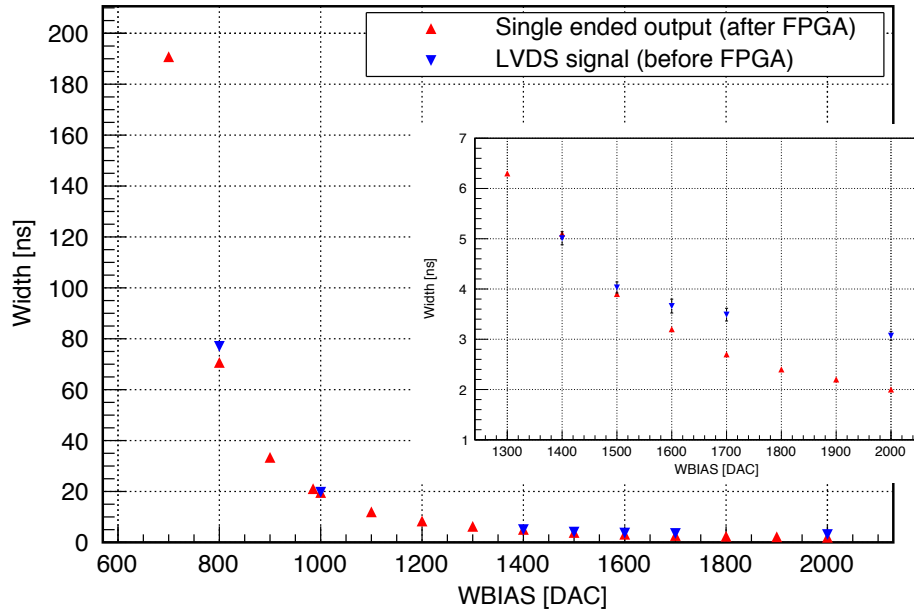


Figure 3.7: Width of the T5TEA trigger output pulse as a function of w_{bias} . The red triangles show the results measured behind the FPGA, the blue ones in front of it. Error bars indicate the stability of the signal width. The smaller plot inside shows a zoomed-in view. This measurement was done with an evaluation board but is transferable to the TARGET modules.

One can see that the signal can be set very precisely in a range from 200 ns to below 4 ns, which therefore meets the requirements. Besides, the signal width is quite stable, which can be seen in the small error bars, only visible in the already zoomed-in view of the figure. At high w_{bias} values, the two measurements start to differ; the signal behind the FPGA is a bit narrower than in front of it, meaning that the FPGA does not negatively affect the signal. The broader signal in front of it is caused by the usage of a probe with the oscilloscope, which complicates the measurement compared to the available connector behind it.

3.1.3 Crosstalk of the trigger path

Another important feature is the occurring crosstalk between the trigger groups and channels since it can profoundly affect the trigger behavior. It can make other groups to issue a trigger signal even if none is present or push the summed signal within one trigger group over the threshold. To investigate the crosstalk, signals are only injected into one channel (or trigger group, respectively), but for all four groups, the trigger signals are counted. To make sure that all groups have the same thresholds, PMT_{ref4} was adjusted in a way that all groups start to trigger on the same signals with an amplitude of 8 mV. Then, signals with an amplitude of 100 mV and a frequency of 1 kHz are injected into one trigger group, and the other groups are examined for registered trigger signals. This is repeated for every trigger group. The results of this investigation are shown in Figure 3.8.

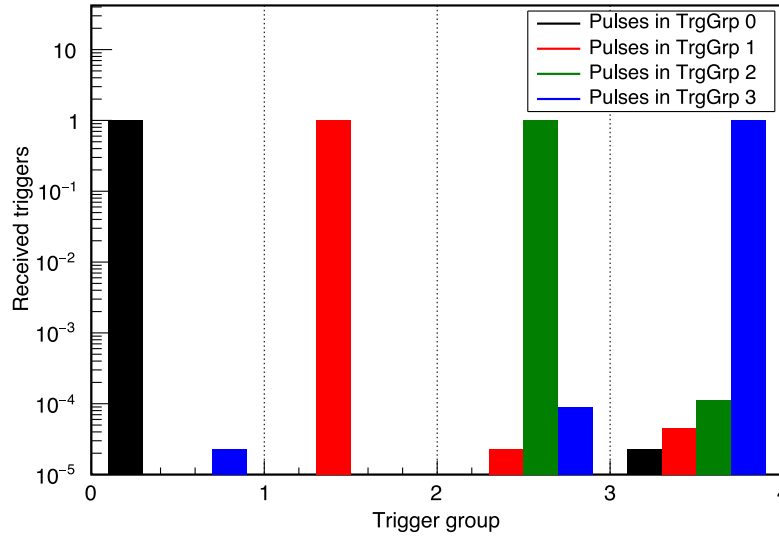


Figure 3.8: Trigger crosstalk measured with an evaluation board. The abscissa shows the trigger group, the colors indicate into which group the signal was injected. Thus, the large bars going up to value one mean that the signal was injected into this trigger group. The smaller bars resemble the crosstalk.

As can be seen, the crosstalk is below 0.01 %, easily meeting the trigger requirement of crosstalk below 10 %. Thus, crosstalk is no problem for the trigger within the evaluation board at all. For the full TARGET module, a very similar behavior is expected.

3.2 TARGET C - digitization

The even more complex ASIC of the current generation is TARGET C, which is used for sampling and digitization. This section will focus on a detailed analysis and characterization of this ASIC as well as testing the low-level calibration methods, which make the transition from pure ADC counts to voltages.

3.2.1 Pedestal calibration and baseline noise

The first step towards a final, calibrated signal is to investigate the pure baseline: a certain VPED value, provided by T5TEA, is set to create the baseline level and is applied to the TARGET C ASIC without any other signals. Events are read out with the external trigger which is driven by a function generator. For all upcoming baseline investigations, a VPED value of 1100 DAC was chosen since this is the baseline level the ASICs will be run at during real measurements. By looking at one example baseline, Figure 3.9 on the left, one can see how the cells (capacitors) in the storage array work differently since they stored different voltage values, converted to ADC counts during the digitization. Also recognizable are some cells which have lower ADC values compared to the average ones. This is a feature of the TARGET ASICs, the last (32nd) cell of each storage block stores lower values. By adding up all baseline events in the taken data set, it becomes even more apparent how big the cell-wise deviation is, shown in Figure 3.9 on the right.

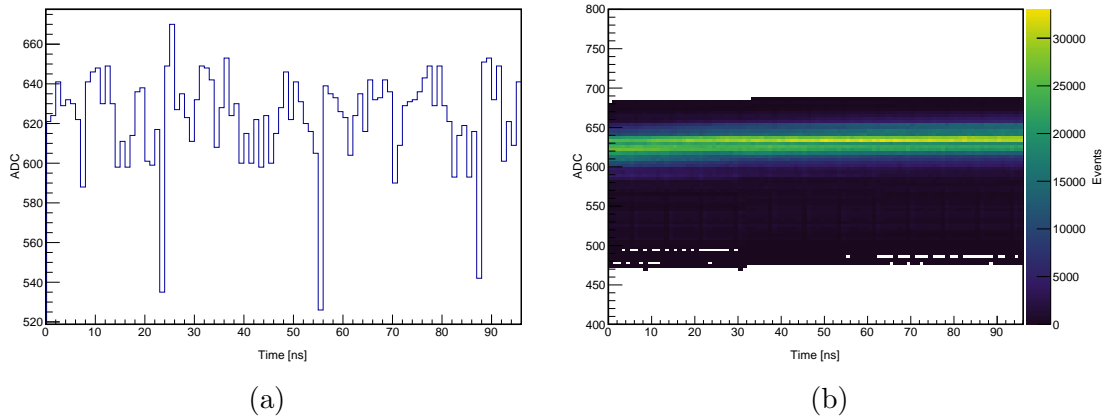


Figure 3.9: Recorded baseline (pedestal) events with a readout window size of 96 samples. One single event (a) and all events in the data set for one channel (b) with an applied VPED value of 1100 DAC. The cell-dependent differences, including the large drops for the 32nd cells of each storage block, are visible.

Another important parameter to characterize the TARGET C ASIC is the so-called baseline noise, which resembles the variation of the measured ADC counts from event to event (in contrast to the cell to cell variations that were shown before). The noise is the spread (standard deviation) of all baseline events. Figure 3.10 shows the resulting noise of one module: the left plot shows how all events from all cells and all channels in one module deviate. The mean baseline level for VPED 1100 DAC lies at 659.5 ADC, with a large spread of 34.24 ADC. The corresponding variations per cell are very low and show a noise of around 4 ADC on average. The single-cell noise overview for each cell of one module (plot on the right) shows that there are deviations from cell to cell and also from storage block to storage block, from channel to channel and even from ASIC to ASIC.

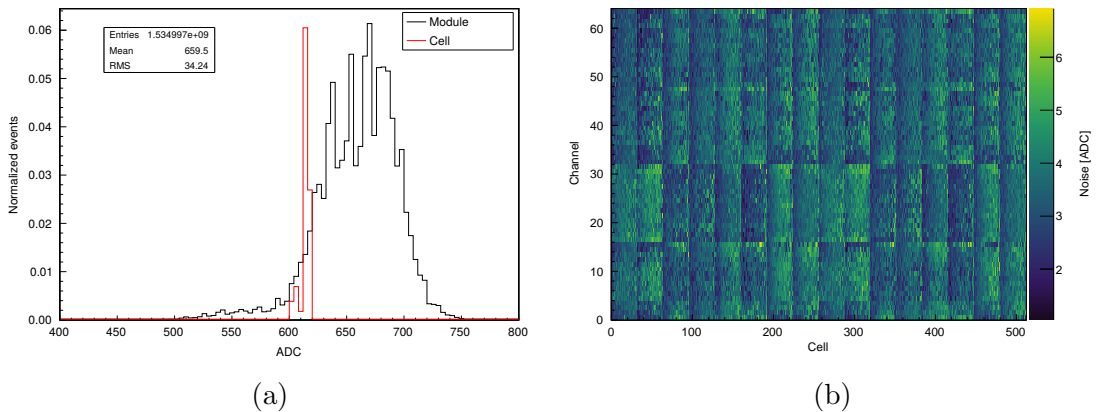


Figure 3.10: Baseline variations and noise for one full module. The measured baseline ADC values (a) are shown for all events and all 64 channels of one TARGET module (black) as well as the single cell noise (red). The statistic box belongs to the whole module noise; the noise of the single shown cell is 3.8 ADC. Additionally, the measured noise for 512 storage cells (abscissa) and each channel (ordinate) of one module is presented (b).

These investigations of the baseline variations clearly show the need to get rid of the cell-dependent differences and of creating a homogeneous behavior on the whole module. The approach to achieve these goals and to calibrate the single cells is explained in the following.

Pedestal calibrations

The first step during low-level calibrations is the pedestal subtraction, which is done to eliminate the differences in the used individual storage capacitors and to push the baseline level to zero. Therefore, a lookup table is created where mean pedestal values for each storage cell and each channel of a TARGET module are stored. Additionally, an influence of the position of the cell in the readout window on the stored voltage was found, which is caused by the finite recharging time of the Wilkinson ramp resulting in smaller voltage values for the second and later blocks. This effect is also likely the main contributor to the large noise in the uncalibrated measurement from above, Fig. 3.10. To consider also this influence, the position of the cell in the readout window is also stored in the lookups. The calibration can be done by subtracting this mean baseline level from the measured data. The resulting baseline noise after calibration is shown in Figure 3.11. The plots resemble the same as the figure above but include the pedestal calibration. Additionally, in Appendix B.3, Figure B.1, an example of a calibrated baseline event is shown.

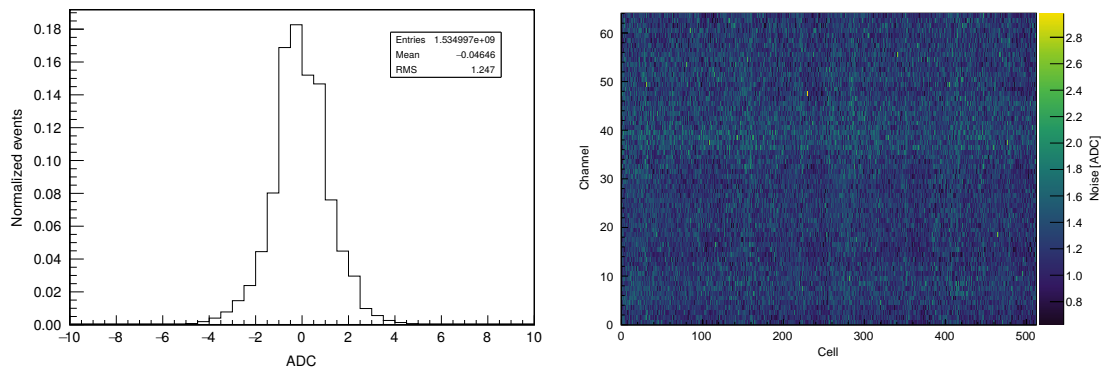


Figure 3.11: Baseline variations and noise for one module after pedestal calibration. Shown are the same plots as above (Fig. 3.10) but with included calibration.

The improvements are clearly visible, the baseline is now centered at around zero how it was desired, and the module wide noise went down to 1.25 ADC. Also, the noise on the module itself is much more homogeneous between the channels and ASICs compared to the uncalibrated investigations.

3.2.2 Signal injection and digitization

Since the pedestal calibration showed to work very well, signals can be injected into the TARGET module, and further investigations and characterizations can be done. To further show the importance of the pedestal calibration, in Figure 3.12 on the left, a small pulse with 12 mV amplitude was injected, and the uncalibrated as well as the calibrated, digitized signals are shown. The uncalibrated measurement was shifted by 600 ADC to match the same level as the calibrated measurement to make both comparable. Without pedestal subtraction, the

small pulse cannot be distinguished from electronic noise, but with included calibration, the pulse becomes clearly visible.

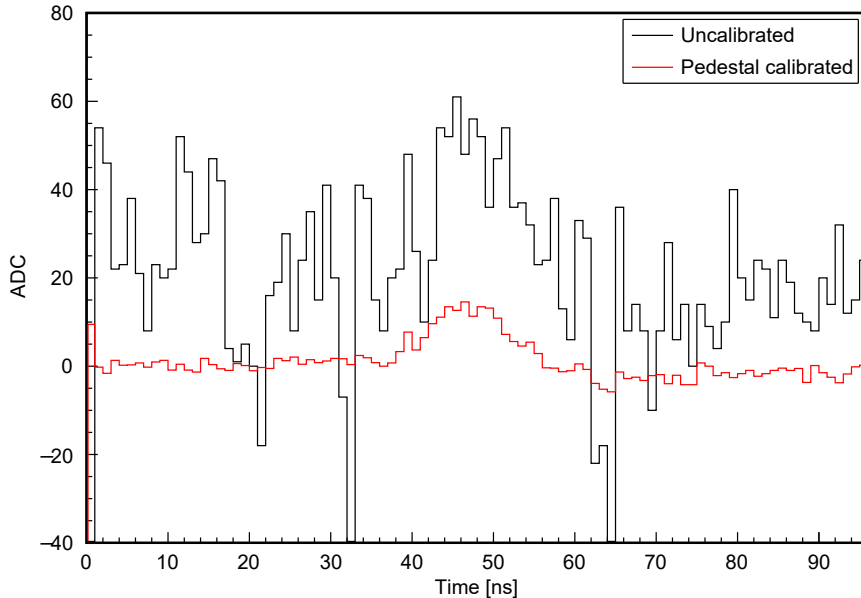


Figure 3.12: Visualization of the need for a pedestal subtraction. The plot shows the comparison of an uncalibrated and a calibrated injected pulse with an amplitude of 12 mV. In the black, uncalibrated waveform, no signal is visible, but after subtracting the pedestal, the signal emerges from the noise.

To visualize how pulses are digitized with a TARGET module in general, signals with varying amplitudes in the range from -312 mV to 2500 mV are injected. Some of those pulses are shown in Figure 3.13. The pulses itself are generated by a function generator and modeled like signals which are expected during real measurements, i.e. signals after the SiPM and preamplifiers. Pulses in the main amplitude range (roughly -312 mV to 1800 mV) show an expected behavior but some undershoot is visible directly after the signal, which depends on the amplitude of the input pulse. If the amplitude is raised above this threshold, the signal starts to saturate, which is visible by a cut-off peak and a tail-like extension of the signal. The width of this extension also depends on the signal amplitude. This feature can, for example, be used for more advanced reconstructions methods in the saturated regime.

3.2.3 Time base tuning and sampling frequency

It was explained beforehand that the measured charges are stored in small capacitors (cells), each corresponding to roughly 1 ns. However, this time interval per cell is not a fixed hardware implementation but settable. It can be either set manually or controlled automatically by a feedback loop, which is the usual mode of operation. The feedback loop itself can be controlled via the two parameters `SSToutFB_Delay` and `VtrimT`, the first one for a rough setting, the latter one for fine-tuning. These two parameters define a control time interval for the feedback loop, which is used internally by the ASIC to set the timing of the switches of each sampling capacitor. Thus, the full control interval must be tuned to be 64 ns corresponding to the 64

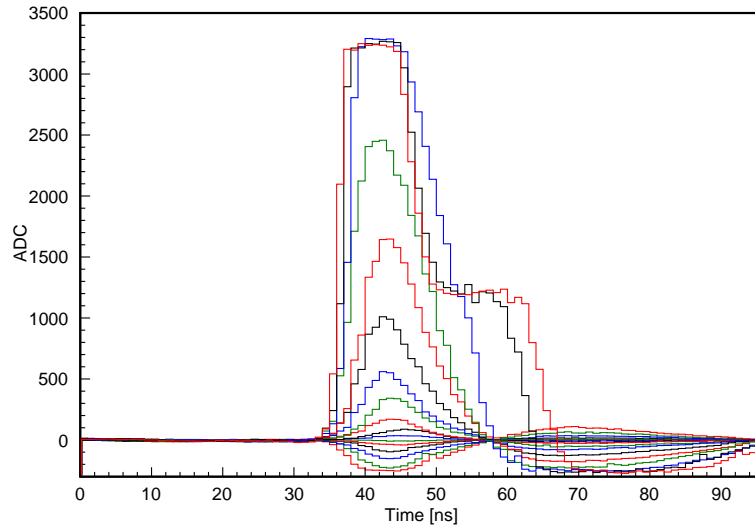


Figure 3.13: Different pedestal calibrated pulses with varying amplitudes (-312 mV to 2500 mV). Each color resembles a certain amplitude. Also visible are distinct characteristics of the TARGET module like the undershoot after the signal or the behavior in the saturated regime (amplitudes larger 1800 mV).

cells in the sampling array.

The time base settings can be best tested and optimized by looking at sine wave signals which are injected into the TARGET module since deviations from such a strongly varying signal can be seen best. Figure 3.14 shows two 128 ns long (corresponding to two full sampling arrays of 64 ns each) measured and pedestal calibrated sinusoid signals at a frequency of 50 MHz and with an amplitude of 200 mVpp. Thereby, the left signal was measured with a well-tuned time base, the right signal with mistuned settings.

For the tuning of the timebase settings, one can look at the transition from the end of the sampling array to its beginning. If the time base is well-tuned, there should be a smooth transition since all cells are filled within the 64 ns interval. This can be determined by fitting two sinusoids to the measured data of two full sampling arrays (see also Fig. 3.14). By using the fit results of the sine waves, one can calculate the phase difference between both functions (corresponding to the transition from the end to the beginning of the sampling arrays).

The parameters `SSToutFB_Delay` and `VtrimT` are then tuned successively in that order since the second one controls the fine-tuning. The first parameter is varied from 53 DAC to 65 DAC in steps of 1 DAC, the latter one from 1040 DAC to 1430 DAC in steps of 10 DAC. The intervals were chosen since the best settings are expected to be found in the middle of these intervals. The best parameter setting is found if the phase difference of both sine waves is minimized. Such a minimization process of both parameters for one ASIC is shown in Figure 3.15. It is enough to do this for one channel since the parameters are only settable for the full ASIC (16 channels). For the ASIC used in this measurement, the best values were found to be 58 DAC for `SSToutFB_Delay` and 1210 DAC for `VtrimT`.

As a verification of the time base tuning, the sampling frequency can be determined. This is done in the same way as the tuning above: sine wave signals are injected into the TARGET module, and sinusoids are fitted to the data. With the known frequency of the signal and

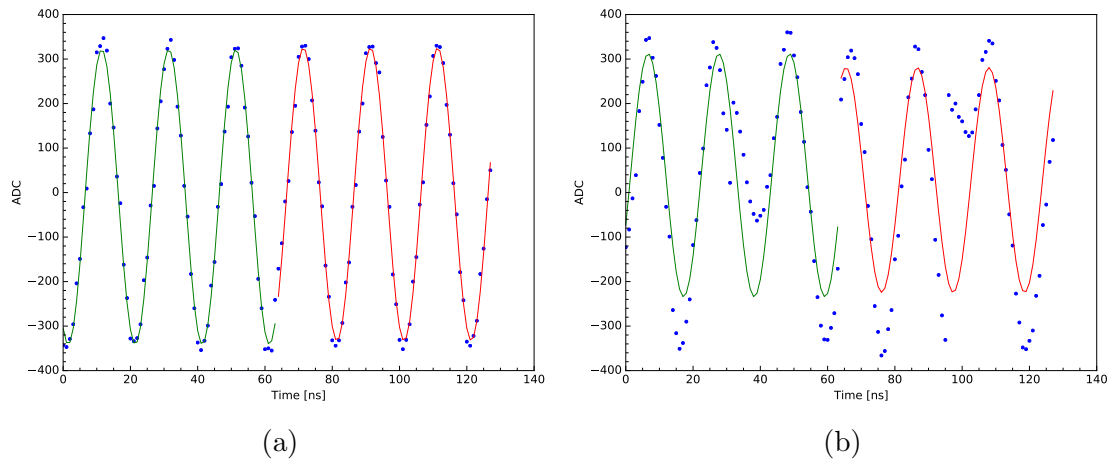


Figure 3.14: Recorded sine waves within a four block (128 cell) readout window, with a frequency of 50 MHz and an amplitude of 200 mVpp. An optimized sine wave (SSToutFB_Delay: 58 DAC) (a) and a sine wave with mistuned settings (SSToutFB_Delay: 66 DAC) (b) shown together with two best-fit sinusoids which visualize the smallest phase difference between the two sampling arrays.

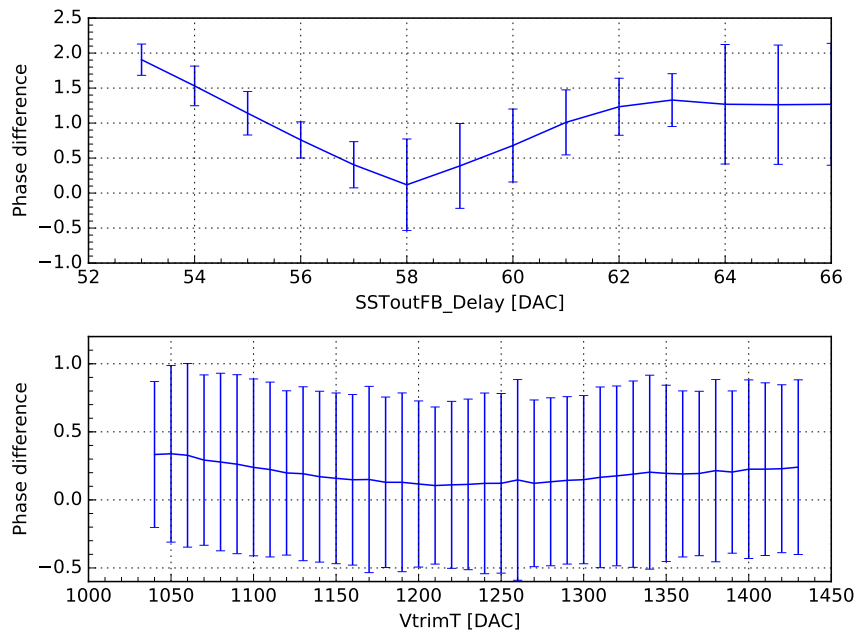


Figure 3.15: A scan through both timebase parameters (SSToutFB_Delay and VtrimT) to find the best settings for the lowest phase difference between the two sampling arrays. About 4500 events were taken per step; the error bars show the standard deviation of each mean value of the phase difference. The best settings for this ASIC were found to be at 58 DAC for SSToutFB_Delay and at 1210 DAC for VtrimT.

the fitted frequency of the used function, the sampling rate can be calculated. The results of the measured sampling frequencies of one ASIC are shown in Figure 3.16. This investigation was also done for one single channel since the results are the same for all channels. As can be seen, the sampling frequency is close to the expected value of 1 GSa/s.

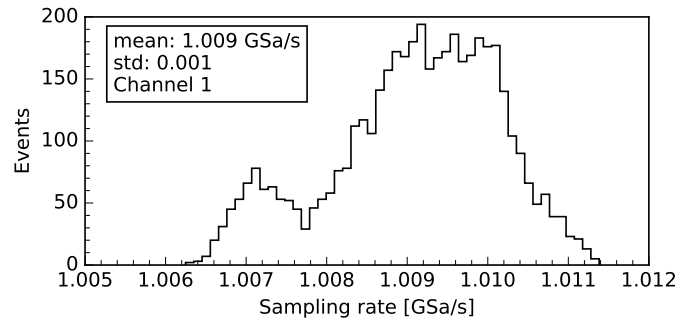


Figure 3.16: Measurement of the sampling frequency of one channel of one ASIC. About 4500 events were used to determine the frequency after optimizing the timebase parameters.

3.2.4 Crosstalk of the sampling path

For TARGET C, crosstalk between the digitization channels is also an essential characteristic and can have significant effects on the reconstructed images. The investigation of the crosstalk is done similarly as it was already carried out for the trigger ASIC T5TEA: a signal is injected into one channel, and all other channels are read out and tested for crosstalk signals. This was done in two different ways, during the first tests on the evaluation board with an applied sinusoid and during later tests on whole modules with SiPM like signals. These two measurements are shown in the following.

Crosstalk with sinusoids

For measurements with an applied sinusoid, the evaluation board with one attached TARGET C ASIC was used. Thus, the crosstalk behavior of only one ASIC with 16 channels was testable but not of the electronic circuits on the final boards of the module. Furthermore, channel 0 was not working at this point of the measurements, so it was left out during the investigations. Varying sine waves from the function generator were injected into channel one, and all channels were readout. Amplitudes between 500 mVpp and 1800 mVpp, as well as frequencies between 1 MHz and 50 MHz, were used to test for influences of these sinusoid characteristics. The results are shown in Figure 3.17, where the mean crosstalk of all channels without a signal is shown as data points.

The mean crosstalk of all channels is in the range of one percent, meeting the requirements. One can see that there is a slight dependence on the frequency since, at the highest setting, a rise in the crosstalk was seen. For different amplitudes, it behaves the other way around because the relative crosstalk drops for higher amplitudes. As this measurement just gives a small insight into the crosstalk behavior and was only carried out to get an overview, more detailed measurements were done with the full module.

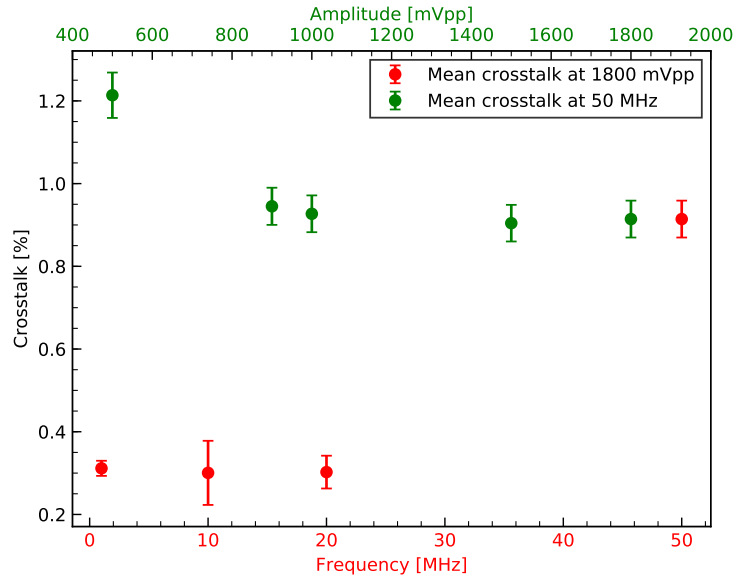


Figure 3.17: Measurement of the crosstalk on one ASIC with sine waves. The signal was injected into one channel, and all others were readout and tested for crosstalk. The data points represent the mean crosstalk of all channels without an injected signal; the error bars show the corresponding standard deviation between the channels.

Crosstalk with pulses

In contrast to the section before, full TARGET modules are now used for further crosstalk investigations. This also gives insight into the crosstalk between different ASICs, which can be caused by the electronic circuits. For more realistic measurements, SiPM like pulses are used, which were already shown in Figure 3.13 before. As no significant impact of the amplitude on the crosstalk was found, only pulses with an amplitude of 500 mV were used. This time, the signal was injected into every channel consecutively, and the others were readout. Since no considerable crosstalk between the primary and the auxiliary board is expected, only the 32 channels on each board are compared. The final data was pedestal calibrated, and the crosstalk levels were calculated with different methods: comparison of the maximum of the signal, of the peak to peak amplitude (since undershoots appear) or of the full waveform integrals. Examples of the injected pulse with some larger crosstalk are shown in Figure 3.18, the results for both boards and all channels, determined with the maximum method, in Figure 3.19. The results of the other methods are left out since the integral only shows minimal crosstalk because it is dominated by the baseline and the peak to peak method because it gives very similar results as the maximum.

These measurements confirm the former results deduced with sine waves and the evaluation board. The crosstalk on the full TARGET module is in the order of one percent or lower for every channel, which meets the requirements again. By taking a closer look at the channels with a large, measured crosstalk, one can see that they are not directly next neighbors and also appear between the two ASICs. This means that the crosstalk is mostly caused by the cables, plugs and electronic circuits on the boards and not inside the ASICs itself.

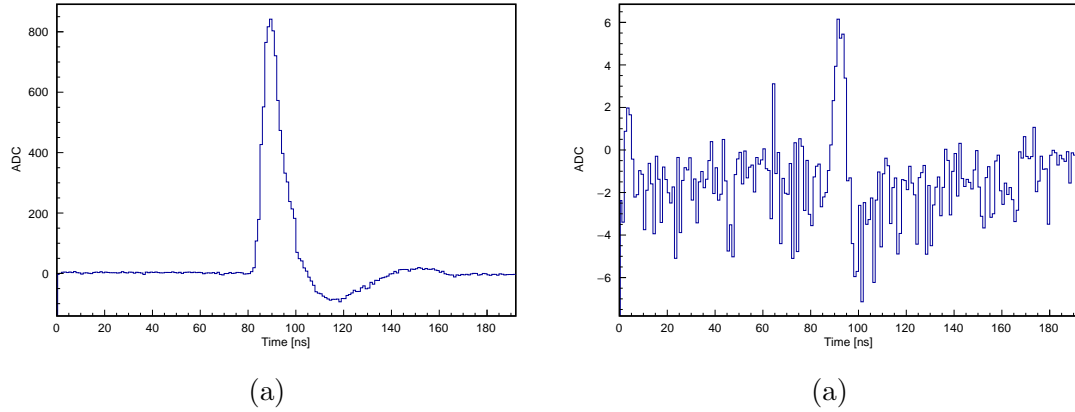


Figure 3.18: Example of the measured crosstalk. The plots show the injected signal (a) and the corresponding crosstalk in another channel (b).

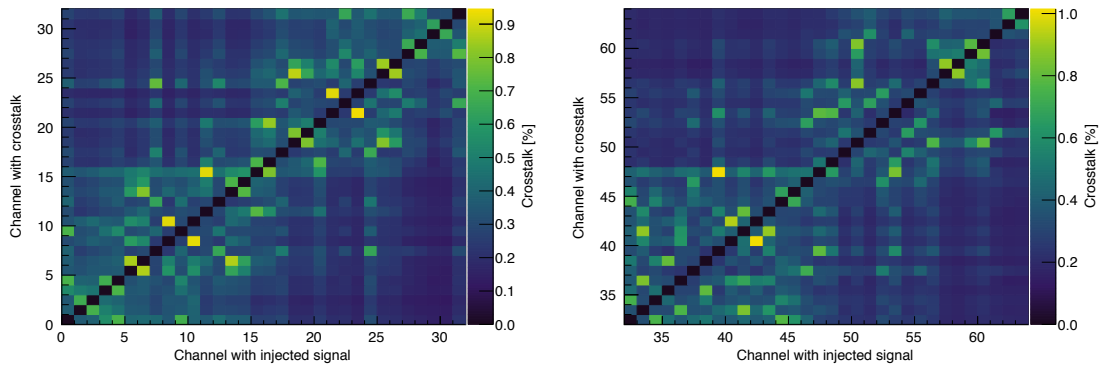


Figure 3.19: Measurement of the crosstalk with SiPM like pulses. The signal had an amplitude of 500 mV and was injected into one channel while all others were readout and investigated for present crosstalk signals. For the results, only two ASICs (32 channels) are combined since they are on the same board on the module (primary and auxiliary board) and only negligible crosstalk is expected between these two. The black spots in the diagonal are the signal channels where no crosstalk is measured. (see also Leach et al. (2020))

3.2.5 DC transfer functions

After the first calibration step, the cell wise correction of pedestal offsets, the next is to eliminate non-linear responses to applied signals during storage and digitization. Furthermore, this calibration step is also needed to translate the digitized samples from ADC counts to voltages in mV. The general way to do this calibration is to apply voltages with a known amplitude to the TARGET ASIC and to measure the corresponding digitized value in ADC counts. If this is done for various input voltages, a lookup table for the translation can be created as it is also done for the pedestal calibration.

Up to now, two different ways to create these lookup tables, called transfer functions, are used, which are distinguished by the type of the injected signal. Either direct current (DC) signals or alternating current (AC) signals can be used. The DC method is outlined in this section, 3.2.5, the AC method in great detail in the next section, 3.2.6, since it was newly developed for TARGET C.

The DC method is mainly used with TARGET 5 and in the prototype camera CHEC-M. Here, a constant voltage with a known value is applied to the TARGET ASIC and the corresponding ADC value after digitization is readout. The DC voltage is varied over the full range that is accessible. For TARGET 5, a well-known voltage can be directly created on the module itself since external DACs are mounted onto the boards, which are already fully characterized by the manufacturer.

However, this is not as easily possible with the current TARGET generation, TARGET C with T5TEA, since the commercial DACs are not part of the module any more but the trigger ASIC is used to create these voltages itself (see the VPED variable). Since the custom-built ASIC is not originally characterized, the exact applied voltage is not known a priori but only the set DAC values. Thus, to fully use the DC method, T5TEA needs to be also characterized in this regard, which was not planned initially. Nevertheless, the DC transfer functions are also measured, but in the end, only the nonlinearities can be investigated and not the transfer from ADC counts to voltage values.

The results of such a DC transfer function are shown in Figure 3.20. The voltage from T5TEA was varied from 500 DAC to 4000 DAC in steps of 100 DAC and covered the full dynamic range of TARGET C. For each voltage step, multiple events are recorded to get good statistics and to read out a signal in all cells. The response of one single cell (red line), as well as the transfer functions and noise of all 4096 storage cells, are shown. The noise is the spread (standard deviation) of each measurement step, characterizing how stable the signal in each storage cell is.

By looking at the transfer function of the single cell, the linear, dynamic range can be determined to be roughly 1000 DAC to 3500 DAC, the point where the saturation is reached. With a closer look, small nonlinearities can be seen that are the reason for the creation of such transfer functions. Also, differences from cell to cell are visible since not all transfer functions behave in the same way. The stability of each cell can be determined by looking at the other plot, which shows the noise. Over the whole VPED range, the noise stays below 5 ADC and thus is comparable to the baseline investigations in Section 3.2.1. Only some cells showed significant noise at 3500 DAC, which is connected to measurement noise and not a real feature of the module.

Currently, also efforts to use this DC method for the creation of full transfer functions of TARGET C are undertaken. Therefore, the created voltage of T5TEA needs to be further characterized so that the exact set voltage is known.

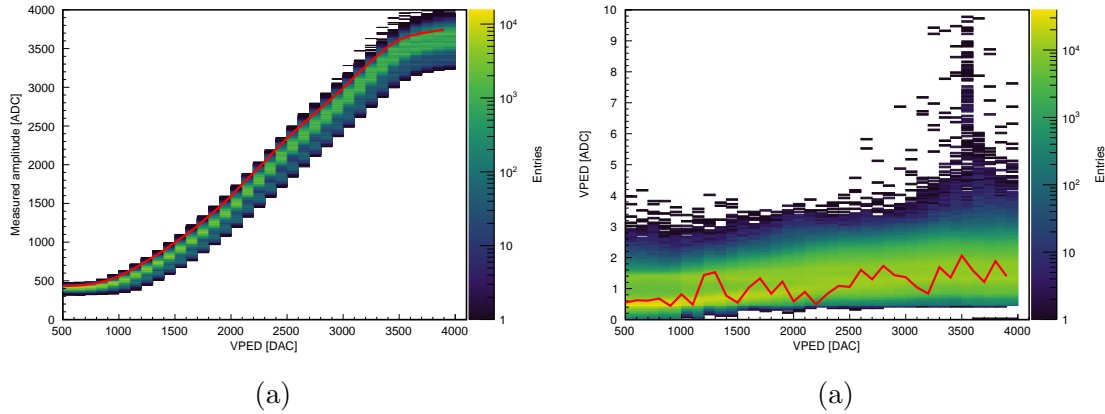


Figure 3.20: DC transfer function (a) as well as the corresponding noise (b) for a whole module as well as a single transfer function for comparison shown in red.

3.2.6 AC transfer functions

As it was already mentioned, the current way to create transfer functions for TARGET C is the AC method. This approach was developed out of two reasons:

- The voltage created by T5TEA is not calibrated, thus, the exact set voltage value is not known and cannot be used for the transfer function creation.
- It was observed that not only the amplitude of the signal affects the digitized values but also its frequency. By using AC signals with an SiPM like shape, which will also be seen during real observations, these effects are already included in the AC transfer function.

The SiPM like signals are modeled after real measurements with SiPMs and are created by a function generator. The digitized ADC counts, as well as the known amplitude of the signals, can be used to create transfer functions as it was done for the DC method. Additionally, all upcoming measurements regarding the transfer functions are done in a temperature stable environment (i.e. a temperature chamber) since an influence of the temperature on the transfer function is expected.

Developed method

The general idea of the AC transfer function is to use SiPM like pulses as input instead of a constant voltage. The use of such pulses is also the largest difference compared to the DC transfer functions and makes the calculation more complex since only the peak value of the pulse and the corresponding cell which stores this value can be used. So, firstly a suitable algorithm is needed to extract the peak ADC values while not needing to much computing time. Basically, three different approaches were tested, but only one showed good enough performance:

- Take a fixed cell in the readout window where the pulse is expected.
- Take the maximum ADC value in the readout window.

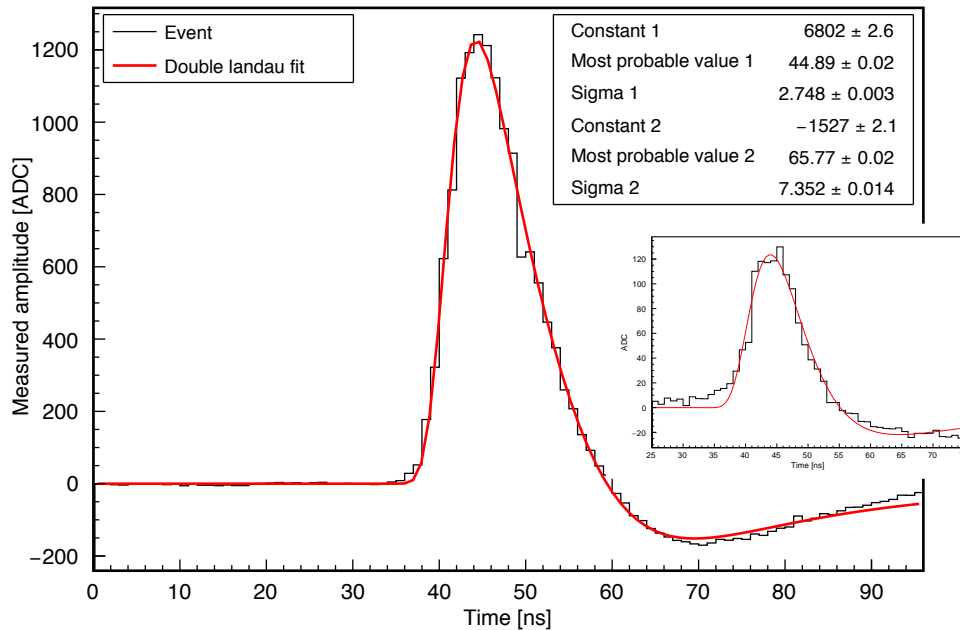


Figure 3.21: A fit of two landau distributions to a SiPM like pulse with an amplitude of 600 mV. The smaller image, showing a pulse with an amplitude of 80 mV, illustrates the advantage of the fit in contrast to taking the maximum bin since the latter one would use the wrong cell.

- Fit a function, which matches the general pulse shape, to determine the location of the pulse in the readout window and take the cell of the function maximum to determine the ADC value.

The advantages and disadvantages of the three methods are visible in Figures 3.21 and 3.22. For the fitted function, a combination of two Landau distributions was used since the pulse shape is asymmetric, which excludes a Gaussian fit, and has an undershoot after the pulse itself.

The method with the best results at the end was the fit of the two Landau distributions (see the red function in Fig. 3.21) since it accounts for various occurring problems. One difficulty is the different behavior of the cells because not all respond to injected amplitudes in the same manner. The smaller illustration in Figure 3.21 shows that some cells tend to have a larger response to the pulse than the cell in the peak position. Thus, by just taking the maximum ADC value in the readout window, one would use the wrong cell that is not in the maximum of the injected pulse. Furthermore, the internal trigger of the TARGET module is only as precise as 1 ns, which causes that the injected pulse can be found in different cells since they also cover a time interval of 1 ns. In addition, the injected pulse can be even further off by a few nanoseconds but the reason for this shift is still unclear. Both effects can be seen in Figure 3.22, where the peak position was determined with the Landau function fit. This variation of the pulse position excludes especially the fixed readout position.

Therefore, it was decided to use the double Landau fit method for the calculation of the AC transfer function. The downside of this approach is the high computation time

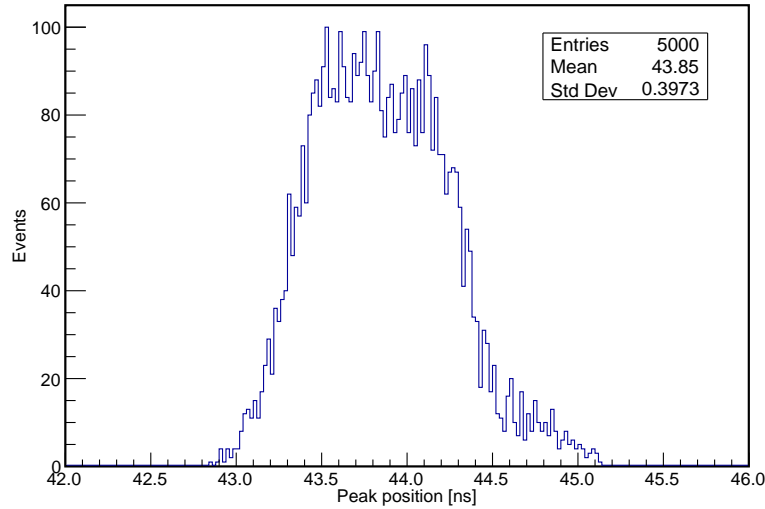


Figure 3.22: Distribution of the determined peak positions in the readout window for one channel. The overall spread of roughly 1 ns is caused by the trigger uncertainty of the ASIC. Some outliers are also recognizable on the right of the distribution.

for the fitting process compared to the other methods, fitting every event of every channel takes even longer than 24 h. Thus, a slightly different approach was developed to reduce the needed computation time while keeping the benefits: only one channel per event was fitted to account for the pulse position movements (jitter), and the position in every other channel was calculated by considering signal transit time differences. The differences in the transit times between the 64 channels of one module can be seen in Figure 3.23 by looking along the abscissa. Also, the pulse position jitter is visible in this figure if looked along the ordinate, which shows 500 consecutive events, thus resembling the time evolution.

The mean peak position per channel, p_i , needs to be determined before the actual AC transfer function is calculated. This can be done by fitting a few hundred events to get the average position (see e.g. Fig. 3.22 again). It is also needed to repeat this for every used signal amplitude since the shape and position slightly changes with rising amplitude (see e.g. Fig. 3.13). Afterward, the event-wise peak position of every channel can be calculated by the following equation,

$$t_{ij} = t_{0j} + (p_i - p_0) , \quad (3.3)$$

where i is the considered channel, j the event number, p_i the beforehand determined mean pulse position per channel and t_{ij} the resulting peak position. For this case, channel 0 was chosen for the double Landau fit and as reference for the other channels. Thus, for every event and every channel, the peak position and the corresponding storage cell can be determined and the ADC value to each input amplitude can be measured.

This is the general approach that is used to determine the AC transfer function, however, some problems still remain: small input pulses as well as high input pulses where the TARGET module reaches saturation. In the first realm, electronic noise starts to distort the pulse shape and makes the fitting process very unstable. In the latter realm, the pulse shape does not follow the double Landau distribution (see e.g. the previous Figure 3.13), which also causes

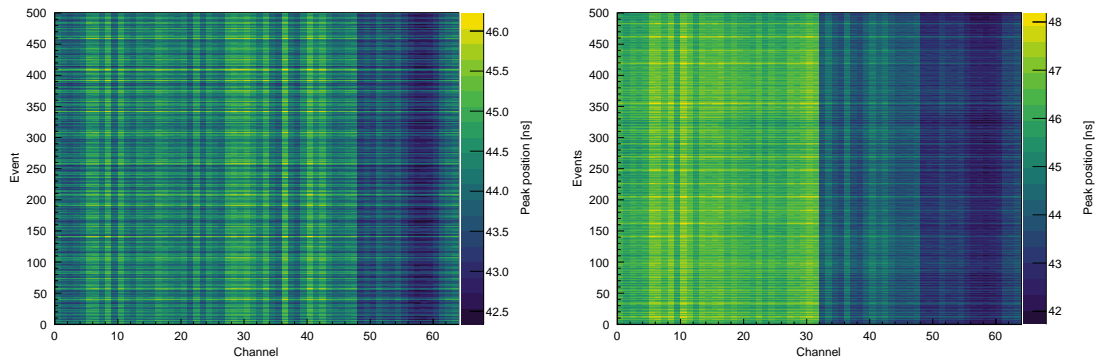


Figure 3.23: Peak position of the signal in the readout window for two modules. Every channel of one module is shown as well as 500 events to visualize the time evolution of the pulse position. Differences between the modules, the channels and also between the events are visible, illustrating the need of an event wise fit.

the fit to fail. Thus, the determination of the mean pulse position in the readout window, as well as the single event fitting, do not work anymore. The current way to deal with these problems is quite simple: look at the nearest amplitude where the fitting process, still works and use it to determine the pulse position for the other amplitudes. The voltage range that is used for the pulse fit is from 40 mV to 1800 mV. On the one hand, this is justified since the peak position in the readout window does not change too much between different amplitudes. On the other hand, wrongly chosen peak positions at small amplitudes do not affect the final transfer functions as much since the main noise contributor at these amplitudes is the electronic noise. Furthermore, in the saturation regime, the pulse itself develops a wide and rather flat plateau at the peak position, which also decreases the problem of wrongly readout ADC values if a wrong position is chosen.

In the regime of saturated pulses, a more dedicated function, which also considers the plateau-like shape of the pulse, could be used for a better peak detection. However, this was not investigated as part of this work. But a similar approach was tested in the work of Heller (2016) or Kraus (2018) for the determination of the charge resolution. Another problem is the so-called cell overflow, which causes too low ADC values and can occur in the saturated regime. This overflow is now already corrected during pedestal calibration and does not cause further problems for the AC transfer function creation. It is explained in more detail in the appendix, Section B.3.2.

The transfer functions should not only work for the positive amplitudes but also cover the negative part correctly. Therefore, two different approaches were developed and tested: the use of negative input pulses or the use of the negative undershoot. The first method is rather straight forward since the same approach as for normal input pulses can be used. However, it takes a longer time to record and analyze the additional negative pulses. The second method is more problematic since the negative amplitude of the undershoot is not directly known and needs to be measured. Nevertheless, the advantage of this method is the reduction of needed data and computation time.

The amplitude of the undershoot can be measured with the help of an oscilloscope (see Appendix B.1 for the exact model). A signal with a known amplitude is injected into the module and sampled after shaping and amplification but in front of the TARGET ASIC. In

this way, the signal is sampled like it is done by the ASIC itself. The results for some injected pulses with the corresponding undershoot amplitude are listed in Table 3.1.

Input amplitude	Undershoot amplitude
48 mV	-10 mV
112 mV	-23 mV
200 mV	-41 mV
280 mV	-58 mV
600 mV	-124 mV
1048 mV	-217 mV
1496 mV	-310 mV
1752 mV	-363 mV

Table 3.1: Measured amplitude of the undershoot for specific input signal amplitudes.

The method is then implemented like the following:

- The position of the minimum of the undershoot in the readout window is determined in the same way as the maximum of the signal itself.
- During the creation of the AC transfer function, the undershoot is used at the mentioned amplitudes in Table 3.1 since only for these, the real amplitude of the undershoot is known.
- If one of these amplitudes is reached, the ADC value of the undershoot is used at the position of the readout window that was determined before. This time no event-wise fit results are used since the undershoot is not as steep as the signal pulse, which causes smaller errors. Furthermore, it even showed that using the fit for the negative part introduced further noise.

Since the method of using the negative undershoot is thought to introduce more uncertainties, it is directly compared to ADC values that were determined with injected negative pulses. The result of this comparison is shown in Figure 3.24.

Both plots show that the method with negative input pulses returns slightly lower results for the measured ADC values of the AC transfer function. Close to zero and at large, negative amplitudes, where saturation is reached, the deviations of both methods become smaller. At an input amplitude of 0 mV, no measured amplitude is expected, however, this is not observed. But the method with negative pulses is in better agreement with 0 mV, suggesting that this method is indeed more accurate and that the undershoot introduces a bias. However, due to the smaller needed storage and computing time, the undershoot method was used for most upcoming measurements. If the most accurate AC TF is needed, the usage of negative amplitudes is recommended.

In addition to the already mentioned findings, some smaller problems regarding the position of 0 ADC were discovered during the analysis of the acquired transfer functions. Since they only show a small impact on the resulting AC transfer functions, their explanation and correction is postponed to the appendix, Section B.3.2.

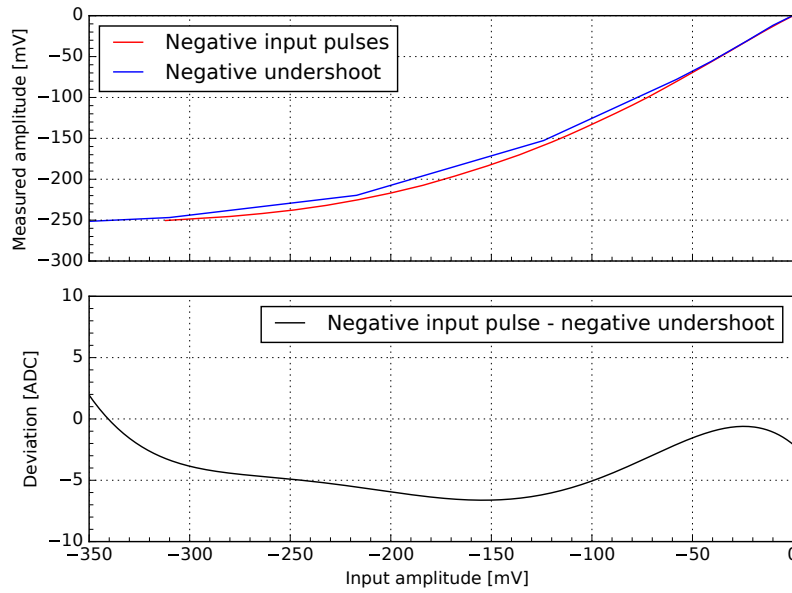


Figure 3.24: Comparison of both methods to determine the negative part of the AC transfer functions. The red curve shows the results with injected negative pulses, the blue curve with the negative undershoot. The lower part of the plot shows the absolute difference of both transfer functions. The parts between the different data points were determined by interpolation with a high order polynomial.

Resulting transfer functions

The resulting transfer functions, determined with the explained methods, are presented in Figure 3.25 with the corresponding noise.

They show a similar behavior as the DC transfer functions before, which is also expected since the general approach is still the same. At high and low input amplitudes the pulse and thus the transfer function saturates, giving the same ADC values for differing input amplitudes. Furthermore, the results for the individual cells deviate to some extent, which was already observed before. With a closer look at the single-cell transfer functions, again, small nonlinearities are visible that will disappear in the final data after calibration with the transfer functions. By looking at the noise in this figure, a structure with two peaks (at roughly 600 mV and 1400 mV) is visible as well as the generally larger noise compared to the DC transfer functions. As the single-cell transfer function in the plot already shows, the two peak structure does not appear in every single cell. As it is shown in the appendix (Section B.6), it actually seems to be caused by the cells of the sampling array. Unfortunately, the final origin of this structure is currently still unknown. The generally higher noise of the AC transfer function is caused by the developed method itself: the maximum of the injected SiPM like signal is not necessarily contained in only one cell but spread over two, caused by the trigger uncertainty. This creates small fluctuations in the measured ADC values from event to event. Furthermore, even after the careful development of this method, it is not guaranteed that for every event, the right cell which corresponds to the signal maximum is chosen and readout. Because of the narrow peak of the signal, even a miss by one cell might cause a large deviation from the real value, which increases the noise.

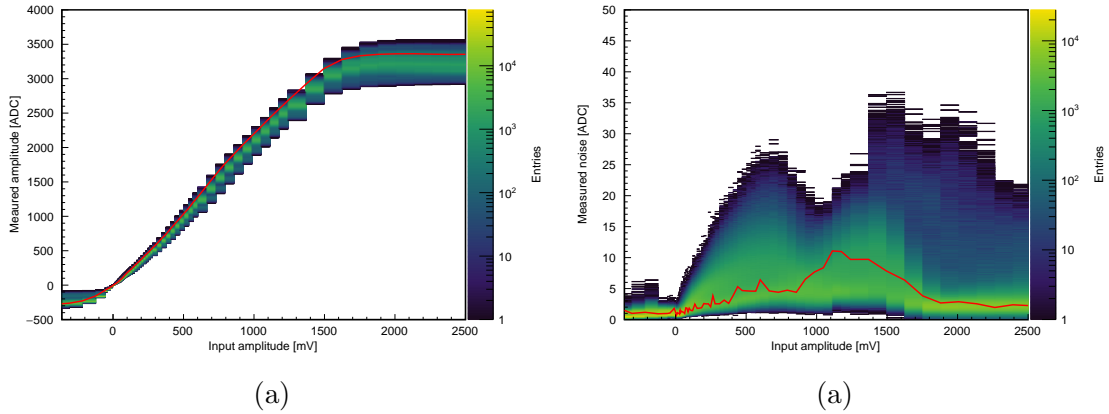


Figure 3.25: AC transfer function (a) as well as the corresponding noise (b) for a whole module as well as a single cell transfer function for comparison in red. For this module, the approach with the negative undershoot was used. (see also Leach et al. (2020))

In addition to comparing this method to the DC transfer functions, which were discussed before (see Fig. 3.20), one can have a look at the results of former TARGET generations (see Fig. 3.26). The overall DC behavior is very similar to the one of the current TARGET generation and also to the new AC approach. A full comparison of the resulting transfer functions is shown in Table 3.2, but not all parameters were calculated for all former ASICs.

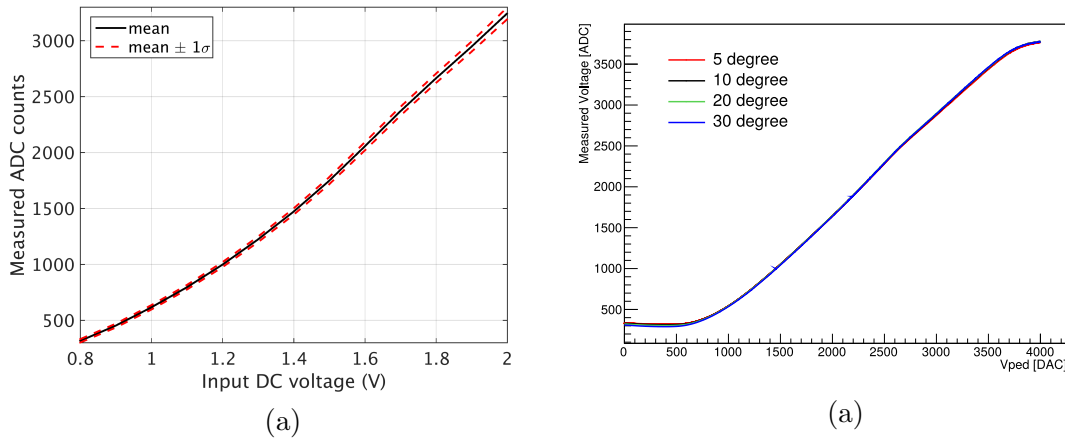


Figure 3.26: DC transfer functions as they were determined for older TARGET generations, TARGET 5 (a, Albert et al. (2017)) and TARGET 7 (b, Kraus (2018)). The unit of the injected signal of TARGET 7 is given in DAC counts, not mV, making the plots not directly comparable.

The calibration of the camera data and even the low-level calibration of the data is not fully fixed and understood, so there is, of course, still room for improvements. Some remaining problems and ideas are:

- Improve the zero crossing of the AC transfer functions since it turned out that with the current approach, not all transfer functions cross zero ADC at the point where no

	TARGET C	TARGET 7	TARGET 5
Quasi linear range	2923 ADC (11.5 bit) 1.5 mV	- 1.5 mV	2928 ADC (11.5 bit) 1.2 mV
Effective dynamic range	10.2 bit	-	11 bit
Integral nonlinearity	51 ADC	-	212 ADC
Differential nonlinearity	0.8	-	-

Table 3.2: Characteristic values regarding the transfer functions for TARGET 5, 7 and C. For T5 and T7 the DC approach was used, for TARGET C the AC approach.

signal is applied.

- Test the temperature dependence of the AC transfer function and try to develop a method to account for potential problems. The first results of such an investigation can already be found in the work of Schaefer (2019).
- Implement a DC transfer function method for the TARGET C modules with T5TEA.

Calibrated signals

To close the section of the AC transfer functions, full calibrated, pedestal correction and transfer function application, measurements are shown. An example pulse with an amplitude of 600 mV is presented in Figure 3.27.

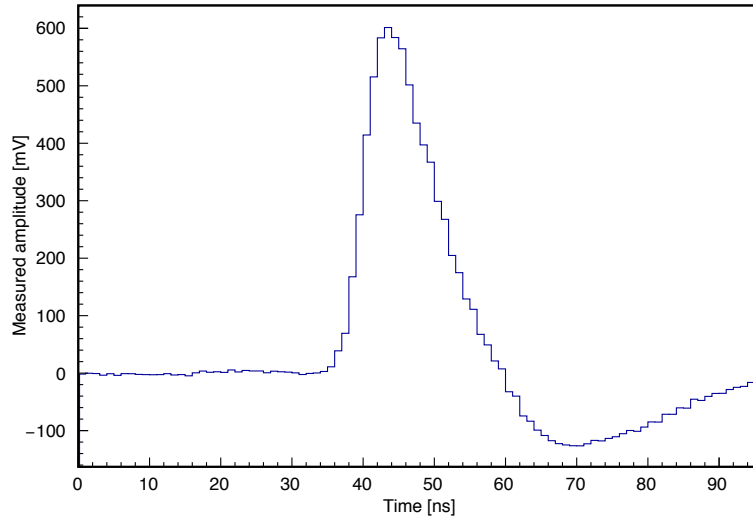


Figure 3.27: A SiPM like pulse after applying pedestal as well as AC transfer function calibration.

Also, the transfer function after full low-level calibration is calculated to verify if all remaining nonlinearities vanished. Therefore, the same data is used again, but this time, pedestal calibration, as well as transfer function calibration, are applied. Besides, the same approach is used as before. These are shown in Figure 3.28. It can be seen that the linear

behavior continues until approximately 1500 mV where the first deviations due to saturation effects start to emerge. Before the saturated regime, the integral nonlinearity is now calculated to be less than 2.0 mV, the differential nonlinearity to be 0.02 mV. Compared to the values before, after transferring the ADC counts to mV, of 26 mV and 0.07 mV, one can see that the transfer function calibration reduced the nonlinearities to a minimum. By looking at the trend of the deviation from the linear fit, some systematic behavior is still remaining. Its origin was not further investigated in the range of this work since it is rather small and had no significant impact on the following investigations.

Furthermore, it was tested if the shift to AC transfer functions from DC TFs resolved the frequency dependence. The detailed investigations are postponed to the appendix, Section B.5.3, but it showed that the observed problematic effects during the calculation of the charge resolution vanished almost completely after using the AC TFs. Only some small effects remain that are an inherent feature of the modules.

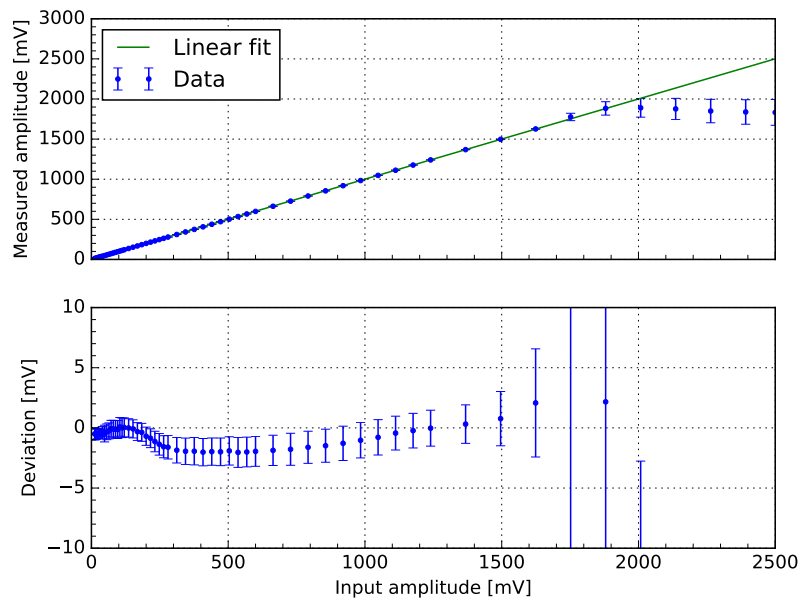


Figure 3.28: A transfer function determined for full calibrated data, pedestal correction and transfer function application, is shown on top with the fit of a linear function. The bottom figure represents the residual from the linear fit.

3.3 TARGET - large scale tests for the camera

After the thorough testing of the first prototype camera CHEC-M with the TARGET 5 modules, the next step in prototyping was to create a camera with the newer TARGET C modules. Since CHEC consists of 2048 pixels, 32 well-working modules are needed. Up to now, 48 modules were tested and characterized, and 32 of the best working ones are used within CHEC-S. The serial numbers of all tested modules which are part of the following investigations are listed in Appendix B.4. During these tests, many of the before explained measurements were carried out, which gives the opportunity to see how the results vary from

module to module, how stable the results are and which problems can occur. The results of the repeated tests of all used modules are summarized and characterized in the following.

Pedestal calibration and baseline noise

First, the pedestal calibrated baseline noise of all the modules can be investigated (see Section 3.2.1). Therefore, data without any signal and roughly 250k events were taken and pedestal calibrated. In contrast to Figure 3.11, the noise is also determined per channel to get a more detailed overview of the modules. The results are shown in Figure 3.29.

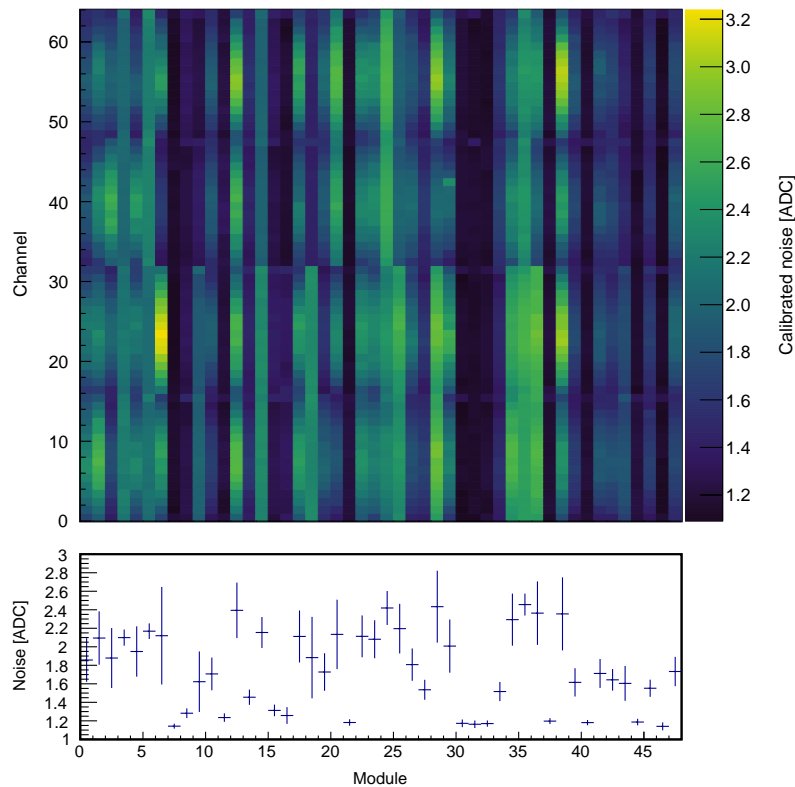


Figure 3.29: Baseline noise of the 64 channels of every tested module (top) as well as the noise of the whole module (bottom). The error bars represent the standard deviation of the different channels on a module.

With a first look at the bottom plot of this figure, one can see that the single module from before was already one of the modules with the lowest noise. Other modules show somewhat larger noise while still staying below three ADC counts. Thus, none of the tested modules show unexpected large noise or baseline problems. The plot above shows the baseline noise of the single channels on each module and reveals some further features:

- If the whole module shows low baseline noise behavior, then also every single channel shows low noise without any outliers (see e.g. modules 30, 31, 32).
- For modules where the baseline noise gets larger, another feature appears: the middle channels of an ASIC show larger noise while outer channels (towards 0 or 15) show

smaller noise (see e.g. module 6). Unfortunately, the origin of this characteristic is still unknown.

- The two boards of the module show a different behavior since the noise between the boards is not generally the same. This can also be observed between the ASICs, however, only to a smaller extent.
- Some boards (e.g. of module 18) show larger noise without any distinct features like the higher noise of the middle channels. This is caused by some faulty digitized blocks where the readout ADC values have too large values (by roughly 4 ADC counts). It appears to be a board wide effect and might be caused by timing problems, but the real cause is (still) unknown.

Summarizing, most of the modules show the expected behavior with very low baseline noise, but some problems and features are still remaining and might be solved in the future.

Time base tuning and sampling frequency

Furthermore, the time base tuning was carried out for every module as well as the sampling frequency was calculated (see also Section 3.2.3). The results of the tuning and the determined sampling frequency are shown in Figure 3.30. The time base works very similarly for every module since the best value was always found to be at 58 DAC for `SSToutFB_Delay`. During the fine-tuning with `VtrimT` some smaller discrepancies in the best values appeared (plot on the left), but most of the modules are centered around 1200 DAC. The same is true for the sampling frequency because most of the modules show the desired sampling frequency around 1 GSa/s, with a mean at 1.015 GSa/s, with only some modules at marginally higher values. This might be caused by the different clocks on the TARGET boards and in the function generator. Small differences in their frequencies can cause the observed differences, however, this was not tested.

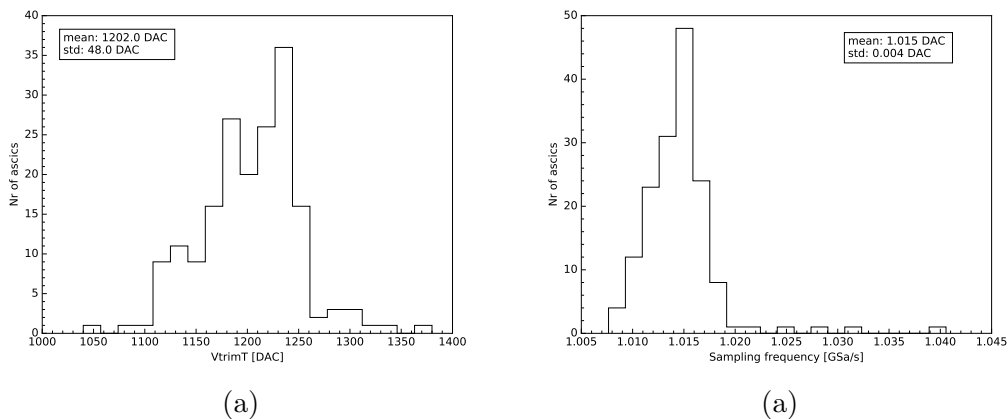


Figure 3.30: Results of the time base tuning and the resulting sampling frequency. The best `VtrimT` values are centered around 1200 DAC (a), the best value for `SSToutFB_Delay` was at 58 DAC for every module. The resulting sampling frequencies after the time base tuning show values around 1 GSa/s (b).

AC transfer functions

Also, AC transfer functions were taken for all modules. Therefore, the same approach as before was used for every module while using the undershoot for negative values to reduce the measurement time. The resulting transfer functions of all cells of all modules are shown in Figure 3.31, where most transfer functions show the expected behavior.

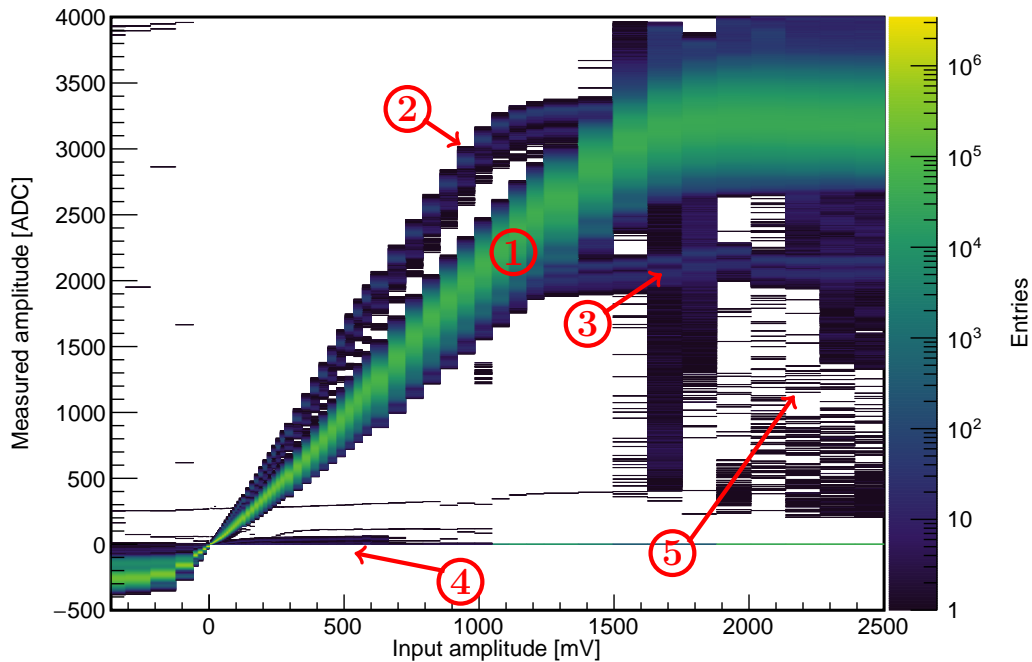


Figure 3.31: Combined AC transfer functions for all measured modules. Most modules showed an expected behavior (1), but also some problems appeared: (2) and (3) are channels that work slightly different since they are steeper or saturate at lower ADC values, respectively. (4) are dead sampling or storage cells which show no, less or random response to injected signals. (5) are cells which show a different behavior in the saturation regime.

The first important point is, of course, that most of the cells of all modules show the same trend (1) for the transfer function as it was calculated in the section before for one module and also for the DC transfer functions or previous TARGET generations. Starting at low amplitudes where the deviation from module to module is rather low and rising until the saturation regime is reached at around 1800 mV. At higher ADC values, the differences in the transfer functions between cells and modules become more evident since the spread is rather large, especially in saturation. The extension to negative values by using the undershoot after the signal worked well for all modules since the results are in agreement with expectations. However, some deviating behavior appeared for some cells and channels. First, two channels showed, in general, the same behavior but one with a steeper rise (2) and the other one with a lower saturation regime at only around 2100 ADC (3). Since the channels still respond in a predictable way to signals, they are usable to some extent nevertheless. But unfortunately, also some more problematic cells emerged, which show not the expected response to injected

pulses. It is apparent that some cells (4) show no or only small or random response. This is caused by not working cells (“dead cells”) in the sampling or storage array. The last recognizable problem affects the saturation regime (5), where some cells show too low ADC values.

Putting the results of the large scale module tests together, most of the tested modules showed a similar good behavior as the single tested module. But also some smaller problems emerged, where especially the large noise and dead cells of some modules are problematic.

Besides the mentioned measurements in this section, also further tests were done by other members of the CHEC community to find the best modules for the camera:

- First tests were done in the beginning to see if the module is working in general (e.g. the programming and communication).
- The trigger ASIC T5TEA was tested in more detail (e.g. triggering and VPED creation).
- The full readout chain was investigated with attached SiPMs.
- The slow signal monitoring was tested.
- And some other small investigations were done.

All these tests showed that most of the modules worked in the desired way, and the 32 best working modules were chosen to be used in the prototype camera CHEC-S.

Final electronic performance - the charge resolution

After the thorough but also specific testing, optimizing and development of calibration procedures of the TARGET modules in the last chapter, the final measure for the low-level performance can be determined with the so-called charge resolution. This value describes how good an injected charge into the full system is extracted. Section 4.1 will define the charge resolution for the whole system. Afterward, Section 4.2 focuses on the determination of the fractional charge resolution caused by TARGET, the full charge resolution with all parts and the comparison with the requirements are then shown in Section 4.3.

4.1 Definition of the charge resolution

The charge resolution for the full camera with all expected contributions for real measurements is shown in Equation 4.1. The charge Q is usually given in units of photoelectrons.

$$\frac{\sigma}{Q} = \frac{1}{Q} \sqrt{\sigma_{\text{TARGET}}^2 + T_w \times NSB + \sigma_{\text{ENF}}^2 Q + \sigma_{\text{sys}}^2 Q^2}. \quad (4.1)$$

The different parts of the charge resolution are:

- σ_{TARGET}^2 describes the electronic noise contribution from the TARGET readout and digitization modules.
- $T_w \times NSB$ describes the influence of photons from the night sky background (NSB). It is assumed that such background photons arrive with a frequency of $NSB = 125$ MHz and are accumulated in a time interval of T_w , which corresponds to the time where the charge is collected.
- $\sigma_{\text{ENF}}^2 Q$ describes fluctuations in the response of the photodetectors to single photoelectrons. For SiPMs, which are used for the current camera prototype CHEC-S, these fluctuations are mainly caused by optical crosstalk and afterpulses (Vinogradov 2012).
- $\sigma_{\text{sys}}^2 Q^2$ describes further uncertainties during the charge extraction that are not covered by the other parts already listed above. Contributing factors include miscalibrations, temperature dependencies that are not accounted for, or any other noise contributors.

Since only the TARGET modules are tested, the one parameter which can be derived by measurements is σ_{TARGET} . To make the results for the charge resolution comparable to CTA requirements, all other noise contributions need to be assumed in a realistic way.

4.2 The electronic charge resolution of TARGET

The fractional charge resolution σ_{TARGET}^2 of the TARGET modules is then defined to be

$$\frac{\sigma_{\text{TARGET}}^2}{Q_{\text{true}}^2} = \frac{1}{Q_{\text{true}}^2} \frac{\sum_{i=0}^N (Q_i - Q_{\text{true}})^2}{N}, \quad (4.2)$$

where Q_i is the measured charge of each individual event and Q_{true} the true, injected charge. This definition covers the standard deviation of all the measured charges as well as the bias. Since no photodetectors are used during the measurements, the approach to determine the charge needs to be changed compared to the methods that are used for the full camera. For the full calibrated camera, the measured charge is connected to the pulse amplitudes of the recorded events via the settable gain, intended to be in the range of 3 mV/p.e. to 4 mV/p.e.. This correlation creates the opportunity to convert the pulse amplitude of injected pulses to the charge in units of photoelectrons. Thus, the resolution can be calculated for every observable that is connected to the amplitude of the injected pulses.

The first step in the determination of the charge resolution is to find well usable observables and to create methods to extract the ‘‘charge’’. To do this, mainly two methods were used and investigated, which are also visualized in Figure 4.1:

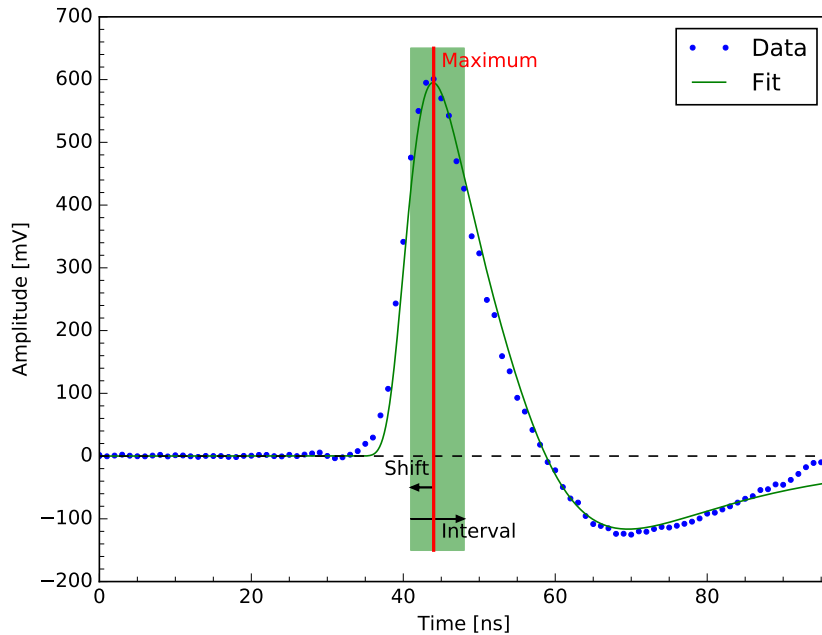


Figure 4.1: Visualization of the charge extraction methods used to determine the fractional charge resolution of the TARGET modules. The charge determination with the maximum ADC value is indicated by the red bar in the middle of the pulse. The fitted function resembles the double landau distribution, which is used to get the peak position. The sum is determined by using the fitted peak position and summing up all ADC values in the highlighted interval.

- **Maximum**, where only the maximum of the injected pulse is used. The maximum is determined by simply using the largest ADC value in the recorded waveform.
- **Sum**, where the ADC values of the pulse are summed. In this case, not the whole pulse is summed but only a small time window around the peak whose length is optimized for the lowest spread of the measured charges (see Appendix B.5.1). The position of the pulse is determined by a double Landau fit as it was done for the AC transfer functions.

A third option that used the integral of the fitted function was dropped since its performance was worse than the other two methods. The reasons for that are uncertainties in the fit since the double landau function does not emulate the pulse shape perfectly. This causes rather large differences in the measured charges, which results in a worse charge resolution. However, it is expected that by using a better fitting function and after further optimization, this approach might give similar results as the other two.

Besides these rather simple approaches, there are also more complex charge extraction algorithms tested within the IACT community (see e.g. Albert et al. (2008); Cogan (2008)). The approach currently used for the CHEC-S camera uses digital filters that use the expected signal shape to extract the measured signal and its charge. Since it uses the cross-correlation of reference pulse and measured pulse to extract the charge, it is called *Cross-Correlation* method (Watson 2018). Here, these more advanced techniques are not used, though, since the simple approaches proved to work well enough for the first investigations carried out here.

Since now, all methods to determine the charge are in place, the different observables need to be calibrated to get the desired charge for the calculation of the charge resolution. The standard way to calibrate the whole camera to get the charge in photoelectrons is

$$Q = \frac{O - O_0}{\gamma_Q} \times \gamma_{FF} , \quad (4.3)$$

where Q is the final charge in photoelectrons, O the measured observable (usually the integral of the pulse) and O_0 the integrated baseline without a present signal. The other calibration factors γ_Q and γ_{FF} are the gain and flat fielding coefficients. For the use of single modules, only the gain γ_Q is needed. O_0 can be dropped since no changes in the baseline are expected after the subtraction of the already taken pedestal. Influences that are expected for the final telescope (like NSB or temperature variations) are not apparent in the lab setup with the single TARGET modules. Furthermore, the flat field coefficient γ_{FF} can also be neglected because no photodetectors are used whose pixel to pixel differences in response to single photoelectrons are compensated by this factor.

The remaining factor γ_Q , which connects the used observable to the charge in photoelectrons, needs to be determined by measurements. Therefore, pulses with known amplitudes (and thus with a known number of photoelectrons) are injected into the modules, then fully calibrated (application of pedestal correction and transfer function), and afterward, the observables are determined. In that way, all measured observables can be transferred to the charge. The results of these measurements for the two methods in the not saturated regime are shown in Figure 4.2. The function connecting the data points is a linear fit, $f(x) = ax$, which was forced to go through the origin. It can be used afterward to calculate the charge from the measured observables.

By using Equation 4.2 from above, the charge resolution can be calculated. During the investigations of the charge resolution, two effects with a negative influence on the final results

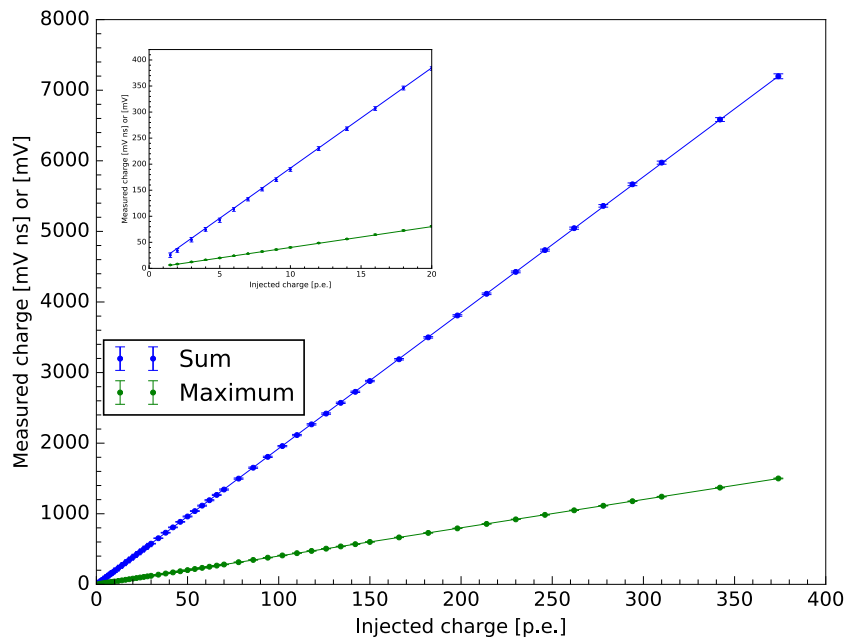


Figure 4.2: Correlation of the measured charge of the two used methods (summation and maximum value) with the injected charge. The charge was calculated from the pulse amplitudes by assuming a gain of 4 mV/pe. The small image in the upper left shows a zoomed-in view of the smaller amplitudes. The line connecting the data points is a linear fit through the origin, the shown errors are the standard deviation of the measured mean values of the observables. Influences of the pulse shape and sampling array were corrected (see Appendix B.5.2 and B.5.3).

were discovered: a change of the pulse shape with rising amplitude caused by the shaper and a dependence of the measured charge on the position in the sampling array. Both effects only influence the summing method but are fortunately correctable. These effects and the applied corrections are illustrated in Appendix B.5.2 and B.5.3. The resulting resolutions after the corrections are shown in Figure 4.3. The error was deduced by repeating the charge extraction ten times and investigating how the results differ from measurement to measurement. For this, the measured data was split into sets with 10k events each on which the charge resolution algorithm was applied. Since this was done within one larger data set, the shown errors might be underestimated compared to completely independent measurements.

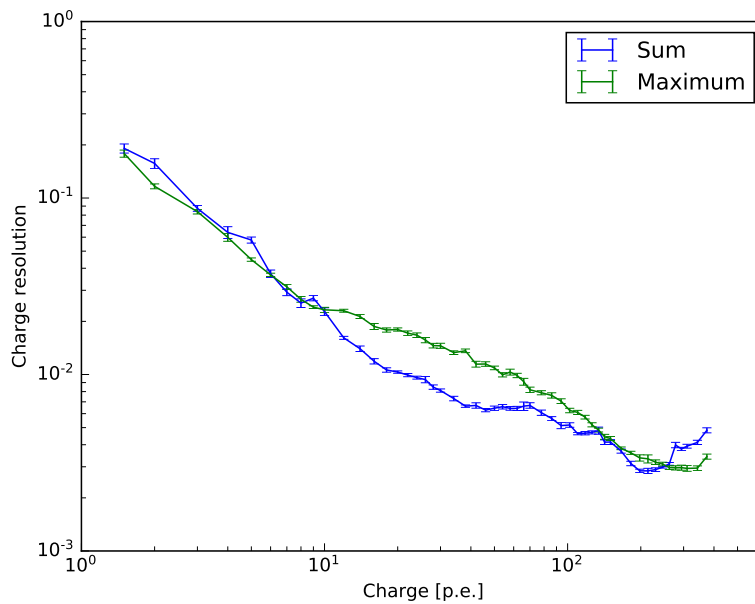


Figure 4.3: Charge resolution of the TARGET modules calculated with different methods. Used were the sum of the ADC counts of the pulse and the maximum ADC value at the peak. Influences of the pulse shape and sampling array on the resolution were corrected. The errors were deduced by repeating the charge extraction ten times.

The resulting performance of both methods is equally well: they show a very similar behavior over the whole non-saturated range with only small differences. At the smallest charges, the resolution is the worst. This is caused by the significant influence of the electronic noise, which makes the charge extraction quite tricky. At intermediate charges from 10 p.e. to around 100 p.e., the summation method gives better results. This is also expected since the use of multiple cells wipes out smaller fluctuations which are still present. At a few 100 p.e., the modules start to saturate, whereby saturation starts at smaller charges for the summation method. Afterward, the charge resolution becomes even worse because of saturation effects. This saturation regime is investigated in more detail in the next section before the full charge resolution is calculated and compared to the CTA requirements.

Saturated pulses

All previous investigations and results were focusing on small and medium amplitudes, meaning below 1500 mV, where the TARGET modules are not in saturation. This section will now focus on large amplitudes, especially the regime where the modules are saturated. How the pulse shapes are affected by such large amplitudes was already shown before, in Figure 3.13: the top of the pulse is cropped at a certain value, developing a plateau instead of a sharp peak, and a tail behind the pulse starts to appear, which tends to become larger for higher input amplitudes. This emerging tail already gives the opportunity to improve the charge extraction algorithm for such high amplitudes by using larger summation windows that consider the tail. The best interval for saturated pulses was found to be at a shift of 7 ns with an interval of 30 ns. This investigation is shown in the appendix, Figure B.7. The charge calibrations for the saturation regime and also the resulting charge resolution are shown in Figure 4.4, now also including the summation method with an extended window.

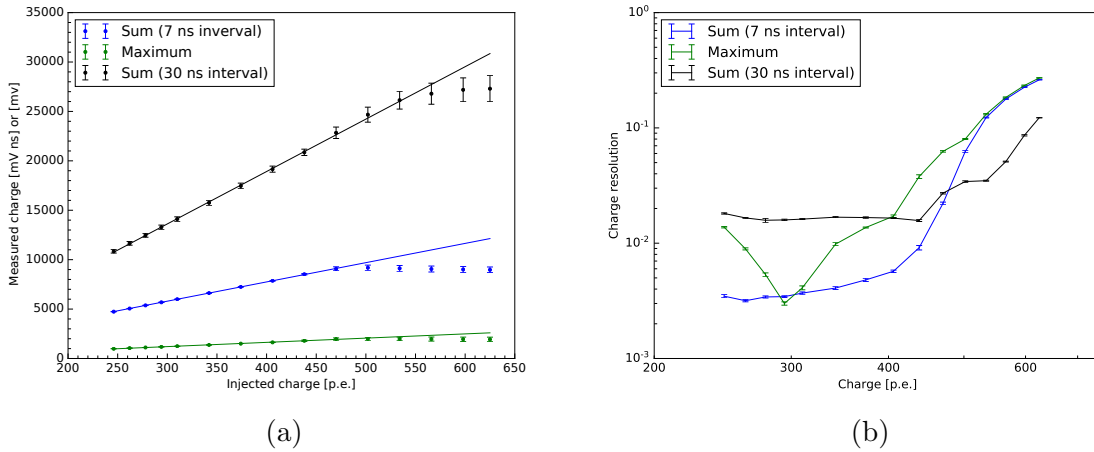


Figure 4.4: Correlation of the measured charge with the injected charge (a) as well as the resulting charge resolution (b) for the saturated regime. The sum method is shown with two different summing intervals, once with the former, small one (3 ns shift, 7 ns interval) and with a larger interval to cover also the emerging tail for saturated events (7 ns shift, 30 ns interval). For comparison, also the results of the maximum method are shown.

By looking at the left plot, which shows the conversion from the measured observable to the charge in photoelectrons, one can see that with the enlarged summation window, the saturation starts later. Thus, the linear charge calibration works also up to higher injected amplitudes. The charge resolution of the extended interval, plot on the right, shows smaller values for saturated pulses (above 500 p.e.) since the bias of the measured charge from the expected charge is smaller than for the shorter window. The downside of this approach is the worse performance at small amplitudes. Before the saturation is reached, the larger summation window collects more electronic noise that results in a worse charge resolution. In comparison to the maximum method, both summation methods are superior in the saturated regime. This is also expected since no information from the tail is considered, only the maximum that is cropped in saturation.

If a broader range with a proper charge reconstruction is needed, this simple adjustment

already helps to achieve this goal. It is even possible to further improve the charge extraction in saturation with other methods. The use of a more dedicated function than the linear description of the correlation of measured observable and expected charge can be used. Also, other observables of the pulse that describe the charge in saturation in a better way than the methods which were used in this context can be utilized. Such investigations were already carried out for the TARGET 7 modules in the work of Heller (2016) and Kraus (2018). However, their approach can not be directly adopted since the former pulse shapes are not comparable to the current one. Also, their approach of fitting a so-called plateau function will not work in the case of TARGET C because of the deviating distortion of the pulse in saturation. Further methods regarding the treatment of such saturated pulses with TARGET C are currently investigated by other members of the CHEC community but were not carried out within the range of this work. Thus, the charge resolution will only be calculated for the non-saturated realm in the following.

4.2.1 Charge resolution of different calibrations, channels and modules

Before moving on to the final, complete charge resolution, the influence of the AC transfer function application on the resulting charge is further investigated. Since all results before were acquired with full low level calibrated data, the same calculations are repeated for data that was only pedestal subtracted. Thereby, the same data sets as before are used. The comparison of the charge resolution for both calibration steps are shown in Figure 4.5.

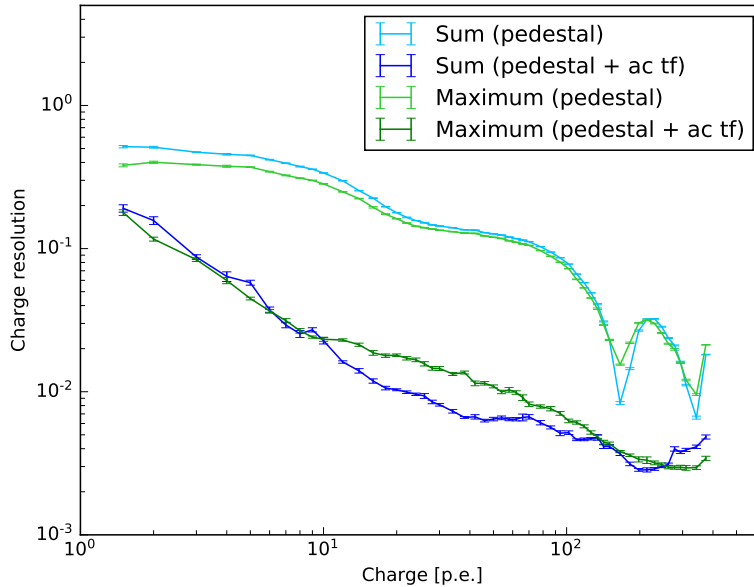


Figure 4.5: Comparison of the charge resolution of pedestal calibrated data (upper graphs) with pedestal and transfer function calibrated data (lower graphs). The charge was determined with two different methods (summation and maximum).

First, for both methods (maximum and sum), the charge resolution for data with applied AC transfer function is clearly better than without applied transfer functions. For the low

charge regime, the resolutions tend to be more similar. This is likely caused by the electronic noise, which dominates at very low amplitudes and is also not removed by the transfer functions. For medium amplitudes, the differences are the largest since there the electronic noise has less impact and the determination of the transfer functions works best. Thus, all existing nonlinearities and AC effects are successfully removed, resulting in the best charge resolution. For the largest amplitudes, where the TARGET modules start to saturate, the differences become smaller again. On the one hand, this is caused by the saturation during the creation of the AC transfer functions: very large input pulses result in basically the same recovered ADC values. If the transfer function is then applied for calibration afterward, small changes in the ADC values can cause significant changes in the amplitude. On the other hand, differences from saturated cell to saturated cell get smaller in pedestal calibrated data when the capacitors reach their limit at the available voltages within TARGET C, and the response to injected pulses does not vary that much anymore. For the interesting range before saturation, the application of the AC transfer functions clearly improves the resolution. Additionally, a bump like structure emerged at around 200 p.e. in the pedestal calibrated data, which is a bias effect.

All former measurements for the charge resolution were carried out for one channel of one module. To check if the results are transferable to all channels and even other modules or if some critical differences emerge, the measurements are repeated for more channels and modules. First, one module was used, and the charge resolution was calculated for all 64 channels. The results for the maximum and the summation method are shown in Figure 4.6. This time, only the correction regarding the pulse position in the sampling array was applied. The correction of the pulse shape was dropped because no bias effects were included. This is justified since the bias is negligible below saturation. The behavior of all channels of this module over the whole non-saturated regime, as well as for both methods, is very similar, as only small deviations are visible. The only interesting observation lies in the beginning of the saturation regime: some channels tend to start to saturate at smaller amplitudes than others, especially compared to the first channel that was tested to full detail before.

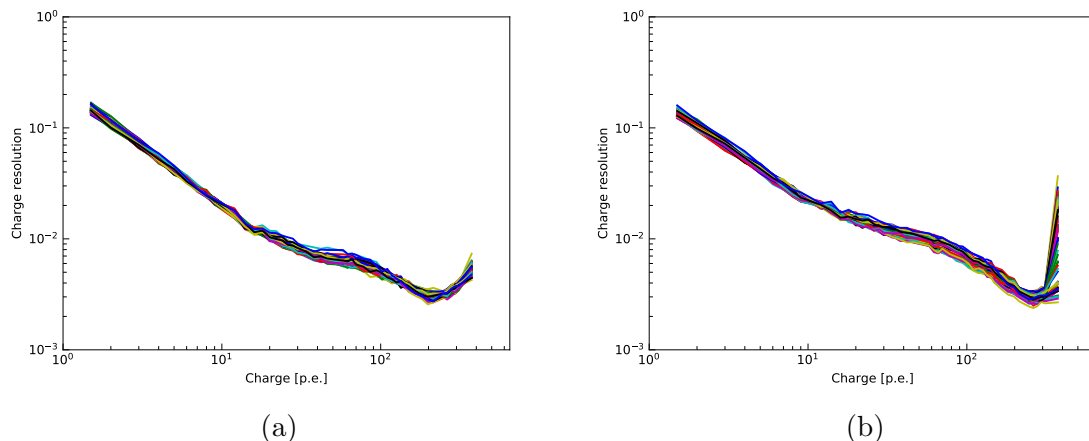


Figure 4.6: Charge resolution of a whole module with all available 64 channels. The resolution was determined with the summation method (a) and the maximum method (b).

The next step is to check the charge resolution of other TARGET modules. Since all modules were already thoroughly tested during the mass tests for the prototype camera (see Section 3.3) without discovering large differences, only some randomly chosen modules are used. Furthermore, only a few channels per module are analyzed for the charge extraction because it showed before that the differences from channel to channel are rather small. This reduces the needed computing time for the investigations to a large extent. The results for seven modules with four tested channels each are shown in Figure 4.7.

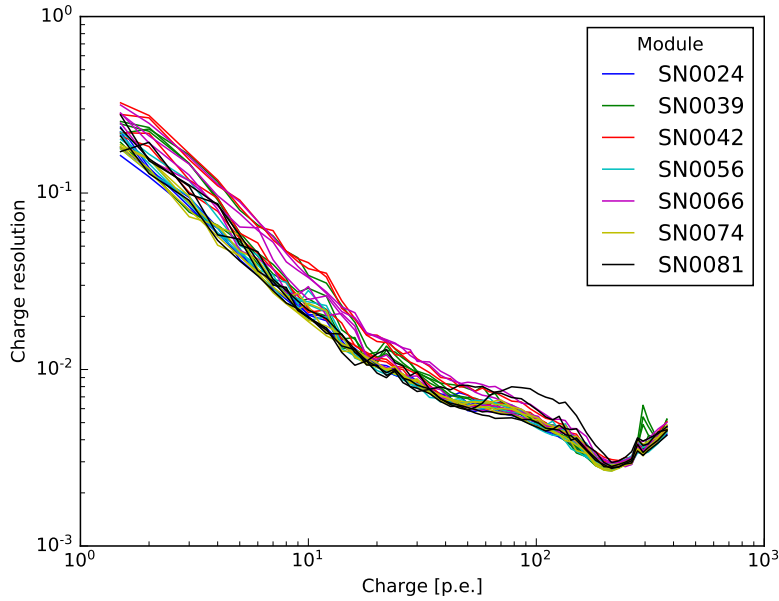


Figure 4.7: Charge resolution of seven different modules, deduced with the summing method. For each module, the first channels of the four ASICs were investigated, thus resulting in 28 TARGET charge resolutions.

The results of the charge measurements with different modules show the already known results from before: after full low-level calibration of the modules, the different channels and modules behave almost the same. Only some tend to have a slightly worse resolution but compared to other contributing factors, see the next section, these differences only play a minor role.

4.3 The final charge resolution

After the detailed determination of the charge resolution of the TARGET modules and the investigations of all its characteristics, the full charge resolution with all other parts (Eq. 4.1) is calculated. The value for σ_{TARGET} is measured and calculated exactly as described above. The expected night sky background was estimated via a small simulation: a rate of 125 MHz for night sky photons was assumed that produce a nearly Gaussian signal with a full width at half maximum of 10 ns. By looking at the resulting signal, one gets a baseline shift of around 1.35 p.e. with a spread of 0.9 p.e.. The shift can be neglected since it is constant and can be corrected, but the spread of 0.9 p.e. is used as the charge contribution by the NSB. This

investigation also gives the same results for both used methods. For the excess noise factor (ENF) σ_{ENF} , a value of 1.2 was assumed, for the systematic error σ_{sys} a value of 5%. Further investigations within the CHEC community showed that the temperature dependency, the main contributor to the additional systematic error σ_{sys} , appears rather as a bias (shift of the measured charge values) than an additional noise. So, the assumed value of 5%, which is added to the charge resolution, might be an overestimation.

The expected charge resolution for the whole system is then compared to the CTA requirements (CTA Consortium 2018c; Watson 2018), Figure 4.8, to see if the measured TARGET performance is good enough to meet the requirements. Since the charge resolution is divided by the CTA requirements, everything below a value of one fulfills the SST requirements. This is met for the whole dynamic range below the saturation regime. It can be seen that the overall influence of the TARGET module to the charge resolution is in the current setup very small, compared to the other contributions. The saturated regime is not further investigated in terms of the CTA requirement since no special event reconstruction was developed. Thus, the requirement would not be met in this regime anyway.

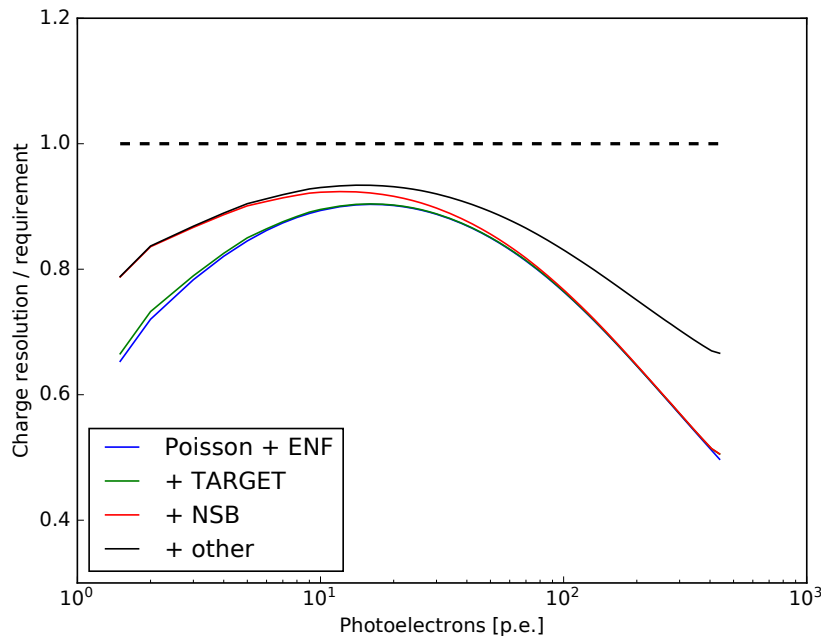


Figure 4.8: Full charge resolution compared to the requirements for the SSTs of CTA with an assumed gain of 4 mV/p.e.. Included are the electronic charge resolution of TARGET, the Poisson limit, the excess noise factor from the photodetector, accumulated photons from the night sky background with 125 MHz as well as additional systematic errors, which were assumed to be 5%.

Conclusion and outlook

At the beginning of this part, the Cherenkov Telescope Array was introduced as the future of very high energy gamma-ray astronomy. It will consist of more than 100 telescopes with three different sizes, thus covering a much larger energy range with better sensitivity compared to current experiments. During the creation of this work, the CHEC camera, developed for the needs of very high energy events, was chosen to be the foundation of the camera for the dual mirror (Schwarzschild-Couder) SSTs. The front end electronics, mainly used for triggering and digitization, consists of custom-built ASICs, directly designed for Imaging Atmospheric Cherenkov Telescopes, called TARGET. The main goal of this work was to test and fully characterize the newest TARGET ASIC generation at this time, TARGET C and T5TEA, and to see if they fulfill the CTA requirements. This included many different tests, the development of calibration techniques and large scale tests of almost 50 modules to find the best working ones for the prototype camera CHEC-S.

T5TEA, responsible for creating first level trigger signals, improved a lot compared to the former generations, which suffered some problems. After the optimization of T5TEA, it is able to trigger on single photoelectron signals (< 4.0 mV) with very small noise (< 1.0 mV). Furthermore, the trigger threshold can be set very accurately, even to thresholds above 100 mV while retaining low noise. Also, when injecting such large input pulses, the trigger path showed only very low crosstalk. Thus, by splitting digitization and triggering into two signal paths, all apparent problems of TARGET 5 and 7 could be overcome, meaning that T5TEA is fulfilling all CTA requirements.

TARGET C, responsible for the digitization of signals, was even more heavily tested. First, investigations with DC signals were carried out: the noise of the baseline after subtracting the pedestal was measured, which showed to be very low, at around 1.25 ADC counts for the whole module at a VPED value of 1100 DAC. Also, DC transfer functions were taken, which showed the expected behavior already known from previous TARGET generations. The modules showed a large range of linear response while remaining noise below 5 ADC for each individual cell. Furthermore, AC signals were injected to test the TARGET modules even further. Sine waves were used to tune the timebase of the module, which controls the charge collection time interval of each cell. After the tuning, the sampling frequency was measured, which showed to be at the desired value of around 1 GSa/s. The crosstalk of the new TARGET modules improved significantly compared to the TARGET 7 generation since it is at the one percent level and for many channels even far below. In contrast to the former transfer function approach, which used DC signals, a new technique was developed to extract

the TARGET transfer functions from AC signals. This was done since the former approach neglected AC effects that showed to worsen the results. This approach showed to work as desired, but some room for improvements still remains.

As a final measurement, the charge resolution of the TARGET modules was determined. Therefore, standard methods were adapted for this TARGET generation and tested as well as further optimized. It became clear that the charge extraction for these TARGET modules still works very well, also compared to former generations. After including all expected contributions to the charge resolution, the CTA requirements are still met. It can be concluded that the current version of the FEEs, especially the TARGET ASICs, are already good enough to be used in future IACT arrays.

Many of the carried out measurements were also repeated for other modules. All these investigations culminated in the prototype camera CHEC-S, see Figure 5.1, which is currently still tested. One of the first milestones was the observation campaign on the ASTRI telescope structure in Sicily, where it observed first Cherenkov light.



Figure 5.1: Picture of the fully-loaded prototype camera CHEC-S. (Leach et al. 2019)

Regarding the development of the TARGET ASICs and modules, the tests carried out in this work, as well as other tests, have shown that the ASICs work mostly as expected and hoped. Also, all the problems that were found in the former TARGET generations could be corrected. Thus, for the final TARGET iteration, which will be used within the cameras for the SSTs of the CTA, only minor changes are needed.

APPENDIX B

Appendix - characterization of the TARGET C and T5TEA ASICs

B.1 Electronic equipment used for the measurements

	Function generator	Oscilloscope
Vendor	Keysight	Agilent (Keysight)
Model	33611A	M-SOX 3054A
Features	80 MHz with < 1 ps jitter 660 MSa/s 14 bit resolution	500 MHz bandwidth 4 GSa/s 8 bit resolution
Manuals	Keysight Technologies (2015)	Keysight Technologies (2017)

Table B.1: Electronic equipment that was used for all measurements regarding the TARGET ASICs.

B.2 T5TEA - configuration values after optimization

Register Name	Register Value	
	Set 1	Set 2
VPED*	1000	1000
	- 1200	-1200
Thresh \diamond	0x000	0x000
PMTref4 \diamond	0xFFFF	0xFFFF
Wbias \diamond	0x3D9	0x4C3
TTbias \diamond	0x44C	0x44C
TTbias_C	0x3E8	0x3E8
VpedBias	0x708	0x708
TRGsumbias	0x960	0x384
TRGGbias	0x76C	0x640
TRGbias	0x3E8	0x3E8

Table B.2: Best working parameters found during the optimization procedure. The VPED value is usually chosen within the given range.

* settable for each channel

\diamond settable for each trigger group

B.3 Target C Measurements

B.3.1 Pedestal Calibration and Baseline Noise

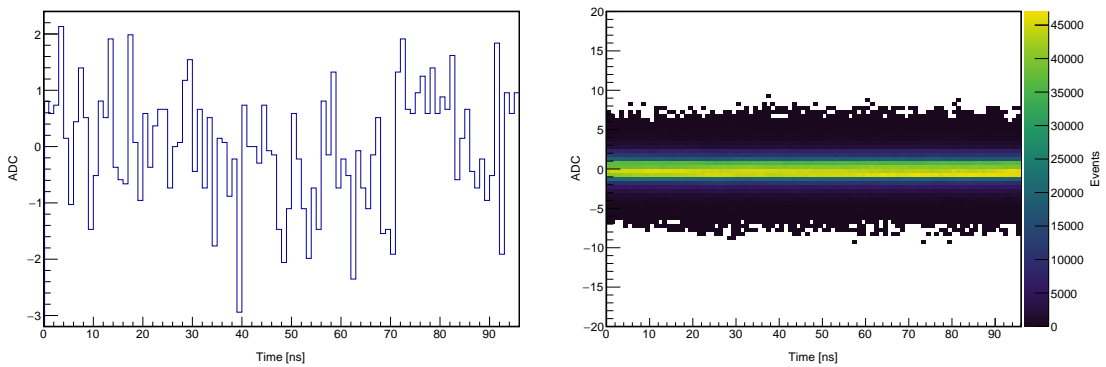


Figure B.1: Recorded calibrated baseline events with a readout window size of 96 samples. The left image shows one single event with an applied VPED value of 1100 DAC after pedestal subtraction, the cell-dependent differences vanished almost completely, only some electronic noise remained. The right plot combines all events in the data set for one channel.

B.3.2 AC Transfer Functions

This section lists some problems and their solutions which were encountered during the creation of the AC transfer function. One problem which was mentioned in Section 3.2.6 is the cell overflow. This overflow is caused by the Wilkinson ADCs during digitization: if the slope of the Wilkinson ramp is too flat, the 12 bit counter reaches its end before the ramp crosses the stored voltage and starts to count from the beginning. The slope of the Wilkinson ramp can be set by a certain parameter and was optimized for one module in a way that the whole range of the counter is accessible. However, the optimized value for this single module does not work for all modules perfectly since some modules show such an overflow. One solution to circumvent this problem would be to optimize the slope of the Wilkinson ramp for every module before the creation of the AC transfer function. Of course, this needs some effort and creates more configuration data per module. Currently, not every single module is optimized in regard to the Wilkinson ramp, but occurring overflow is corrected during the step of pedestal calibration. If a cell with overflow is detected within a signal, it is corrected by adding 4096 ADC, accounting for the restarting of the 12 bit counter. After detecting this problem and figuring out a solution, it was implemented into TargetCalib, the software which manages the calibration of TARGET data (Watson 2018). Figure B.2 shows an example event with occurring overflow, as well as its correction.

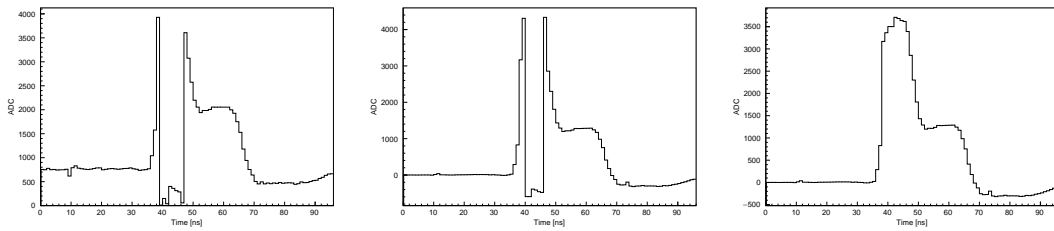


Figure B.2: Example of a highly saturated pulse with overflow cells and their correction after calibration. The plot to the left shows the raw, saturated pulse where cells with overflow are visible. The one in the middle the same pulse after pedestal calibration without any overflow correction. The one on the right the pedestal calibrated pulse as well but with applied overflow correction.

Furthermore, it was found that for some modules, the baseline of recorded data including pulses was not at 0 ADC what would be expected after subtracting the pedestal offset for each cell. This is caused by the temperature dependence of the pedestal values for each cell. Although all data for the AC transfer functions was taken in a temperature stable environment (a temperature chamber at 23°C), it takes a few minutes for the TARGET module to stabilize thermally after starting data taking. Since the recorded dataset without pulses, which is used for the pedestal calibration, was taken at the beginning, not every module was at a stable temperature. So, from pedestal run to data runs with pulses, the pedestal values of each cell shifted slightly, causing a subtraction of a wrong value. This can be seen for one module in Figure B.3 on the left.

For the AC transfer functions, this effect was then corrected: for every event, the first 30 cells in front of the pulse (see also Fig. B.3) are used to calculate the mean baseline shift away from 0 ADC. This value then is added to the determined ADC value that is used for the AC transfer function. This procedure is only done for amplitudes below 500 mV since then

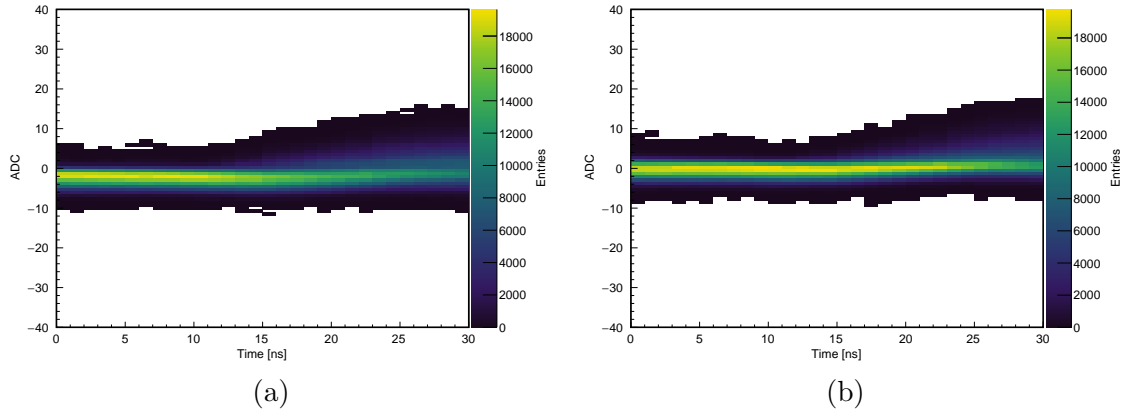


Figure B.3: Result of the applied baseline correction. Shown is the mean baseline of 100k events for 30 cells directly in front of the pulse. (a) Without any correction, a slight shift of the baseline is recognizable, resulting in a mean below 0 ADC. (b) With applied correction, this shift vanishes.

the pulse becomes too large and also extends into the first 30 cells (which is already visible in the figure). For amplitudes above this threshold, the ADC value is shifted by the value of the last correctly calculated baseline shift. This is justified since the module is already thermally stable at this point and the baseline does not change anymore. The baseline after this correction is also shown in Figure B.3 on the right where it is at 0 ADC as expected.

This baseline correction is especially crucial for small amplitudes since a shift of a few ADC counts affects these the most. To see the improvement for low amplitudes, the zero-crossing of the transfer function can be investigated. This is indicated in Figure B.4, where the transfer functions are shown at around 0 ADC, on the one side without baseline correction, on the other side with applied correction. The enhancements are clearly visible: without the correction, the differences from channel to channel are quite large and are also shifted away from 0 ADC towards negative values. With applied correction, all channels cross 0 ADC and the spread becomes much lower. However, the effect of the baseline correction is not always as large as for this module since it showed the largest shift that was observed.

But even after this correction of the baseline, still not all transfer functions cross 0 ADC when no signal is applied. This is caused as no data point at 0 mV was included in the transfer function. To further reduce the shift at very small amplitudes, an additional data point at the pedestal level is added. This is done when the calibration files are created with the TARGET Calib software (Watson 2018). The resulting transfer functions, which are used for the full calibration, are shown in Figure B.5.

Another abnormality that was found during the creation of the AC transfer functions was the behavior of the measured noise. In contrast to the DC transfer function approach, which showed low and rather constant noise, the noise acquired by the AC approach is larger and shows a characteristic structure with two peaks at around 600 mV and 1400 mV. It was found that this noise also depends on the place of the injected pulse in the sampling array: the trend of the noise is the same for every storage cell that is connected to the same sampling cell. Some of them have low noise in general, some show only considerable noise in one peak, some in both peaks. Figure B.6 shows this behavior for two different sampling cells. Unfortunately, the final cause of this behavior could not be found.

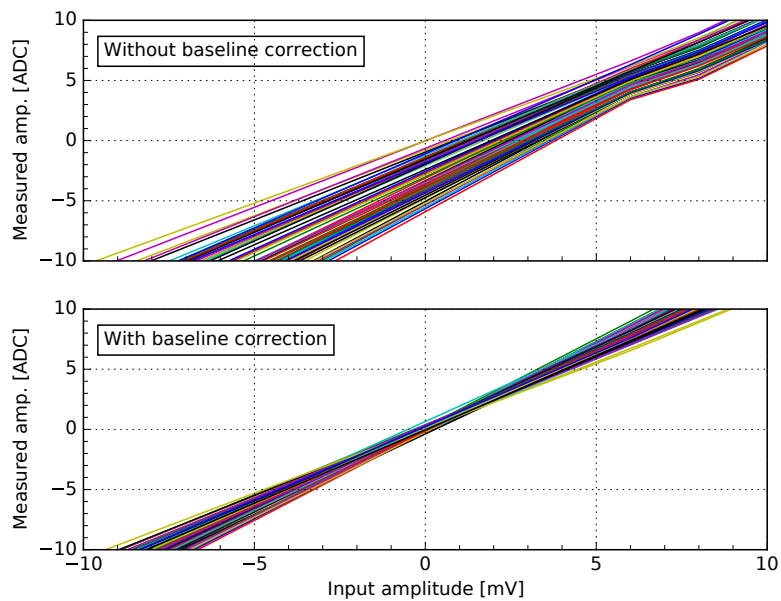


Figure B.4: Effect of the baseline correction on the zero-crossing of the AC transfer function. The upper plot shows the mean transfer function for the 64 channels of one module, the lower plot shows the same module with applied correction.

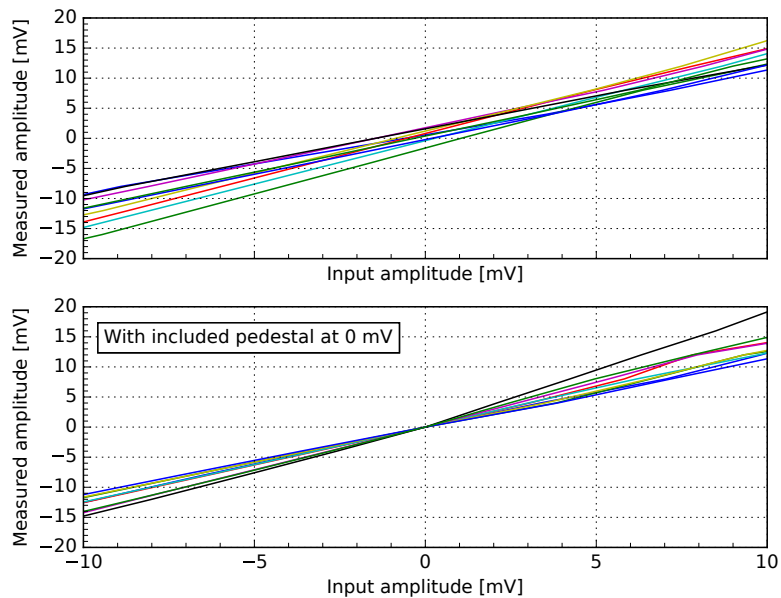


Figure B.5: Effect of adding an additional data point at 0 mV created from the taken pedestal.

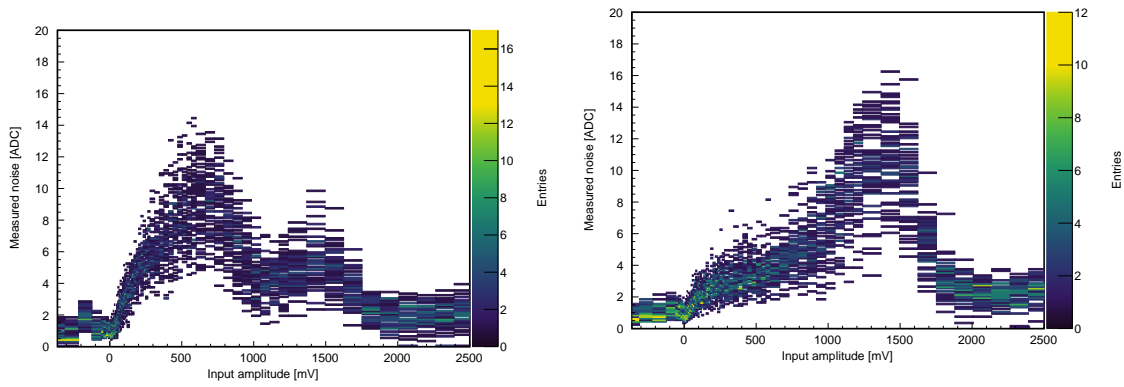


Figure B.6: Measured noise of the AC transfer functions for two different sampling cells.

B.4 Available and tested modules

SN0020	SN0037	SN0056	SN0070
SN0021	SN0038	SN0057	SN0071
SN0022	SN0039	SN0060	SN0072
SN0023	SN0040	SN0061	SN0073
SN0024	SN0041	SN0062	SN0074
SN0025	SN0042	SN0063	SN0075
SN0027	SN0043	SN0064	SN0076
SN0028	SN0044	SN0065	SN0077
SN0029	SN0045	SN0066	SN0078
SN0030	SN0048	SN0067	SN0079
SN0031	SN0049	SN0068	SN0080
SN0036	SN0051	SN0069	SN0081

Table B.3: A list of the serial numbers of all modules which were tested for the prototype camera CHEC-S (see Section 3.3).

B.5 Charge resolution

B.5.1 Optimization of the summing method

In order to get the best summing interval to achieve the lowest possible charge resolution, different positions in relation to the maximum (shift) and intervals are tested. For each interval, the resolution of the summed charge is calculated.

The data that is used for the optimization, as well as for all further measurements of the charge resolution, is the same that was used for the determination of the AC transfer functions before: waveforms with pulses with different amplitudes are injected into the modules and samples of 96 ns are readout. Thereby, the event readout is triggered by external signals, which are also created by the function generator. Afterward, all data is calibrated, pedestal subtraction, as well as the application of the transfer functions.

The results of the optimization of the summing interval are shown in Figure B.7. The optimization was done for two amplitude regimes, lower ones as well as large amplitudes where the TARGET modules are already in saturation. Therefore, pulses with 96 mV and 2264 mV were taken. The two investigations are needed since, in the saturated regime, the height of the digitized waveforms does not increase anymore, but the pulses tend to develop a tail that grows with larger amplitudes. Thus, one is able to extract a more accurate charge with a larger summing interval. The best intervals are

- for the lower amplitudes a summation window of 5 ns with a shift of 2 ns
- and for saturated pulses a summation window of 30 ns with a shift of 7 ns.

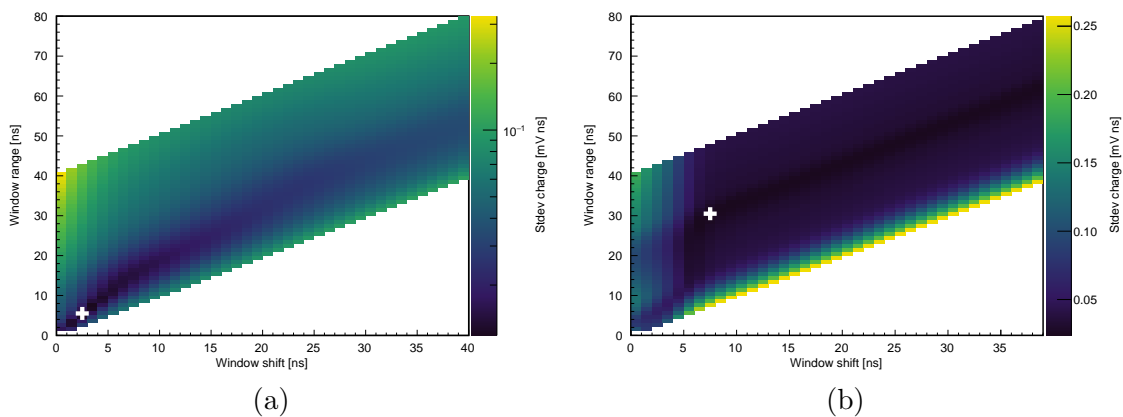


Figure B.7: Optimization of the shift and width of the summation window for the charge extraction. Shown are the best parameter combinations for 96 mV (a) and for 2264 mV (b), which corresponds to already saturated pulses. The results with the lowest noise are marked with the white cross: for (a) a shift of 2 ns and a summation window of 5 ns works best and a shift of 7 ns with a summation window of 30 ns for (b), respectively.

B.5.2 Influence of the shaping on the pulse shape

During the investigations and measurements of the charge resolution, a distinct bias of the measured sum from the expected one (calculated by the linear fit, see e.g. Fig. 4.2) was found. This bias also changed with changing pulse amplitude. Since such a bias is not expected after pedestal and transfer function calibration, it was further investigated. By looking at the pulse shapes at different amplitudes, it was discovered that the sum, especially the width of the pulses, changed with rising amplitudes. However, the calibrated amplitudes stayed the same, thus, the maximum method of the charge calculation is not affected by this effect. To quantify this effect, the mean full width at half maximum (FWHM) was determined for all input amplitudes. The measured widths are shown in Figure B.8 on the left, where a significant change of the measured FWHMs is visible. Thus, the width is indeed changing with rising amplitudes and has an effect on the measurement. The reason for the changing pulse shape can be found in the shapers and amplifiers on the TARGET modules, which change their behavior slightly for different input amplitudes. To see if the shapers and amplifiers cause the observed bias, the expected area below the pulse is calculated from the measured FWHM by using the integration interval that is also used for the sum method. For these calculations, the pulse shape is approximated with a Gaussian distribution, which is justified for such small summation windows. Then, the deviation of the calculated area is compared to a linear rise, which would be expected. Also, the bias of the measured charge is determined and compared to the calculated area. The results of these investigations are also shown in Figure B.8, on the right.

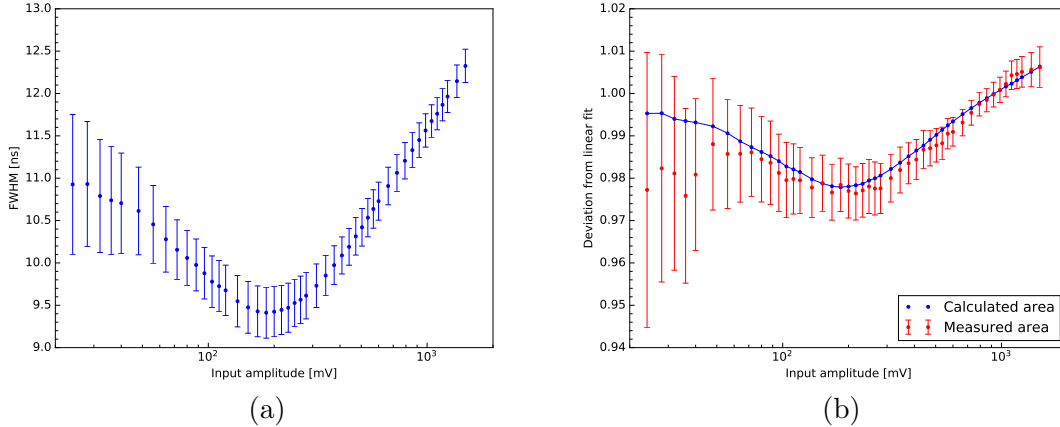


Figure B.8: Influence of the shaping on the pulse shape with rising amplitudes. The plots show the measured FWHM of the pulse with its standard deviation (a) and the deviation of the expected area and the measured area from a linear behavior (b). Values at one resemble a perfect linear behavior.

It is clearly visible that the observed bias in the charge resolution is very similar to the bias caused by the changing FWHM of the pulse shapes. This is true for almost the full, not saturated amplitude range, only for the smallest amplitudes the behavior starts to differ. This is likely caused by the rising influence of the electronic noise, which makes the measurement and calculation more complicated and sensitive to uncertainties.

Since the origin of the charge resolution bias can be mainly accounted to the changing

shape of the width, these effects can be corrected. This is done by scaling the measured area according to the calculated, expected area, which is shown in the above figure. This correction is applied to all charge resolution plots in Chapter 4 unless stated otherwise.

B.5.3 Influence of the position in the sampling array on the measured area

In the work of Kraus (2018), it was discovered that the waveform observables which are used for the calculation of the charge resolution depend heavily on the position in the sampling array. Deviations from the mean measured area of up to ten percent were observed. The origin of this effect was connected to the used transfer function approach, which used DC signals and neglected AC effects. This was also the reason for changing to an AC approach for the transfer function creation, see Section 3.2.6. To check if switching to the new calibration technique removed this unwanted behavior, the mean measured area was calculated for every pulse position in the sampling array. This is shown in Figure B.9 on the left. Again, a dependency on the position in the sampling array is visible, however, it is much smaller, only in the range of one percent deviation from the mean measured area. These results are also observed for all input amplitudes, except very small ones where the electronic noise dominates, and are also stable over time. Therefore, it can be concluded that the significant AC effects which were observed before vanished but some smaller dependencies remained. The largest remaining dependencies are located at the transition region from the first sampling block to the second one (cell 31 to cell 32) and especially from the end of the sampling array to the beginning (so from cell 63 to cell 0). This problem is connected to the charge collection time of each individual cell which is normally set to 1 ns in the case of TARGET C. Due to the design of the TARGET ASICs it is not possible to control this time interval perfectly for all cells, especially the last cells of the sampling blocks tend to differ from the expected 1 ns interval. If these cells are smaller (larger), they sample a smaller (larger) amount of the injected signal. This means for the summing method, which uses the sum of certain cells as the measured charge, that a smaller (larger) than expected part of the waveform is summed. This can be seen in the mean measured charge, as it is shown in Figure B.9.

Because this effect is stable over the whole storage array and even over time, it can be easily corrected afterward. This is done by creating a lookup table, similar to the plot on the left in Figure B.9, for every amplitude by using the first few thousand events of every data set. The events afterward are then used for the charge resolution calculation, including this correction. The results are shown in the plot on the right in this figure: the extension to larger areas (and also to a smaller extent to smaller areas) vanishes and results in a smaller charge resolution. This correction is also applied to every measurement in Chapter 4 unless stated otherwise.

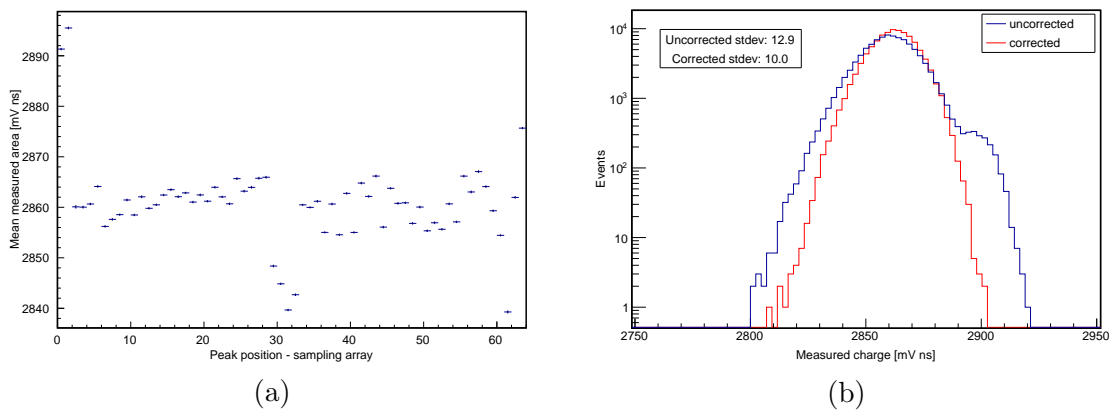


Figure B.9: (a) Dependency of the mean measured area, and thus the charge, from the pulse position in the sampling array. Clear deviations from the mean area are visible for the block transitions from cell 31 to cell 32 and from 63 to 0. (b) The resulting charge distributions before and after correction of the sampling cell dependencies are also shown. The results were deduced for an amplitude of 600 mV.

Bibliography

- Aab, A., Abreu, P., Aglietta, M., et al. 2018, *Astrophysical Journal*, 868, 4
- Aartsen, M. G., Ackermann, M., Adams, J., et al. 2018a, *Advances in Space Research*, 62, 2902
- Aartsen, M. G., Ackermann, M., Adams, J., et al. 2018b, *Advances in Space Research*, 62, 2902
- Abbasi, R., Abdou, Y., Abu-Zayyad, T., et al. 2010, *The Astrophysical Journal Letters*, 718, L194
- Abbasi, R., Abe, M., Abu-Zayyad, T., et al. 2016, *Astroparticle physics*, 80, 131
- Abbasi, R., Abe, M., Abu-Zayyad, T., et al. 2018, *The Astrophysical Journal*, 865, 74
- Abdo, A. A., Ackermann, M., Ajello, M., et al. 2010, *Physical Review Letters*, 104, 101101
- Abdollahi, S., Ackermann, M., Ajello, M., et al. 2017, *Phys. Rev. D*, 95, 082007
- Abe, K., Fuke, H., Haino, S., et al. 2016, *The Astrophysical Journal*, 822, 65
- Abramowski, A., Aharonian, F., Ait Benkhali, F., et al. 2014, *Phys. Rev. D*, 90, 122007
- Acharya, B. S., Actis, M., Aghajani, T., et al. 2013, *Astroparticle Physics*, 43, 3
- Ackermann, M., Ajello, M., Albert, A., et al. 2015, *The Astrophysical Journal*, 799, 86
- Ackermann, M., Ajello, M., Allafort, A., et al. 2013, *Science*, 339, 807
- Ackermann, M., Ajello, M., Atwood, W., et al. 2012, *The Astrophysical Journal*, 750, 3
- Adriani, O., Akaike, Y., Asano, K., et al. 2019, *Physical review letters*, 122, 181102
- Adriani, O., Barbarino, G., Bazilevskaya, G., et al. 2013, *The Astrophysical Journal*, 770, 2
- Ageron, M., Aguilar, J. A., Al Samarai, I., et al. 2011, *Nuclear Instruments and Methods in Physics Research A*, 656, 11
- Aguilar, M., Aisa, D., Alpat, B., et al. 2015, *Physical Review Letters*, 114, 171103
- Aguilar, M., Alberti, G., Alpat, B., et al. 2013, *Physical Review Letters*, 110, 141102
- Aguilar, M., Ali Cavasonza, L., Ambrosi, G., et al. 2016, *Phys. Rev. Lett.*, 117, 231102

- Aharonian, F., Akhperjanian, A., De Almeida, U. B., et al. 2008, *Physical Review Letters*, 101, 261104
- Aharonian, F., Akhperjanian, A. G., Aye, K.-M., et al. 2004, *Astroparticle Physics*, 22, 109
- Aharonian, F., Akhperjanian, A. G., Bazer-Bachi, A. R., et al. 2006, *Astronomy and Astrophysics*, 457, 899
- Ahn, E.-J., Engel, R., Gaisser, T. K., Lipari, P., & Stanev, T. 2009, *Physical Review D*, 80, 094003
- Ahn, H. S., Seo, E. S., Adams, J. H., et al. 2006, *Advances in Space Research*, 37, 1950
- Albert, A., Funk, S., Katagiri, H., et al. 2017, *Astroparticle Physics*, 92, 49
- Albert, J., Aliu, E., Anderhub, H., et al. 2008, *Nuclear Instruments and Methods in Physics Research A*, 594, 407
- Aleksić, J., Alvarez, E. A., Antonelli, L. A., et al. 2012, *Astroparticle Physics*, 35, 435
- Alfaro, R., Alvarez, C., Álvarez, J., et al. 2017, *Physical Review D*, 96, 122001
- Aloisio, R., Berezhinsky, V., & Gazizov, A. 2012, *Astroparticle Physics*, 39, 129
- Aloisio, R., Blasi, P., & Serpico, P. 2015, *Astronomy & Astrophysics*, 583, A95
- An, Q., Asfandiyarov, R., Azzarello, P., et al. 2019, *Science Advances*, 5, eaax3793
- Antoni, T., Apel, W., Badea, F., et al. 2004, *The Astrophysical Journal*, 612, 914
- Apel, e. W., Arteaga, J., Badea, A., et al. 2010, *Nuclear Instruments and Methods in Physics Research Section A: Accelerators, Spectrometers, Detectors and Associated Equipment*, 620, 202
- Apel, W., Arteaga-Velázquez, J., Bekk, K., et al. 2011, *Physical Review Letters*, 107, 171104
- Apel, W., Arteaga-Velazquez, J., Bekk, K., et al. 2012, *Astroparticle Physics*, 36, 183
- Apel, W., Arteaga-Velazquez, J., Bekk, K., et al. 2014, *Advances in Space Research*, 53, 1456
- Arthur C. Clarke. 1962, in *Profiles of the Future: An Inquiry into the Limits of the Possible*
- Asakimori, K., Burnett, T. H., Cherry, M. L., et al. 1998, *The Astrophysical Journal*, 502, 278
- Atkin, E., Bulatov, V., Dorokhov, V., et al. 2018, *JETP Letters*, 108, 5
- Atwood, W. B., Abdo, A. A., Ackermann, M., et al. 2009, *Astrophysical Journal*, 697, 1071
- Baade, W. & Zwicky, F. 1934, *Proceedings of the National Academy of Sciences*, 20, 259
- Bartoli, B., Bernardini, P., Bi, X., et al. 2015, *Physical Review D*, 91, 112017
- Bass, S. A., Belkacem, M., Bleicher, M., et al. 1998, *Progress in Particle and Nuclear Physics*, 41, 255

- Bechtol, K., Funk, S., Okumura, A., et al. 2012, *Astroparticle Physics*, 36, 156
- Bell, A. 1978, *Monthly Notices of the Royal Astronomical Society*, 182, 147
- Bell, A. R. 2013, *Astroparticle Physics*, 43, 56
- Berge, D., Funk, S., & Hinton, J. 2007, *Astronomy and Astrophysics*, 466, 1219
- Bernlöhner, K. 2001, CORSIKA and sim_telarray – Simulation of the imaging atmospheric Cherenkov technique, https://www.mpi-hd.mpg.de/hfm/~bernlöhner/sim_telarray/Documentation/sim_hessarray.pdf, last revised: August 31, 2018
- Bernlöhner, K. 2008, *Astroparticle Physics*, 30, 149
- Bernlöhner, K., Carrol, O., Cornils, R., et al. 2003, *Astroparticle Physics*, 20, 111
- Bethe, H. & Heitler, W. 1934, *Proceedings of the Royal Society of London. Series A, Containing Papers of a Mathematical and Physical Character*, 146, 83
- Biland, A. 2011, *International Cosmic Ray Conference*, 9, 195
- Blandford, R. D. & Ostriker, J. P. 1978, *The Astrophysical Journal*, 221, L29
- Blasi, P., Amato, E., & Serpico, P. D. 2012, *Physical Review Letters*, 109, 061101
- Bleicher, M., Zabrodin, E., Spieles, C., et al. 1999, *Journal of Physics G Nuclear Physics*, 25, 1859
- Bolz, O. 2004, Absolute Energiekalibration der abbildenden Cherenkov-Teleskope des H.E.S.S. Experiments und Ergebnisse erster Beobachtungen des Supernova-Überrests RX J1713.7-3946, PhD Thesis at Ruprecht-Karls-Universität Heidelberg
- Byrum, K., Humensky, T. B., Benbow, W., et al. 2015, *ArXiv e-prints*
- Caprioli, D. 2012, *Journal of cosmology and astroparticle physics*, 2012, 038
- Catalano, J. 2016, Characterization of a custom designed trigger ASIC (T5TEA) for the Cherenkov Telescope Array, Bachelor Thesis at Friedrich-Alexander-Universität Erlangen-Nürnberg
- Cherenkov, P. A. 1934, *Doklady Akademii Nauk SSSR*, 2, 451
- Cherenkov Telescope Array Consortium, T., :, Acharya, B. S., et al. 2017, *ArXiv e-prints*
- Cogan, P. 2008, *International Cosmic Ray Conference*, 3, 1369
- Collaboration, T. A., Collaboration, P. A., et al. 2018, *arXiv preprint arXiv:1801.01018*
- Cornils, R., Gillessen, S., Jung, I., et al. 2003, *Astroparticle Physics*, 20, 129
- Cortina, J. & Teshima, M. 2015, in *International Cosmic Ray Conference*, Vol. 34, 34th International Cosmic Ray Conference (ICRC2015), 943
- Coste, B., Derome, L., Maurin, D., & Putze, A. 2012, *Astronomy and Astrophysics*, 539, A88

- CTA Consortium. 2018a, CTA Observatory, <https://www.cta-observatory.org>, accessed: 31.08.2018
- CTA Consortium. 2018b, CTA Observatory Performance, <https://www.cta-observatory.org/science/cta-performance>, accessed: 31.08.2018
- CTA Consortium. 2018c, CTA Requirements, <https://jama.cta-observatory.org>, accessed: 18.07.2018
- De Naurois, M. & Rolland, L. 2009, *Astroparticle Physics*, 32, 231
- Derbina, V. A., Galkin, V. I., Hareyama, M., et al. 2005, *The Astrophysical Journal*, 628, L41
- Drescher, H. J., Hladik, M., Ostapchenko, S., Pierog, T., & Werner, K. 2001, *Physics Reports*, 350, 93
- Engel, R. 1999, in *International Cosmic Ray Conference*, Vol. 1, 415
- Fang, K., Kotera, K., & Olinto, A. V. 2012, *The Astrophysical Journal*, 750, 118
- Fang, K. & Murase, K. 2018, *Nature Physics*, 14, 396
- Fasso', A., Ferrari, A., Roesler, S., et al. 2003, arXiv e-prints, hep
- Fermi, E. 1949, *Phys. Rev.*, 75, 1169
- Fesefeldt, H. 1985, *The simulation of hadronic showers: physics and applications*, Tech. rep.
- Fletcher, R. S., Gaisser, T. K., Lipari, P., & Stanev, T. 1994, *Physical Review D*, 50, 5710
- Frank, I. M. & Tamm, I. E. 1937, *Compt. Rend. Acad. Sci. URSS*, 14, 109, [Dokl. Akad. Nauk SSSR14,no.3,107(1937); Usp. Fiz. Nauk93,no.2,388(1967)]
- Funk, S. 2005, *A new population of very high-energy gamma-ray sources detected with H.E.S.S. in the inner part of the Milky Way*, PhD Thesis at Ruprecht-Karls-Universitaet Heidelberg
- Funk, S., Jankowsky, D., Katagiri, H., et al. 2017, in *American Institute of Physics Conference Series*, Vol. 1792, 6th International Symposium on High Energy Gamma-Ray Astronomy, 080012
- Gaisser, T. K., Stanev, T., & Tilav, S. 2013, *Frontiers of Physics*, 8, 748
- Giavitto, G., Ashton, T., Balzer, A., et al. 2015, in *34th International Cosmic Ray Conference (ICRC2015)*, Vol. 34, 996
- Ginzburg, V. L. & Syrovatsky, S. 1961, *Progress of Theoretical Physics Supplement*, 20, 1
- Glicenstein, J. F., Abril, O., Barrio, J.-A., et al. 2015, in *International Cosmic Ray Conference*, Vol. 34, 34th International Cosmic Ray Conference (ICRC2015), 937
- Green, D. M. 2016, *Measurement of the cosmic-ray proton spectrum from 54 GeV to 9.5 TeV with the Fermi Large Area Telescope*, PhD Thesis at University of Maryland

- Guo, Y.-Q. & Yuan, Q. 2018, *Chinese Physics C*, 42, 075103
- Hahn, J., De los Reyes, R., Bernlöhr, K., et al. 2014, *Astroparticle Physics*, 54, 25
- Hahn, J., Gast, H., Reyes, R., et al. 2013, Heidelberg Data Quality Selection, H.E.S.S. internal note
- Hanlon, W. F. 2008, *The Energy Spectrum Of Ultra High Energy Cosmic Rays Measured By The High Resolution Fly's Eye Observatory In Stereoscopic Mode*, PhD Thesis at the University of Utah
- Heck, D., Knapp, J., Capdevielle, J. N., Schatz, G., & Thouw, T. 1998, CORSIKA: a Monte Carlo code to simulate extensive air showers.
- HEGRA Collaboration: A. Daum. 1997, arXiv Astrophysics e-prints
- Heller, T. 2016, *Verbesserung der Ladungsaufösung einer Gamma -Strahlungskamera*, Bachelor Thesis at Friedrich-Alexander-Universitaet Erlangen-Nuernberg
- Hess, V. F. 1912, *Phys. Z.*, 13, 1084
- H.E.S.S. Collaboration, Abdalla, H., Abramowski, A., et al. 2018a, *Astronomy and Astrophysics*, 612, A1
- H.E.S.S. Collaboration, Abdalla, H., Aharonian, F., et al. 2018b, *A&A*, 620, A66
- H.E.S.S. Consortium. 2019, H.E.S.S. High Energy Stereoscopic System, <https://www.mpi-hd.mpg.de/hfm/HESS/>, accessed: 14.10.2019
- Hillas, A. M. 1984, *Annual Review of Astron and Astrophys*, 22, 425
- Hillas, A. M. 1985, *International Cosmic Ray Conference*, 3
- Hillig, C. 2019, *Analyzing The Cosmic Ray Spectrum Based On Imaging Atmospheric Cherenkov Telescope Data nUsing Deep Learning Methods*, Master Thesis at Friedrich-Alexander-Universitaet Erlangen-Nuernberg
- Hinton, J. 2004, *New Astronomy Reviews*, 48, 331 , 2nd VERITAS Symposium on the Astrophysics of Extragalactic Sources
- Hinton, J. A. & Hofmann, W. 2009, *Annual Review of Astron and Astrophys*, 47, 523
- Hofmann, W., Jung, I., Konopelko, A., et al. 1999, *Astroparticle Physics*, 12, 135
- Holder, J., Acciari, V. A., Aliu, E., et al. 2008, in *American Institute of Physics Conference Series*, Vol. 1085, American Institute of Physics Conference Series, ed. F. A. Aharonian, W. Hofmann, & F. Rieger, 657–660
- Holler, M., Chevalier, J., Lenain, J. P., Sanchez, D., & de Naurois, M. 2017, *International Cosmic Ray Conference*, 35, 755
- Hörandel, J. R. 2003, *Astroparticle Physics*, 19, 193
- Hörandel, J. R. 2004, *Astroparticle Physics*, 21, 241

- Hu, H. 2009, arXiv e-prints
- IceCube Collaboration and others. 2018, *Science*, 361, eaat1378
- Jogler, T. & Funk, S. 2016, *The Astrophysical Journal*, 816, 100
- Jules Verne. 1873, *Around the World in Eighty Days* (Pierre-Jules Hetzel)
- Keysight Technologies. 2015, Keysight Trueform Series Wellengenerator, <https://literature.cdn.keysight.com/litweb/pdf/33500-90911.pdf>, accessed: 21.02.2019
- Keysight Technologies. 2017, Keysight InfiniiVision 3000 X-Series Oszilloskope, <https://literature.cdn.keysight.com/litweb/pdf/75019-97094.pdf>, accessed: 21.02.2019
- Kraus, M. 2018, *The Cosmic-Ray Electron Anisotropy Measured with H.E.S.S. and Characterization of a Readout System for the SST Cameras of CTA*, PhD Thesis at Friedrich-Alexander-Universitaet Erlangen-Nuernberg
- Lagage, P. & Cesarsky, C. 1983, *Astronomy and Astrophysics*, 125, 249
- Le Blanc, O., Fasola, G., Dournaux, J.-L., et al. 2017, ArXiv e-prints
- Leach, S., Lapington, J., Ross, D., et al. 2020, *Nuclear Instruments and Methods in Physics Research Section A: Accelerators, Spectrometers, Detectors and Associated Equipment*, 952, 161746
- Leach, S., Lapington, J., Williams, J., Duffy, C., et al. 2019, *Nuclear Instruments and Methods in Physics Research Section A: Accelerators, Spectrometers, Detectors and Associated Equipment*
- Lewis, D. A. 1990, *Experimental Astronomy*, 1, 213
- Liu, W., Bi, X.-J., Lin, S.-J., Wang, B.-B., & Yin, P.-F. 2017, *Physical Review D*, 96, 023006
- Longair, M. S. 2011, *High energy astrophysics* (Cambridge university press)
- Maccarone, M. C. 2017, ArXiv e-prints
- Matthews, J. 2005, *Astroparticle Physics*, 22, 387
- Mewaldt, R. A., Yanasak, N. E., Wiedenbeck, M. E., et al. 2001, *Space Science Reviews*, 99, 27
- Mitchell, A., Marandon, V., & Parsons, R. 2015, in *34th International Cosmic Ray Conference (ICRC2015)*, Vol. 34, 756
- Montaruli, T., Consortium, C., sub-Consortium, S.-., et al. 2015, in *International Cosmic Ray Conference*, Vol. 34, *34th International Cosmic Ray Conference (ICRC2015)*, 1043
- Ohm, S. & Hinton, J. 2011, *Proceedings of the International Astronomical Union*, 7, 382
- Ohm, S., van Eldik, C., & Egberts, K. 2009, *Astroparticle Physics*, 31, 383
- Ostapchenko, S. 2011, *Physical Review D*, 83, 014018

- Ostapchenko, S. 2014, *Physical Review D*, 89, 074009
- Otte, N., Biteau, J., Dickinson, H., et al. 2015, in *International Cosmic Ray Conference*, Vol. 34, 34th International Cosmic Ray Conference (ICRC2015), 1023
- Parsons, R., Bleve, C., Ostapchenko, S., & Knapp, J. 2011, *Astroparticle Physics*, 34, 832
- Parsons, R. & Hinton, J. 2014, *Astroparticle Physics*, 56, 26
- Pierog, T. & Werner, K. 2009, *Nuclear Physics B Proceedings Supplements*, 196, 102
- Pierre Auger Collaboration. 2015, *Nuclear Instruments and Methods in Physics Research Section A: Accelerators, Spectrometers, Detectors and Associated Equipment*, 798, 172
- Pretz, J. 2015, in *International Cosmic Ray Conference*, Vol. 34, 34th International Cosmic Ray Conference (ICRC2015), 25
- Ptuskin, V., Zirakashvili, V., & Seo, E.-S. 2010, *The Astrophysical Journal*, 718, 31
- Ptuskin, V., Zirakashvili, V., & Seo, E.-S. 2013, *The Astrophysical Journal*, 763, 47
- Puehlhofer, G., Bauer, C., Bernhard, S., et al. 2015, in *International Cosmic Ray Conference*, Vol. 34, 34th International Cosmic Ray Conference (ICRC2015), 1039
- Pühlhofer, G. 2017, in *American Institute of Physics Conference Series*, Vol. 1792, 6th International Symposium on High Energy Gamma-Ray Astronomy, 080002
- Punch, M., Collaboration, H., et al. 2001, in *International Cosmic Ray Conference*, Vol. 7, 2814
- Ranft, J. 1999a, arXiv e-prints, hep
- Ranft, J. 1999b, arXiv e-prints, hep
- Reif, M. 2017, *Study of CHEC-S TARGET C Module Trigger Performance*, Bachelor Thesis at Friedrich-Alexander-Universitaet Erlangen-Nuernberg
- Riehn, F. & et al. 2017, in *International Cosmic Ray Conference*, Vol. 35, 35th International Cosmic Ray Conference (ICRC2015)
- Schaefer, J. 2016, *Parameter optimization of the T5TEA-ASIC for the Cherenkov Telescope Array*, Bachelor Thesis at Friedrich-Alexander-Universitaet Erlangen-Nuernberg
- Schaefer, J. 2019, *Temperature dependent aspects of the Compact High Energy Camera (CHEC-S) Front End Electronic (FEE) calibration*, Master Thesis at Friedrich-Alexander-Universitaet Erlangen-Nuernberg
- Schioppa, E. J., Cadoux, F., Christov, A., et al. 2015, ArXiv e-prints
- Schure, K. M. & Bell, A. R. 2013, *Monthly Notices of the RAS*, 435, 1174
- Schwarzschild, K. 1905, *Astronomische Mitteilungen der Universitaets-Sternwarte zu Goettingen*, 10

- Seo, E.-S., Anderson, T., Angelaszek, D., et al. 2014, *Advances in Space Research*, 53, 1451
- Shilon, I., Kraus, M., Büchele, M., et al. 2019, *Astroparticle Physics*, 105, 44
- Sol, H., Greenshaw, et al. 2017, *ArXiv e-prints*
- Stahl, B. 2014, internal study
- Strong, A. W., Moskalenko, I. V., & Ptuskin, V. S. 2007, *Annual Review of Nuclear and Particle Science*, 57, 285
- Strong, A. W., Moskalenko, I. V., & Reimer, O. 2004, *The Astrophysical Journal*, 613, 962
- Tanabashi, M., Hagiwara, K., Hikasa, K., et al. 2018, *Phys. Rev. D*, 98, 030001
- Tavani, M., Barbiellini, G., Argan, A., et al. 2009, *Astronomy and Astrophysics*, 502, 995
- Thoudam, S. & Hörandel, J. R. 2013, *arXiv preprint arXiv:1308.1357*
- Thoudam, S. & Hörandel, J. R. 2014, *Astronomy & Astrophysics*, 567, A33
- Tibaldo, L., Vandenbroucke, J., Albert, A., et al. 2015, in *International Cosmic Ray Conference*, Vol. 34, 34th International Cosmic Ray Conference (ICRC2015), ed. A. S. Borisov, V. G. Denisova, Z. M. Guseva, E. A. Kanevskaya, M. G. Kogan, A. E. Morozov, V. S. Puchkov, S. E. Pyatovsky, G. P. Shoziyoev, M. D. Smirnova, A. V. Vargasov, V. I. Galkin, S. I. Nazarov, & R. A. Mukhamedshin, 932
- Tomassetti, N. 2012, *The Astrophysical Journal Letters*, 752, L13
- Tomassetti, N. 2015a, *Physical Review D*, 92, 081301
- Tomassetti, N. 2015b, *The Astrophysical Journal Letters*, 815, L1
- Uchiyama, Y., Aharonian, F. A., Tanaka, T., Takahashi, T., & Maeda, Y. 2007, *Nature*, 449, 576
- Varner, G., Ruckman, L., & Wong, A. 2008, *Nuclear Instruments and Methods in Physics Research A*, 591, 534
- Varner, G., Ruckman, L. L., Schwiening, J., & Va'vra, J. 2007a, in *International workshop on new photon-detectors PD07*, Citeseer
- Varner, G. S., Ruckman, L. L., Nam, J. W., et al. 2007b, *Nuclear Instruments and Methods in Physics Research A*, 583, 447
- Vassiliev, V., Fegan, S., & Brousseau, P. 2007, *Astroparticle Physics*, 28, 10
- Vink, J. & Laming, J. M. 2003, *The Astrophysical Journal*, 584, 758
- Vinogradov, S. 2012, *Nuclear Instruments and Methods in Physics Research A*, 695, 247
- Völk, H. J., Berezhko, E. G., & Ksenofontov, L. T. 2005, *Astronomy & Astrophysics*, 433, 229
- Völk, H. J. & Bernlöhr, K. 2009, *Experimental Astronomy*, 25, 173

- Walter, M. 2012, 100 Years of Cosmic Rays
- Watson, J. J. 2018, Calibration and Analysis of the GCT Camera for the Cherenkov Telescope Array, PhD Thesis at Brasenose College, University of Oxford
- Watson, J. J. & Zorn, J. 2019, arXiv preprint arXiv:1907.09252
- Weekes, T. C., Cawley, M., Fegan, D., et al. 1989, *The Astrophysical Journal*, 342, 379
- Werner, K. 1993, *Physics Reports*, 232, 87
- Werner, K., Liu, F.-M., & Pierog, T. 2006, *Physical Review C*, 74, 044902
- White, R., Schoorlemmer, H., & CTA GCT project, f. t. 2017, ArXiv e-prints
- Winkler, C., Diehl, R., Ubertini, P., & Wilms, J. 2011, *Space Science Reviews*, 161, 149
- Yoon, Y., Anderson, T., Barrau, A., et al. 2017, *The Astrophysical Journal*, 839, 5
- Yoon, Y. S., Ahn, H. S., Allison, P. S., et al. 2011, *Astrophysical Journal*, 728, 122
- Zatsepin, V. & Sokolskaya, N. V. 2006, *Astronomy & Astrophysics*, 458, 1
- Zhang, S.-N., Bi, X., Chen, G., et al. 2017, *PoS*, 1077
- Zorn, J., White, R., Watson, J. J., et al. 2018, ArXiv e-prints

Acknowledgements/Danksagung

Nun ist das Ende dieser Dissertation also endlich erreicht. Und wenn man sich nochmal die letzten Jahre an harter Arbeit durch den Kopf gehen lässt, so wird schnell klar, dass der erfolgreiche Abschluss der Arbeit nur durch die Unterstützung anderer Personen möglich war. Die folgende Seite möchte ich deshalb nutzen, all diesen zu danken.

Als erstes möchte ich natürlich Prof. Dr. Stefan Funk danken, der es mir ermöglicht hat, meine Arbeit hier am ECAP zu verfassen und mich hierbei tatkräftigt unterstützt hat. Außerdem gab er mir auch immer wieder die Gelegenheit, meine Arbeit auf Konferenzen vorzutragen, mich auf diversen Workshops weiter zu bilden und die H.E.S.S. Teleskope in Namibia live zu erleben.

Weiterhin möchte ich insbesondere Ira Jung-Richardt und Adrian Zink danken. Danke Ira, dass du immer ein offenes Ohr für meine Probleme bei der H.E.S.S. Analyse hattest, immer Ideen hattest, die mir weiterhelfen konnten und auch für das Korrekturlesen meiner Arbeit. Danke Adrian, dass du mich in das Gebiet der Hardware trotz meinem geringen Vorwissen eingeführt hast, mir immer geholfen hast, wenn ich mal auf dem Schlauch stand und ebenso zum Ende meine Arbeit Korrektur gelesen hast.

Meine lieben Bürokollegen in der 309: Alex, Manu und Stefan, aber natürlich auch Kaori, Florian und Jacky, die später eingezogen sind. Vielen Dank, dass ich euch Tag für Tag sehen durfte (ja, ernst gemeint). Danke, für die vielen interessanten Diskussion und Unterstützung bei diversen Problemen, aber auch für die sehr angenehme und lockere Atmosphäre.

Aber natürlich auch ein großes Dankeschön an die gesamte Gamma Gruppe in Erlangen. Allen voran Johannes und Lars, die mir oft bei Problemen mit H.E.S.S. und dessen Analyse Software weitergeholfen haben, aber auch Prof. Dr. Christopher van Eldik, der mir auch immer wieder alle möglichen Fragen beantworten konnte. Außerdem möchte ich Marc danken, der neben allen arbeitsrelevanten Fragen auch für alles Drumherum ein offenes Ohr hatte, und natürlich Gabi Eckner, die bei allen organisatorischen Dingen eine sehr große Hilfe war. Neben diesen Personen im Speziellen, möchte ich jeden in der Gruppe für die super Arbeitsatmosphäre danken. Aber es war nicht alles nur Arbeit, ich werde auch alle Aktivitäten mit euch, seien es Pub-Abende, sportliche Unternehmungen oder auch einfach nur das gemeinsame Mittagessen, vermissen. Ihr wart nicht nur einfach Kollegen, sondern Freunde.

Ebenso ein Dankeschön an das gesamte ECAP, es hat Spaß gemacht die letzten Jahre in eurer Gesellschaft zu verbringen. Hier möchte ich auch noch Kay Graf hervorheben, der mir stets bei Fragen rund ums Computing weiterhelfen konnte.

Aber auch neben der Arbeit gab es natürlich viel Unterstützung. Danke Simon, Matthias und Markus für die Schafkopfabende und die Feierabendbiere, die nach geleisteter Arbeit immer wieder für Entspannung sorgten. Außerdem, Matthias, vielen Dank für die super Zeit in Namibia bei den Teleskopen und im Urlaub danach. Aber auch allen anderen Leuten hier in Erlangen, die ich während meines Studiums und meiner Promotion kennen lernen durfte und mit denen ich gerne Zeit verbracht habe. Auch möchte ich meinen Freunden in der Heimat danken, die ich teilweise fast so lange kenne wie ich lebe. Ich kann euch nicht alle beim Namen nennen, aber vielen Dank für den Rückhalt aus der Oberpfalz.

Zu guter letzt möchte ich noch meinen Eltern danken: Danke, dass ihr mich mein ganzes Leben lang unterstützt habt, ihr habt mir alles ermöglicht was ich wollte und mit eurer Unterstützung maßgeblich dazu beigetragen, dass ich diese Arbeit schaffen konnte. Ich hätte mir nur gewünscht, dass auch mein Vater noch das Ende mit erleben hätte dürfen...